

**SIMULTANEOUS OPTICAL AND MR IMAGING OF TISSUE WITHIN IMPLANTED  
WINDOW CHAMBER: SYSTEM DEVELOPMENT AND APPLICATION IN  
MEASURING VASCULAR PERMEABILITY**

by

Mir Farrokh Shayegan Salek

---

A Dissertation Submitted to the Faculty of the

DEPARTMENT OF OPTICAL SCIENCES

In Partial Fulfillment of the Requirements

For the Degree of

DOCTOR OF PHILOSOPHY

In the Graduate College

THE UNIVERSITY OF ARIZONA

2013

**THE UNIVERSITY OF ARIZONA  
GRADUATE COLLEGE**

As members of the Dissertation Committee, we certify that we have read the dissertation prepared by Mir Farrokh Shayegan Salek, titled Simultaneous Optical and MR Imaging of Tissue within Implanted Window Chamber: System Development and Application in Measuring Vascular Permeability and recommend that it be accepted as fulfilling the dissertation requirement for the Degree of Doctor of Philosophy.

\_\_\_\_\_ Date: (7/29/2013)  
Eric Clarkson

\_\_\_\_\_ Date: (7/29/2013)  
Arthur Gmitro

\_\_\_\_\_ Date: (7/29/2013)  
Mark Pagel

\_\_\_\_\_ Date: (7/29/2013)  
Natarajan Raghunand

Final approval and acceptance of this dissertation is contingent upon the candidate's submission of the final copies of the dissertation to the Graduate College.

I hereby certify that I have read this dissertation prepared under my direction and recommend that it be accepted as fulfilling the dissertation requirement.

\_\_\_\_\_ Date: (            )  
Dissertation Director: Arthur Gmitro

**STATEMENT BY AUTHOR**

This dissertation has been submitted in partial fulfillment of the requirements for an advanced degree at the University of Arizona and is deposited in the University Library to be made available to borrowers under rules of the Library.

Brief quotations from this dissertation are allowable without special permission, provided that an accurate acknowledgement of the source is made. Requests for permission for extended quotation from or reproduction of this manuscript in whole or in part may be granted by the author.

SIGNED: Mir Farrokh Shayegan Salek

## ACKNOWLEDGEMENTS

Dr. Arthur Gmitro: For being the best adviser a PhD student can expect to have: Supportive at all stages, encouraging, meticulous, knowledgeable patient and ethical. This dissertation would not have been accomplished without his exceptional support.

Dr. Mark Pagel: For providing exceptional support in the areas of MRI, cancer biology and chemistry, also for encouraging and motivating me at all times.

Dr. Natarajan Raghunand and Dr. Eric Clarckson: Being in my defense committee and providing support.

Dr. Jean-Phillip Galons and Dr. Ted Trouard: Providing helpful comments and consultation on the diffusion weighted and DCE MRI problems.

Dr. Dominique Jennings: For founding some of the basis of this work especially in the areas of animal care and molecular agent labeling, and also for sharing her experience at full scale.

Christine Howison, Bethany Skovan and Gillian Paine: For providing animal models and helping with the animal model experiments.

Constanin Job: Making a MRI surface coil and helping with the MRI scanner issues.

Dr. Ronie George: For encouraging me in this research.

Dr. Jalal Shayegan: My dad, for supporting me at all stages and giving the most insightful advices based on his very deep understanding of me.

ABRC grant: For funding this research.

## TABLE OF CONTENTS

<b>LIST OF FIGURES .....</b>	<b>10</b>
<b>LIST OF TABLES .....</b>	<b>12</b>
<b>ABSTRACT .....</b>	<b>13</b>
<b>CHAPTER 1: INTRODUCTION.....</b>	<b>14</b>
1.1: Overview .....	14
1.2: Motivation for Simultaneous Imaging .....	14
1.3: Window Chambers .....	15
1.4: Animal Preparations .....	16
1.5: Summary of the Dissertation .....	16
<b>CHAPTER 2: MOLECULAR AGENT .....</b>	<b>18</b>
2.1: Overview .....	18
2.2: The Contrast Agent Applied.....	18
2.2.1: The Optical CA.....	18
2.2.2: The MRI CA.....	19
2.2.3: The Molecular Agent (MA).....	21
2.3: Labeling BSA.....	22
<b>CHAPTER 3: IMAGING SYSTEMS .....</b>	<b>25</b>
3.1 Overview .....	25
3.2 MRI Scanner and Surface Coil.....	26
3.3 Imaging with an Imaging Fiber Bundle .....	28
3.4 Imaging with a Small Camera.....	30
3.5 Illumination System for the relay imaging system.....	34
3.6 The Relay System .....	36
3.7 Comparison of the Dual Modality Systems.....	40

## TABLE OF CONTENTS - Continued

<b>CHAPTER 4: MEASURING VASCULAR PERMEABILITY WITH OPTICAL MICROSCOPY .....</b>	<b>42</b>
4.1: Overview .....	42
4.2: Two Compartment Model .....	43
4.3: Measuring Vascular Kinetic Parameters in DSFC with Confocal Microscopy [1] .....	45
4.4: Measuring Vascular Kinetic Parameters, Method of Wu, et al. [2] .....	46
4.5: Measuring Vascular Kinetic Parameters, Method of Yuan, et al. [4] .....	48
4.5.1: Outline .....	48
4.5.2: Assumptions .....	48
4.5.3: Distinguishing the IV and EV components of the Signal .....	49
4.5.4: Estimating Vascular Kinetics of the MA .....	49
4.5.5: Estimating $K_{trans}$ .....	50
4.6 Analysis of Previous Methods and New Methodology .....	51
4.6.1 Outline .....	51
4.6.2 Determining the IV and EV Signal Components .....	52
4.6.3 Measuring Kinetic Parameters .....	54
4.6.4 Applied Methodology .....	56
 <b>CHAPTER 5: MEASURING VASCULAR PERMEABILITY WITH MRI .....</b>	 <b>58</b>
5.1: Overview .....	58
5.2: Tissue Modeling .....	60
5.3: The Dynamic Sequence .....	60
5.4: The $T_1$ Sequence .....	61
5.5: Water Exchange .....	61
5.5.1: Theory .....	61
5.5.2: Adjacent Water Exchange Compartments .....	63
5.5.3: Transverse Relaxation .....	64
5.5.4: Water Exchange Status Prior to MA Injection .....	64

## **TABLE OF CONTENTS - Continued**

5.5.5: Water Exchange Status after MA Injection.....	65
5.5.6: Water Exchange Status in Our Experiments.....	65
5.6: T <sub>2</sub> Effect on the Signal.....	67
5.7: Partial Volume Effect.....	68
5.7.1: Introduction.....	68
5.7.2: Measuring AIF.....	69
5.7.3: Measuring Extravascular Concentration.....	70
5.7.4: Partial Volume Effect and Water Exchange.....	72
5.7.5: A Suggested Approach.....	72
5.8: Application of Diffusion MRI in DCE-MRI.....	74
5.8.1: Introduction.....	74
5.8.2: DWI Sequence.....	75
5.9: Applied Methodologies.....	76
5.9.1: Introduction.....	76
5.9.2: Estimating Kinetic Parameters.....	76
5.9.3: Diffusion Weighted Imaging.....	77
<b>CHAPTER 6: RESULTS AND DISCUSSION .....</b>	<b>79</b>
6.1: Overview.....	79
6.2: The Experiments.....	79
6.3: Analysis Programs.....	80
6.4: Testing the Analysis Programs.....	81
6.5: Tissue Structure.....	81
6.6: Measuring T <sub>1</sub> .....	82
6.7: Measuring T <sub>2</sub> and Compensating Its Effect.....	83
6.8: Concentration Measurement in MRI.....	84
6.9: Signal Fluctuation.....	86
6.9.1: Introduction to the Problem.....	86
6.9.2: Two Examples.....	87
6.9.3: Investigation of the Source of Signal Fluctuations.....	90

## **TABLE OF CONTENTS - Continued**

6.9.4: Conclusion.....	94
6.10: Estimating Vascular Kinetic Parameters .....	94
6.10.1: Summary .....	94
6.10.2: Estimation Process .....	96
6.10.3: Results.....	96
6.11: Diffusion Weighted Imaging (DWI).....	100
<b>CHAPTER 7: FUTURE DIRECTIONS .....</b>	<b>103</b>
7.1: Overview .....	103
7.2: Instrumentation.....	103
7.3: Experimentation .....	104
7.4: MA and Animal Preparation .....	105
7.4: DCE-MRI .....	105
7.5: Simultaneous Dual Modality Imaging Applications .....	106
7.5.1: Measuring Vascular Kinetic Parameters .....	106
7.5.2: Other Applications .....	106
7.6: Conclusions .....	107
<b>APPENDIX .....</b>	<b>108</b>
Appendix 5.A.1: Exact Solution to the Modified Bloch Equation .....	108
Appendix 5.A.2: Estimating MA Concentration in the IV and EV Compartments .....	109
Appendix 5.A.3: Guided Bi-Exponential Fitting to the $T_1$ Sequence Signal.....	109
Appendix 6.A.1: Experiments.....	110
Appendix 6.A.2: MRI Sequences Details for Each Experiment .....	113
Appendix 6.A.3: Estimated $T_1$ Values (ms).....	115
Appendix 6.A.4: Comparison of MRI and Optical Signal Intensity.....	115
Appendix 6.A.5: Kinetic Parameters Estimations .....	130
<b>REFERENCES .....</b>	<b>134</b>
Chapter 1.....	134

**TABLE OF CONTENTS - Continued**

Chapter 2.....	136
Chapter 3.....	137
Chapter 4.....	138
Chapter 5.....	139
Chapter 6.....	142
Chapter 7.....	145

## LIST OF FIGURES

Fig. 1.1 Plastic Window Chamber Design.....	16
Fig 2.1 Absorption of Tissue .....	19
Fig 2.2 Relaxation Rates Versus Concentration of Gd-DTPA .....	22
Fig. 3.1 MR surface coil built by Constantin Job .....	27
Fig. 3.2 Doty surface coil.....	27
Fig. 3.3 Overall simultaneous MR/Optical imaging system design .....	28
Fig. 3.4 System 2, imaging with imaging fiber without folding mirror.....	29
Fig. 3.5 Sample images of the window chamber obtained with Optical and MR imaging by system .....	30
Fig. 3.6 System 3, imaging with small camera .....	32
Fig 3.7 Sample images by small camera system.....	33
Fig. 3.8 Diagram of the illumination system. ....	35
Fig. 3.9 Illustration of combining two positive lenses to create a more powerful tunable negative lens .....	36
Fig. 3.10 Relay system diagram.....	38
Fig. 3.11 Relay system.....	39
Fig. 3.12 Simultaneous MR and optical images of a window chamber .....	40
Fig. 6.1 Images of a window chamber taken with the dual modality imaging system.....	82
Fig 6.2 $T_1$ value at each pixel, and total intravascular to total proton density ratio .....	83
Fig 6.3 $T_2$ value measured before and immediately after the injection of the MA.....	84
Fig 6.4 $r_1C$ at $t=0$ , and the difference between $r_1C$ at $t=30$ min and $t=0$ . ....	85
Fig 6.5 $r_2C$ at $t=0$ , and the difference between $r_2C$ at $t=30$ min and $t=0$ .....	86
Fig 6.6 $r_2C/ r_1C$ at $t=0$ , and the difference between $r_2C/ r_1C$ at $t=30$ min and $t=0$ .....	86
Fig. 6.7 Signal intensity in the three ROIs that were highlighted in Fig. 6.1. ....	88
Fig. 6.8 Optical and MR signal intensity in V_ROIs.....	89
Fig. 6.9 Optical and MR signal intensity in corresponding V_ROIs and H_ROIs.....	90
Fig 6.10 MRI signal intensity as temperature was varied by means of switching hot air current	91
Fig 6.11 $k_{ep}$ in healthy tissue.....	98
Fig 6.12 $k_{ep}$ in tumor center .....	98
Fig 6.13 $v_e$ in tumor center.....	98

## LIST OF FIGURES - Continued

Fig 6.14 $k_{ep}$ in tumor edge .....	99
Fig 6.15 ADC estimates by fitting high b values to the diffusion signal equation.....	99
Fig 6.16 $v_e$ in tumor edge.....	99
Fig. 6.17 ADC estimates by fitting high b values to the diffusion signal equation.....	101
Fig. 6.18 ADC estimates by fitting low b values to the diffusion signal equation.....	101
Fig. 6.19 Vessel distribution obtained by DWI with diffusion gradient along three orthogonal axes .....	101
Fig. 6.20 Vessel distribution obtained by DWI with diffusion gradient along three orthogonal axes .....	102

## LIST OF TABLES

Table 2.1 Relaxivity of Gd-DTPA, and Gd-DTPA Labeled Albumin. ....	20
Table 2.2 T1 and T2 at various concentration of Gd-DTPA(23)-BSA in PBS .....	21
Table 2.3 Relaxivity of Gd-DTPA <sub>23</sub> -BSA .....	22
Table 3.1 CX408 CMOS camera .....	31
Table 3.3 Mechanical specifications of Object FullCure720.....	38
Table 4.1 List of Assumptions .....	52
Table 5.1 Upper limit for the transverse relaxation effect on signal intensity as a result of water exchange. ....	64
Table 5.2 Typical values of the exchange rates relative to longitudinal relaxation rates .....	67
Table 5.3 Typical values of the exchange rates relative to transverse relaxation rate.....	67
Table 5.4 Upper limit estimates of T <sub>2</sub> effect on signal intensity at different concentrations of the MA in the blood and TE=10 ms .....	68

## **ABSTRACT**

Simultaneous optical imaging and MRI of a dorsal skin-fold window chamber mouse model is investigated as a novel methodology to study the tumor microenvironment. Simultaneous imaging with two modalities allows for cross-validation of results, integration of the capabilities of the two modalities in one study and mitigation of invasive factors, such as surgery and anesthesia, in an in-vivo experiment.

To make this investigation possible, three optical imaging systems were developed that operated inside the MRI scanner. One of the developed systems was applied to estimate vascular kinetic parameters of tumors in a dorsal skin-fold window chamber mouse model with simultaneous optical and MRI imaging. The target of imaging was a molecular agent that was dual labeled with both optical and MRI contrast agents. The labeling of the molecular agent, characteristics of the developed optical systems, the methodologies of measuring vascular kinetic parameters using optical imaging and MRI data, and the obtained results are described and illustrated.

## CHAPTER 1: INTRODUCTION

### 1.1: Overview

The first section of this dissertation describes a methodology to do fluorescence and bright field microscopy inside an MRI scanner and also perform MRI. The imaging subject is a mouse Dorsal Skin Fold window Chamber (DSFC). However, the same methodology could be applied to other imaging subjects as long as the subject is appropriate for imaging with both MRI and optical microscopy.

The second section of this dissertation serves as an example of the application of the developed imaging system. Vascular permeability is measured using both methods by injecting a molecular agent that is labeled with both MR and optical contrast agents. The applied optical methodology to measure vascular permeability is based on previously published approaches with some modifications. Dynamic Contrast Enhanced (DCE) MRI is applied to measure vascular permeability from MR images. Several complications in measuring vascular permeability with DCE-MRI were addressed or investigated. The major complications were the transverse relaxation effect, water exchange, and the partial volume effect. The degree of transverse relaxation effect and water exchange was exacerbated by the high concentration of MR contrast agent in the vasculature. High concentrations were applied to partially compensate for the low permeability of the molecular agent used in the study. Partial volume effect refers to the mixing of different tissue types in one voxel due to lack of sufficient imaging resolution. In DCE-MRI, partial volume effect is usually not a major issue because the agent concentration in the vasculature is determined by fixing an MR voxel inside a large artery or vein inside the subject of study. This is not possible in two dimensional imaging of the DSFC. New methodologies were introduced to address the partial volume effect.

### 1.2: Motivation for Simultaneous Imaging

Many biomedical imaging modalities such as PET, optical imaging, MRI, and ultrasound imaging have been applied to study the tumor microenvironment (TM) [1]. These imaging modalities are based on interaction of different forms of energy with tissue and derive contrast from different biophysical mechanisms. Extraction of quantitative biophysical or physiological parameters from images is almost always associated with certain assumptions and approximations. Due to the specific nature of the image formation process, certain modalities are more suitable or precise for particular applications. Recently, increasing attention has been paid to combining several imaging modalities to take advantage of independent sources of information [2-4]. At a minimum, use of

more than one modality allows for cross validation of measurements obtained with different modalities.

In addition to validation, multi-modality imaging can allow for measurement of multiple parameters in a single study. For example, there are several physiological parameters that are critical in studying the TM; such as pH, vascularity, vascular permeability, oxygenation level, metabolism, and interstitial fluid pressure [3, 6-14]. These parameters typically have different values in tumor compared to normal tissue and vary with the degree of development and malignant potential of the tumor [6]. Measurement of these parameters can improve basic understanding of cancer biology and subsequently yield better treatment and prevention strategies. In addition, many parameters are interrelated and their relationship can characterize processes occurring in the TM during tumor growth and metastatic spread [6, 15-17]. For example, abnormal vasculature, can lead to hypoxia, lower extracellular pH, and result in high interstitial pressure [5]. Therefore, measurement of multiple parameters could better delineate the pathophysiology of the particular disease process and lead to selection of more appropriate therapies [19-25].

While in some applications it is possible to image sequentially using different modalities and combine the results during analysis, there are certain applications where it is essential, or highly beneficial, to image using multiple modalities simultaneously. This can be due to the dynamic nature of the biological phenomena or the physiological conditions that might change due to factors such as anesthesia, contrast agent injection, temperature, oxygenation level, or circadian rhythm [26, 27]. It has been shown, for example, that tumor blood flow and  $pO_2$  can fluctuate significantly over time scales of less than 1 hour [28, 29]. Simultaneous imaging can also reduce the experiment time and minimize the side effects of surgical intervention, manipulations, injections, and anesthesia.

### **1.3: Window Chambers**

Window chambers are support structures that frame a section of tissue and have been widely employed to study TM. Window chambers allow repeated study of the same tissue through multiple experiments at different times. Most studies on window chambers have been carried out with optical microscopes. However, MRI, ultrasound imaging, and nuclear imaging of window chamber models have also been reported [3, 30-31]. The concept of this dual modality system is expandable to applications other than window chamber models that are appropriate for both MRI and optical microscopy.

Non-metallic window chambers are required in order to carry out MR imaging experiments. Plastic window chambers were designed in SolidWorks, based on the geometry of a widely used titanium prototype [32-34]. The printed window chambers were fabricated with an Objet Connex350 multi-material 3D printer system [35]. The plastic window chambers are lighter than the titanium counterparts and appear to be well tolerated by the mice. Figure 1.1 shows the design of the plastic window chamber.

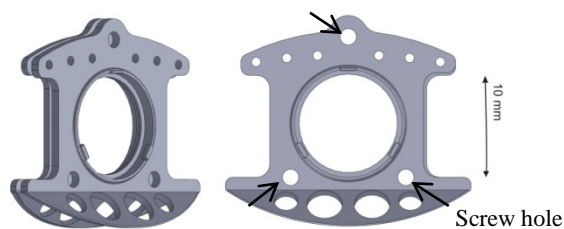


**Fig. 1.1.** Plastic window chamber designed to be used in the MR scanner. The tissue lies between the two parts of the window chamber. The two parts of the window chamber are held together by three screws that pass through the indicated holes.

#### 1.4: Animal Preparations

The plastic window chambers were implanted on 8-9 week old male severe combined immunodeficient (SCID) mice. All animal procedures were done in accordance with approved University of Arizona Institutional Animal Care and Use Committee (IACUC) protocols. Approximately  $3 \times 10^6$  green fluorescent protein (GFP) transfected PC-3 human prostate cancer cells were injected under the window chamber two days following the chamber implantation. Cells were injected via a syringe needle inserted just below the surface in a tissue region near the center of the chamber. The animals were maintained in individual cages in a temperature and humidity controlled environment. Details on the implantation procedure of mouse dorsal skin fold chambers can be found elsewhere [33, 36].

For imaging experiments a tail vein catheter was placed so that a molecular agent (MA) could be delivered in a controlled manner with the animal stationary inside the magnet. Both animal temperature and respiratory rate were monitored during imaging experiments. Animal temperature was controlled through a computer controlled warm air delivery system and monitored by a fiber optic rectal probe. Respiratory rate was monitored via an airflow bellows placed under the animal and controlled by varying the gas anesthesia delivery rate.

#### 1.5: Summary of the Dissertation

In chapter 2, the development and specifications of the dual MR-optical CA are described. The contrast agents for optical and MR sensitivity were conjugated to Bovine Serum Albumin (BSA). The carrier molecule, BSA, with the conjugated contrast agents is called the MA throughout this dissertation. The MR and optical properties of the dual-labeled MA are explained in this chapter.

In chapter 3, the development process and specifications for four optical imaging systems that were investigated are described. The first three systems are reviewed very briefly since they were not applied in the final studies. The fourth and final system had better imaging specifications and is described in detail. Examples of images obtained with each of the four systems are shown in the chapter. The surface coils that were used for MR imaging are also discussed as part of the dual modality imaging system development.

In chapter 4, three methodologies of measuring vascular permeability with optical fluorescence microscopy in mouse DSFC are reviewed and analyzed. Based on the analysis of these three methodologies, a new approach is introduced. The new approach is applied later in chapter 6 to measure vascular permeability using the optical fluorescence images of the MA in the tissue. At the beginning of chapter 4, the simple two compartment model of tissue used to estimate vascular permeability, is described. The two compartment model is also applied in chapter 5.

Chapter 5 focuses on DCE-MRI and the application of DCE-MRI in window chamber models. Based on the applied MRI sequence and MA dose, the errors caused by  $T_2$  relaxation of the agent, water exchange, and partial volume effect are estimated. It is suggested that partial volume effect could be partially accounted for by taking advantage of the signal intensity profile in the window chamber immediately after injection of the contrast agent, or by partial elimination of vascular signal by diffusion weighted imaging. Finding partial volume ratios within voxels also allows more precise compensation of  $T_2$  relaxation and water exchange effects.

The experimental results are presented and discussed in chapter 6. In this chapter, the theories that were explained in chapters 4 and 5 are applied to measure vascular permeability with optical and MR modalities in the mouse DSFC. The analysis methodologies are validated by applying them to a simulated phantom with known parameters. The obtained results are also compared to the results published in the literature.

## CHAPTER 2: MOLECULAR AGENT

### 2.1: Overview

In this chapter, the molecular agent (MA) that was used in the study of tumor vascular permeability with the dual modality imaging system is described. The MA was labeled simultaneously with both optical and MRI contrast agents (CAs). The simultaneous labeling allowed direct comparison of the results obtained from both modalities. The optical CA that was used was Alexa Fluor 647 and is described in section 2.2.1. The MR CA, described in section 2.2.2, was Gd-DTPA. The MA was bovine serum albumin conjugated to both optical and MR CAs and is described in section 2.2.3. The procedure that was used to label the carrier protein with optical CA is described in section 2.3.

### 2.2: The Contrast Agent Applied

#### 2.2.1: The Optical CA

The criteria that are critical in optical CA selection are emission/excitation wavelength in tissue's low absorption/scattering spectrum, optical and chemical stability, high fluorescence QE and availability of suitable chemical binding groups on the molecule. Other factors that should be considered are the sensitivity of the photo-detector to the emission wavelength of the CA and the availability of the light source at the excitation wavelength.

The scattering property of tissue is determined by Mie theory [1] and scattering generally reduces as a function of wavelength in the visible to NIR wavelength band. Therefore, regarding scattering, higher wavelength has slight preference to lower wavelength.

The absorption/wavelength relationship varies among different tissues. However, most tissues have low absorption at red/near infrared wavelengths [2]. Below 600 nm wavelength, the absorption of blood is significant. Fig. 2.1 shows the absorption of four main tissue components that absorb in the 600-1000 nm range. Depending on the amount of these constituent components in tissue, total tissue absorption varies. In most tissues, total absorption is close to minimum in the 650-800 nm wavelength range [3].

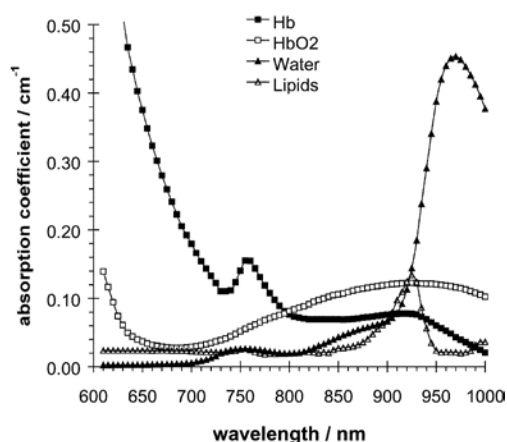


**Fig 2.1.** Absorption of major absorbing components of tissue in wavelength range 600-1000 nm<sup>1</sup>

The detector used in the system is a silicon CCD, (Microfire Camera, Kodak KAI-2020 image sensor). The QE of photon/electron conversion of the detector peaks at 450 nm and gradually reduces as a function of wavelength. Therefore, lower wavelengths have slight preference to higher wavelengths, but the effect of detector QE on the experiment results is not significant. The most readily available source for the experiment in the wavelength range of interest was a HeNe Laser at 633 nm.

The dye that best matched all the requirements was Alexa Fluor 647. Alexa Fluor is a family of fluorescent dyes developed by Life Technologies (formerly Invitrogen Inc.) that cover the visible to near infra-red wavelength range. Alexa Fluors have excellent photo-stability and high QE [4]. Alexa Fluor fluorescence usually retains its efficiency after binding to proteins and other large molecules [4] and is mostly pH insensitive over a wide range [4]. Alexa Fluor 647 was chosen because of the light absorption properties of the tissue as well as the laser light source available (HeNe 633). Alexa 647 was preferred over Alexa 633 because it has 2.5 times higher quantum efficiency [5], is more stable (according to a Life Technologies technical assistant), and is in a slightly less absorbing portion of the spectrum. The molecular weight of Alexa Fluor 647 is 1.3 kDa [6].

Another optical CA that has comparable performance with Alexa Fluor is DyLight produced by Dyomics. A study has shown that DyLight 594 is 1.5 times brighter than Alexa 594 and is slightly more photo-stable [7]. However, Alexa Fluor was chosen because it was used successfully in previous experiments [8].

### 2.2.2: The MRI CA

A CA in MRI changes the longitudinal and transverse relaxation times of nuclear spins. Eq. 2.1 and 2.2 describe these relations [9, 10]:

---

<sup>1</sup> Fig. 2 of reference 2.

$$\frac{1}{T_1} = \frac{1}{T_{10}} + r_1 C \quad (2.1) \text{ and}$$

$$\frac{1}{T_2} = \frac{1}{T_{20}} + r_2 C \quad (2.2),$$

where  $T_{10}$  and  $T_{20}$  are the native longitudinal and transverse relaxation times of the tissue, respectively,  $r_1$  and  $r_2$  are the longitudinal and transverse relaxivities of the CA, respectively, and  $C$  is the concentration of the CA. In gradient echo sequences the transverse relaxation also depends on the variability of the local magnetic field. In this case,  $T_2$  is replaced by  $T_2^*$  in Eq. 2.2. [10]. Inverse values of  $T_1$  and  $T_2$  are the relaxation rates of the tissue and are symbolized by  $R_1$  and  $R_2$ .

The MR CA used in this research was Gd-DTPA. Gd-DTPA is called Magnevist™ by Bayer Schering Pharma who markets it. Gd-DTPA by itself is a non-specific (also called non-selective) linear ionic MR CA [11, 12]. Linear means that it does not have carbon cycles in its molecular structure. Non-specific means that it is not specific to a particular tissue. Gd-DTPA by itself is clinically approved. The relation between longitudinal and transverse relaxation rates of human blood plasma and Gd-DTPA concentration has been shown to be strictly linear in the range of 0 to 16 mM [11]. Also the transverse relaxivity of Gd-DTPA is lower than most other MR CA which makes it more suitable for DCE-MRI, which is dependent on  $T_1$  contrast.

The longitudinal relaxivity of Gd-DTPA in human blood plasma at 0.2, 1.5 and 3 T for concentrations up to 16 mM were reported to be 4.7, 3.9 and 3.3  $\text{mmol}^{-1}\text{s}^{-1}$ , respectively [13]. This indicates a decrease of 17% and 15% from 0.5 T to 1.5 T and 1.5 T to 3 T, respectively. These results are not exactly compatible with results obtained by Hittmair, et al. in bovine plasma [14]. According to Kalavagunta, et al. the longitudinal relaxivity of Gd-DTPA at 3T and 7T are 3.59 and 3.48  $\text{mM}^{-1}\text{s}^{-1}$ , respectively [15]. Kalavagunta, et al. measured the relaxivity of ProHance™, which is a conventional gadolinium chelate and Vasovist™, which binds to albumin [16]. The longitudinal relaxivity of ProHance™ did not change significantly with magnetic field strength; but the relaxivity of Vasovist™ decreased with field strength [16]. The reported values of relaxivity of Gd-DTPA and albumin bound Gd-DTPA are summarized in table 2.1 along with the relaxivities of Vasovist and Prohance.

**Table 2.1.** Relaxivity of Gd-DTPA, and Gd-DTPA labeled Albumin, literature review.

Contrast Agent	Field (T)	Environment	Dose	Relaxivity ( $r_1$ )
Gd-DTPA [13]	0.2, 1.5 ,3	Plasma	Up to 16 mM	4.7, 3.9, 3.3
Gd-DTPA [25]	2	Plasma	0.2 mmol/tissue kg	4.9
Gd-DTPA [14]	0.47, 1.5, 3, 4.7	Plasma	0.25-0.5 mM	3.8, 4.1, 3.7, 3.8
Gd-DTPA [14]	1.5	Human blood	0.25-0.5 mM	4.3
Gd-DTPA(23)-BSA [26]	4.7	Mouse blood		173.65
Gd-DTPA(31)-HSA [25]	2, 0.25	Plasma	2.4 $\mu\text{mol/tissue kg}$	313, 424

The transverse relaxivity is dependent on the contrast agent concentration. Pintaske, et al. reported the transverse relaxivity of GdDTPA ( $R_2^*$ ), as 9.6, 5.3 and 5.2  $\text{mmol}^{-1}\text{s}^{-1}$  at 0.2T, 1.5T and 3T,

respectively [13]. Kalavagunta, et al. estimated the relation between concentration and transverse relaxivity for Gd-DTPA by the following relation [15]:

$$r_2^* \text{ (mM}^{-1}\text{s}^{-1}\text{)} = 1.4[\text{Gd}]^2 + 8.7[\text{Gd}] + 26.4. \quad (2.3)$$

The relaxivity of Gd-DTPA increases with macromolecular content in the solution [17]. Gd-DTPA relaxivity in tissue can be 30-70% more than in saline [17]. Pintaske, et al. measured the  $r_1$  and  $r_2$  values of Gd-DTPA in blood and plasma at 1.5 T; the longitudinal and transverse relaxivities in blood were 4.3 and 4.4 respectively which were 30% and 11% higher than the measured values in saline [13]. This factor could lead to incompatibility in concentration measurements in different tissues, and subsequently lead to error in measuring vascular kinetic parameters.

### 2.2.3: The Molecular Agent (MA)

Both the MR and optical CAs (Gd-DTPA and Alexa Fluor 647) were conjugated to biotinylated bovine serum albumin (BSA). Biotin tag makes BSA reactive to avidin. By injecting avidin into blood, biotinylated BSA reacts with avidin and gets cleared from blood through the liver [18]. The molecular weight of BSA is 66.5 kDa. The molecular weight of the biotinylated-BSA-(Gd-DTPA)<sub>23</sub> was measured before and after labeling with Alexa Fluor at 83.3kDa and 86.2 kDa in one case. The measurement was done by the Mass Spectroscopy facility at University of Arizona, Department of Chemistry and Biochemistry. The average number of Alexa Fluor dye molecules per MA molecule is obtained by dividing the molecular weight difference by the alexa fluor molecular weight:

$$\text{Alexa Fluor per MA molecule} = \frac{86.2-83.3}{1.3} = 2.23$$

BSA has many amine groups on the protein surface that allow it to be labeled with Gd-DTPA and Alexa Fluor. This was a key reason for using albumin. In addition, the vascular permeability to albumin is significantly affected by angiogenesis [19-21] and is altered in tumors [22, 23]. However, due to the low extravasation of BSA from the vasculature, it is difficult to measure the signal enhancement in the extra-vascular tissue [24]. This effect was partially offset by injecting a higher dose of MA and correcting for adverse  $T_2$  effect on the signal as described in chapters 5 and 6. The diverse chemical groups on albumin for binding allow it to be used as a carrier of therapeutic drugs [20, 25]. The longitudinal relaxivity of Gd-DTPA labeled BSA per Gd-DTPA molecule is higher than Gd-DTPA by itself [18, 23, 26]. At 2 T, the longitudinal relaxivity of albumin-(Gd-DTPA)<sub>31</sub> per molecule of Gd-DTPA, is three times more than Gd-DTPA [26].

In order to measure the relaxivity of Gd-DTPA conjugated to BSA,  $T_1$  and  $T_2$  were measured at concentrations of 2, 5, 10, 15 and 25 mg / ml. To measure  $T_1$ , a spin-echo MRI sequence was employed with TE fixed at 10.63 ms and TR varied over the values 31.25, 50, 62.5, 100, 125, 250, 500, 700, 1000, 1500, 2500, 3500, 6500 ms. In order to improve SNR at low TR values, signal averaging was performed. To measure  $T_2$ , TR was fixed at 6500 ms and TE was varied over the values 10.63 ms, 21.26 ms, 31.89 ms and 42.52 ms at the same concentrations of 2, 5, 10, 15 and

25 mg / ml. Depending on SNR, between 2 to 4 TE values were used in the  $T_2$  estimation. Longitudinal relaxivity changed linearly with concentration in the range of concentrations investigated. Transverse relaxivity also changed close to linearly except at the highest concentration. The values of  $T_1$  and  $T_2$  measured at different concentrations of Gd-DTPA conjugated to BSA are shown in table 2.2. The relaxivities were measured in units of mmol of Gd-DTPA. This is equivalent to the molar concentration of BSA multiplied by the number of Gd-DTPA labels per molecule of BSA, i.e. 23. In Fig. 2.2, the relaxation rates are plotted as a function of Gd-DTPA concentration.

**Table 2.2.**  $T_1$  and  $T_2$  at various concentration of BSA- Gd-DTPA<sub>23</sub> in PBS

C (mM)	0.55	1.37	2.74	4.11	6.85
$T_1$ (ms)	139.3	61.85	34.91	23.82	14.33
$T_2$ (ms)	44.42	19.10	9.777	6.411	5.044

**Table 2.3.** Relaxivity of Gd-DTPA<sub>23</sub>-BSA

Unit	Gd-DTPA $\text{mM}^{-1}\text{s}^{-1}$
$r_1$	9.7
$r_2$	37.2 (0 mM to 4.11 mM)

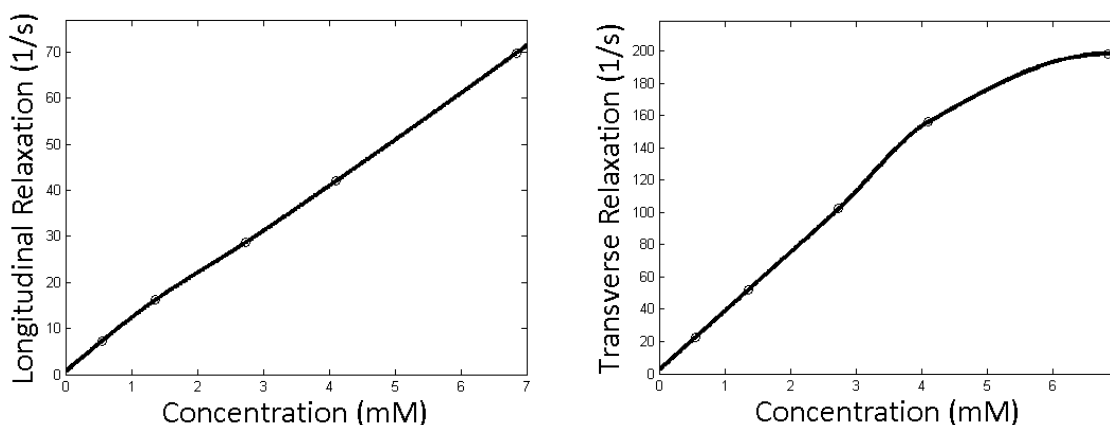


**Fig 2.2.** Relaxation rates versus concentration of Gd-DTPA. The relaxation rates are interpolated by piecewise hermite cubic interpolation algorithm using Matlab interp1 function.

### 2.3: Labeling BSA

BSA was labeled first with Gd-DTPA and then with Alexa Fluor 647. The procedure for labeling BSA by Gd-DTPA is described in the literature [27]. The Gd-DTPA in this research was synthesized by Dr. Eugene Mash in the Synthetic Chemistry Core of the University of Arizona Cancer Center. BSA was labeled with 23 Gd-DTPA molecules per molecule of BSA. Given the fact that other groups have labeled albumin with over 35 Gd-DTPA molecules [28, 29], there are many amine sites on the protein which were left empty to be labeled by Alexa Fluor.

Alexa Fluor is produced with a variety of reactive groups. Alexa fluor 647, carboxylic acid, succinimidyl ester was used to label BSA since it makes a stable carboxamide bond with protein. The labeling protocol was based on Life Technologies manual [5]. However, there were slight modifications. Since optical fluorescence intensity was not a limitation in the experiments, the goal was to maximize the percentage of dye that is labeled to protein, rather than maximizing the number of dye molecules per protein molecule. Therefore, the amount of dye per protein that was used, was less than recommended. The labeling procedure was as follows:

- 1- 0.1-0.2 M Sodium bicarbonate buffer was created.
- 2- The target pH for the protein-dye reaction is 8.3. However, according to the Life Technologies technician, a pH in the range of 8-9 is acceptable. Since the pH of sodium bicarbonate solution was in the target pH range (between 8-9), there was no need to tune the pH by adding base or acid. In one experiment, the pH of the buffer was set to the optimum value of 8.3 by adding HCl. However, the synthesized agent, killed the mice in which it was administrated. The reason is not known to us.
- 3- Protein (biotinylated Gd-DTPA-BSA) was dissolved in the buffer at a concentration of 20 mg/ml. In the Life Technologies manual [5], the recommended protein concentration for IgG antibody is 5-20 mg/ml. Since the molecular weight of IgG is about twice that of Gd-DTPA BSA, the initial estimate for the concentration of BSA was 2.5-10 mg/ml. However, higher concentration of protein was used to reduce the volume of solution in gel filtration and lyophilization in the following steps.
- 4- The Alexa Fluor dye was directly dissolved in the protein solution. The weight ratio of dye to protein in the solution was between 1/50 to 1/70. The Life Technologies manual suggests dissolving the dye first in a hydrophobic solvent such as DMSO or DMF. However, since Alexa Fluor 647 is also soluble in water, this step was not done.
- 5- In some experiments, a small amount of sodium azide was added to sterilize the solution. The ratio used was about 0.5 mg of sodium azide per 100 mg of protein. In the Life Technologies manual it is mentioned that the presence of low concentrations of sodium azide (<3 mM) does not interfere with the conjugation reaction.
- 6- The solution was stirred by magnetic stirring bars at lab ambient temperature for about 1 hour. According to the Life Technologies technician, the reaction mostly takes place in the first 10 minutes. The dye either reacts with the protein or hydrolyzes in the first few minutes.
- 7- According to the Life Technologies manual, the reaction could be stopped by adding freshly prepared 1.5 M hydroxylamine to the protein solution with the volume ratio of 1/10. The solution should then be incubated for an additional 1 hour. This step removes weakly bound dyes from protein molecules; therefore, potentially eliminating the risk of dye molecules separating from the protein during the experiment. This step was not carried out in our experiments. A Life Technologies technician stated that this step is only necessary when the reaction must stop at a certain point of time.
- 8- In order to separate free dye and salt from labeled protein, the solution was passed through a gel filtration column. Sephadex G-25 PD-10 pre-packed columns were used. The

exclusion limit for these columns is 5 kDa. The height of the columns is 5 cm. This is lower than recommended 30 cm column in the MP manual. Therefore, the free dye and protein bands were not always clearly separated.

- 9- In order to further purify the labeled protein from free dye and salt, the output solution from gel filtration was dialyzed for at least 1 day in pre-made dialysis cassettes (Thermo Scientific, Side-A-Lyzer Dialysis Cassette). The cutoff molecular weight of the cassettes was 10-30 kDa. In the protocol it is recommended that if dilution by gel filtration is not desirable, extensive dialysis could be a replacement procedure for removal of free dye. However, our experiments proved that even extensive dialysis over several days does not remove the free dye molecules from solution completely. A Life Technologies technician mentioned that dialysis to remove free dye might take up to one week.
- 10- The purified labeled protein was separated from solution by lyophilization. Prior to lyophilization, the solution was frozen either by immersing the solution container in liquid nitrogen or leaving it in  $-70^{\circ}\text{F}$  refrigerator.

## CHAPTER 3: IMAGING SYSTEMS

### 3.1 Overview

A major goal of this work was to build an optical imaging system that can image mouse dorsal skin-fold window chamber (DSFC) at the iso-center of an MRI scanner. The imaging system must be capable of white light and fluorescence imaging. Imaging parameters of interest are light sensitivity, spatial resolution, SNR, and uniformity of sensitivity across the window chamber. The criterion for establishing the values for these parameters was the ability to track MA in the tissue over time in order to measure the permeability of the vasculature in the tumor and healthy tissue. This specific criterion depends on the method of analysis of images used to measure vascular permeability and also the resolving power needed in the measurement of vascular permeability. Since this system is aimed for other applications as well, the ultimate goal was to achieve the highest sensitivity and spatial resolution and minimum image distortion with the available financial and technical resources.

A major challenge in designing this system was the high magnetic field in the MR scanner and the sensitivity of MRI to image degradation by electromagnetic noise. Therefore, no magnetic material could be incorporated in any part of the imaging system that resided inside the MR bore. It was also preferred that no electrical current would flow inside the MR bore due to the possibility of electromagnetic interference with MRI. In addition, the optical system had to fit inside the open bore of the 7T magnet, which was 12 cm in diameter with the required gradient coil in place. Since an additional tubular shaped RF shield was used to reduce electromagnetic noise, the available space for the experimental system was reduced to an inner diameter of 10.5 cm.

A total of four different systems were developed and investigated for imaging inside the MR scanner. The first two systems were based on imaging with an imaging fiber bundle. The third system used a small CMOS camera, which could operate inside the MR scanner with limited interference with the MRI [3]. The fourth system used an optical imaging relay system to image the window chamber to a camera that resided outside the MR bore. Most of the studies described in this dissertation were done using the last imaging system [4]. In this chapter, the developed imaging systems are described in the order mentioned (e.g. the small camera system will be called System 3).

In section 3.2, the MRI system and the incorporated surface coils to image the window chamber, are described. In sections 3.3, 3.4 and 3.6, the developed optical imaging systems are explained with the order that was mentioned in the previous paragraph. The optical illumination set-up that was used in the relay imaging system (system 4) is explained in section 3.5. For each optical imaging system, sample obtained images are shown.

### 3.2 MRI Scanner and Surface Coil

The initial experiments with systems 1 and 2 were done on a Bruker Biospec 4.7T MRI system (Bruker Biospin, Billerica, MA). The inner diameter of this scanner with the gradient coils in place was 12 cm. The first system, which was developed by Yuxiang Lin, operated inside a volume coil that was inserted in this system [1, 2]. The volume coil was used for RF excitation. The inner diameter of volume coil was 7 cm.

Subsequent MR imaging was done on a Bruker Biospec 7T MRI system (Bruker Biospin, Billerica, MA). The inner diameter of this scanner with the gradient coil in place was also 12 cm. An additional cylindrical tube was inserted inside the bore of the gradient coil. This tube acted as an electromagnetic shield to reduce the external field interference with the MR scanner RF signal. The inner diameter of this tube was 10.5 cm.

In order to improve the RF signal detection sensitivity and also to eliminate use of an RF volume coil, which would further reduce the available space for fitting the imaging apparatus, in systems 2 to 4, an RF surface coil was used for both excitation and MR signal reception. Reception of RF signal by a surface coil improves the SNR over use of a volume coil due to the higher filling factor and coil proximity to the tissue. More uniform excitation by a volume coil might have a slight advantage; however, since the tissue in the window chamber is quite thin, the uniformity of a surface coil is adequate. The surface coil was designed to fit centered on top of the window chamber with minimal distance between tissue and coil. Two different surface coils were investigated for imaging the window chamber with the 7T MRI scanner. Both coils had a center frequency of 300 MHz required for application in the 7T MR scanner ( $2\pi\gamma B = 3 \times 10^8$  Hz). The first coil was developed by Constantin Job at the Biological Magnetic Resonance (BMR) facility at the University of Arizona (UA) (called Job Coil from now on). This coil is shown in Fig. 3.1. The non-magnetic tune and match capacitors on this coil were purchased from ASAP Electronics (55H01). The diameter of this coil was 13 mm. Tuning and matching was done by two long plastic rods connected on one end to the adjustable capacitors on the coil and extended out the back side of the scanner. After inserting the animal and the imaging system in the MR scanner, the coil was tuned and matched. Although this coil had acceptable performance, tuning and matching was often not very stable and difficult to obtain. Also, preliminary analysis proved that sensitivity (coil Q factor) was less than expected.

Assuming that tuning and matching are perfect, the surface coil SNR is proportional to the integral of magnetic field generated over the tissue of interest divided by all resistive losses in the tissue and the circuit [5, 6]. The resistive losses in the tissue are a result of electromagnetic coupling of tissue and coil due to the conductivity of the tissue and the capacitance loss. Because of the isolation of the window chamber from the rest of the tissue and the small volume of the tissue within window chamber, this component is not the dominant source of noise in this study [6]. However, a slightly smaller surface coil helps in further reducing it. The resistive noise in the circuit is generated by the loss of power in all the capacitors and wiring. At 300 MHz the skin

depth of copper is  $3.8 \mu\text{m}$  [7]. Therefore, its resistance is relatively high at this frequency. It is important that wiring be minimized both to reduce the electromagnetic interference and to reduce the resistive noise. Where wiring is inevitable, such as the coil itself, it is possible to reduce the resistance by increasing the surface area of the wiring. Capacitors should have minimum magnetism. This is achieved by eliminating the nickel barriers in capacitor terminations. However, for small surface coils, it is also important that bulk susceptibility of capacitors be minimized.

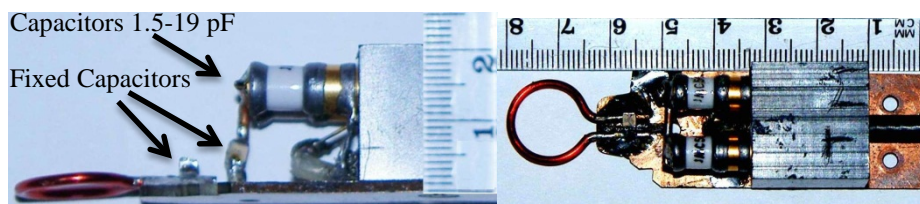


**Fig. 3.1.** MR surface coil built by Constantin Job (Job Coil).

To achieve these objectives, a second coil was purchased from Doty Scientific (Doty Scientific, Columbia, SC). Fig. 3.2 shows this coil. This coil was a single-tune surface coil (part # 99657). The coil was ordered un-covered, as a cover would have blocked the ability to image the tissue through the center of the coil. The diameter of the coil was 12 mm. The rough tuning was done by a screw on the coil (protrusion at the bottom in Fig. 3.2). The final tuning/matching was done by a remote matching network, which was connected to the coil through a BNC connector and extended to the outside of the MR scanner bore. We measured the Q factor of the two coils with no loading. The values for Job coil and Doty coil were 75 and 200, respectively.



**Fig. 3.2.** Doty surface coil.

The Doty coil was much easier to tune and match. The wiring in the Doty coil was absolutely minimal. The coil itself consisted of two parallel layers of wire, which reduced its ohmic resistance. The capacitors were much smaller and had less bulk susceptibility. There was also more attention paid to optimization of the circuit geometry [6]. The rods which were used to tune and match the Job coil were a source of instability. Any motion in these rods could lead to changes in the tuning and matching properties of the coil. The Job coil was particularly sensitive to opening and closing the back door of the MR scanner. This was eliminated in Doty coil by using the remote matching network.

### 3.3 Imaging with an Imaging Fiber Bundle

Fig. 3.3 shows the system developed by Yuxiang Lin (System 1) [1]. The overall system is very similar to the second design, which was also based on imaging fiber bundle (System 2). As mentioned before, system 1 fitted in a volume coil with 7 cm diameter. Therefore, it had more spatial constraint than system 2, which used a surface coil for both RF excitation and reception. The surface coil for Systems 1 and 2 was a 14 mm single-tune Doty coil that was available in the BMR facility for MRI at 4.7T. The mechanical parts of both systems 1 and 2 were made of plexiglass (PMMA polymer) and were constructed in the Radiology Research Lab machine shop at UA.

Two light sources, a laser for fluorescence excitation and a white light source for brightfield imaging, were coupled to plastic illumination fibers via 20x, 0.35 NA microscope objective lenses. At the other end of the fiber, the laser light illuminated the window chamber from above and the white light from below. Either light source could be turned on or off to determine the mode of imaging (fluorescence, brightfield, or both). The trans-illumination light was reflected through a right-angle prism towards the tissue. A fold mirror directed the emitted or transmitted light to a gradient index (GRIN) lens (Grintech, GT-IFRL-100-020-50-CC) that imaged the window chamber to the distal end of the imaging fiber bundle (Fujikura, FIGH-30-650S). The imaging fiber transfers the light to outside of the MR scanner. An optical imaging

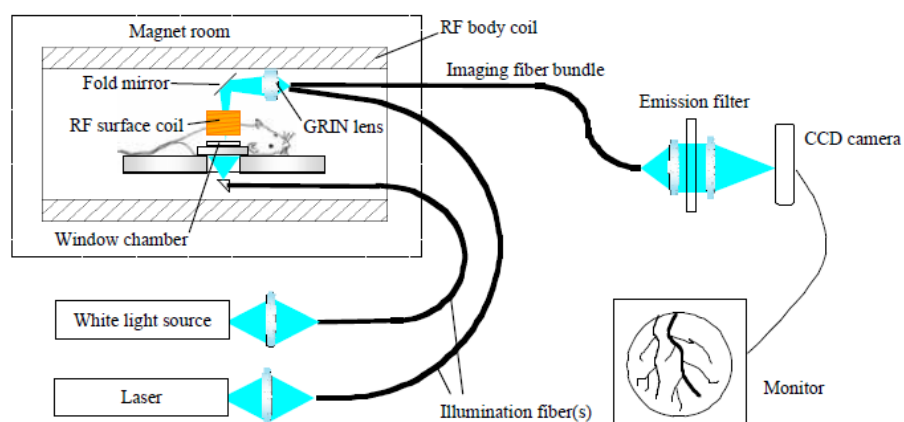


**Fig. 3.3.** Overall simultaneous MR/Optical imaging system design (image taken from reference 1).

system imaged the other end of the fiber to a camera. Emission filters were used to block the laser light in fluorescence imaging mode.

When attached to the fiber, the GRIN lens had a working distance of 20mm to the tissue surface and a nominal magnification from fiber to tissue of  $-1:22.26$ . The desired magnification was calculated by dividing the imaging diameter of the fiber bundle by the window chamber diameter, which was  $-1:18.7$ . With the achieved magnification, the slight larger area of the window chamber is seen by the fiber. The GRIN lens can be modeled approximately by a thin lens at the center of

the GRIN lens. By setting a distance between the GRIN lens and the imaging fiber bundle, the imaging system magnification was tuned to the desired value. The space between the GRIN lens and the imaging fiber was filled with UV curing lens bond optical cement (Summer Optical, VTC-2). The clarity of the image was monitored while the lens was being glued to the fiber.

One of the goals for the system was modularity so that the mouse could be imaged with or without the simultaneous optical and MR imaging capability, in the MR scanner. At the same time, it was desired that the mouse could be easily transferred from the MRI scanner to a microscope or other imaging systems. System 2 was a redesign to meet these goals and consisted of three sections: a mouse holder (MH) on which the mouse was situated, the optical imaging section which held the fiber optic components for illumination and collection, and a platform to which the surface coil was attached, which had slots for the mouse holder and the optical imaging section to be align the components. Fig. 3.4 illustrates System 2. Because volume coil was not used in system 2, the available volume for system 2 was more than system 1. In this system, instead of using a folding mirror, the imaging fiber bundle and epi-illumination fibers were bent to face the window chamber directly from above.

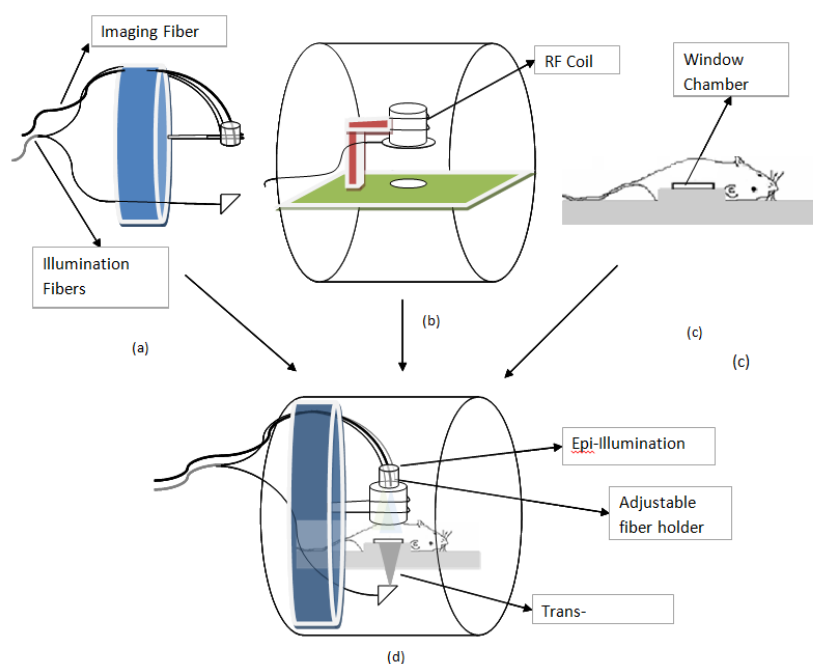


**Fig. 3.4.** System 2, imaging with fiber bundle without folding mirror.

A few sample images taken with systems 1 are shown in Fig. 3.5. The overall SNR of the optical images is low due to the low etendue of the imaging system. The etendue is limited by the imaging fiber bundle area and the NA. The light collection area could be increased by incorporating more than one optical imaging fiber, at the cost of increasing the complexity of the system. The other possible solutions were increasing the illumination intensity or increasing the amount of CA in the tissue by increasing the number of labeled Alexa-fluor dye molecules per albumin. Increasing the

laser power would also help, but would increase quenching of the optical CA as well as increase the system cost of the laser source. The extra heat generated by the absorption of laser light could also be problematic. Imaging with more than one imaging fiber would add to the complexity of the system both in hardware and image processing (registration of multiple images).

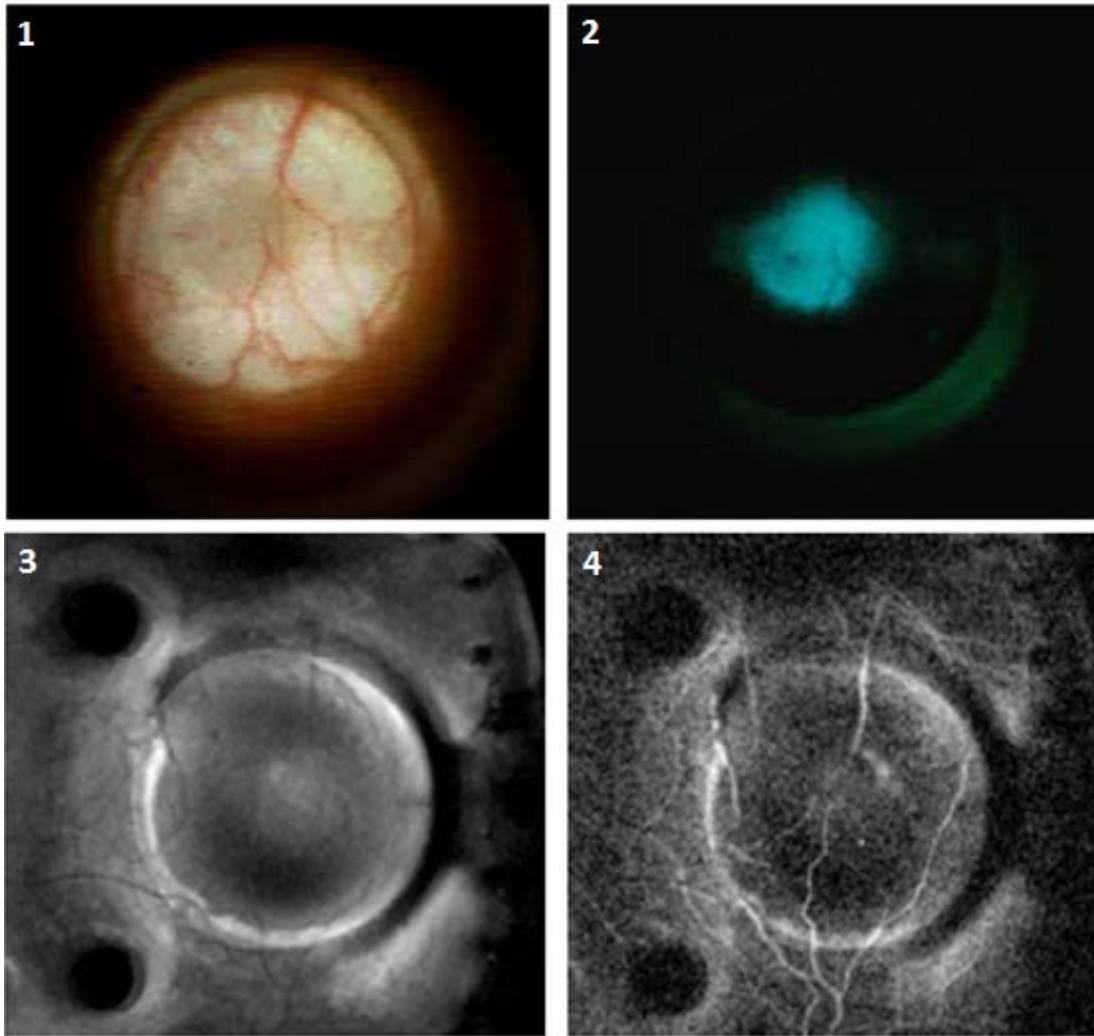


**Fig. 3.5.** Sample images of the window chamber obtained with Optical and MR imaging by system 1, MR images were taken on the 4.7T system, FOV = 2.56 cm x 2.56 cm. 1- Optical bright field imaging. 2- Optical fluorescence imaging of GFP tumor illuminated with Argon 480 nm laser. 3- Imaging tissue structure with MRI, spin-echo sequence, TR=500, TE = 9.6ms, 2 averages. 4- MRI-DCE image after MA injection, TR = 100 ms, TE = 9.6 ms, 1 average.

### 3.4 Imaging with a Small Camera

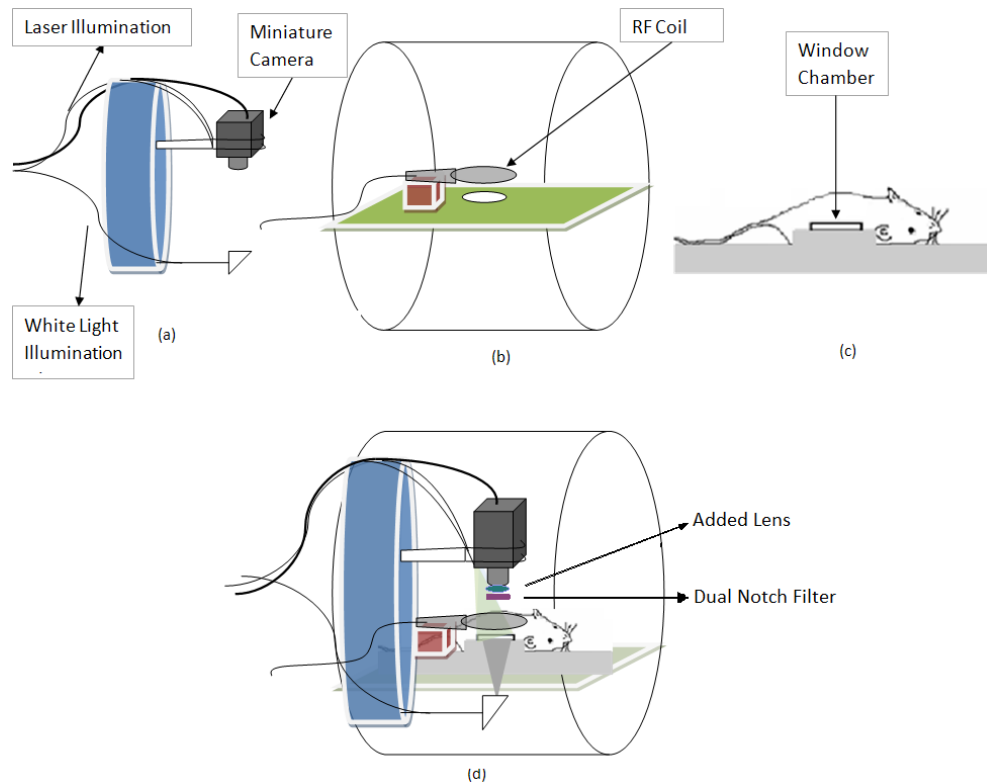
The imaging fiber systems were limited by low etendue and low resolution. By imaging the window chamber to a CMOS or CCD detector directly, the light collection and resolution could be increased. However, operating a camera inside MR scanner has two problems: the high

magnetic field in the MR scanner can interfere with camera operation and the camera operation can create noise in the MR signal. Initial tests showed that several of our cameras would not operate inside the MR scanner. However, we found a small CMOS camera (CX408 – [www.rf-links.com](http://www.rf-links.com)) that did operate inside the scanner. Interference with the MR signal was present but not significant. The output of the camera was in CCIR format which was converted to USB signal via a converter outside of the MR scanner. The specs of this camera are summarized in table 3.1.

**Table 3.1.** CX408 CMOS camera – Obtained from [www.rf-links.com](http://www.rf-links.com).

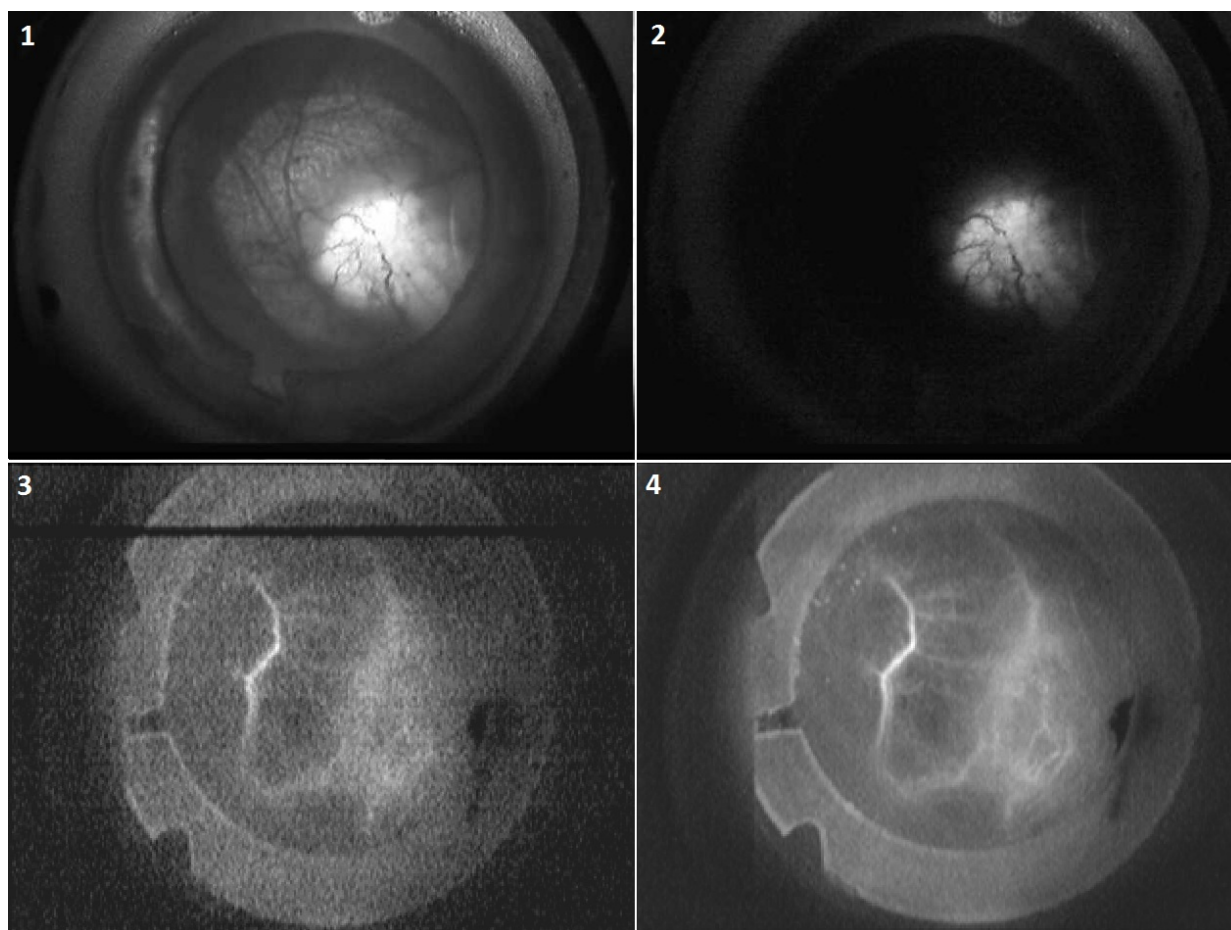
<b>Image Sensor:</b> ¼" B/W Camera
<b>Video System:</b> CCIR / EIA
<b>Number of Effective Pixels:</b> 500x582
<b>Scanning System:</b> 2:1 interlace
<b>Resolution:</b> 240 TV lines
<b>SNR:</b> More than 46 dB
<b>Minimum Illuminator:</b> 0.5 Lux at F1.4
<b>Electronic Shutter:</b> 0.16 ms - 0.02 s
<b>Horizontal Synch Frequency:</b> 15.625 kHz
<b>Vertical Synch Frequency:</b> 50 Hz
<b>Gamma:</b> 0.45

Fig. 3.7 shows a diagram of System 3 (small camera system). This system was designed with Rhinoceros 3-D modeling software (McNeed and Associates) and similar to systems 1 and 2, constructed from plexiglass in the Radiology Research Lab machine shop at UA. The illumination was identical to System 2. The system was also modular similar to System 2. The window chamber was imaged to the camera via a doublet lens ( $D = 6.25$  mm,  $f = 20$  mm). This lens operated in combination with the original lens on the camera to produce a from sensor to tissue magnification of 4.5. A dual notch emission filter was installed in the optical path to block 633 nm HeNe and 488 nm Argon laser light (Semrock, NF01-488/645) allowing fluorescence excitation at either wavelengths.



**Fig. 3.6.** System 3, imaging with small camera.

Sample images taken by System 3 are shown in Fig. 3.7. Similar quality images were also obtained with system 2. The main problems with this camera were low sensitivity and lack of manual controls. Particularly, the auto-gain and non-unity gamma factor were problematic. The possible solution was modification of the camera circuit to shut down the auto-gain. However, that did not seem readily feasible. In addition, the camera's sensitivity was low due to the small size of the sensor (1/4").



**Fig 3.7.** Sample images by small camera system. 1- White light trans-illumination and Argon laser epillumination. 2- GFP signal by Argon 480 nm fluorescence imaging alone. 3- A frame of video, after injection of the MA, inside the MR scanner. Illumination is only by HeNe 633 nm Laser. The line is a result of interference with MR RF signal. The line appeared in every few frames. 4- Average of 50 video frames.

The approach was further investigated by testing more sophisticated cameras. The goal was to find a high quality camera that would operate inside the MR scanner. A mechanical constraint was set by the MR bore diameter. Alternative cameras might also require a fold mirror and/or optics to divert the optical path and image the window chamber on the camera detector. Many cameras were considered and a few were tested. The following cameras were tested inside the MRI scanner: Sentech STC-TB83USB-B (Sensor Technologies America, Inc.), Sentech STC-160CS, and Hitachi Kokusai KPM1AN (Hitachi Kokusai Electric Inc.) were tested in the magnet. STC-TB83USB-B shut down as it entered the scanner. STC-160CS, which was a similar camera but without an aluminum case, stopped working after the test. The Hitachi camera did operate inside the scanner. This camera transferred the signal via coaxial cable unlike the other two cameras which transferred the signal via USB cable. The Hitachi camera's metallic cover was removed to reduce the magnetic force on the camera; however, considerable magnetic force still existed on the

camera. A possible solution was replacing the magnetic resistors and capacitors incorporated in the camera circuit, but this idea was not tested. A camera that was considered, but not tested inside the magnet, was PixeLink PL-B954HF-BL model (PixeLINK Corp., Ottawa, Canada). The CCD in this camera is connected to the main board through a cable. The cable is 4" long. An idea was to elongate this cable to move the main circuit board outside of the MR scanner. However, due to high frequency of the signals from CCD, the maximum length for this cable, according to the company, was 1 ft, which is not long enough to move the circuit board sufficiently far from the magnet isocenter.

If the camera is not directly aligned on top of the window chamber, additional optics are necessary to relay the image to the camera detector. Therefore, it was decided that an optical relay system could be built to lengthen the distance between the window chamber and camera such that the camera is outside of the MR bore. In this case, the amount of electromagnetic interference is reduced as are the magnetic forces on the camera itself. This also simplified mounting and positioning of the camera. This is the approach of System 4.

### **3.5 Illumination System for the relay imaging system**

In System 4, the window chamber is illuminated with white light from below the window chamber and blue and red laser lights for above. White light imaging is used to show the tissue structure. Laser light is used to excite the green fluorescent protein (GFP) labeled tumor and the fluorescence CAs used in the experiment. In vascular permeability measurements, the optical CA was Alexa-Fluor 647 (see chapter 2 section 2.2.1). While intensity uniformity is a plus for both white light and laser illumination, it is more critical for laser illumination since it is intended to be used for quantitative studies. However, even for epi-illumination, precise uniformity is not required since the methods that were used to measure vascular permeability do not depend on the absolute intensity of illumination of the window chamber.

The illumination source for white light transillumination imaging was a tungsten halogen lamp coupled to a fiber optic cable (Dolan Jenner, Fiber-Lite PL-750A). The laser light illumination sources were an Argon blue laser (488 nm) and HeNe red laser (633 nm). Both the Argon and HeNe lasers had 7 mW optical power. Each laser produced about 2 mW at the tissue.

The illumination light was transferred to the setup inside the MRI scanner bore via optical fibers. White light was transferred by a thick plastic fiber ( $D = 1$  mm). Laser light was transferred through two glass fibers with NA of 0.39 and a core diameter of 300  $\mu\text{m}$  (FT-300-UMT, Thorlabs). The use of glass fibers improved efficiency of light transfer. For example, PMMA optical fiber absorption at 488 nm and 633 nm wavelengths is about 130 dB/km and 400 dB/km [6]. This absorption would lead to an optical power loss of 8.5% and 24% respectively in the 3 m cables that were used in the experiment.

The diagram of the illumination system is shown in Fig. 3.8. The two laser beams are first combined via a dichroic beam combiner. The combined beam is then expanded into two beams through a beam-splitter. The two beams are focused on two fibers by doublet lenses. The two beams are transferred through two fibers to the window chamber inside the MR scanner. Having two beams improves the illumination uniformity since the fibers are arranged to illuminate the window chamber from an angle on either side of the central imaging path. The illumination system was constructed on a cart to make it portable. This cart was situated at the entrance of the MR scanner room at the time of the imaging experiments.

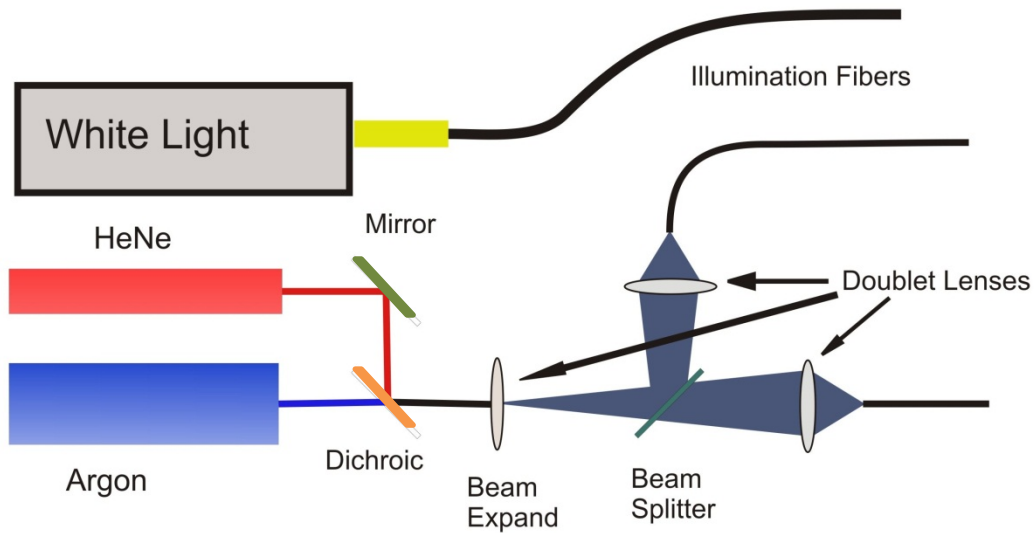


**Fig. 3.8.** Diagram of the illumination system.

To achieve a uniform illumination of the full field of the window chamber, the required NA of the optical beam out of the fiber depends on the distance between the distal end of the fiber and the object. To achieve a short distance between fiber and tissue, it was necessary to fill the entire NA of the fiber. The diameter of the laser beam was approximately 1 mm. In order to fill the NA completely, the focal length of a single focusing lens would have to be:

$$f = \frac{D_{\text{beam}}}{2NA} = \frac{1}{2 \times 0.39} = 1.22 \text{ mm.} \quad (3.1)$$

This effective focal length was achieved by means of two positive lenses in tandem. The net focal length of the two lenses is obtained from the following relation:

$$f^{-1} = f_1^{-1} + f_2^{-1} - f_1^{-1}f_2^{-1}d \quad (3.2)$$

If the distance of the two lenses is more than the summation of their focal lengths, the net lens would have a negative focal length. The absolute value of the optical power of these lenses ( $f^{-1}$ ) increases as the distance between the two lenses increases. The distance between the rear principle plane and the rear of the second lens, called here  $d_{\text{rpp}}$ , is:

$$d_{rPP} = -f_2^{-1}fd \quad (3.3)$$

The distance between the rear of the second lens and the rear focal plane, called here  $d_{rf}$ , is:

$$d_{rf} = f + d_{rPP} = f(1 - f_2^{-1}d) \quad (3.4)$$

The combined lens will have negative power if  $d > f_1 + f_2$ . In this case, since  $f_2^{-1}d > 1$ , both  $d_{rPP}$  and  $d_{rf}$  will be positive. This means that the rear focal point of the combined lens is to the right of the second lens. Therefore,  $f$ , and subsequently NA, could be adjusted by varying  $d$ . Fig. 3.9 illustrates the combined lens.

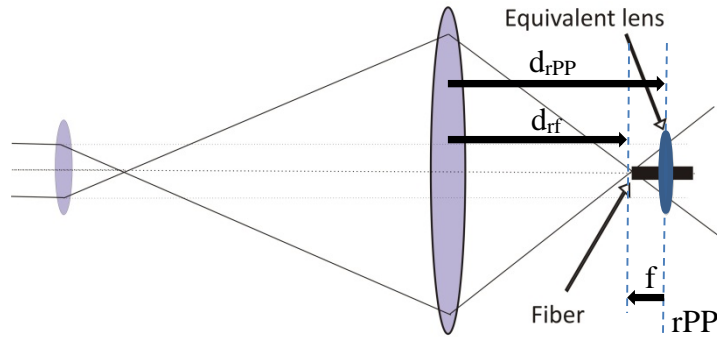


**Fig. 3.9.** Illustration of combining two positive lenses to create a more powerful tunable negative lens.

### 3.6 The Relay System

The purpose of the relay system is to image the window chamber, which sits at the isocenter of the MRI scanner bore, to at least 10 cm outside of the end of the magnet to avoid significant electromagnetic interference between the camera and the MRI system. The length of the MR bore from the isocenter to the edge is 67.8cm. Therefore, the relay path should be at least 78.8 cm. The relay system must fit into a cylindrical RF shield that slides into the MR gradient coil bore. The inner diameter of the RF shielded cylinder is 10.5 cm. A mirror is used to fold the imaging path of the window chamber down the scanner axis (Fig. 3.10). The object size is the diameter of the window chamber, which is 11mm. The image size is determined by the size of the optical detector. The camera used was an Optronics Microfire color CCD camera. The CMOS detector size for this camera is 11.84 x 8.88 mm. Therefore, the target magnification tissue to camera detector is 0.8. However, since the edges of the window chamber are not of critical importance in the pursuing studies, the target magnification was set between 0.8 and 1. Besides satisfying the abovementioned criteria, the design goal was to maximize the NA, minimize aberrations in order to achieve the highest possible image quality and minimize the cost of development.

The image quality achievable is dictated by the camera detector, the optical aberrations inherent in the optical design, and increased aberrations as a result of opto-mechanical system positioning inaccuracies. In order to set a goal for the target spot size in the optical design, these factors were

analyzed. The pixel size on the Microfire camera is  $7.4 \times 7.4 \mu\text{m}$ . The diffraction limited spot diameter,  $D_{\text{diff}}$ , at the detector is:

$$D_{\text{diff}} = \frac{1.22\lambda}{\text{NA}} = \frac{0.77}{\text{NA}} \quad (3.5)$$

where NA is the numerical aperture of the beam at the detector. For a NA of 0.105, the diffraction limit spot size would be roughly equivalent to the camera pixel size. However, the window chamber is about 0.5 mm thick. The resulting defocus, if imaging system is focused at the center of the tissue, would be  $\pm 250 \mu\text{m}$ . The spot size caused by this defocus would be:

$$D_{\text{dl}} = 2\text{NA} \times 250 \mu\text{m} = 500 \mu\text{m} \times \text{NA} \quad (3.6)$$

where  $D_{\text{dl}}$  stands for image spot diameter as a result of defocus. Therefore, as the NA increases, the system would be more sensitive to object depth and resolution would degrade.

Several designs for the relay system were tested. As a first step, symmetric relay systems with unity magnification were designed. Later the magnification was tuned by slight modification to the design. The designs were based on a traditional relay system with two identical doublets in the center and two identical lenses near the object and image positions [8]. Since these designs were symmetric, all odd aberrations were zero at the image plane. Spherical and longitudinal chromatic aberrations were also small since the doublets at the center were operating at their designed object-image conjugates. The two lenses near the object and image planes, were intended to increase the NA without increasing the even aberrations significantly or reducing the relay length. However, in most designs it was difficult to fit a lens close to the window chamber due to mechanical constraints of the mirror and mouse holder. In addition, more elements increased the sensitivity of the system to mechanical misalignments or deformations of the mounting system.

The final relay design consisted of just two infinity corrected doublets with  $F=400 \text{ mm}$ ,  $D=75 \text{ mm}$  (Edmund Optics, NT45-419). The magnification of the system was 0.88 and the detector space NA was 0.097. The total relay path length was 82.4 cm. The average theoretical rms spot radius of the relay system across the 1 cm field of view at the tissue, as determined through simulation of the lens design, is  $15 \mu\text{m}$ . Focusing is done manually by translating the camera slightly inside its mounting structure. The normal tissue within the window chamber is about  $500 \mu\text{m}$  thick. The tumor regions can be thicker at later stages of tumor growth. Assuming that the imaging system is focused on the center of the tissue, the outer tissue would have an approximate defocus of  $250 \mu\text{m}$ . By inserting defocus into the simulation, the average RMS spot radius across 1 cm field of view at the object for defocus of  $250 \mu\text{m}$  and  $500 \mu\text{m}$  are  $20 \mu\text{m}$  and  $45 \mu\text{m}$  respectively.

A diagram of the relay system is shown in Fig. 3.10. The MR surface coil sits above the window chamber. White light illumination is provided from under the tissue for bright field imaging. Laser light illuminates the tissue from above (epi-illumination) for fluorescence imaging. The mirror above the window chamber folds the imaging path down the MR bore axis. Since a metallic mirror interfered with the Doty surface coil tuning, a dielectric mirror was used instead. The laser light

wavelengths are blocked by a filter with transmission nulls at the excitation wavelengths of 488 nm and 633 nm (Semrock, NF01-488/645). The filter is placed in front of the camera detector. An additional single HeNe notch filter (Semrock, NF03-633E) was incorporated to improve the rejection of the HeNe light.

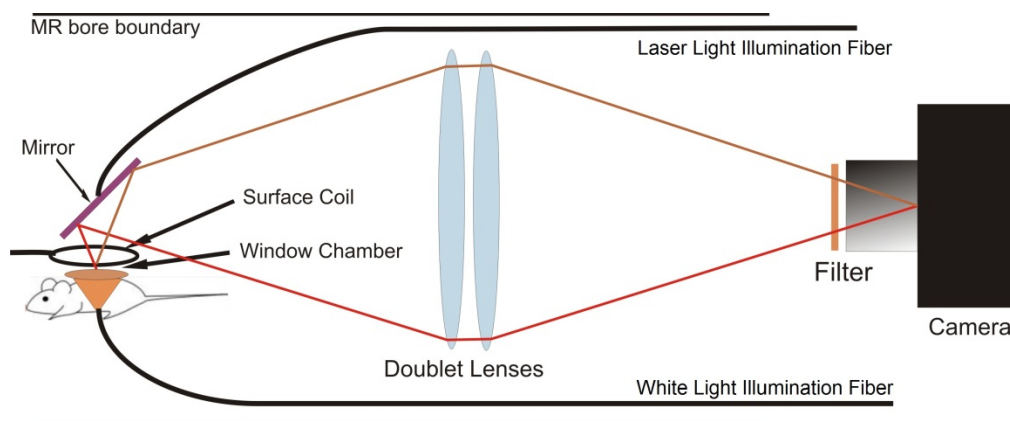


**Fig. 3.10.** Relay system diagram.

The system was designed with SolidWorks and printed with an Objet 3D printer (Objet Ltd., Object Connex350) in three sections, which were attached to each other to make the full length system. A mirror mount, part of the lens mount, and other small parts were also printed as separate pieces and added to the system. A channel was included in the system to deliver temperature-controlled air to the vicinity of the animal to maintain it at physiological temperature. The material used for printing was Objet FullCure720 [9]. Some of the mechanical properties of this material are listed in table 3.3. Mechanical properties could be improved by using new Objet materials, such as FullCure850 or RGD525 [9], which are stiffer and less temperature sensitive.

**Table 3.3.** Mechanical specifications of Object FullCure720 [9].

Tensile Strength (MPa)	50-65
Modulus of Elasticity (MPa)	2000-3000
Flexural Strength (MPa)	80-110
Flexural Modulus (MPa)	2700-3300
Water absorption (%)	1.5-2.2
HDT, °C @ 0.45 MPa (°C)	45-50
Glass Transition Temperature (°C)	48-50

Fig. 3.11 shows the relay system as built. The mouse sits on a mouse holder (MH) (Fig. 3.11c). The window chamber is fixed to the MH by the extension of the three screws that hold the window chamber parts together (screws indicated in Fig. 1.1). Isoflurane gas anesthesia is delivered to the

animal through a connection at the end of the MH. The MH slides into the imaging system under the RF surface coil. Fig. 3.11d shows the end section of the relay system with the MH in place.

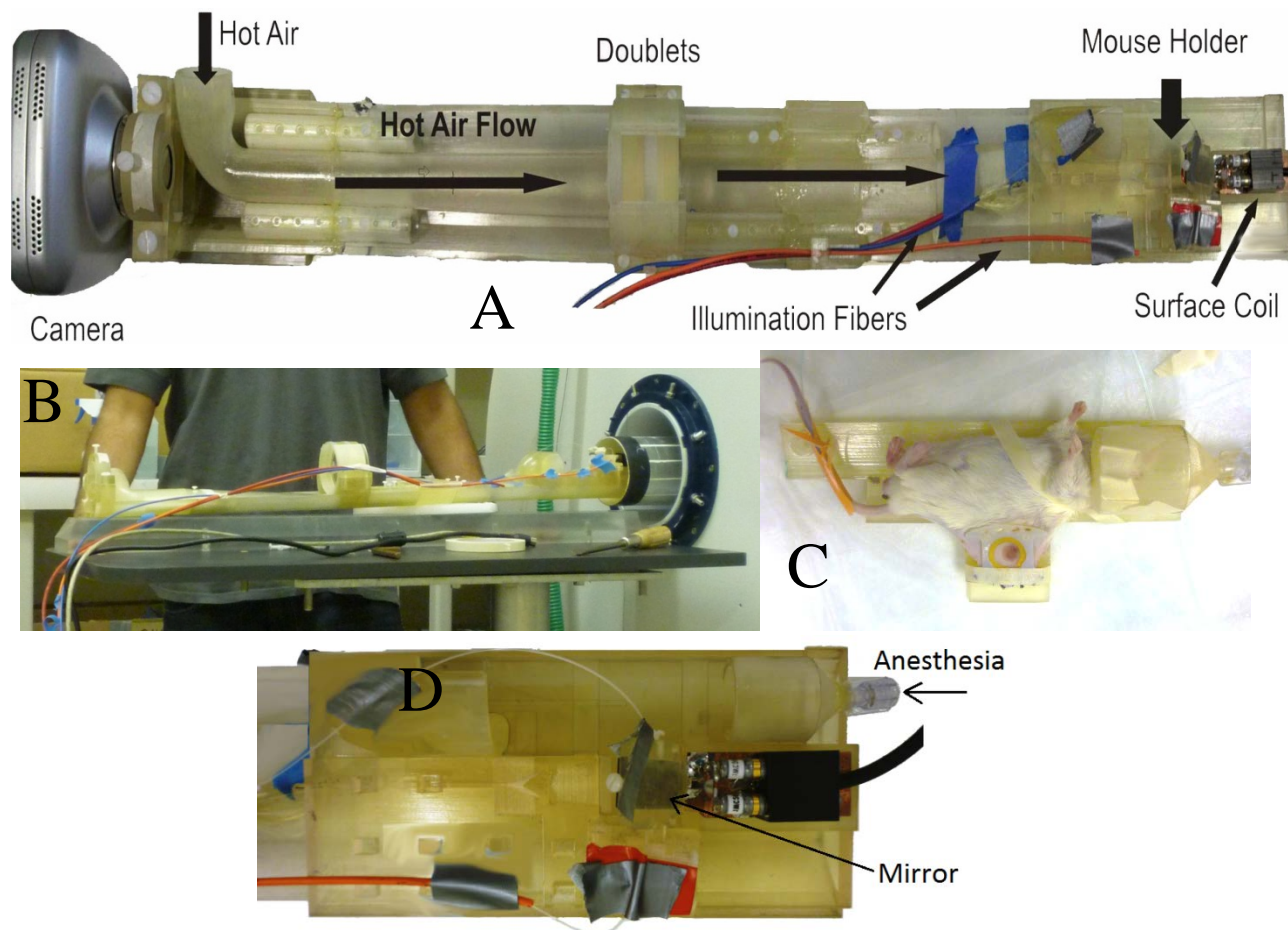


**Fig. 3.11.** Relay system, A. top view of the relay system. B. The side view of relay system as it is being inserted in the MR bore. The camera is not installed in this photo. C. Mouse Holder (MH) D. MH sits on the dual modality imaging system. Anesthesia is channeled to the mouse head. There is a channel under the window chamber which conveys the white light.

Sample images, obtained simultaneously with MRI and the optical relay system (System 4), are shown in Fig. 3.12. The MR images were obtained using a spin-echo sequence with,  $TE = 10.747$  ms,  $FOV = 2.56$  cm x  $2.56$  cm and a 5 mm slice thickness (only the center section of the images, with the window chamber, are shown). Fig 3.12.a shows an MR image of the window chamber before CA injection with  $TR = 500$  ms and a  $256 \times 256$  matrix. The tumor is brighter primarily due to the greater thickness of the tissue in the tumor area. Fig 3.12.b is the equivalent optical image of the tissue structure. The tissue is illuminated with both white light and Argon 488 nm laser. The tumor is green due to the fluorescence of GFP. Fig 3.12.c is an MR image after CA injection. In this image,  $TR = 250$  ms and the data matrix is  $128 \times 128$  pixels. The vasculature contrast (hyper intensity) is caused by the reduced longitudinal relaxation time effect of Gd-DTPA

labeled to BSA. Fig 3.12.d shows the distribution of Alexa Fluor 647 labeled to BSA in the window chamber. The illumination source is the 633 nm HeNe laser.

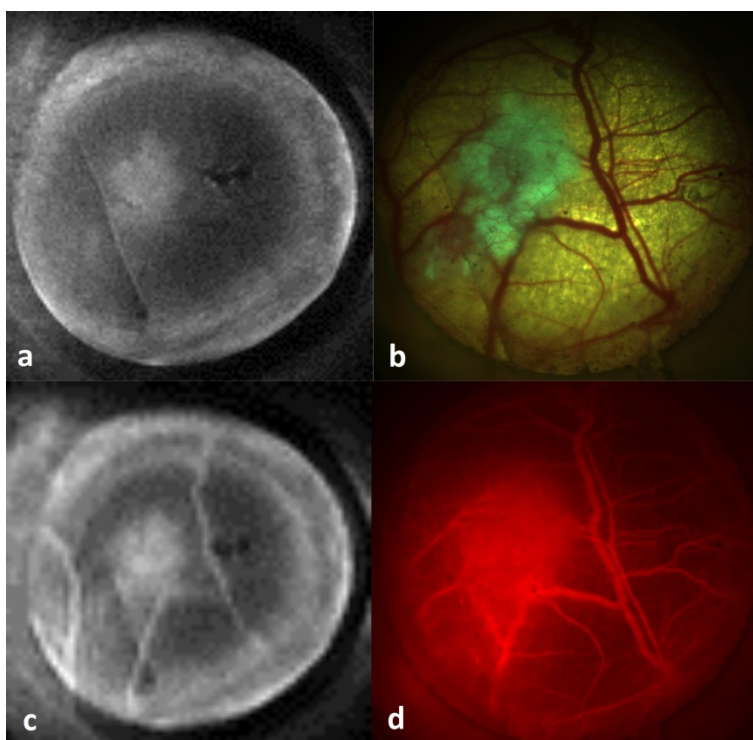


**Fig. 3.12.** Simultaneous MR and optical images of a window chamber. a Structural MR image of the window chamber. b Window chamber illuminated with white light trans-illumination and argon 488 nm laser epi-illumination. c, d Single frame MR image (c) and optical (d) image from a sequence of images acquired after CA injection.

### 3.7 Comparison of the Dual Modality Systems

The disadvantage of imaging with fiber bundles is the low resolution of the imaging fiber and low sensitivity of the system due to low light collection ability. The space bandwidth product (number of resolvable pixels or fibers) of commercial imaging fiber bundles is limited to less than 100,000. The fiber bundle that was used in this research had only 30,000 elements. Due to the small size of the imaging fiber bundle and limited numerical aperture (NA) of the fibers, the light collection efficiency is low. There are additional losses in imaging the proximal end of the fiber bundle to the camera detector due to reflections from the surfaces of the fiber and lenses.

The issue of low etendue of the optical system (light collection area multiplied by light collection solid angle) also exists for the small CMOS camera that was used in System 3. In addition, the camera used was not of high quality. It did not have manual gain controls, the gain was not linear, and changing the integration time was not possible. However, the resolution of system 3 was theoretically higher than that of systems 1 and 2. The camera had 240 TV lines, which is

approximately equal to 480x480 pixels in a square field of view. However, in practice the resolution was lower due to optical aberrations.

The use of more sophisticated cameras inside the magnet was investigated. Almost all cameras stopped working or interfered with the magnetic field uniformity as they entered the MR scanner. In order to make these cameras compatible with operation in an MRI environment, significant changes would have to be made in them. Even with these changes, it is not clear if the electromagnetic interference would be adequately eliminated.

The relay system improved both sensitivity and resolution compared to the three previous systems. The problem with the relay system was the mechanical instability. To avoid electromagnetic interference and also to reduce cost of development, the system was made of plastic. The drawback is the low stiffness and high thermal expansion coefficient of plastic. As a result, the plastic relay system could bend as a result external forces or expand/shrink as a result of temperature change. This resulted in small shifts in the images acquired over time, which required image registration as a post processing step in analyzing dynamic image sequences.

## CHAPTER 4: MEASURING VASCULAR PERMEABILITY WITH OPTICAL MICROSCOPY

### 4.1: Overview

In this chapter, three methods to measure vascular kinetic parameters of molecular agents (MAs) with optical fluorescence microscopy are reviewed and analyzed [1-3]. Based on the error analysis of these methodologies and capabilities of the dual modality imaging system (described in chapter 3) a new methodology is introduced. In all these methods, a mouse dorsal skin-fold window chamber (DSFC) is imaged. One of the methods is based on 3-D scanning of the window chamber with confocal fluorescence microscopy [1]; the other methods are based on epi-fluorescence microscopy of the tissue [2-3]. The more accurate approach to this problem is imaging by confocal microscopy. However, since the dual modality imaging system is not capable of confocal microscopy, inevitably, regular epi-fluorescence microscopy was applied in the processing of collected data.

Vascular permeability is measured based on a two-compartment model in which the MA is in exchange between the intra-vascular (IV) and extra-vascular (EV) compartments as described in section 4.2. The kinetic parameters describing the dynamics of a MA in the tissue can be investigated by measuring the concentration of the agent in the IV and EV compartments throughout a period of time. This can be done by labeling the MA with a fluorescent contrast agent (CA) and injecting it into the vasculature. There are two problems in measuring vascular kinetics from the measured fluorescent signal intensity: 1) Determining the signal in each of the two compartments from the measured signal intensity. 2) Converting fluorescence signal intensity to MA concentration.

Since resolution is not high enough to have voxels that reside entirely in one compartment, signal from each voxel is a weighted summation of the fluorescence in the two compartments. The first problem is further aggravated by the presence of multiple tissues in each voxel. A mouse dorsal skin-fold window chamber consists of epidermis, subcutaneous tissue and striated muscle tissues [3]. Unless confocal microscopy is used, these tissues are not resolvable. Therefore, only the weighted average of vascular kinetic parameters in all these tissues can be measured.

In order to convert fluorescence signal intensity to the number of MA molecules in a voxel, the effects of absorption and scattering of both excitation and emission light should be considered as well as the spatial variation of excitation light and optical system collection efficiency, particularly as a function of tissue depth.

In order to convert the number of MA molecules to concentration, the volume of the voxel must be known. This is usually not possible in regular fluorescence microscopy since the voxel thickness is equal to the unknown thickness of the tissue being imaged. The location of the focal plane of the imaging system in the tissue also changes the voxel volume.

Application of confocal or 2-photon fluorescence microscopy addresses most of the abovementioned problems. Therefore, the approach based on using a confocal microscope is reviewed first followed by the methods of epi-fluorescence imaging, which is what our system is capable of implementing. Only the basic methodology of each approach is described. The assumptions that were inherent in the application of each method are mentioned in an ordered format in each section. These assumptions are later summarized in table 4.1 in section 4.6.

## 4.2: Two Compartment Model

Tracer kinetics in tissue can be analyzed via compartmental or distributed models. Compartmental models divide tissue into different compartments with uniform distribution of MA in each compartment. In contrast, distributed models allow for a gradient in MA concentration in each compartment [5]. The number of compartments depends on the tissue under study and complexity of the model. In certain tissues, additional compartments are required due to the variety of the tissue types present.

The three approaches that are reviewed in this chapter are all based on a two compartment model. As mentioned, in the two-compartment model, the MA is in exchange between the IV and the EV compartments in the tissue under study [4-6]. In addition, it is assumed that the MA is uniformly distributed in each of the plasma (IV) and interstitial (EV) compartments. Wu, et al. demonstrated that the assumption of uniform distribution of BSA in the interstitial space can lead only to insignificant error [2].

BSA, like most other MAs, does not enter the cells in either compartment within the time frame and sensitivity limit of the experiments. Therefore, the IV and EV compartments are often referred to as the plasma and interstitial compartments. The EV compartment is also referred to as the extra-cellular extra-vascular compartment [8]. However, the MA might not be able to move freely in the interstitial space; therefore, the available volume in the interstitial space depends on the molecular structure of the MA [1, 7]. In general, as the molecular weight of the MA increases, the available volume for it in the interstitial space decreases [9]. To make the discussions general, the plasma and interstitial compartments are only referred to as the IV and EV compartments, respectively, in this text.

The IV compartment is in exchange with the entire tissue in the body; but, the EV compartment is in exchange only with the IV compartment in the tissue under study. Therefore, the concentration in the IV compartment is determined by the dynamics of the MA in the entire body. However, the EV concentration is only determined by the IV concentration and the kinetics of the MA between the IV and EV compartments. Lymphatic drainage and cell uptake of MA is ignored in this model.

The basic kinetic equation between two adjacent compartments is:

$$K_{\text{trans}} = \frac{J_s}{C_i - C_e}, \quad (4.1)$$

where  $K_{\text{trans}}$  is the transfer constant,  $J_s$  is the molecular flow of MA between the two compartments per unit total volume of tissue containing the two compartments, and  $C_e$  and  $C_i$  are the concentrations of the MA in the two compartments. In the context of measuring vascular kinetics,  $C_i$  and  $C_e$  stand for the IV and EV concentration of the MA, respectively. Since the EV compartment is in exchange only with the IV compartment, it is possible to write the following relationship for  $J_s$ :

$$J_s = \frac{1}{V_T} \frac{d(C_e V_E)}{dt} = \frac{V_E}{V_T} \frac{dC_e}{dt} = v_e \frac{dC_e}{dt}, \quad (4.2)$$

where  $V_E$  is the volume of the EV compartment,  $V_T$  is the total tissue volume and  $v_e$  is the ratio of  $V_E$  to  $V_T$ . By incorporating Eq. 4.2 in Eq. 4.1 and rearranging, one can write the following differential equation:

$$v_e \frac{dC_e}{dt} = K_{\text{trans}}(C_i - C_e). \quad (4.3)$$

Eq. 4.10 can be written in the integral form as:

$$v_e C_e(t) = K_{\text{trans}} \int_0^t e^{-k_{\text{ep}}(t-\tau)} C_i d\tau, \quad (4.4)$$

where  $k_{\text{ep}}$  is the rate constant defined by

$$k_{\text{ep}} = \frac{K_{\text{trans}}}{v_e}. \quad (4.5)$$

As will be discussed later,  $k_{\text{ep}}$  is useful in comparing MRI and optical measurements of vascular kinetics. The physiological interpretation of  $K_{\text{trans}}$  depends on the mechanism of transfer of the MA between the two compartments [5]. If flow of blood into the space is the limiting factor,  $K_{\text{trans}}$  is equal to blood plasma flow per unit volume of tissue. However, since the applied MA, labeled BSA, has high molecular weight, the concentration of MA in blood is essentially uniform and the limiting factor in vascular-interstitial transport is the properties of the vessels. In this case,  $K_{\text{trans}}$  is equal to permeability ( $P$ ) multiplied by surface area ( $S$ ) per unit volume of tissue ( $V_T$ ):

$$K_{\text{trans}} = \frac{PS}{V_T} \quad (4.6)$$

and

$$k_{\text{ep}} = \frac{PS}{V_E}. \quad (4.7)$$

Signal intensity in fluorescence microscopy is proportional to the number of MA molecules in the volume of tissue from which the signal is measured. The concentration of MA is equal to the number of MA molecules divided by the respective volume. For the intravascular compartment:

$$C_i = \frac{N_i}{V_I} = \frac{N_i}{V_v(1-H_T)}, \quad (4.8)$$

and for the extravascular compartment:

$$C_e = \frac{N_e}{V_E}, \quad (4.9)$$

where  $N_i$  and  $N_e$  are the number of MA molecules in the IV and EV compartments, respectively;  $V_I$  and  $V_v$  are the IV compartment volume and the intra-vascular volume, respectively, and  $H_T$  is the hematocrit.  $V_i = V_v(1-H_T)$  is the plasma (IV compartment) volume. By incorporating Eq. 4.7-4.9 in Eq. 4.4 one can derive the following integral relationship between the number of MA molecules in the IV and EV compartments:

$$N_e(t) = \alpha \int_0^t e^{-k_{ep}(t-\tau)} N_i(\tau) d\tau, \quad (4.10)$$

where

$$\alpha = K_{trans} \frac{V_T}{V_v(1-H_T)} = k_{ep} \frac{V_E}{V_v(1-H_T)} = \frac{PS}{V_v(1-H_T)}. \quad (4.11)$$

In order to obtain the kinetic parameters, either the concentrations of the MA (obtained from MRI signal enhancement) or the number of MA molecules (obtained from optical signal intensity) in the two exchanging compartments are fitted to Eq. 4.4 or Eq. 4.10. The exact method of fitting the measured data to Eq. 4.4 or Eq. 4.10 is described in section 6.10.2.

### 4.3: Measuring Vascular Kinetic Parameters in DSFC with Confocal Microscopy [1]

The method of using confocal microscopy for measuring vascular kinetic parameters was described in the work of Dreher, et al. [1]. The in-plane resolution of the imaging system described in this paper was 512x512 pixels over a 460x460  $\mu\text{m}$  field of view, and optical slice thickness was 7.1  $\mu\text{m}$ . This corresponds to a voxel size of 0.90x0.90x7.1  $\mu\text{m}$ . This resolution was enough to select voxels that were entirely extra-vascular or intra-vascular. In reference [1] the terms extra-vascular and intra-vascular refer to both the intra-cellular and extra-cellular spaces in these two volumes as opposed to the IV and EV compartments described earlier, which refer only to the extra-cellular spaces. The vasculature was identified during the experiment by injection of Rhodamine-labeled 2-MDa dextran (red fluorescent MA, Molecular Probes) which remained mostly intravascular during the experiment. The MAs under study, which were injected together with the Rhodamine agent, were either green fluorescent Dextran or BSA labeled with Alexa Fluor 488 (both from Molecular Probes).

In order to measure the EV volume, the concentrations of MA in the extra-vascular and intra-vascular regions were measured at quasi-steady state when net transfer of MA was zero. It was assumed that this occurs in the tumor at the end of the experiment, which was 30 minutes after injection (assumption 1.1). The estimated EV volume by this method is equal to the available volume to the MA in the interstitial space – and not the entire interstitial space volume. In the

quasi-steady state, the EV and IV concentrations are equal. Therefore, the EV compartment volume can be obtained from:

$$C_e(30m) = C_i(30m) \Rightarrow \frac{N_e}{V_E} = \frac{N_i}{V_v(1-H_T)} \Rightarrow V_E = \frac{N_e(30m)}{N_i(30m)} \times V_v(1 - H_T). \quad (4.12)$$

The total number of MA molecules in any compartmental volume,  $N_i$  and  $N_e$ , were replaced by the measured signal intensities in the MA kinetic equations from that compartment. The inherent assumption is that relation between intensity and number of MA molecules is linear and the same in both compartments. This assumption is valid here since the depth of imaging was limited to 100  $\mu\text{m}$ , which is much less than the combined effective attenuation factor of the tissue and the MA within it at the excitation and emission wavelengths of the applied MA. At higher tissue thickness, the absorption effect of the MA must be considered before assuming linear relation between signal intensity and concentration of MA.

#### **4.4: Measuring Vascular Kinetic Parameters, Method of Wu, et al. [2]**

The methodology of Wu, et al. [2] is described here with slight modification in the notation and presentation format. The same is done below in section 4.5 in describing the methodology of Yaun, et al. [3]. These changes are done to make understanding and comparison of the methods more clear. The assumptions of these methodologies are stated in sections 4.4 and 4.5. The extent of the validity of these assumptions and their effect in the final measurements are discussed in section 4.6.

Due to the lack of optical sectioning and insufficient spatial resolution, it is typically not possible to select voxels that are entirely in the IV or EV compartments. In order to delineate the optical signal in these two compartments, two assumptions are made. First, it is assumed that after the injection of MA, the MA remains intravascular for a short period of time. In this initial time period, the fluorescent signal is entirely from the IV compartment (assumption 2.1). This point in time is labeled as the time origin ( $t=0$ ) in the rest of this chapter. This approximation holds if vascular permeability to the MA is low, as it is in the case of labeled BSA. The second assumption is that the EV component of the signal has uniform spatial distribution across the region where the vascular permeability is to be estimated (assumption 2.2).

The approach described in reference [2] is as follows. Two ROIs are selected: one on a small vessel with no underlying out of focus vessels (ROI1) and the other on a small region of tissue that encompasses that vessel (ROI2). The signal intensity per unit area in both ROIs is a mixture of IV and EV components. However, the IV component accounts for a larger portion of the total signal in ROI1 in comparison to ROI2. The equations for the signal intensities per unit area in the two ROIs are:

$$I_{1T}(t) = I_{1i}(t) + I_{1e}(t) \quad (4.13)$$

$$I_{2T}(t) = I_{2i}(t) + I_{2e}(t), \quad (4.14)$$

where  $I_{1T}$  and  $I_{2T}$  are the total fluorescent intensity per unit area from the two ROIs, respectively, and  $I_{1i}$ ,  $I_{2i}$ ,  $I_{1e}$  and  $I_{2e}$  are the IV and EV components in each of the two ROIs. Since signal intensities are assumed to be linear with the amount of CA,  $I_{2i}$  and  $I_{2e}$  are proportional to  $I_{1i}$  and  $I_{1e}$ , respectively. Thus Eq. 4.13 can be written as

$$I_{1T}(t) = a_{1i}I_{2i}(t) + a_{1e}I_{2e}(t), \quad (4.15)$$

where  $a_{1i}$  and  $a_{1e}$  are constants of proportionality. Assumptions 2.1 and 2.2 lead to:

$$\text{Assumption 2.1: } a_{1i} = \frac{I_{1i}(t)}{I_{2i}(t)} = \frac{I_{1i}(0)}{I_{2i}(0)} = \frac{I_{1T}(0)}{I_{2T}(0)} = b. \quad (4.16)$$

$$\text{Assumption 2.2: } I_{1e}(t) = I_{2e}(t) \Rightarrow a_{1e} = 1. \quad (4.17)$$

Eq. 21-24 are combined to obtain the IV and EV components of optical signal in ROI1:

$$\begin{bmatrix} I_{1T}(t) \\ I_{2T}(t) \end{bmatrix} = \begin{bmatrix} b & 1 \\ 1 & 1 \end{bmatrix} \begin{bmatrix} I_{2i}(t) \\ I_{2e}(t) \end{bmatrix} \Rightarrow \begin{bmatrix} I_{1i}(t) \\ I_{1e}(t) \end{bmatrix} = \frac{1}{b-1} \begin{bmatrix} 1 & -1 \\ -1 & b \end{bmatrix} \begin{bmatrix} I_{1T}(t) \\ I_{2T}(t) \end{bmatrix}. \quad (4.18)$$

Eq. 4.17 is converted to measured signal intensity by applying the following relation:

$$k = \frac{I_i/N_i}{I_e/N_e} \quad (4.19),$$

which yields the following integral equation

$$I_e(t) = k^{-1} \alpha \int_0^t e^{-k_{ep}(t-\tau)} I_i(\tau) d\tau \quad (4.20).$$

The parameter  $k$  accounts for the difference in the absorption coefficient of light in the two compartments. Its value is 1 when absorption is low. In the paper describing the method,  $k$  was measured from ex-vivo experiments by comparing signal intensity of CA dissolved either in 20% H<sub>T</sub> blood or PBS. The obtained values were 0.604 and 0.744 for TRITC ( $\lambda_{exc/em}=554/583\text{nm}$ ) and FITC ( $\lambda_{exc/em}=495/521\text{nm}$ ), respectively. However, it could be argued that this measurement of  $k$  does not simulate tissue exactly, since in vivo, the vasculature is embedded in the tissue, and therefore, fluorescent light from either compartment experiences the absorption of both compartments.

To determine permeability from the estimated  $\alpha$ , the average vascular surface area to volume ratio in ROI2 was determined ( $S/V_v$  in Eq. 4.11). This was done by measuring the diameter of in-focus vessels in ROI2. The value for the hematocrit ( $H_T$ ) was obtained from a separate study with the same animal preparation procedure. The systematic value of hematocrit in arteries is 40% [10]; however, the hematocrit in microvasculature is lower than arteries [11]. The hematocrit of tumor and healthy tissue microvasculature was found to be 18% and 25%, respectively [2].

In reference [2], permeability and  $k_{ep}$  were both estimated; but transfer constant ( $K_{trans}$ ) was not estimated. As mentioned in section 4.2, if the permeability to the MA is low, as is the case for BSA,  $K_{trans}$  would be equal to the permeability surface area product per unit volume of tissue. The volume of tissue consists of both the intra-cellular and extra-cellular tissue. Since the intra-cellular tissue does not affect the kinetics of the MA, its only effect on the optical signal is through scattering and absorption. Therefore, in order to measure  $K_{trans}$  from fluorescent signal, the volume of tissue must be estimated by its absorption/scattering effect. This is done by Yuan, et al. [3] as described in section 4.5.

The notations used here are slightly different from the notations of Wu, et al. [2]. In their paper, the IV and EV compartments are called vascular and interstitial compartments and are identified with the subscripts “v” and “i”, respectively.

## **4.5: Measuring Vascular Kinetic Parameters, Method of Yuan, et al. [4]**

### **4.5.1: Outline**

In the method developed by Yuan, et al. [4], the permeability of tumor vasculature to Texas-Red labeled BSA was estimated. It was stated in the paper that the method is not sufficiently accurate to determine the slow extravasation of BSA in healthy tissue. In addition to estimating vascular permeability,  $K_{trans}$  was also estimated.

In this method, in addition to the mouse under study, another mouse, without tumor implantation under its window chamber, was used to measure the rate of extravasation of CA from the vasculature. The mouse in which vascular permeability is estimated in the tumor is called USM (under study mouse) and the tumor free mouse is called TFM (tumor free mouse).

Three ROIs were selected: one on TFM and two on USM. The ROI on TFM was selected on an artery and its immediate surroundings. This ROI is called RTFM. One ROI on USM was selected on the region where vascular permeability was to be estimated. This ROI is called RUSM. Another ROI on USM was selected on a clear vessel near the surface of the window chamber and is called RCV (region of clear vessel). With the help of RCV, the relationship between the signal intensity and MA concentration is obtained.

### **4.5.2: Assumptions**

Three assumptions were made to delineate the IV and EV components of the signal. The first assumption (assumption 3.1) is that CA remains intra-vascular for a short period after its injection in the vasculature. This assumption is the same as assumption 2.1 in section 4.4. The second assumption (assumption 3.2) is that the EV component of the fluorescent signal from RTFM is negligible during the course of the experiment. The third assumption (assumption 3.3) is that the rate of MA clearance from the vasculature is the same in the TFM and USM.

In calculating the concentration gradient between the two compartments, it is assumed that, due to slow extravasation, the EV concentration of the MA is negligible in comparison to the IV concentration (assumption 3.4). Therefore, the EV concentration ( $C_e$ ) in the right side of the Eq. 4.3 is ignored. This assumption is in clear contradiction with assumption 1.1 in section 4.3 which states that the CA distribution reaches to an equilibrium status at the end of the experiment. However, the methodology of Yuan, et al. is also applicable without making this assumption.

In order to measure the vascular to total tissue volume ratio, which is required to measure  $K_{trans}$ , several additional assumptions were made. It was implicitly assumed that the excitation light intensity is uniform across the tissue surface (assumption 3.5). There were also several assumptions made in calculating light collection efficiency as a function of tissue depth that will not be discussed here. In calculating the light collection efficiency across the tissue, the tissue thickness was assumed to be 1 mm (assumption 3.6). Finally it was assumed that MA fluorescence in capillaries experiences the same absorption/scattering as the EV compartment (assumption 3.7). The inherent reasoning behind this assumption is that capillaries are spread uniformly across the tumor tissue.

All the assumptions are summarized in table 4.1.

#### 4.5.3: Distinguishing the IV and EV components of the Signal

The IV signal component of RTFM ( $I_{RTFM,i}$ ) is assumed to be equal to the total signal ( $I_{RTFM,T}$ ) (assumption 3.2, Eq. 4.21). The IV component of RUSM ( $I_{RUSM,i}$ ) is equal to a constant,  $r$ , multiplied by the IV component of RTFM (assumption 3.3, Eq. 4.22); this constant is determined by the ratio of the signal intensities at  $t=0$  in the vasculature (assumption 3.1, Eq. 4.23). The relationships are therefore:

$$I_{RTFM,T}(t) = I_{RTFM,i}(t) \quad (4.21)$$

$$I_{RUSM,T}(t) = r \times I_{RTFM,i}(t) + I_{RUSM,e}(t) \quad (4.22)$$

$$r = \frac{I_{RUSM,i}(0)}{I_{RTFM,i}(0)} = \frac{I_{RUSM,T}(0)}{I_{RTFM,T}(0)} \quad (4.23)$$

where  $I_{RUSM,T}$  and  $I_{RUSM,e}$  are the total and EV component of RUSM signal intensity, respectively. From Eq. 4.21 and 4.22, the IV and EV signals in the RUSM are:

$$I_i(t) = I_{RUSM,i}(t) = r^{-1} \times I_{RTFM,T}(t) \quad (4.24)$$

$$I_e(t) = I_{RUSM,e}(t) = I_{RUSM,T}(t) - r \times I_{RTFM,T}(t). \quad (4.25)$$

#### 4.5.4: Estimating Vascular Kinetics of the MA

The kinetic parameters were determined in a manner similar to section 4.2, the only difference was assumption 3.4 such that:

$$K_{\text{trans}} = \frac{J_s}{C_i}. \quad (4.26)$$

Assumption 3.4 leads to the following relationship between the signals in the two compartments:

$$I_e(t) = \alpha \int_0^t I_i(\tau) d\tau, \quad (4.27)$$

where  $\alpha$  is defined in Eq. 4.11 and  $k$  (defined in Eq. 4.19) is assumed equal to 1 due to the low absorption of light at the corresponding wavelengths ( $\lambda_{\text{exc/em}}=596/615\text{nm}$ ). Here,  $V_v$  and  $S$  correspond to the vascular volume and surface area in RUSM. It can be seen that the rate constant ( $k_{\text{ep}}$ ) is not present in Eq. 4.27. Therefore, the rate constant could not be estimated.

#### 4.5.5: Estimating $K_{\text{trans}}$

According to Eq. 4.11, in order to determine  $K_{\text{trans}}$  from  $\alpha$ , the ratio of the IV compartment volume to total tissue volume must be obtained in RUSM. The concentration and volume appear together as a product in signal-concentration relationships. The MA concentration in the vasculature is obtained in RCV where vascular volume can be measured. Then the value of concentration in the IV signal component of RUSM is replaced by the value obtained in RCV. In this process, it is assumed that apart from tissue absorption and scattering effects, the relation between signal intensity and number of MAs is the same in RCV and RUSM. This is true if the excitation light irradiance is the same in these two ROIs (Assumption 3.5).

RCV is on a clear vessel near the top surface of the tissue. The imaging system is focused on the top surface of the window chamber. According to assumption 1, MA agent is strictly intra-vascular at  $t=0$ . Since the vessel is near the top, the absorption/scattering effects and depth of focus issues can be neglected. Therefore, the total fluorescent light power  $F_{P0}$  generated at  $t=0$  by the vessel is given by

$$F_{P0} = kN = k \frac{1}{4} \pi d^2 l \times C_i^{t=0} (1 - H_{\text{TV}}), \quad (4.28)$$

where  $N$  is the total number of MA molecules in the vessel,  $k$  is a constant that relates the signal intensity in the absence of absorption and scattering to the number of MA molecules,  $d$  is the diameter of the vessel,  $l$  is the length of the vessel in RCV, and  $H_{\text{TV}}$  is the hematocrit in the vessel.

In order to take into account the absorption, scattering and depth sensitivity of the imaging system across the tissue, a parameter called the optical correction function (OCF),  $\Psi(h)$ , was defined as:

$$\Psi(h) = \int_0^h rCE(z) dz, \quad (4.29)$$

where  $rCE(z)$  is the ratio of light collection efficiency at depth  $z$  to depth 0, and  $h$  is the tissue thickness. OCF was estimated from separate experiments. The details of calculations and the inherent approximations and assumptions in estimating OCF are discussed in the paper. The relationship between average signal intensity and number of MA molecules in RUSM is:

$$I_T = \frac{1}{A} k \iiint C \times rCE(z) dv = \frac{1}{A} k \frac{N_T}{Ah} \int rCE(z) Adz = \frac{1}{A} k N_T \frac{\Psi(h)}{h} \approx \frac{1}{V_T} k N_T \Psi(1mm) = k C_T \Psi(1mm), \quad (4.30)$$

where  $I_T$  is the total signal intensity per unit area,  $N_T$  is the total number of MA molecules in RUSM,  $A$  is the area of RUSM, and  $C_T$  is the average concentration of MA in the tissue. The approximation in Eq. 4.30 is equivalent to assumption 3.6.

According to assumption 3.7, when MA is confined in the vasculature,  $N_T$  in Eq. 4.30 can be replaced by  $N_{cp}$ , where  $N_{cp}$  is the number of CA molecules in the capillaries. For this case at  $t=0$  (assumption 3.1):

$$I_{T0} = k N_{cp0} \frac{\Psi(1)}{V_T} = k C_i^{t=0} V_i \frac{\Psi(1)}{V_T} = k C_i^{t=0} V_{cpv} (1 - H_{Tc}) \frac{\Psi(1)}{V_T}, \quad (4.31)$$

where  $I_{T0}$  and  $N_{cp0}$  refer to the values of  $I_T$  and  $N_{cp}$  at  $t=0$ ,  $V_T$  is the tissue volume,  $V_{cpv}$  is the capillary volume ( $= V_{i,RUSM}/(1-H_{Tc})$ ) and  $H_{Tc}$  is the hematocrit in the capillary. By replacing  $C_i^{t=0}$  from Eq. 4.28, the vessel to tissue volume ratio is:

$$\frac{V_{cpv}}{V_T} = \frac{\pi d^2 I_{T0}}{4 F_{p0} \Psi(1)} \times \frac{1 - H_{Tv}}{1 - H_{Tc}} \quad (4.32)$$

Yuan, et al. assumed both  $H_{Tv}$  and  $H_{Tc}$  to be equal to 30%. This value was taken from the work of Brooks, et al. [6].

In summary, the IV compartment volume to total tissue volume ratio is obtained in two steps. First, the relationship between signal intensity and MA concentration is obtained in RCV at  $t=0$  where vascular volume can be measured and absorption and scattering is ignored (Eq. 4.28). Second, the absorption and scattering in RUSM is accounted for by a series of assumptions and approximations. At the same time, it is assumed that the average signal intensity per area in RUSM is only dependent on the average concentration of the MA and not the distribution of MA molecules between the IV and EV compartments (assumption 7, Eq. 4.30). By taking advantage of the signal-concentration relationship obtained in the RCV, and the absorption and scattering estimate in RUSM, the relation between signal intensity and average concentration across RUSM volume is found. The average concentration in RUSM at  $t=0$  is equal to  $C_i V_i / V_T$ . In this way, the  $V_i / V_T$  ratio is introduced in the signal equation.

## 4.6 Analysis of Previous Methods and New Methodology

### 4.6.1 Outline

In sections 4.6.2 and 4.6.3 the assumptions and approximation involved in the three methods described in sections 4.3-4.5 are analyzed. In section 4.6.4, the approach that is applied in our research is summarized. Table 4.1 lists the assumptions made in the previous sections.

**Table 4.1.** List of Assumptions

Section	Assumption #	Assumption
4-3	1.1	Eq. 4.12: At $t > 30$ min, $C_e = C_i$
4-4	2.1	Eq. 4.16: $I_i(0) = I_T(0)$
	2.2	Eq. 4.17: $I_{1e}(t) = I_{2e}(t)$
	2.3	Eq. 4.19: $k = \frac{I_e/N_e}{I_i/N_i}$
4-5	3.1	Eq. 4.23: $I_i(0) = I_T(0)$
	3.2	Eq. 4.21: $I_{RTFM,T}(t) = I_{RTFM,i}(t)$
	3.3	Applied in Eq. 4.22: $I_{RUSM,i}(t) = r \times I_{RTFM,i}(t)$
	3.4	Implied in Eq. 4.26: $C_e(t) \ll C_i(t)$
	3.5	Excitation light intensity is the same in RUSM and RCV
	3.6	Applied in Eq. 4.30: $\Psi(h) = \Psi(1)$
	3.7	Applied in Eq. 4.31: Capillary fluorescence experiences the same absorption and scattering as the interstitial fluorescence

#### 4.6.2 Determining the IV and EV Signal Components

In this section the assumptions made in finding the IV and EV components of the signal are discussed. Assumption 2.1 (= Assumption 3.1) holds well if MA extravasation from the vasculature is slow. This is the case for the MA used in our work (labeled BSA). High temporal resolution in optical imaging helps to identify the earliest point of time when MA is distributed in all vasculature, but has not yet leaked out into the extravascular space.

The validity of assumption 2.1 can be verified by analyzing the estimated interstitial signal values. Three situations might happen. If  $t=0$  is selected late, the MA would be in both the IV and EV compartments at  $t=0$  (case 1). However, if  $t=0$  is selected too early, the MA might have been distributed fully in the arteries but not the capillaries (case 2) or be in the capillaries but not the veins (case 3). To simplify the explanations consider  $b$  (defined in Eq. 4.16), and its estimated value,  $b_m$ , determined from the ratio of the signals in the two regions of interest at  $t=0$ :

$$b = \frac{I_{1i}^{\infty}}{I_{2i}^{\infty}}, \quad b_m = \frac{I_{1T}^{t=0}}{I_{2T}^{t=0}} \quad (4.33, 4.34)$$

$I_{1i}^{\infty}$  and  $I_{2i}^{\infty}$  refer to the signals at the time where the concentration is uniformly distributed in the vasculature. Since the volume ratio of the IV compartment to the EV compartment is higher in ROI1, in case 1, where  $t=0$  is selected too late,  $b_m < b$ . The relation between  $b_m$  and  $b$  in cases 1, 2 and 3 are described in the following equations:

$$\text{case 1: } b_m = \frac{I_{1T}^{t=0}}{I_{2T}^{t=0}} = \frac{I_{1e}^{t=0} + I_{1i}^{t=0}}{I_{2e}^{t=0} + I_{2i}^{t=0}} = \frac{I_{1i}^{t=0}}{I_{2i}^{t=0}} \left\{ \left( \frac{I_{1e}^{t=0}}{I_{1i}^{t=0}} + 1 \right) / \left( \frac{I_{2e}^{t=0}}{I_{2i}^{t=0}} + 1 \right) \right\} < \frac{I_{1i}^{t=0}}{I_{2i}^{t=0}} \approx \frac{I_{1i}^{\infty}}{I_{2i}^{\infty}} = b$$

$$\text{case 2 \& ROI1 is on an artery: } b_m = \frac{I_{1T}^{t=0}}{I_{2T}^{t=0}} \approx \frac{I_{1i}^{t=0}}{I_{2i}^{t=0}} > \frac{I_{1i}^{\infty}}{I_{2i}^{\infty}} = b$$

case 3 & ROI1 is on a vein:  $b_m = \frac{I_{1T}^{t=0}}{I_{2T}^{t=0}} \approx \frac{I_{1i}^{t=0}}{I_{2i}^{t=0}} < \frac{I_{1i}^{\infty}}{I_{2i}^{\infty}} = b$

The estimated value of the EV signal in region 1 using the estimated value  $b_m$ ,  $I_{e,m}$ , and according to Eq. 4.18, is given by the following relationship:

$$I_{e,m} = \frac{I_{1T}-b_m I_{2T}}{1-b_m} = \frac{I_{1T}-b I_{2T}}{1-b_m} + \frac{b-b_m}{1-b_m} I_{2T} = I_e \frac{1-b_m}{1-b} + \frac{b-b_m}{1-b_m} (I_e + I_{2i}) = I_e + \frac{b-b_m}{1-b_m} I_{2i}. \quad (4.35)$$

Therefore, if the timing for  $t=0$  is not right, the estimated EV signal would depend on the IV signal. Since at  $t=0$ ,  $I_e \approx 0$  and  $b_m > 1$ , in cases 1 and 3,  $I_{e,m} > 0$  and in case 2,  $I_{e,m} < 0$ .

Assumption 2.2 states that the two ROIs, ROI1 on the vessel and ROI2 containing the vessel and its surrounding, have zero EV content difference. Since vasculature is embedded in the tissue, the larger the vessel, the less valid is this assumption. However, if the vessel is very small, the difference between the IV components becomes very small as well. Therefore, the determinant of the matrix in Eq. 4.18 approaches zero. This would make the equations more sensitive to noise. Therefore, there is a trade-off on the size of the vessel in ROI1 relative to the accuracy of the EV and IV signal estimates in ROI2. In addition, the other surrounding and underlying vasculature can additionally increase the EV content difference or reduce the IV content difference between of the two ROIs.

Assumption 3.2 ( $I_{RTFM,T}(t) = I_{RTFM,i}(t)$ ), holds well since signal intensity from large vessels is significantly higher than signal from the EV compartment of healthy tissue during the entire course of the experiment. The approximation could be further improved by selecting the RTFM only on the vessel and not on its surrounding.

Assumption 3.3 was investigated by the MRI research community as well for DCE-MRI. It was shown that applying this approximation could lead to significant error [12, 13]. The MA plasma clearance can vary as a function of cardiac output, distribution of CA in the body, kidney function, etc. [14]. In addition, since there is no tumor in the TFM, the effect of tumor uptake in removing CA from the blood is ignored. These variables are in addition to the parameters that are only partially controllable, such as temperature, respiration rate and heart rate. Therefore, we avoid this assumption in our analysis. It should be mentioned that this assumption is also in contradiction to the philosophy behind simultaneous dual-modality imaging which strives to eliminate errors resulting from experimental variability between multiple measurements.

With the estimates of the IV and EV signal intensities in an ROI, the rate constant ( $k_{ep}$ ) can be estimated by fitting the IV and EV signals to Eq. 4.20. Therefore,  $k_{ep}$  can be measured with optical imaging with higher confidence than permeability and  $K_{trans}$ . The factors that contribute to the accuracy in estimation of  $k_{ep}$  are: 1- the ability to separate the IV and EV components of the signal, and 2- the linear relation between signal intensity and concentration in each compartment. As explained in detail in chapter 5, both these factors, especially the later factor, are not as valid in MRI as they are in optics. Therefore, the rate constant obtained by optical imaging is a standard

with which to assess DCE-MRI results. The following section discusses the potential to estimate vascular permeability and  $K_{\text{trans}}$  with optical methods.

#### 4.6.3 Measuring Kinetic Parameters

It is assumed that the diameter of vessels can be measured from images. In order to measure  $K_{\text{trans}}$  using the Yuan, et al. method, the diameter of one large vessel is needed (the vessel in RCV). However, in order to measure vascular permeability as described in section 4.4, the average diameter of all vessels in ROI2 must be measured, which is difficult to do. Yuan, et al. [3] explained that due to scattering, vessel diameters in the image appear larger in epi-illumination DCE fluorescence imaging and smaller in trans-illumination white light imaging. In the former case, scattering of fluorescent light from the vasculature makes the vessels appear larger. In the latter case, the vessels are the dark regions due to the higher absorption coefficient of the blood. In this case, the scattering of the light from extra-vascular regions into the darker vascular regions, makes the vessels to appear smaller. As a first approximation, Yuan, et al. approximated the vessel diameter as the average of the diameters measured in trans and epi-illumination. The average vessel diameter measured by Yuan, et al. in the implanted LS174T human colon tumor in mouse dorsal skin-fold window chamber implanted on SCID mice was 167  $\mu\text{m}$  [3] while Wu, et al. reported 47  $\mu\text{m}$  average vessel diameter in R3230 mammary tumor implanted on dorsal skin flap window chamber on female Fischer-344 rats [2]. Yuan et al., in another publication measured average vessel diameter both on R3230 Fisher Rat and SCID mice mammary carcinoma. The reported values were 20.7  $\mu\text{m}$  and 30.4  $\mu\text{m}$  respectively [15].

Estimating vascular permeability using the method of section 4.4 was not always feasible in our set-up; because determining the diameter of the vessels in thick tissue areas (e.g. tumors) was not possible due to out of focus and scattered light. In areas with high vascular content, individual vessels were not distinguishable. This was particularly true in tumor regions. As explained in section 3.6, a limitation in spatial resolution results from out of focus light, which can be improved only by reducing the NA or restricting the tissue thickness. Wu, et al. [2] restricted the tissue thickness in the window chamber to 200  $\mu\text{m}$ . However, limiting tissue thickness might alter tumor growth behavior [16].

In the method described by Yuan, et al., to find the relationship between CA concentration and signal intensity, the IV fluorescent signal of a clear in-focus vessel was measured at  $t=0$  (Eq. 4.28). Then it was assumed that the signal-concentration relation was the same in RUSM except for the effect of absorption and scattering. This is true if the illumination irradiance is the same in both the RUSM and the RCV (assumption 3.5). In the dual modality imaging system, the illumination intensity has about  $\pm 15\%$  variation across the area of the window chamber. Therefore, RCV and RUSM should either be close to one another or the illumination non-uniformity should be considered in the error analysis.

While tumor thickness varies between 0.5 mm to 2 mm (according to the paper), an average 1 mm thickness was assumed (assumption 3.6:  $\Psi(h) \approx \Psi(1)$ , Eq. 4.30). This essentially translates into stating that light from tissue depth beyond 0.5 mm would not have a significant effect on total collected light, and therefore, tissue thickness could be represented by an average value. According to the measurements of light collection efficiency in the paper:

$$\frac{\Psi(1)-\Psi(0.5)}{\Psi(0.5)} = 0.48$$

$$\frac{\Psi(2)-\Psi(1)}{\Psi(2)} = 0.058$$

Therefore, assuming a tissue thickness of 1 mm can lead to up to 48% error in the estimated value of  $K_{\text{trans}}$ , if the actual tissue thickness is 0.5 mm. This error is in addition to the approximations that were made in calculating the correction function. The tissue absorption is lower in the excitation-emission wavelengths used in our experimental apparatus (633nm-665nm in our setup versus 596nm-615nm in Yaun, et al. [3]); Therefore, deeper tissue contribute more in the total fluorescent light. As a result, assuming a representative tissue thickness would lead to higher error.

Assumption 3.6 was made in conjunction with neglecting light collection efficiency drop across the vessel in the RCV (Eq. 4.17). According to the estimation of light collection efficiency, this would lead to a minimum of 10% error per 100  $\mu\text{m}$  thickness of the vessel. This effect would lead to underestimation of  $F_{\text{P0}}$  (Eq. 4.28). If assumption 3.6 leads to over estimation of  $\Psi(h)$ , according to Eq. 4.32, these two sources of error tend to cancel each other; otherwise if  $\Psi(h)$  is underestimated, the two errors would add up.

In our analysis, we do not apply assumption 3.6, and as a consequence  $K_{\text{trans}}$  cannot be estimated from  $\alpha$ . As investigated, if  $\Psi(h)$  is obtained accurately, the error caused by inserting a fixed value for  $\Psi(h)$  could be over 48%. In the work by Yuan, et al.,  $\Psi(h)$  is a combination of two factors: 1) “the axial resolution and the effective sampling thickness of the optical system.” 2) the scattering and absorption effect of the tissue. These two factors are obtained separately and corrections made afterwards. The first factor is supposed to account for the optical system light collection efficiency as a function of distance to its focal plane. However, the fluorescent signal behaves like a lambertian source. In this case, according to conservation of Etendue in the absence of absorption and scattering, the spatially integrated light collection efficiency is the same in any plane perpendicular to the optical axis. Therefore, it appears that the first factor is just a re-consideration of the scattering and absorption effects. This factor is measured ex-vivo by measuring the average fluorescent light collection efficiency of MA solution in wells with various depths. However, the paper does not mention the dimensions of these wells. Therefore, it is difficult to assess the validity of the measurement. If the wells’ diameter is on the order of the depth, it is expected that average light collection efficiency drops as a function of well depth. However, the dimensions of a tumor in a window chamber are usually considerably larger than its thickness. Therefore, we expect that distance to focal point by itself does not affect the total collected light. If the first factor is invalid,

the assumption of fixed tissue thickness (assumption 3.6) would result in significantly higher error in total light collection efficiency.

Assumption 1.1 ( $t > 30$  min,  $C_e = C_i$ ) can be used to find the EV to IV volume ratio. This is possible if  $I_e$  and  $I_i$  can be separately measured and  $I_e/I_i$  is converted to  $N_e/N_i$  (Eq. 4.12). The study by Dreher, et al. [1] demonstrates that this assumption is valid for albumin in tumor. The applicability of this assumption can be verified by applying Eq. 4.4. Assuming  $C_i$  to remain constant:

$$C_e = k_{ep} \int e^{-k_{ep}(t-\tau)} C_i d\tau = C_i (1 - e^{-k_{ep}t}). \quad (4.36)$$

In order for  $C_e$  to be within 10% of  $C_i$

$$(1 - e^{-k_{ep}t_{eq}}) = 0.9 \Rightarrow t_{eq} = \frac{2.3}{k_{ep}}, \quad (4.37)$$

where  $t_{eq}$  is the time at which the CA is in equilibrium between the IV and EV compartments. As will be described in section 5.5.6,  $k_{ep}$  for BSA in PC-3 human prostate tumor xenografts is about  $8 \times 10^{-4} \text{ s}^{-1}$ . Therefore, in our experiment,  $t_{eq}$  is about 48 min. Many tumor cell lines have higher permeability to albumin than PC-3 [17, 18]. Our experiments usually lasted either 32 minutes or 40 minutes after the injection of the MA. However, in some experiments, we carried out optical imaging for as long as 2 hours. In reality,  $C_i$  decreases gradually over time. The reduction of  $C_i$  would make the two compartments reach equilibrium earlier than estimated in Eq. 4.37.

#### 4.6.4 Applied Methodology

The Wu, et al. approach, described in section 4.4, is accurate if the ROI in which the vascular permeability is to be determined satisfies the conditions specified in section 4.6.1. In summary, the ROI must include a small clear vessel surrounded by a uniform tissue. By applying this method, both rate constant and permeability can be measured.

If a clear small in-focus vessel is not distinguishable in the tissue region of interest, the methodology of section 4.4 is not applicable, and a new methodology which is similar to the method described in section 4.5, can be applied. To account for CA vascular clearance, instead of RTFM, a region on a large vessel in the USM is selected. We call this region, RPVS (region of peak vessel signal). To reduce the contribution from the EV compartment, the RPVS is selected on the center of a large vessel. The resulting equations to determine the EV and IV signals are similar to Eq. 4.21-4.25 except RTFM should be replaced by RPVS. Assumption 1.1 ( $t > 30$  min,  $C_e = C_i$ ) could be incorporated to validate the values obtained for  $k_{ep}$  and  $\alpha$  in the tumor. By rearranging Eq. 4.11 and 4.12 the following relation is obtained:

$$\frac{\alpha}{k_{ep}} = \frac{V_v(1-H_T)}{V_E} \approx \frac{N_i(t > 30 \text{ min})}{N_e(t > 30 \text{ min})} \approx \frac{I_i(t > 30 \text{ min})}{I_e(t > 30 \text{ min})}. \quad (4.38)$$

Also by applying assumption 1.1 and assumption 2.1 (equivalent to assumption 3.1), the volume of the IV compartment could be obtained:

$$V_{E,RUSM} = \frac{I_e(t>30\text{min})}{I_i(t>30\text{min})} \times V_{I,RUSM} = \frac{I_e(t>30\text{min})}{I_i(t>30\text{min})} \times \frac{I_{T,RUSM}^{t=0}}{I_{T,RPVS}^{t=0}} \times V_{I,RPVS}, (4.39)$$

where  $V_{E,RUSM}$ ,  $V_{I,RUSM}$  and  $V_{E,RPVS}$  refer to the volumes of the EV and IV compartments in RUSM and RPVS.

Permeability can be estimated as long as average vascular surface to volume ratio can be determined in the RUSM. As mentioned in section 4.6.2,  $K_{\text{trans}}$  is not estimated directly from the images due to the high errors involved in the approximation of this parameter; instead  $K_{\text{trans}}$  is estimated by either multiplying the typical value of  $v_e$  by  $k_{\text{ep}}$  or typical value of  $v_p$  by  $\alpha$ . In the next chapters, we demonstrate that  $K_{\text{trans}}$  can be estimated by incorporating the MR data in the analysis of optical images.

## CHAPTER 5: MEASURING VASCULAR PERMEABILITY WITH MRI

### 5.1: Overview

The objective of this chapter is to describe the estimation of vascular kinetic parameters of the macromolecular agent (MA) in a mouse dorsal skin-fold window chamber via DCE-MRI. The MA was labeled with a MR contrast agent (CA) as described in Chapter 2. Similar to chapter 4, the kinetics of the MA in the tissue is approximated by a two compartment model. The two compartment model is described in section 4.2. However, due to the complexities of MRI, additional details must be considered to relate MRI signal to MA concentration. These details are described in section 5.2.

In DCE-MRI, the distribution of the MA is tracked by measuring the relaxation effect of the MA on the MRI signal intensity. The MA alters  $T_1$ ,  $T_2$  and  $T_2^*$  of the tissue. Usually a  $T_1$  weighted sequence is used to measure the extravasation kinetics of the MA in the tissue [1, 2].  $T_2^*$  weighted sequences are more appropriate for perfusion measurements in situations where the MA stays intravascular in the tissue under study [3]. We used a  $T_1$  weighted spin-echo sequence to measure vascular kinetics. The details of this sequence are described in section 5.2. The equations relating MRI signal intensity and MA concentration in a spin-echo sequence for a homogenous media are [4]:

$$S = k\rho \left(1 - e^{-\frac{TR}{T_1}}\right) e^{-\frac{TE}{T_2}}, \quad (5.1)$$

$$\frac{1}{T_1} = \frac{1}{T_{10}} + r_1 C, \quad (5.2)$$

$$\frac{1}{T_2} = \frac{1}{T_{20}} + r_2 C, \quad (5.3)$$

where  $S$  is the signal intensity,  $k$  is a constant that depends on the MRI scanner,  $\rho$  is the water proton density in the tissue,  $TR$  is the repetition time,  $T_1$  and  $T_2$  are the longitudinal and transverse relaxation times of the tissue,  $T_{10}$  and  $T_{20}$  are the native longitudinal and transverse relaxation times of the tissue without the MA,  $r_1$  and  $r_2$  are longitudinal and transverse relaxivities of the MA, and  $C$  is the concentration of the MA in the tissue. For simplicity, we usually assume that  $k=1$ . The inverse of relaxation time is the relaxation rate and is indicated by the letter  $R$ :  $R_j = T_j^{-1}$ ,  $j=1$  or  $2$ . With the right choice of parameters, i.e. by having  $TE \approx 0$ , the  $T_2$  dependence of Eq. 5.1 can be eliminated. In order to determine the MA concentration, signal intensity prior to injection of the MA is compared to the signal intensity after MA injection. In this way, the concentration of the MA can be obtained according to:

$$rC = -\frac{1}{T_{10}} - \frac{1}{TR} \ln \left( 1 - \frac{S}{S_0} \left( 1 - e^{-\frac{TR}{T_{10}}} \right) \right), \quad (5.4)$$

where  $S_0$  is the signal intensity in the absence of MA and  $S$  is the signal intensity after addition of the MA. In order to find relaxivity ( $r$ ) from relaxivity concentration product ( $rC$ ), the relaxation time of the signal in tissue must be obtained as a function of MA concentration. This is possible in a calibration experiment in which the exact concentration of the MA is known. However, a calibration experiment can usually be avoided, since the relaxivity concentration product ( $rC$ ) can replace concentration ( $C$ ) in MA kinetic equations as long as relaxivity is the same in the exchanging tissues.

Two MRI sequences are used; one to track the MA in the tissue and the other to measure the native  $T_1$  ( $T_{10}$ ) of the tissue. The former sequence is called the dynamic sequence in this dissertation and is described in section 5.3. The latter sequence is called the  $T_1$  sequence and is described in section 5.4.

The mechanism of signal change is more complex in MRI than in optics. In MRI, MA in one compartment can enhance or reduce the signal in the other compartment through the processes of water exchange and magnetic coupling. The issue of water exchange between compartments is discussed in section 5.5.

At high concentrations of the MA, it is not possible to ignore the effect of the MA on  $T_2$ , because, in spin-echo imaging, TE cannot be shortened beyond a limit determined by the timing constraints of the sequence. In section 5.6 the  $T_2$  effect on the signal intensity and methods to compensate this effect are analyzed and described.

Similar to optical imaging, a major challenge in MRI for extraction of vascular parameters, is to separate the intravascular and extravascular components of the signal. As mentioned in chapter 4, the mixing of the signal from different compartments is referred to as the partial volume effect. In MRI, due to the more complex concentration-signal relationship, the separation of the two compartments is more involved. The available methodologies to handle the partial volume problem relevant to DCE-MRI analysis are discussed in section 5.7. In addition, a new methodology is introduced that can help in separating vascular and interstitial compartments.

In section 5.8 the possibility of using diffusion weighted MRI (DW-MRI) to separate the intravascular and extravascular signal is explained. Diffusion weighted MRI is a method to estimate the average apparent diffusion of water molecules in different tissues. Diffusion weighted MRI is sensitive to perfusion as well as diffusion, since capillary perfusion is similar to diffusion except at a faster time scale. Therefore, fast diffusion in many tissues corresponds only to the intravascular water molecules.

In section 5.9 the methodologies are summarized that were applied to the MR images to estimate the vascular kinetic parameters and to resolve the partial volume effect.

## 5.2: Tissue Modeling

Similar to chapter 4, for the kinetic behavior of the MA in the tissue, a two compartment model is assumed, in which the MA is in exchange between the extracellular portions of the intravascular (IV) and the extravascular (EV) compartments. The two compartment model was defined in section 4.2. The kinetics of the MA in the two compartment model is described by Eq. 4.3. However, in MRI, the MA also affects the intra-cellular water signal.

As will be discussed in sections 5.5 and 5.6, the MA alters the relaxation time of intra-cellular water through the processes of non-local magnetic susceptibility and water exchange. Therefore, there are really four compartments that affect the signal intensity: intravascular-extracellular (IV) or plasma, intravascular-intracellular (II), extravascular-extracellular (EV) or interstitial, and extravascular-intracellular (EI). The IV and II compartments often appear together in signal-concentration relations. In this case, the summation of these two compartments will be referred to as the vascular compartment and will be indicated with the subscript “v”. Similarly, the combination of the EV and the EI compartments will be referred to as the non-vascular compartment and will be indicated with the subscript “n”.

As explained in section 4.2, the entire interstitial space might not be available to the MA depending on its molecular weight. However, the water in the entire interstitial space is usually available to the MA. Therefore the interstitial space can be divided into two compartments. The first compartment is the space in which the MA can move freely. This compartment affects both the kinetic and signal intensity equations. The second compartment is the space that the MA cannot enter. The second compartment does not affect the MA kinetic equation directly. However, the water protons within the first and second compartment affect the signal intensity equivalently due to the rapid water movement within the interstitial space. To make analysis simpler, we consider the second EV compartment as part of the EI compartment in vascular kinetic parameter estimation.

## 5.3: The Dynamic Sequence

The dynamic sequence is used to estimate the MA distribution in the tissue. The slice thickness for the dynamic sequence used in this work was 5 mm, covering the window chamber thickness. The FOV in the majority of the MRI experiments was set to 2.56 cm x 2.56 cm. The image matrix was set to 128 x 128. Therefore, each pixel corresponded to a 200  $\mu\text{m}$  x 200  $\mu\text{m}$  square area on the window chamber. The repetition time (TR) was usually set to 250 ms; in a few experiments, TR was set to 195 ms. The corresponding frame rates are  $32^{-1} \text{ s}^{-1}$  and  $25^{-1} \text{ s}^{-1}$ , respectively. The TE was set to the minimum possible value, which was either 8.207 ms or 10.474 ms depending on the applied sequence. At each repetition, either 1 or 8 echoes were collected. The reason for multi-echo imaging was to allow compensation of the  $T_2$  effect as will be described in section 5.6. The imaging was carried out over 34 or 42 minutes depending on the experiment. The details of the MRI sequences to image the dynamics of the MA in the tissue are listed below for convenience.

The first sequence generates images from two echoes (RARE factor = 2) and therefore is more dependent on the  $T_2$  of the tissue.

Dynamic Sequence 1) TR = 250 ms, TE = 8.21 ms, imaging matrix = 128x128, number of averages = 2, refocus flip angle = 158.9, RARE Factor = 2, scan time per frame = 32 s. Number of Echoes = 1.

Dynamic Sequence 2) TR = 250 ms (or 195 ms), TE = 10.75 ms, imaging matrix = 128x128, number of averages = 1, refocus flip angle = 180, RARE Factor = 1, scan time per frame = 32 s or 25 s, Number of Echoes = 1 or 8.

The second sequence replaced the first sequence because of its lower dependence on  $T_2$  shortening by MA, and its capability to estimate  $T_2$  at each time point.

## 5.4: The $T_1$ Sequence

In order to measure native  $T_1$  ( $T_{10}$ ), a series of spin-echo images with varying TR was acquired. The  $T_{10}$  was estimated by fitting the signal intensity to the TR values in Eq. 5.1. The fitting algorithm used was Matlab's non-linear least square method. The spatial resolution and FOV were the same as the dynamic sequence. The repetition times varied in different experiments. In earlier experiments, a spin-echo sequence with RARE-factor = 2 was used. The sequence parameters were: TR (ms) = 375, 750, 1500, 3000, 6000, TE = 9.07 ms, N Ave = 1.

In later experiments, a single echo spin-echo sequence was applied. The main reason for using a single echo instead of two echoes was compatibility with the dynamic sequence. The TR times used in later experiments were: TR (ms) = 31.25, 62.5, 125, 250, 500, 1000, 2000, 5000. The number of averages, in most experiments were, respectively: 16, 8, 4, 4, 2, 1, 1, 1. The additional TRs in the later experiments were taken to allow for double exponential fitting of the signal intensity as will be discussed in section 5.7.

## 5.5: Water Exchange

### 5.5.1: Theory

Water exchange refers to the coupling of the relaxation times of adjacent compartments as a result of the water molecules moving through compartments boundaries [5]. MA changes the relaxation time of the water protons in the compartment in which it resides. However, the water molecules can move from one compartment to the other during the relaxation period. In this way, the extent of the relaxation effect of the MA expands from one compartment to the adjacent compartments.

The basic theory of water exchange in MRI was described by McConnell, et al., in 1958 [6]. McConnell modified the Bloch equations to describe the magnetic resonance of a nuclear species that transfers back and forth between two magnetic environments. In water exchange theory, magnetic environments are equivalent to tissue compartments. In 1970 Leigh [7] derived exact

solutions to the modified Bloch equations that McConnell developed. By applying approximations to the solutions obtained by Leigh, McLaughlin, et al. [8] were able to categorize water exchange into different regimes depending on the tissue relaxation times and the rate of exchange. In their work, they divided the water exchange into fast and slow regimes. In later works [9], exchange rates lying between the fast and slow regimes were referred to as intermediate. The exact solutions to the modified Bloch equations are given in Appendix 5.A.1.

The fast, slow or intermediate exchange regimes refer to either longitudinal  $T_1$  or transverse  $T_2$  relaxation times. In the fast exchange regime, the water exchange is fast enough that the two compartments relax with the same time constant. In this regime, the MA in either compartment affects the relaxation time of water protons in both compartments equally. In the slow exchange regime, the time constant of one compartment may be affected by the other compartment, but the two compartments relax with different resolvable time constants. Fast and slow exchange regimes are defined mathematically in the following [5, 8]:

Defining the terms:

$\tau_A, \tau_B$ : Mean residence time of water protons in compartments A and B.

$T_j$ : Either the longitudinal ( $j=1$ ) or transverse ( $j=2$ ) relaxation time of the exchanging compartments.

$T_{jA}$  and  $T_{jB}$ : Refer to either the longitudinal or transverse relaxation times in compartments A and B in the absence of water exchange.

$$\frac{1}{\tau} = \frac{1}{\tau_A} + \frac{1}{\tau_B}, \quad \Delta\left(\frac{1}{T_j}\right) = \left| \frac{1}{T_{jA}} - \frac{1}{T_{jB}} \right|,$$

$f_A = \frac{V_A}{V_A+V_B}$ ,  $f_B = \frac{V_B}{V_A+V_B}$ ,  $V_A, V_B$ : volume of A and B compartments and  $f_A$  and  $f_B$  are the volume fractions of the two compartments.

Fast exchange:

$$\frac{1}{\tau} \gg \Delta\left(\frac{1}{T_j}\right); \quad (5.5)$$

$$\frac{1}{T_j} = \frac{f_A}{T_{jA}} + \frac{f_B}{T_{jB}}; \quad (5.6)$$

Slow exchange:

$$\frac{1}{\tau} \ll \Delta\left(\frac{1}{T_j}\right); \quad (5.7)$$

$$\frac{1}{T_j} = \begin{cases} \frac{1}{T_{jA}} + \frac{1}{\tau_a} \\ \frac{1}{T_{jB}} + \frac{1}{\tau_b} \end{cases}; \quad (5.8)$$

In the above equations, it is assumed that the water protons in the two exchanging compartments have the same resonance frequency. If there are only two compartments which are in exchange, then the ratio of mean residence times of water molecules in the two compartments is equal to the ratio of their volumes:

$$\frac{\tau_A}{\tau_B} = \frac{V_A}{V_B} \quad (5.9)$$

In most tissue, proton density is approximately proportional to the volume. Therefore:

$$f_A = \frac{\rho_A}{\rho_A + \rho_B}, \quad (5.10)$$

$$f_B = \frac{\rho_B}{\rho_A + \rho_B}, \quad (5.11)$$

$$\frac{\tau_A}{\tau_B} = \frac{\rho_A}{\rho_B}. \quad (5.12)$$

### 5.5.2: Adjacent Water Exchange Compartments

Water exchange couples the intra-cellular and extra-cellular sub-compartments in both vascular and non-vascular compartments (i.e. the IV and II compartments and the EV and EI compartments). It also couples the IV and EV compartments. The exchange situation can be summarized via the diagram below, where arrows indicate exchange:

Water exchange: II ↔ IV ↔ EV ↔ EI

MA exchange: IV ↔ EV

The reported values of  $\tau$  ( $= \frac{1}{\tau_A} + \frac{1}{\tau_B}$ ) for water exchange between II & IV, IV & EV and EV & EI in mouse striated muscle tissue are 10 ms, 40-100 ms and 150-1000 ms respectively [5, 10]. These values correspond to the exchange rates of  $100 \text{ s}^{-1}$ ,  $10\text{-}50 \text{ s}^{-1}$  and  $1\text{-}7 \text{ s}^{-1}$ .

The exchange between compartments couple to one another. Since the IV and the EV are in exchange with two other compartments, their relaxation times should ideally be determined by considering the exchange with all interchanging compartments simultaneously. For example, the EV and IV compartments might be in fast exchange regime in the absence of the EI compartment. But in the presence of the EI compartment, the actual exchange regime between the EV and IV compartment might be intermediate or slow.

### 5.5.3: Transverse Relaxation

The transverse relaxation effect of a MA extends beyond the boundaries of the compartments by water exchange as well as by creating magnetic field inhomogeneity across the compartmental boundaries. The latter effect will be discussed in section 5.6. Generally, due to the faster transverse relaxation process, water exchange is slower relative to transverse relaxation rates in comparison to longitudinal relaxation rates. Since the experiments performed in this work are DCE-MRI with minimum TE value, transverse relaxation affects the signal intensity only when  $T_2$  is very short. Here we argue that only the transverse relaxation effect of water exchange between the IV and II compartments affects the signal intensity significantly.

The effect of transverse relaxation coupling on signal intensity in a compartment, according to Eq. 5.1, is a factor equal to  $\exp(-/+TE*\Delta R_2)$ , where  $\Delta R_2 = \Delta(T_2^{-1})$  is the transverse relaxation rate change caused by water exchange. Water exchange effect on relaxation rates are caused by water protons in one compartment being replaced by water protons in the neighboring compartments. The maximum effect of water exchange on relaxation times in a compartment happens in the situation where the replaced water protons have the most different relaxation status compared to the ones existing in the compartment. Considering this extreme case, it can be concluded that the change in relaxation rate, as a result of water exchange, can never be greater than the exchange rate, i.e.  $\Delta R_2 < \Delta(\tau_c^{-1})$  where  $\tau_c$  is the mean residence time of the water proton in a compartment. For two compartments, this maximum change in relaxation rate happens when the relaxation rates of the two exchanging compartments are sufficiently different, i.e. the slow exchange regime. Considering slow exchange, the maximum transverse relaxation effect on the signal intensity caused by water exchange, between each pair of exchanging compartments, is summarized in table 5.1. To simplify the estimations, the reciprocal summation of the mean residence times of water protons in the two compartments is used instead of the mean residence time in each compartment. Therefore, the maximum effect of water exchange is exaggerated in table 5.1.

**Table 5.1.** Upper limit for the transverse relaxation effect on signal intensity as a result of water exchange.

Exchanging Compartment	IV-EV	EV-EI	IV-II
$\exp(TE/\tau)^*$	1.25	1.07	2.7

\*  $\tau$  is the reciprocal summation of mean residence times of water protons in the exchanging compartments as defined in section 5.5.1.

The data in table 5.1 indicates that water exchange between the IV and II compartments might affect signal intensity significantly. The effect of transverse relaxation on signal intensity will be discussed in section 5.6.

### 5.5.4: Water Exchange Status Prior to MA Injection

Prior to MA injection, the difference between the  $T_1$  values of adjacent compartments is small. Therefore, the water exchange is usually in the fast exchange regime. For example, the  $T_1$  of muscle and blood at 7T are about 1.73 s and 1.9 s, respectively [11, 12]. In this case:

$$\Delta\left(\frac{1}{T_1}\right) = \frac{1}{1.73} - \frac{1}{1.9} = 0.052 \text{ s}^{-1} \ll \frac{1}{\tau_{\text{II-IV}}}, \frac{1}{\tau_{\text{IV-EV}}}, \frac{1}{\tau_{\text{EV-EI}}}.$$

Therefore, in regions that include only extra-vascular tissue and capillaries, the longitudinal relaxation rate of the II, IV, EV and EI compartments will be averaged according to Eq. 5.6. Only on larger vessels, where the mean residence time of water protons in the vessel is much longer, double exponential behavior of signal intensity as a function of TR might exist.

Before the injection of the MA, the water exchange does not change the total signal intensity as long as  $\text{TR}/T_{1v}$  and  $\text{TR}/T_{1n} \ll 1$ , where  $T_{1v}$  and  $T_{1n}$  are the longitudinal relaxation time of vascular and non-vascular compartments respectively. In order to illustrate this, we consider the signal intensity from a region of tissue. In one case, we assume fast water exchange between the compartments and in the other case, we assume no exchange. In the no exchange situation, using the first term in a Taylor series expansion of the exponential terms, the signal intensity is:

$$S = \rho_v \left(1 - e^{-\frac{\text{TR}}{T_{1v}}}\right) + \rho_n \left(1 - e^{-\frac{\text{TR}}{T_{1n}}}\right) \approx \rho_v \frac{\text{TR}}{T_{1v}} + \rho_n \frac{\text{TR}}{T_{1n}}$$

In the fast exchange situation (Eq. 5.6) the signal intensity is:

$$S = (\rho_v + \rho_n) \left(1 - e^{-\frac{\text{TR}}{\rho_v + \rho_n} \left(\frac{\rho_v}{T_{1v}} + \frac{\rho_n}{T_{1n}}\right)}\right) = \text{TR} \left(\frac{\rho_v}{T_{1v}} + \frac{\rho_n}{T_{1n}}\right)$$

Therefore, the signal intensity is the same with and without water exchange between the compartments.

### 5.5.5: Water Exchange Status after MA Injection

Injection of MA induces a significant relaxation rate difference between the compartments. Due to the very fast rate of water exchange between the IV and II compartments, the IV-II exchange is usually in the fast exchange regime after MA injection despite the large  $T_1$  difference between the two compartments [5, 10]. The water exchange rate between the EV and EI compartments can be fast, slow or intermediate depending on the concentration of the MA in the EV compartment and the type of the tissue [13-14]. The IV-EV exchange is usually in the slow exchange regime in the presence of a significant MA concentration gradient.

### 5.5.6: Water Exchange Status in Our Experiments

The exchange regime between the four compartments of the tissue is estimated at four doses of MA and at two points of time. One time point is immediately after distribution of the MA in the vasculature. Similar to chapter 4, this point of time is defined as the origin of time,  $t=0$ . The other point of time is at  $t=30$  min. Three of the MA doses that are listed correspond to the doses that were applied in most experiments. The fourth dose of the MA is a lower dose that is suggested for consideration in future experiments. The assumed values for physiological and MR parameters are

summarized here. The details of the calculations are included in appendix 5.A.2. The water exchange regime estimations are summarized in Table 5.2.

In order to determine the exchange regimes, the concentrations of the MA in each compartment and its relaxivity must be known. The relaxivity of the MA in saline was measured in chapter 2. It is expected that the longitudinal relaxivity of the MA is slightly higher in the blood than saline due to the higher macromolecular content in the blood [15]. However, for simplicity, the same longitudinal relaxivity, as measured in saline, will be assumed in the blood.

The concentration of the MA in the IV compartment is determined by the injection dose, the estimated blood volume of the mouse, and the clearance rate of the MA from the blood. The concentration of the MA in the EV compartment is estimated using literature values for the vascular kinetic parameters. Based on the estimated concentrations, the relaxivity of the MA, and the water proton exchange rate between compartments, the exchange regime between each pair of compartments is estimated. As mentioned in section 5.5.2, water exchange between multiple different compartments can affect one another. Since water exchange between the IV and EV compartments is much slower than the other two exchanges, the IV-EV water exchange is considered after considering the IV-II and EV-EI water exchange effects on relaxation rates.

The volume of blood in milliliters is approximately 6-8% of the mouse weight in grams [16, 17]. About 60% of the blood volume is plasma [18]. An estimated mouse weight of 27 mg is considered based on measurements and literature values [18]. The injection doses that are evaluated are 5, 15, 30 and 45 mg. The molar mass of MA (biotinilated BSA-(Gd-DTPA)<sub>23</sub>-(Alexa Fluor 647)) was measured at about 86 kDa. The plasma clearance time ( $\tau_{cl}$ ) of MA is assumed to be  $8 \times 10^3$  s, as estimated by Yuan et al. [19, 20]. The concentration in the EV compartment is estimated assuming a two compartment model (section 4.2) and solving the following equation:

$$v_e C_e(t) = K_{trans} e^{-k_{ep}t} \int_0^t C_i(0) e^{-\tau/\tau_{cl}} e^{k_{ep}\tau} d\tau = \frac{k_{ep} C_i(0) (e^{-t/\tau_{cl}} - e^{-k_{ep}t})}{k_{ep} - 1/\tau_{cl}} \quad (5.13)$$

Vascular kinetics of labeled BSA has been estimated by various groups [19-34]. Wu et al. estimated  $K_{trans}$  of BSA in PC-3 human prostate tumor xenografts implanted in nude mice at  $8 \times 10^{-5} \text{ s}^{-1}$  [33]. Their result is comparable to the value of  $K_{trans}$  obtained by Gossman, et al. for the R3327 rat prostate cancer line [34]. The available volume fraction in the extravascular space for 70 kDa Dextran in rat fibrosarcoma was estimated at 0.1 [35]. Therefore, the value of  $k_{ep}$  is estimated at  $8 \times 10^{-4} \text{ s}^{-1}$  in tumor. Wu, et al. estimated that the vascular permeability in healthy tissue for BSA is about one third of R3230Ac mammary adenocarcinoma [22]. Here we assume that the  $k_{ep}$  and  $K_{trans}$  of the healthy tissue are also one third that of the tumor.

**Table 5.2.** Typical values of the exchange rates relative to longitudinal relaxation rates in five water exchange components in the tissue. The exchange rate at t=0 and t=30 min are estimated based on MA injections of 5, 15, 30, 50 mg corresponding to 0.05, 0.16, 0.32 and 0.53 mmol Gd-DTPA/Kg. The details of the calculations are included in Appendix 5.A.2.

Exchanging Compartments	Typical water exchange rate (1/τ) s <sup>-1</sup>	$\Delta(1/T_1)$ estimate (s <sup>-1</sup> ) at t=0	Exchange Regime	$\Delta(1/T_1)$ estimate (s <sup>-1</sup> ) at t=30 min	Exchange Regime
IV-II	100	11, 34, 68, 113	Fast-interm	9.1, 18, 55, 91	Fast-interm
EV-EI H*	20-50	0	Fast	3.8, 12, 23, 38	Fast-Interm
IV-EV H	1-7	9.1, 27, 55, 91	Slow	6.8, 21, 41, 68	Slow
EV-EI T*	20-50	0	Fast	7.6, 23, 45, 76	Fast-Interm
IV-EV T	1-7	6.8, 20, 41, 68	Interm-Slow	4.6, 14, 28, 46	Interm-Slow

\* The letter “H” indicates healthy tissue and the letter “T” indicates tumor.

**Table 5.3.** Typical values of the exchange rates relative to transverse relaxation rate. As mentioned in section 5.5.3, only the effect of IV-II water exchange component on transverse relaxation might affect signal intensity significantly. The exchange rate at t=0 and t=30 min are estimated based on MA injection concentration of 5, 15, 30, 50 mg. The details of the calculations are included in Appendix 5.A.2.

Exchanging Compartments	Typical water exchange rate (1/τ) s <sup>-1</sup>	$\Delta(1/T_2)$ estimate (s <sup>-1</sup> ) at t=0	Exchange Regime	$\Delta(1/T_2)$ estimate (s <sup>-1</sup> ) at t=30 min	Exchange Regime
IV-II	100	5.1, 14, 27, 43	Fast	4.3, 11, 21, 35	Fast

## 5.6: T<sub>2</sub> Effect on the Signal

According to Eq. 5.1-5.3, the MA affects the signal intensity by increasing both longitudinal and transverse relaxation rates. The longitudinal and transverse effects of the MA act in opposite directions on the signal intensity. In DCE-MRI, in order to reduce the effect of the MA on transverse relaxation, the value of TE is minimized. However, a minimum value of TE is set by the MRI scanner and the applied sequence. At high concentrations of MA, the transverse relaxation effect of the MA can be significant even at the minimum TE value [36, 37]. In such cases, it is possible to measure MA concentration by including both longitudinal and transverse relaxation in the signal equation [38]. However, this requires knowledge of both longitudinal and transverse relaxivities of the MA in the tissues under study. In addition, it complicates the equations and possibly increases the error in estimating the concentrations. A simple approach to the problem of T<sub>2</sub> effect on signal intensity is to measure T<sub>2</sub> at each time point and eliminate its effect on signal intensity. This was done in our study by using a multi-echo pulse sequence.

The MA affects the transverse relaxivity of tissue through three processes [39]: 1- Perturbing magnetic field homogeneity locally around the MA molecule. 2- Creating bulk susceptibility gradients across adjacent compartments caused by MA paramagnetic properties and concentration gradients. 3- Water exchange, discussed in section 5.5.3. The first process is a true T<sub>2</sub> relaxation process, is very fast, and is not reversible by spin-echo refocusing pulse. The second process

couples the adjacent compartments. The characteristic time for this process is on the order of tens of milliseconds and is therefore, only partially compensated by spin-echo refocusing pulse [39].

The  $T_2$  effect of the MA on the signal intensity can be determined using the transverse relaxivity of the MA estimated in section 2.2.3. In chapter 2, we measured  $T_2$  at several concentrations of BSA-(Gd-DTPA)<sub>23</sub> in saline. The transverse relaxation dependence on MA concentration was not linear at high concentrations of the MA. It has been shown that in blood, the transverse relaxation rate dependence on Gd-DTPA concentration is not linear even at low concentrations as well and reaches a local minimum at a certain concentration of Gd-DTPA [11]. This is because of the susceptibility mismatch between plasma and red blood cells, which shortens the native  $T_2$  of the blood. At the concentration of Gd-DTPA corresponding to the local minimum of  $T_2$ , the susceptibility of plasma and red blood cells matches each other. Therefore, the transverse relaxation effect of Gd-DTPA is lower in the blood than saline. The MRI signal attenuations in saline due to transverse relaxation change at 6.85 mM, 4.11 mM, 2 mM and 0.67 mM of Gd-DTPA and 10 ms echo time are summarized in table 5.3. These concentrations correspond to the estimated concentrations in the vessel immediately after injection of 0.05, 0.16, 0.32 and 0.53 mmol Gd-DTPA/Kg i.e. the same concentrations that were investigated in section 5.5.6. These values can serve as an upper limit of signal attenuation as a result of  $T_2$  effect of MA assuming the relaxivity of the MA affects the blood plasma and hematocrit uniformly.

**Table 5.4.** Upper limit estimates of  $T_2$  effect on signal intensity at different concentrations of the MA in the blood and TE=10 ms. The concentrations represent the concentration of the MA inside the vessel immediately after injection of 0.05, 0.16, 0.32 and 0.53 mmol Gd-DTPA/Kg.

Concentration (mM)	6.8	4.1	2	0.67
$\frac{e^{-\frac{TE}{T_2}}}{e^{-\frac{TE}{T_{20}}}}$ @TE =10 ms	0.14	0.21	0.48	0.78

According to the concentration of the MA in the EV compartment estimated in section 5.5.6 and the transverse relaxation effect of MA on signal intensity estimated in table 5.3, MA affects the signal intensity significantly through modifying the transverse relaxation in the EV compartment. However, the total effect on signal intensity outside larger vessels in normal tissue is not significant; as indicated by our experiments. This is due to the much smaller volume of the EV compartment relative to the EI compartment. In tumor regions where vessel density is high,  $T_2$  effect can reduce the total tissue signal intensity even outside large vessels. Compensation of transverse relaxation effect is complicated by the partial volume effect as will be discussed in section 5.7.

## 5.7: Partial Volume Effect

### 5.7.1: Introduction

In MRI of mouse dorsal skin-fold window chamber, it is usually not possible to have an entire voxel either inside or outside of a vessel. The mixing of extravascular and intravascular regions is

a major obstacle in measuring the concentration of the MA in either compartment. In MRI literature, the intravascular MA concentration is referred to as the arterial input function (AIF). Arterial and venous concentrations of MA can be significantly different if the MA extravasation in the tissue is fast. In slow extravasation, the difference between the arterial and venous concentrations is mostly in the initial time after injection. Partial volume effect also distorts relaxation measurements prior to the injection of the MA, if adjacent compartments have different relaxation times.

Partial volume effect is more complicated in 2-D MRI than 2-D optical microscopy. One reason is the lower resolution of MRI. Another reason is the non-linear signal-concentration relationship in MRI. The non-linear relationship causes the estimated concentration to be less than the average concentration across the tissue volume. The deviation from linearity increases as concentration increases.

### **5.7.2: Measuring AIF**

The approaches taken to determine the AIF can be categorized into three groups [1]: 1- Invasively sample the blood either from the same mouse or a cohort of representative mice. 2- Measure signal in a vessel that is larger than the voxel size. 3- Measure concentration in a tissue with known vascular kinetic parameters and estimate the AIF by solving the vascular kinetic equations.

The first approach, in addition to being invasive, has low time resolution if the blood is taken from the mouse under experiment; this is due to the very low blood volume in mice (1.2-2 ml) [40]. If the concentration is measured in other mice, the physiological and biological variability of the mouse and the tumor is ignored. Measuring signal in a voxel in an artery is a good candidate as long as there is a large enough vessel in the imaging field of view. Blood flow is a potential problem in measuring concentration in a large vessel. However, there are algorithms that can compensate for the in-flow effects [41]. The third approach to measure AIF is called the reference region model (RRM) [42]. The RRM is an inverse approach. The accuracy of this method depends on the accuracy of the assumed values of vascular kinetic parameters in the reference region. The RRM can be used to estimate the AIF from the MA concentration in the tumor or healthy tissue by using the kinetic parameters obtained from the literature. However, since our goal is to validate the measurements of vascular kinetic parameters in the healthy and tumor tissue within the window chamber, this method is not applicable. In addition, the measurement of the concentration in the extravascular tissue is also subject to partial volume effect as will be discussed in section 5.7.3.

We applied the second approach to determine the AIF. The problem in our setup is that the volume coil is removed to create space for the optical imaging system and there is no large vessel in the field of view of the surface coil. Therefore, while we measured AIF in the largest vessel in the window chamber, the partial volume effect was still significant.

### 5.7.3: Measuring Extravascular Concentration

To estimate extravascular concentration, an ROI on the tissue of interest is selected. This ROI will be called T\_ROI (T for tissue). Usually, the microvascular content of T\_ROI is either ignored or considered later in the kinetic parameter estimation process.  $C_T$  is defined as the average concentration of the MA in T\_ROI assuming that MA is distributed in the entire tissue within T\_ROI. If the microvascular content of MA in the T\_ROI is ignored, then  $C_T$  is:

$$C_T = v_e C_e, \quad (5.14)$$

where  $v_e$  is the fractional volume of the EV compartment within T\_ROI and  $C_e$  is the concentration of the MA in the EV compartment. As discussed previously, the MA affects the signal intensity in the EV and the EI compartments. Therefore, in the absence of microvasculature, the measured concentration in the extravascular space is equal to  $C_T$ , i.e. the volume average of the concentration in the EV and the EI compartments. By replacing  $C_e$  in the two compartment model kinetic equation (Eq. 4.3), by its value in Eq. 5.14, the vascular kinetic equation becomes:

$$\frac{dC_T}{dt} = K_{\text{trans}} \left( C_i - \frac{C_T}{v_e} \right). \quad (5.15)$$

If the microvasculature content is not ignored,  $C_T$  is equal to:

$$C_T = v_e C_e + v_i C_i, \quad (5.16)$$

where  $v_i$  is the fractional volume of the IV compartment within T\_ROI. By replacing  $C_e$  in Eq. 4.3 by its value in Eq. 5.16, the following kinetic equation is obtained:

$$\frac{dC_T}{dt} = K_{\text{trans}} \left( C_i - \frac{C_T}{v_e} + \frac{v_i C_i}{v_e} \right) + v_i \frac{dC_i}{dt}. \quad (5.17)$$

Although Eq. 5.17 accurately describes the relationship between  $C_T$ ,  $C_i$ , and vascular kinetic parameters, the process of obtaining  $C_T$  is not straightforward.  $C_T$  can be obtained from the signal intensity in T\_ROI by applying Eq. 5.4 assuming that the tissue consists of one compartment. The relationship between the MA concentration and the signal intensity can be summarized as:

$$C = f(S/\rho) \quad (5.18)$$

where  $\rho = \frac{S_0}{\left(1 - e^{-\frac{TR}{T_{10}}}\right)}$ , is the proton density, and  $f$  is the functional relation between  $C$  and  $S/\rho$

defined in Eq. 5.4. The function  $f$  depends on the native relaxation times of the tissue. If all the water compartments within T\_ROI, i.e. IV, II, EV and IE, are in fast exchange, then the assumption of one compartment in obtaining  $C_T$  is correct. However, usually the IV-EV water exchange is slow. If the IV-EV water exchange is ignored (equivalent to zero) and the IV-II and the EV-EI water exchanges are fast, the estimated  $C_T$  ( $\hat{C}_T$ ) would equal to:

$$\hat{C}_T = f\left(\frac{S_T}{\rho_T}\right) = f\left(\frac{S_v + S_n}{\rho_T}\right) = f\left(\frac{\rho_v f^{-1}(C_v) + \rho_n f^{-1}(C_n)}{\rho_T}\right), \quad (5.19)$$

where  $S_v$  and  $S_n$  are the signal intensities originating from vessel and non-vessel compartments within  $T\_ROI$ , respectively.  $C_v$  and  $C_n$  are, respectively, equal to  $C_i$  and  $C_e$  multiplied by the fractional volume of the extracellular subcompartments, within intravascular and extravascular spaces. Mathematically:

$$C_v = C_i(1 - H_T) \quad (5.20)$$

and

$$C_n = \frac{V_E}{V_N} C_e = \frac{V_E/V_E}{V_N/V_T} C_e = \frac{v_e}{\left(1 - \frac{v_i}{(1-H_T)}\right)} C_e, \quad (5.21)$$

where  $V_N$  and  $V_T$  are the non-vascular and total tissue volume. Assuming uniform tissue density,  $\rho_v = \frac{\rho_i}{1-H_T}$  and  $\rho_n = \rho_T \left(1 - \frac{v_i}{(1-H_T)}\right)$  where  $\rho_i$  and  $\rho_T$  are the IV compartment and total tissue proton density in  $T\_ROI$ . By replacing  $C_e$  and  $C_n$  from Eq. 5.20 and 5.21 in Eq. 5.19.

$$\hat{C}_T = f\left(\frac{\left(\frac{\rho_i}{1-H_T} f^{-1}(C_i(1-H_T)) + \rho_T \left(1 - \frac{v_i}{(1-H_T)}\right) f^{-1}\left(C_e \frac{v_e}{\left(1 - \frac{v_i}{(1-H_T)}\right)}\right)\right)}{\rho_T}\right). \quad (5.22)$$

If  $f$  is linear (as it is at low concentrations,) Eq. 5.22 can be simplified to:

$$\hat{C}_T = \frac{\rho_i f^{-1}(C_i) + \rho_e f^{-1}(C_e)}{\rho_T} = v_i C_i + v_e C_e. \quad (5.23)$$

At high concentrations, the linearity assumption can lead to significant error. According to the relaxivity values of BSA-(Gd-DTPA)<sub>23</sub> in PBS obtained in section 2.2.3, assuming  $TR=250$  ms and  $T_1=1.6$  s, the signal intensity deviates from its linear estimation by 30% at Gd-DTPA concentration of 0.3 mM (corresponding to 0.015 mmol Gd-DTPA/Kg). At this concentration, the signal intensity in the vessel is about 4 times higher than the signal before the injection of the MA and 60% of the saturated signal intensity that occurs at very high concentration of the MA. The problem is that at this concentration in the vessel, the concentration in the extravascular tissue would be very low due to the slow extravasation rate of the MA from the vasculature. The intravascular and extravascular signals are mixed in  $T\_ROI$ . If the extravascular signal is significantly lower than the intravascular signal, measuring the concentration in the extravascular tissue becomes difficult due to the low signal to noise ratio.

### 5.7.4: Partial Volume Effect and Water Exchange

At low concentrations, if the relaxivities of the MA as well as the native relaxation rates are the same in the adjacent compartments, water exchange does not affect the total signal from the two compartments. The reason is that at low concentrations, the signal-concentration relationship is approximately linear. In order to illustrate this, we assume two adjacent compartments A and B. If MA is entirely in compartment A, at low concentration, in the absence of water exchange, the signal intensity from compartment A ( $S_A$ ) and the total signal intensity ( $S_{AB}$ ) are:

$$S_{A,ne} = \rho_A \left( 1 - e^{\frac{-TR}{T_{1A}}} e^{-TRrC_A} \right) \approx \rho_A \left( 1 - e^{\frac{-TR}{T_{1A}}} (1 - TRrC_A) \right) = S_{A0} + \rho_A e^{\frac{-TR}{T_{1A}}} TRrC_A, \quad (5.24)$$

$$S_{AB,ne} = S_{A,ne} + S_{B0}, \quad (5.25)$$

where  $S_{A0} = \rho_A \left( 1 - e^{\frac{-TR}{T_{1A}}} \right)$ ,  $S_{B0} = \rho_B \left( 1 - e^{\frac{-TR}{T_{1B}}} \right)$ , the subscript “ne” stands for no-exchange, and  $T_{1A}$  and  $T_{1B}$  are the native  $T_1$  of the A and B compartments, respectively. The transverse relaxation effect is ignored due to the low MA concentration and short TE in DCE-MRI. Water exchange between two compartments, has the highest possible effect on the signal intensity in the fast exchange regime. In the fast exchange regime:

$$S_{AB,fe} \approx \rho_A \left( 1 - e^{\frac{-TR}{T_{1A}}} (1 - TRrC_{AB}) \right) + \rho_B \left( 1 - e^{\frac{-TR}{T_{1B}}} (1 - TRrC_{AB}) \right) = S_{A0} + S_{B0} + TRrC_{AB} \left( \rho_A e^{\frac{-TR}{T_{1A}}} + \rho_B e^{\frac{-TR}{T_{1B}}} \right), \quad (5.26)$$

where  $C_{AB} = C_A \frac{\rho_A}{\rho_A + \rho_B}$  and the “fe” subscript stands for the fast exchange situation. If  $T_{1A} \approx T_{1B}$ :

$$S_{AB,fe} = S_{A0} + S_{B0} + TRr e^{\frac{-TR}{T_{1A}}} C_{AB} (\rho_A + \rho_B) = S_{A0} + S_{B0} + \rho_A TRr e^{\frac{-TR}{T_{1A}}} C_A = S_{AB,ne}. \quad (5.27)$$

### 5.7.5: A Suggested Approach

#### 5.7.5.1: Summary

In order to separate the intravascular and extravascular signals, a new methodology is introduced. As will be discussed in chapter 6, our data were not of sufficient quality to test this methodology. Nevertheless, we introduce this methodology to be applied in the future if the problem of signal fluctuation is resolved. In this methodology, it is assumed that the IV-II and the EV-EI compartments are in fast water exchange and the EV-IV water exchange is neglected. The  $T_2$  effect of the MA on the signal intensity is also ignored. Therefore, this methodology works properly at low concentrations, when water exchange between the IV and the EV compartments does not affect the total signal intensity as described in section 5.7.4.

In this new methodology, the spatial distribution of the intravascular component of the signal, multiplied by an unknown scale factor, is obtained by comparing the signal intensity shortly after injection of the MA to the signal intensity prior to the injection of the MA. Similar to chapter 4, the earliest time that the MA is distributed more or less uniformly in the vasculature, is assigned as the origin of time, i.e.  $t=0$ .

Using the obtained relative spatial distribution of the intravascular signal and the  $T_1$  sequence, a map of the extravascular tissue  $T_1$  ( $T_{1n}$ ) is found. Finally by fitting the data to a bi-exponential curve, vascular compartment  $T_1$  ( $T_{1v}$ ) and non-vascular compartment proton density are found.

### 5.7.5.2: Finding Relative Intravascular Distribution Map

Assuming  $TE \ll T_{2i}$  and  $T_{2v}$ , the signal intensity in a voxel prior to injection of the MA is:

$$S_0 = \rho_v \left(1 - e^{-\frac{TR}{T_{1v}}}\right) + \rho_n \left(1 - e^{-\frac{TR}{T_{1n}}}\right). \quad (5.28)$$

Ignoring water exchange, or assuming that water exchange does not affect the total signal intensity, after injection of the MA at  $t=0$ , signal intensity is:

$$S^{t=0} = \rho_v \left(1 - e^{-\frac{TR}{T_{1v}}} e^{-TR R_1 C_v}\right) + \rho_n \left(1 - e^{-\frac{TR}{T_{1n}}}\right). \quad (5.29)$$

By subtracting  $S_0$  from  $S^{t=0}$ :

$$S^{t=0} - S_0 = \rho_v e^{-\frac{TR}{T_{1v}}} (1 - e^{-TR R_1 C_v}) = K \rho_v. \quad (5.30)$$

where  $K$  is a constant that does not depend on the pixel location. Therefore, a relative spatial distribution of the intravascular signal is obtained.

### 5.7.5.3: Finding $T_{1n}$

Two ROIs are selected: one on a vessel and the other on the tissue under study. The signal intensities in these two regions, prior to MA injection, ignoring water exchange between the EV and IV compartments, are:

$$S_1 = \rho_{v1} \left(1 - e^{-\frac{TR}{T_{1v}}}\right) + \rho_{n1} \left(1 - e^{-\frac{TR}{T_{1n}}}\right), \quad (5.31)$$

$$S_2 = \rho_{v2} \left(1 - e^{-\frac{TR}{T_{1v}}}\right) + \rho_{n2} \left(1 - e^{-\frac{TR}{T_{1n}}}\right). \quad (5.32)$$

Using the relative intravascular signal map obtained (Eq. 5.31), the ratio of  $\rho_{v2}$  to  $\rho_{v1}$  can be obtained. Assuming that the two ROIs have the same values of  $T_{1n}$  and  $T_{1v}$ :

$$S_2 - S_1 \frac{\rho_{v2}}{\rho_{v1}} = f\left(\frac{\rho_{v2}}{\rho_{v1}} \rho_{n1}, \rho_{n2}\right) \left(1 - e^{-\frac{TR}{T_{1n}}}\right), \quad (5.33)$$

where  $f$  is a function that does not depend on TR and  $T_{1n}$ . By fitting the values obtained by Eq. 5.33 at different TRs to a single exponential curve,  $T_{1n}$  can be obtained. This process can be used to find  $T_{1n}$  in any region in the tissue as long as there is a region with different vascular content and the same intravascular and extravascular longitudinal relaxations. If one ROI is on a tumor region, the other should be on the tumor as well so as to keep the relaxation times the same.

#### 5.7.5.4: Finding other Parameters by Bi-exponential Fitting

A straightforward way to find the other parameters, i.e.  $T_{1v}$ ,  $\rho_n$  and  $\rho_v$ , is to fit a bi-exponential curve to the  $T_1$  sequence on a large vessel. Bi-exponential fitting is generally prone to error; however, since  $T_{1n}$  is determined and approximate ranges of  $T_{1v}$ ,  $\rho_v$  and  $\rho_n$  are known, double exponential fitting may be possible. An initial estimate for  $T_{1v}$  can be obtained from the literature or by fitting a single exponential curve to the  $T_1$  sequence on a large vessel within the window chamber. The  $T_1$  sequence image with the highest TR, is approximately proportional to  $\rho_v + \rho_n$ . The ratio of  $\rho_v$  to  $\rho_n$  in the tissue is also approximately known. This prior knowledge can be incorporated into the fitting routine to reject non-realistic results.

We applied this method to measure  $T_1$ . The double exponential fitting was done both on a large vessel and also on a larger ROI that included the vessel and the surrounding tissue. Unfortunately, the fitting was unsuccessful. One of the estimated  $T_1$  values was always unrealistically low. In appendix 5.A.3, an estimation approach is suggested to overcome this problem.

## 5.8: Application of Diffusion MRI in DCE-MRI

### 5.8.1: Introduction

Diffusion weighted imaging (DWI) is an MRI technique that creates contrast based on the rate of the incoherent motion of water protons within a voxel [43]. The incoherent motion of water protons is caused by diffusion as well as intravoxel non-directional perfusion of blood or other fluids. Our goal is to use DWI to find the distribution of the vascular and non-vascular proton density components ( $\rho_v$  and  $\rho_n$ ) within the window chamber.

In DWI, the signal intensity from a homogenous tissue is obtained from the following relation:

$$S = S_0 \exp(-bD), \quad (5.34)$$

where  $b$  is an imaging parameter, that depends on the strength and timing of diffusion weighting gradient,  $D$  is the apparent diffusion coefficient (ADC) of water protons in the tissue and  $S_0$  is the signal intensity at  $b=0$ , i.e. when no diffusion gradients are applied. ADC is a term that represents both restricted diffusion and perfusion acting like diffusion on a larger scale [44]. The free diffusion of water in tissue is blocked by cell membranes and endothelial barriers [45]. Perfusion in general results in a greater motion than diffusion. However, there can be directionality to perfusion. The perfusion of water in capillaries is generally multidirectional in an MRI voxel and therefore appears similar to diffusion but with a higher diffusion coefficient. The perfusion of

water in larger vessels has directionality to it. Directional flow results in an overall phase shift rather than a reduction in signal amplitude. However, voxels on larger vessels usually have a high ADC value because the motion of the flowing blood is not uniform across the vessel.

Due to the presence of diffusion and perfusion in a voxel, signal intensity in real tissue consists of more than one ADC value [46, 47]. ADC caused by perfusion is about an order of magnitude higher than that of water diffusion in tissue [44, 46]. The molecular diffusion of water in tissue is about  $10^{-3}$  mm<sup>2</sup>/s. The ADC caused by perfusion is usually higher than  $10^{-2}$  mm<sup>2</sup>/s. In very slow perfusion in capillaries, ADC of tissue can be lower than  $10^{-2}$  mm<sup>2</sup>/s but still higher than the ADC of pure water diffusion in tissue [46]. Generally, b values less than 300 s/mm<sup>2</sup> are appropriate to measure the ADC caused by perfusion and b values higher than 300 s/mm<sup>2</sup> are needed to accurately measure the diffusion coefficient of water molecules in tissue [46, 47].

The difference between the ADC caused by perfusion and diffusion creates the possibility of separating diffusion and tissue perfusion in small vessels and capillaries [44]. There is controversy as to the accuracy of measuring intravascular perfusion parameters with DWI [47]. Generally it is not possible to measure perfusion when there is any other form of fluid flow in tissue such as in lymphatic channels [47]. In order to separate diffusion and perfusion, multiple b values are required [47-50]. Wirestam, et al. were able to obtain blood volume and flow in the brain by DWI and correlate these values with the results obtained by DSC-MRI [49]. In their work, the DWI was processed by non-linear fitting of the diffusion sequence data to a bi-exponential curve. Separation of diffusion and perfusion in DWI has also been performed successfully in the liver by independent component analysis [50].

Strong diffusion gradients, particularly at higher b values, create eddy currents in conducting components of the MRI scanner. The eddy currents cause distortion of the image. The distortion is in the form of translation, shear and scaling [51]. In order to accurately separate the intravascular content by DWI, the distortion caused by diffusion gradients should be compensated prior to estimating ADC. Since in DWI two magnetic gradients are applied with opposite polarity and time gap between them, DWI is very sensitive to the imaging subject motion [52]. The window chamber model in our experiment had the advantage of small size and fixed position. The small size makes the tissue within window chamber less sensitive to the eddy currents created by the diffusion gradients. As described in chapter 3, window chamber is pinned to the animal holder (Fig. 3.11.c). Therefore, it has very small motion.

### **5.8.2: DWI Sequence**

We imaged the tissue in the window chamber at multiple b values applied along three orthogonal directions. Separating perfusion and diffusion should be independent of the direction of the applied gradient, if perfusion is non-directional. Applying diffusion gradients along different directions allowed comparison of the obtained results. The exact sequence parameters were: TR = 500 ms, TE = 20 ms, b = 0, 20, 40, 60, 80, 100, 200, 400, 800 smm<sup>-2</sup>.

The exact b values experienced by the tissue is somewhat different than the applied b values due to the other sources of magnetic field gradient such as the imaging phase and frequency encoding gradients. The exact b values were extracted from the “method” file generated by the MRI scanner.

To separate the intravascular content of voxels, higher number of b values, particularly at larger b values, are preferred [49]. Since only signal intensity at b values over 300 are free from intravascular water protons, multiple b values over 300 allows for more accurate fitting of the data to the perfusion free diffusion signal. In addition, compensation of the image distortion caused by the applied diffusion gradient is necessary [51]. It is possible to reduce the imaging distortions caused by diffusion gradients by using a twice refocused spin-echo gradient [52].

## **5.9: Applied Methodologies**

### **5.9.1: Introduction**

The vascular kinetic parameters in the experiments were estimated according to the methodologies that are described in section 5.9.2. The AIF was measured based on the second approach that was introduced in section 5.7.2, i.e. by measuring the concentration in a voxel on a large vessel within the window chamber. To measure the extravascular content four approaches were taken that will be described in section 5.9.2.

DWI sequence was carried out only in a few experiments. As mentioned in section 5.8, using DWI to separate the intravascular signal from the extravascular signal is not trivial. Nevertheless, as an initial assessment of the method, DWI was used in two experiments to separate the intravascular and extravascular signals. The procedure of applying DWI to separate the intravascular and extravascular proton densities is described in section 5.9.3.

### **5.9.2: Estimating Kinetic Parameters**

The AIF in MRI is obtained from the signal intensity in a few voxels that had the highest ratio of intravascular to extravascular content within the window chamber. In order to find these voxels, the concentration of the MA in all voxels is measured immediately after the distribution of the MA ( $t=0$ ) assuming uniform distribution of the MA within all voxels. A few voxels with the highest concentration at  $t=0$  are taken as entirely intravascular. These voxels are called V\_ROI (V for vessel). The estimation of AIF is not completely accurate due to the partial volume effect as described in section 5.7.2.

To measure the extravascular signal, an ROI is selected in the tissue of interest apart from the larger vessels. This ROI is called T\_ROI. Four approaches were pursued to measure the concentration of the MA in the extravascular region:

- 1) The intravascular content of T\_ROI is ignored.  $C_e/v_e$  is obtained from Eq. 5.4 assuming uniform distribution of the MA in T\_ROI.  $K_{trans}$ ,  $k_{ep}$  and  $v_e$  are obtained by fitting the dynamic sequence to Eq. 4.3.
- 2) The intravascular signal component of each voxel is estimated from the signal enhancement immediately after the distribution of the MA ( $t=0$ ). The intravascular signal component of T\_ROI is cancelled out by the intravascular signal component of V\_ROI according to the following equation:

$$\hat{S}_n = S_{T\_ROI} - \frac{S_{T\_ROI}^0}{S_{V\_ROI}^0} S_{V\_ROI}, \quad (5.35)$$

where  $\hat{S}_n$  is the estimated extravascular signal component of  $S_{T\_ROI}$ .  $S_{V\_ROI}^0$  and  $S_{T\_ROI}^0$  are the signal from V\_ROI and T\_ROI, respectively at  $t=0$ . As it was described in section 5.7.2, in the absence of water exchange,  $S_{V\_ROI}^0$  and  $S_{T\_ROI}^0$  are equivalent to the intravascular signal component at  $t=0$  in their corresponding ROIs.  $K_{trans}$ ,  $k_{ep}$ ,  $v_e$  are estimated by fitting the dynamic sequence data to Eq. 4.3.

- 3) Intravascular signal component of T\_ROI is considered in the MA kinetic equation.  $C_T$  is obtained by assuming uniform distribution of the MA in T\_ROI.  $K_{trans}$ ,  $k_{ep}$ ,  $v_e$  and  $v_p$  are obtained by fitting the dynamic sequence data to Eq. 5.17.
- 4)  $\hat{S}_n$  is obtained similar to approach 2. However, the kinetic parameters are obtained by fitting the dynamic sequence data to Eq. 5.17. The inclusion of the  $v_i C_i$  term can help to cancel out the residual vascular signal that remains in  $\hat{S}_n$  after applying Eq. 5.35 due to the residual leakage of the MA at  $t=0$ , the non-uniformity of the MA distribution in the vasculature at  $t=0$ , or signal enhancement factors such as water exchange.

If the results obtained by approaches 2 and 4, are more accurate than approaches 1 and 3, it is an indication that the methodology described in section 5.7.2 can improve kinetic parameter estimation. However, as will be described in chapter 6, due to what is believed to be fluctuation of vessels diameter, it was not possible to predict the intravascular proton density distribution within the window chamber. Therefore, approaches 2 and 4 were usually not more accurate than approaches 1 and 3 in estimating kinetic parameters.

### 5.9.3: Diffusion Weighted Imaging

In this section, the exact steps that were taken to obtain vascular compartment proton density from the diffusion measurements are described. To measure the vascular compartment proton density, first it was assumed that at high  $b$  values, the signal from the vascular compartment has faded away due to its high ADC value:

$$S_n(b \geq 200) \approx S(b \geq 200), \quad (5.36)$$

where  $S_n$  is the signal from the non-vascular compartment and  $S$  is the total signal intensity. With this assumption, the following steps were taken to estimate the vascular distribution of the signal:

1- The non-vascular compartment signal intensity at each voxel was fit to a single exponential curve at  $b_h = 200, 400$  and  $800$  ( $h$  stands for high):

$$S_n = \rho_n e^{-b_h D_D} \quad (5.37)$$

where  $\rho_n$  stands for the non-vascular compartment proton density, and  $D_D$  stands for the diffusion component of ADC.  $\rho_n$  and  $D_D$  are obtained by fitting  $S_n$  and  $b_h$  values to Eq. 5.37.

2- To obtain the vascular compartment of proton density, first the extravascular component of the signal was removed from the total signal intensity. Then, the low  $b$  values were fitted to the remaining signal:

$$S_v = S - S_n \quad (5.38)$$

$$S_v = \rho_v e^{-b_l D_p} \quad (5.39)$$

where  $\rho_v$  stands for the vascular compartment proton density,  $D_p$  stands for the perfusion component of ADC and  $b_l$  stands for lower  $b$  values, i.e.  $b = 0, 20, 40, 60, 80$  and  $100 \text{ smm}^{-2}$ .  $\rho_v$  and  $D_p$  are obtained by fitting  $S_v$  and  $b_l$  values to Eq. 5.37.

The above mentioned steps could be repeated by obtaining  $S_n$  from Eq. 5.38 and inserting it in Eq. 5.37. However, when applied to the experiments, extra repetitions deteriorated the obtained results. The reason is the inaccurate estimation of  $S_v$  by Eq. 5.39 in our model. Therefore, the abovementioned steps were carried out only once. It is advised to set the limit for high  $b$  values in Eq. 5.37 at 300 instead of 200 [47]. But since only two  $b$  values were above 200, we set the limit at 200. The methodology was tested by setting the limit for high  $b$  values at 400 and 100 as well. However, the intravascular distribution obtained by setting the  $b$  limit at 200 was more similar to the intravascular distribution obtained by optical imaging.

## CHAPTER 6: RESULTS AND DISCUSSION

### 6.1: Overview

In this chapter the results obtained with the dual modality imaging system are summarized and analyzed. The main objective besides testing the dual modality system was to measure vascular permeability. The theory of the analyses performed on optical images were described in chapter 4 and summarized in section 4.6.4. The MRI analysis theory were described in chapter 5 and summarized in sections 5.9.

In section 6.2 the performed experiments are reviewed. The experiments were analyzed with a Matlab GUI program that was developed as part of this work. This program is briefly reviewed in section 6.3. The developed Matlab program was tested with a simulation phantom as described in section 6.4. A few sample images of tissue structure obtained with the dual modality imaging system are shown in section 6.5. To measure the MA concentration with DCE-MRI, first the native  $T_1$  of the tissue must be obtained. An obtained distribution of  $T_1$  is shown in Fig. 6.6. As described in section 6.6, the  $T_2$  effect of the MA was compensated by measuring  $T_2$  at each time point of the dynamic sequence. Sample measurements of  $T_2$  across the window chamber at different time points during the experiment are shown in section 6.7. Sample images of derived MA concentration at different time points are shown in section 6.8. A major issue in the analysis of the obtained results was fluctuation of the signal intensity in both optical imaging and MRI. The possible reasons for signal fluctuations are discussed in section 6.9. In section 6.10, the results of kinetic parameter estimation are reported.

### 6.2: The Experiments

Among the 30 experiments that were performed, 8 experiments are selected for dual modality analysis. In these 8 experiments, MRI and optical imaging were done successfully, the mouse survived the experiment, and unlabeled fluorescent dye did not exist at appreciable levels in the injected MA solution. The conditions of various experiments, including the 8 well performed experiments, are summarized in Appendix 6.A.1.

The employed MRI sequences evolved over time. At first, a fast spin echo MRI sequence with RARE factor equal to 2 was applied to obtain the dynamic sequence (see section 5.3). Fast spin-echo allowed for two averages during a 32 second scan time. However, the second echo was more sensitive to  $T_2$ . Later, the dynamic sequence was carried out with a RARE factor = 1, multi echo sequence. The images obtained at multiple echo times allowed for the measurement of  $T_2$  at each time point in the dynamic sequence. The  $T_1$  sequence was also performed with more  $T_1$  values to improve the precision of  $T_1$  estimation and also to measure more than one  $T_1$  value in a voxel by double exponential fitting. The final experiments also involved a diffusion sequence. As described in section 5.8, the diffusion sequence was applied in order to address the partial volume effect. The

details of the MR sequences of many of the performed experiments are summarized in appendix 6.A.2.

The optical imaging was similar in all experiments. The brightfield and GFP images were taken with white light and argon laser sources prior to the injection of the MA. The dynamic sequence was mostly carried out at 2 seconds per frame. An issue was setting up the right integration time for the dynamic images prior to the injection of the MA. The integration time was estimated based on prior experiments and the dose of the MA. The integration time in the dynamic images ranged between 250 ms to 500 ms. In some experiments, the integration time was not selected properly at first and was changed after the injection of the MA. In these cases, the change of the integration time was compensated after imaging by properly scaling images to correspond to a common integration time.

The dose of the injected MA in the early experiments was about 50 mg (approximately equivalent to 22  $\mu\text{mol MA/kg}$  of tissue). However, during the course of the experiments, the dose of the MA was reduced from 50 mg to 10 mg (equivalent to 4.4  $\mu\text{mol MA/kg}$ ). The higher dose of MA was applied in the earlier experiments based on previous work [1] and to compensate for the low rate of extravasation of BSA from blood vessels. The MA dose was later reduced to reduce the transverse relaxation effect, as described in section 5.6 and also to simplify the complexity of analysis caused by water exchange as described in section 5.5. However, more accurate DCE-MRI results were not obtained at lower dose of MA. In optical imaging, high dose of the MA can cause fluorescence signal intensity saturation in thicker vessel due to absorption of the laser by the MA.

### **6.3: Analysis Programs**

Two GUI programs were developed for analyzing MRI images and two for analyzing the optical fluorescence images. All of these programs display image sequences and allow for selecting regions of interest for analysis.

Of the two programs for each modality, one is used to register the images in a sequence to compensate for animal or imaging system motion. Automatic registration of sequential frames based on signal intensity differences, correlations, or combination of these methods were not successful. Therefore, registration was done manually. To register images, the user moves along the sequence of frames and shifts them to compensate for image motion. Drawing ROIs helps to focus on distinct regions and observe their motion relative to the boundaries of the selected ROIs. The program can display up to 5 regions of the image simultaneously. The registration program for optics can also compensate for signal intensity changes caused by variation of the optical imaging system integration time. This is done by observing signal behavior before and after the change. In MRI, the program can register the  $T_1$  and the dynamic sequence images against mouse motion.

The second program for each modality is used to analyze the images. Rectangular ROIs are used for most of the analyses. Free style drawing of ROIs is also possible, but only some of the analysis

tools developed can be applied to non-rectangular ROIs. The program allows for plotting signal intensity in each ROI versus time, spatial distribution of signal intensity within the ROI, and estimation of vascular kinetic parameters based on the signal intensity in different ROIs. In MRI, the program can measure  $T_1$  based on single and double exponential fitting, measure  $T_2$  at each frame, compensate for the  $T_2$  effect on the signal, and also measure the apparent diffusion coefficient. Both MRI and optics programs allow for saving image frames and can apply pixelwise arithmetic operations to the saved frames including: summation, subtraction, multiplication, division, multiplication and powering to a factor, logarithm and exponentiation. These mathematical operations allow for enhancing the contrast and comparison of the image frames. The programs can also save the experiment data and the performed analyses to a file. The performed analyses can be uploaded to the programs from the saved file for future analysis.

#### **6.4: Testing the Analysis Programs**

The performance of the programs was successfully tested using a software simulated phantom. The phantom consisted of two vessels crossing one another in a rectangular tissue. The vessels only partially occupied the volume of the tissue. The partial volume effect outside of the vessels was simulated by inserting a random percentage of intravascular content to the pixels outside of the two vessels. The AIF was simulated by different functions; one of these was a shifted arctan multiplied by a shifted exponential decay. Extravascular concentration of the MA was calculated according to the AIF and the assumed values of vascular kinetic parameters. A uniform level of noise was added to the signal intensity in each pixel. The phantom did not simulate the effect of water exchange. The program generated accurate results in the absence of noise and partial volume effect. When noise and partial volume effect were present, the estimated kinetic parameters were not as accurate, but were within the expected range. Since water exchange between compartments was not simulated, in the presence of partial volume effect, the analysis methods 2 and 4 described in section 5.9 (which were based on cancelling the vascular content of  $T\_ROI$  by using the vascular content of  $V\_ROI$ ), estimated the kinetic parameters more accurately than analysis methods 1 and 3.

#### **6.5: Tissue Structure**

Fig. 6.1 shows optical and MRI images of the window chamber taken simultaneously with the dual modality imaging system. The top two images, Fig. 6.1.a and 6.1b, were taken before the MA injection. The tumor is easily observed in the combination trans-illumination and GFP fluorescence optical image (Fig. 6.1.b). The corresponding tumor area is brighter in the MR image (Fig 6.1.a) mainly due to the greater tissue thickness in the tumor area. Fig. 6.1.c and 6.1.d are MRI and optical images after MA distribution in the vasculature ( $t=0$ ). The ROIs shown on these images are used to determine the signal intensities in vascular (V), tumor (Tu) and healthy (H) tissue regions for estimation of vascular kinetic parameters.

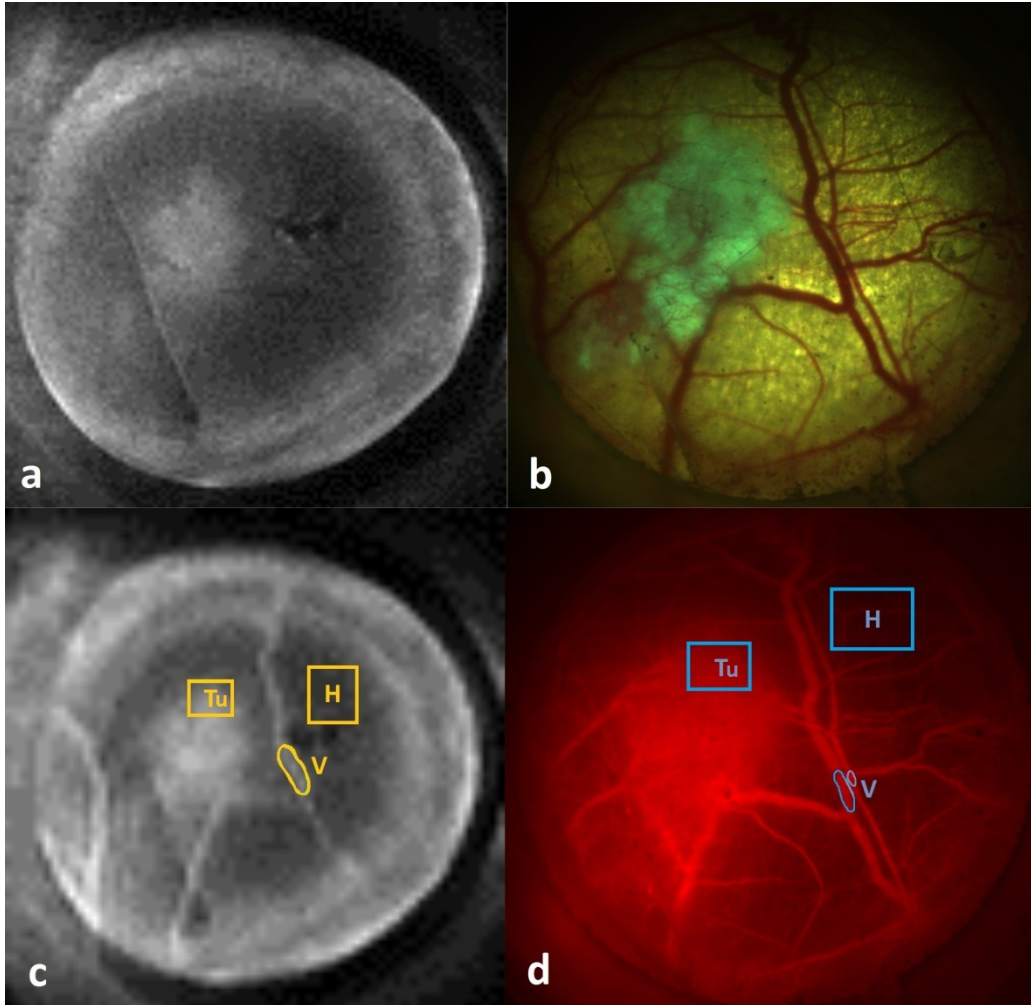


**Fig. 6.1.** Images of a window chamber taken with the dual modality imaging system (Experiment 4: 0980-00-3, 12/17/2010): a. Structural MRI image of the window chamber. TR = 500 ms, TE = 10.7 ms, imaging matrix = 256x256, 2 averages. b. Window chamber illuminated with white light trans-illumination and argon 488nm laser epi-illumination. c, d. Single frame MRI (c) and optical (d) image from the image sequences acquired after MA injection. MRI sequence is the first sequence in section 5.3. Three ROIs on vessel (V), tumor (Tu) and healthy tissue (H) are selected. In the optical image, the ROI on vessel has two parts, one on vein and the other on artery. In MRI it is not possible to separate artery and vein. The additional small arterial section in the optical image was selected to account for the presence of arterial signal in the vessel ROI in MRI.

## 6.6: Measuring $T_1$

The  $T_1$  was estimated based on single and double exponential fittings using Matlab code. Since in most cases, double exponential fitting did not give meaningful results, the  $T_1$  value estimated by single exponential fitting is reported. The average  $T_1$  value in tumor, healthy tissue and vessels in each experiment is summarized in appendix 6.A.3. In most cases, the measured  $T_1$  on even the largest vessels in the window chamber was not distinguishable from the surrounding tissue. This

is believed to be due to the partial volume effect and the relatively small difference between the intravascular and extravascular  $T_1$  values. A  $T_1$  map of the tissue within the window chamber in one of the experiments is shown in Fig. 6.2 and is compared to the relative intravascular content of each pixel in the image.



**Fig 6.2.**  $T_1$  value measured at each pixel (left). The values are obtained by fitting the  $T_1$  sequence data to the model equation. The distribution of  $A\rho_v/\rho_T$ , where  $A$  is an unknown constant, and  $\rho_v$  and  $\rho_T$  are the intravascular and total tissue proton density (right). Except in a few pixels, it is not possible to distinguish the vessels in the left image. (Experiment 1: 0563-R2, 8/13/2010)

### 6.7: Measuring $T_2$ and Compensating Its Effect

As mentioned in section 5.3, in many experiments a multi-echo dynamic sequence was employed. The signal intensities at multiple echoes of each repetition were fit to a single exponential decay curve. Only the first four echoes were used since beyond the fourth echo, the SNR was poor. The estimated  $T_2$  values in one of the experiments, before and after injection of the MA, are shown in Fig. 6.3. The obtained  $T_2$  values in the vessels after injection of the MA, are higher than the intravascular  $T_2$  values estimated in section 5.6. The discrepancy is due to both partial volume effect and also the effect of red blood cells in reducing the MA effect on transverse relaxation as described in section 5.6.

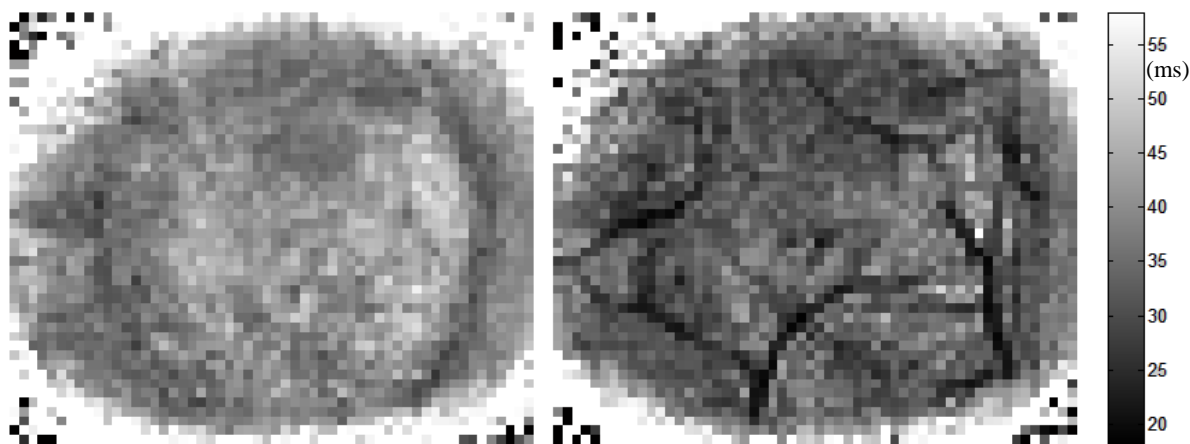


**Fig 6.3.** T2 value measured before the injection of the MA (left) and immediately after the injection of the MA ( $t=0$ , right). (experiment 0554-R1, 12/15/2011)

## 6.8: Concentration Measurement in MRI

The  $r_1C$  product ( $r_1$ : longitudinal relaxivity, C: concentration) at each time point was estimated according to Eq. 5.4 assuming that each voxel is a homogenous single compartment. If multiple echoes were recorded, the  $T_2$  effect was compensated prior to applying Eq. 5.4. The  $r_1C$  distribution immediately after injection of the MA (average of  $r_1C$  in frames 8-9), for one of the experiments, is shown in Fig. 6.4.a. In Fig 6.4.b, the difference between the  $r_1C$  distribution 30 minutes after the injection of the MA (average of  $r_1C$  in frame 63-64) and that immediately after the distribution of the MA in the vasculature, are shown for the same experiment.

Application of transverse relaxation in measuring perfusion related parameters of vasculature is called dynamic susceptibility contrast enhanced MRI (DSC-MRI). DSC-MRI is usually not appropriate for measuring vascular permeability for the following reasons: 1- The relationship between transverse relaxation rate ( $R_2$ ) and MA concentration is not always linear (for example in the blood). 2- Transverse relaxivity ( $r_2$ ) depends on the tissue type [2]. 3- The MA in one compartment affects the transverse relaxation rate of neighboring compartments through bulk susceptibility effect of the MA (explained in section 5.6).

Measurement of MA concentration by DCE-MRI has problems particularly at higher concentration. At higher concentrations, MA effect on  $T_2$  makes Eq. 5.4 inaccurate. Also, as explained in section 5.5.3, water exchange affects longitudinal relaxation more than transverse relaxation. Water exchange can both complicate and simplify the calculations depending on the compartments that are in water exchange. The fast exchange between intracellular and extracellular compartments makes  $r_1C$  measurement easier. However, the expansion of signal enhancement from microvessels to the surrounding tissue due to water exchange complicates  $r_1C$  measurements. In the measurement of  $r_2C$ , in addition to water exchange, the magnetic field perturbation by MA alters the  $T_2$  of the intracellular water. The amount of this influence is not known. As an experiment, we estimated  $r_2C$ , across tissue at the same time points and for the same

mouse as shown in Fig 6.4. The results are shown in Fig 6.5. Fig 6.4.b is clearer and has higher contrast than Fig. 6.5.b. Fig 6.6 illustrates the normalized ratio of  $r_2C$  to  $r_1C$ . According to the  $r_1$  and  $r_2$  values estimated in section 2.2.3, the  $r_2C/r_1C$  is approximately equal to 4 in saline at concentrations below 4 mM. At higher concentrations, the  $r_2C/r_1C$  decreases because of saturation of the  $T_2$  effect of the MA. However, the estimated value of  $r_2C/r_1C$  in Fig 6.6.a is mostly over 10. The reason might be the  $T_2$  shortening due to the MA concentration gradient between different compartments. The vessels could not be distinguished in Fig. 6.6. This means that the  $r_2C/r_1C$  ratios in the intravascular and extravascular regions are similar.

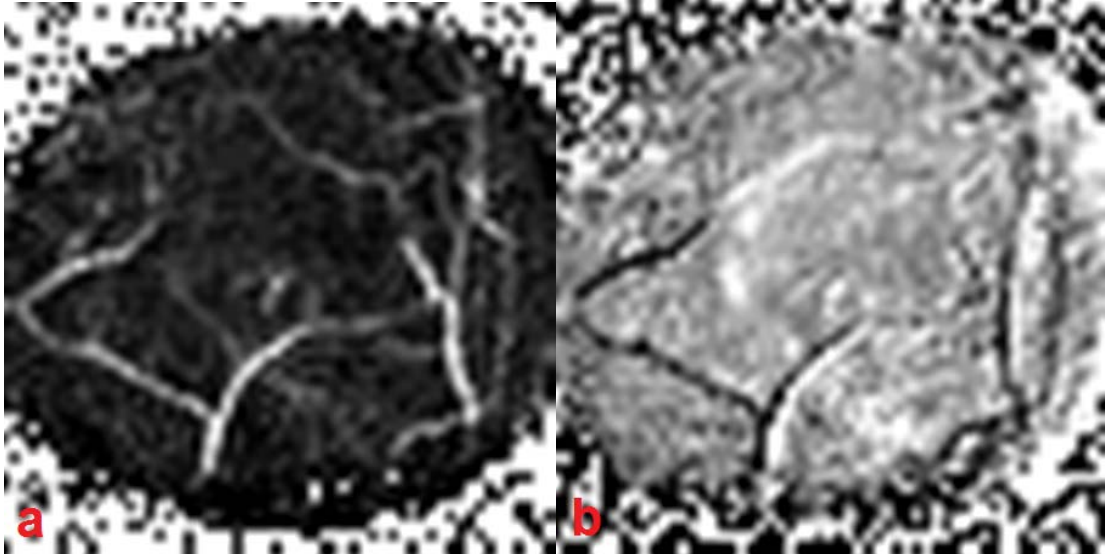


**Fig 6.4.** a.  $r_1C$  at  $t=0$  (experiment 0554-R1, 12/15/2011). The intensity map range corresponds to (0, 1)  $s^{-1}$ . The maximum value of  $r_1C$  was 1.3  $s^{-1}$ . b. The difference between  $r_1C$  at  $t=30$  min and  $t=0$ . The range of the signal is: (-0.2, 0.2)  $s^{-1}$ . The white strip at the right side of some of the bigger vessels in Fig 6.4.b, indicating high signal intensity, is probably due to small tissue shift between  $t=0$  min and  $t=30$  min.

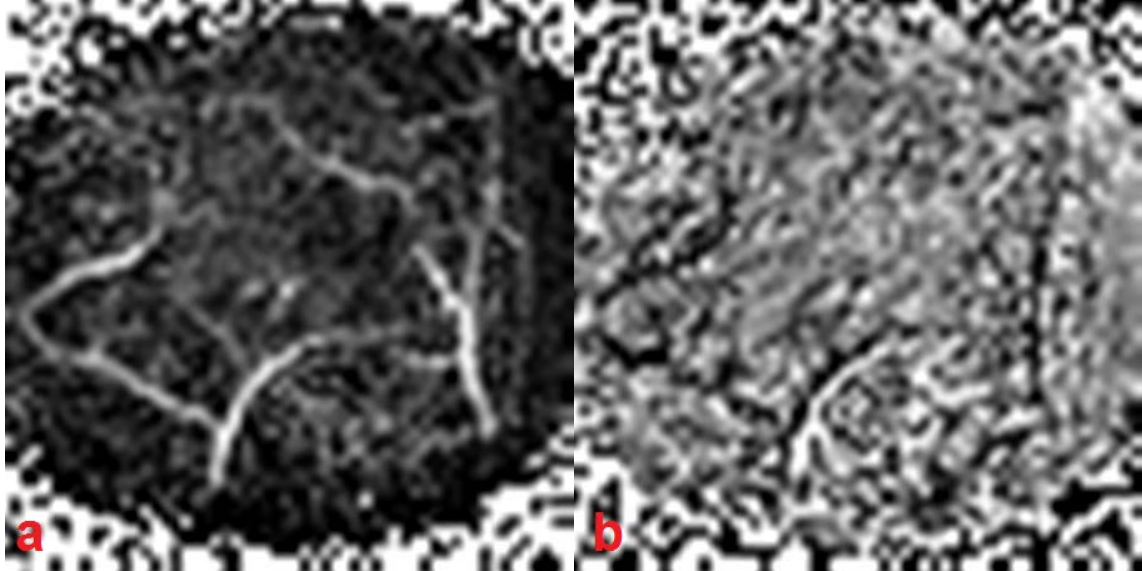


**Fig 6.5.** a.  $r_2C$  at  $t=0$  (experiment 0554-R1, 12/15/2011). The intensity map range corresponds to  $(0, 25)$  s-1. b. The difference between  $r_2C$  at  $t=30$  min and  $t=0$ . The range of the signal is:  $(-5, 5)$  s-1.

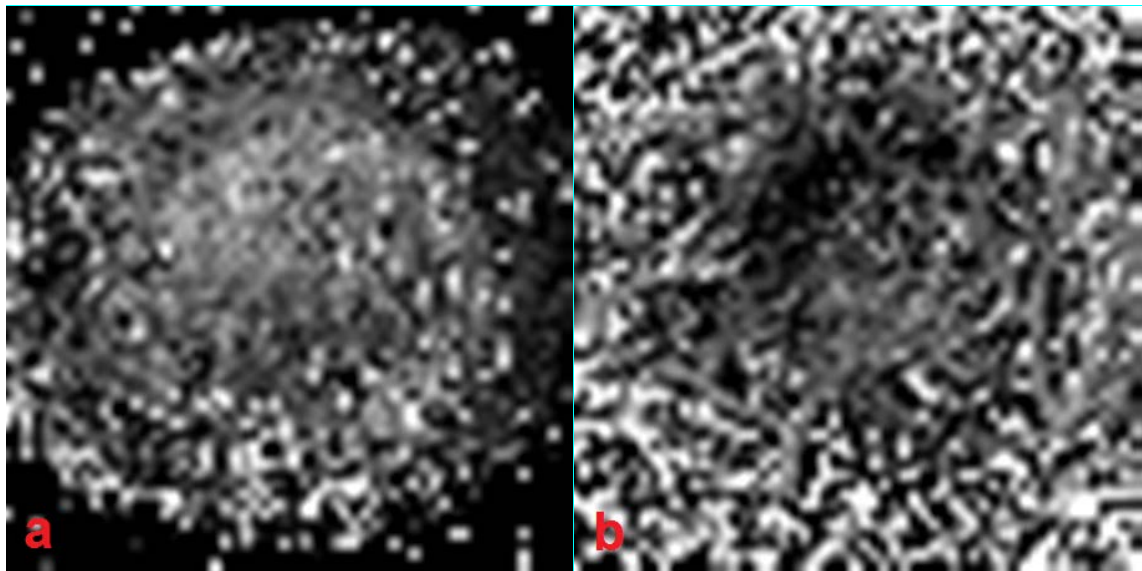


**Fig 6.6.** a.  $r_2C / r_1C$  at  $t=0$  (experiment 0554-R1, 12/15/2011). The intensity map range corresponds to  $(10, 80)$ . b. The difference between  $r_2C / r_1C$  at  $t=30$  min and  $t=0$ . The range of the signal is:  $(-25, 25)$  s-1.

## 6.9: Signal Fluctuation

### 6.9.1: Introduction to the Problem

In many experiments, both the optical and MRI signals fluctuated temporally with a varying duration in the range of a few minutes. The fluctuations were not consistent with expectations of the kinetics of the MA inside and outside the vessels. In most cases, the optical and MRI signal

fluctuations were correlated. However, in a few cases, the optical and MRI signals were anticorrelated or not correlated. It appeared that the amplitude of signal fluctuation was dependent on the intravascular content of the ROI. In optics, distinguishing the intravascular and extravascular signal was more difficult because unlike MRI, there was no tissue signal in the absence of the MA. In some experiments, the MRI signal fluctuation had significantly higher amplitude relative to the total signal intensity than optical signal fluctuation, but still the two signal fluctuations still seemed to be related.

The signal intensity versus time for both optical and MRI images of experiments 1-8 are plotted in Appendix 6.A.4. The signal intensities in the corresponding ROIs for the two modalities are plotted on the same graph. To make the comparison easier, the signal intensity in the two modalities are normalized to one another. In addition to the 8 well performed experiments, the MRI signal intensities versus time are plotted for a few other experiments as well. Temperature and respiration are also plotted as a function of time in the experiments where this information was recorded.

### 6.9.2: Two Examples

We compare the signal intensity in corresponding ROIs in the two modalities for two of the experiments (Experiment 4: 0980-00-3, 12/17/2011 and Experiment 7: 0254-R1-1, 07/16/2012). In the first discussed experiment, Experiment 4, the MR and optical signal intensity fluctuations in V\_ROI are anticorrelated. In the second discussed experiment, the MR and optical signal intensity fluctuations are correlated.

In the first experiment, a MA dose of 52 mg, approximately corresponding to 22  $\mu\text{mol}$  MA/kg of tissue, was injected in the mouse tail vein. This is the highest dose that we applied in our experiments and it is significantly higher than the dose that it is usually applied by other groups in DCE-MRI of Gd\_DTPA labeled albumin i.e. about 30  $\mu\text{mol}$  Gd\_DTPA/kg [3, 4], equivalent to 1.36  $\mu\text{mol}$  MA/kg in our experiment. As discussed in chapter 5, this choice may cause complications in the interpretation of the data due to the transverse relaxation and water exchange effects in MRI and the MA absorption of laser light in optical imaging.

The optical and MRI images of the window chamber prior to and post MA distribution in this experiment are shown in Fig. 6.1. In Fig. 6.1.c and 6.1.d, three ROIs were selected: one on a large vessel (V\_ROI), one on the tumor (Tu\_ROI), and one on healthy tissue (H\_ROI). Because of the capillaries present in tissue, the signal from each of the selected ROIs consists of both intravascular and extravascular components. However, the ROI selected on the vessel has significantly higher relative intravascular component.

The signal intensities versus time from these ROIs (V\_ROI, Tu\_ROI and H\_ROI) are shown in Fig. 6.7. The MRI signal intensities are normalized to the signal intensity before the injection of

the MA. In both modalities, signal intensities in V\_ROI fluctuate with a varying duration in the range of a few minutes after the injection of the MA. Fluctuations also exist in Tu\_ROI and H\_ROI with smaller amplitudes. Similar signal intensity fluctuation behavior was observed in other experiments as well.

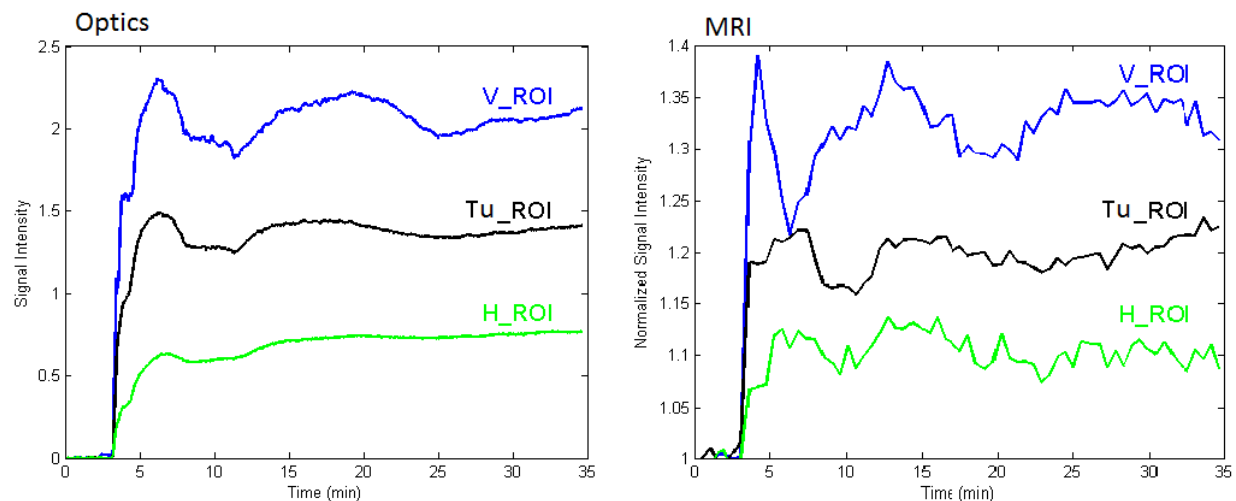


**Fig. 6.7.** Signal intensity in the three ROIs that are highlighted in Fig. 6.1. The left graph is from the optical image sequence and the right graph is from the MR image dynamic sequence. Optical signal intensity has arbitrary units. MR signal intensity is normalized to the signal intensity before MA injection.

In Fig. 6.8, the signal intensities in the V\_ROIs for both modalities are shown together. The amplitudes of the MRI signal intensity is normalized to the optical signal intensity to make comparison easier. It appears that the signal fluctuations have an anticorrelated behavior in the two modalities in this experiment, which implies that the fluctuations are not caused by imaging system error but by some sort of physiological or environmental parameter that affects the optical and MR signals in the vasculature in an opposite way.

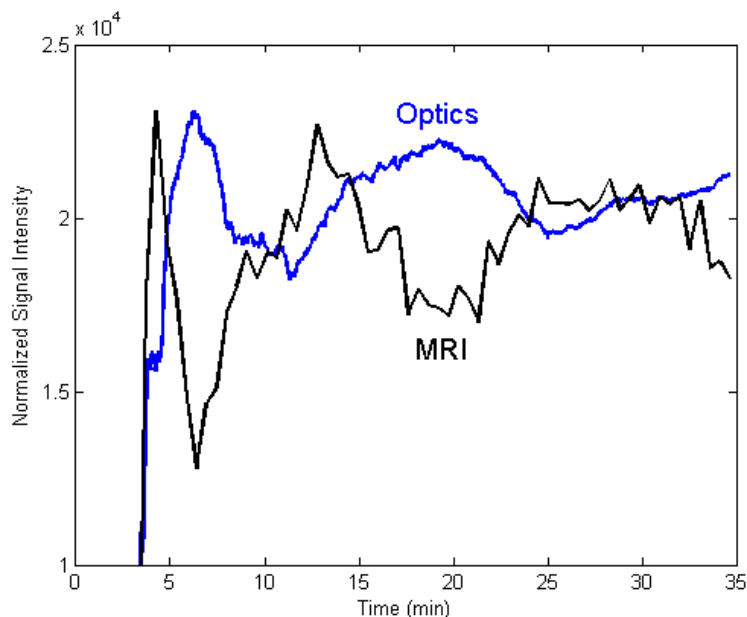


**Fig. 6.8.** Optical and MR signal intensity in V\_ROIs a. The global minimum and maximum of MR signal intensity are normalized to their optical counterparts to simplify comparison of the data.

In many experiments, the signal fluctuations of the optical and MRI modalities were correlated and not anti-correlated. In Fig. 6.9, the signal intensities for another experiment are plotted in the two modalities. In Fig. 6.9.a, the corresponding ROIs are on vessel (V\_ROI) and in Fig. 6.9.b, the corresponding ROIs are on a healthy tissue region (H\_ROI). For both pairs of ROIs, the optical and MRI signal intensities are correlated. In this experiment, 16 mg of MA was injected which is about 1/3 of the dose injected in Experiment 4. Temperature and respiration rate were monitored in this experiment. Temperature rose gradually from 33.5 to 34.3 over the time of the dynamic data collection. Respiration rate dropped from 30 to 27 with small fluctuations in between. The temperature and respiration rate variation with time for this experiment are plotted in Appendix 6.A.4.

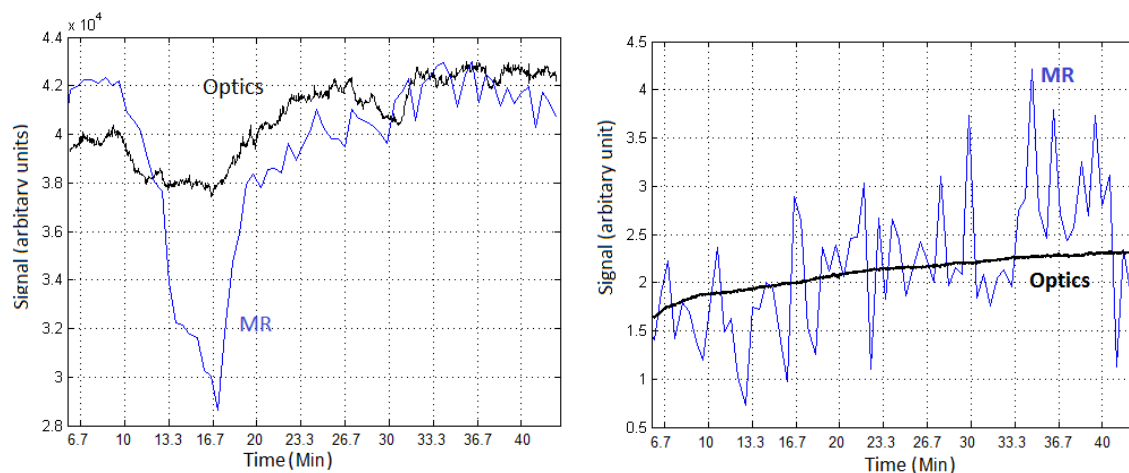


**Fig. 6.9.** Optical and MR signal intensity in corresponding V\_ROIs (left graph) and H\_ROIs (right graph). The average of optical and MRI signal intensities are equated to simplify comparison of the data (Experiment 7: 0254-R1-1, 07/16/2012).

### 6.9.3: Investigation of the Source of Signal Fluctuations

#### 6.9.3.1: Summary

The observed signal fluctuations might be caused by MA concentration fluctuations, physiological variations in the mouse, or ambient environmental changes that either directly affect the signal intensity or indirectly affect the signal intensity through altered physiology of the mouse. In this section, we investigate the effects of temperature, anesthesia, respiration rate, blood flow and transverse relaxation effect of the MA on signal fluctuations.

#### 6.9.3.2: Temperature

Temperature can affect the signal intensity both directly and indirectly. The direct effect is by changing the optical or MRI signal enhancement properties of the MA, the MRI signal of the tissue itself, or the responses of the optical and/or MRI systems. In prior research, it has been shown that  $T_1$  weighted MRI signal intensity, in the absence of CA, increases with temperature [5] and that optical fluorescence signal intensity of Rhodamine B dye decreases with temperature [6]. These findings are not automatically applicable to our studies because of different experimental conditions and large range of temperature variation in the above mentioned studies.

While the goal was to keep the mouse body temperature at an approximate constant level during the in-vivo experiments, the mechanism of maintaining the animal temperature in early experiments was by blowing intermittent hot air around the mouse. This caused temperature variation in the surface coil as well as the exposed window chamber tissue. The temporal behavior of the heating system and the signal oscillation were at similar time scales. In addition, mouse body temperature sometimes varied by as much as 3-4 °C during the course of the earlier experiments. In later experiments (Experiment 5 and after), the intermittent hot air flow was replaced by a constant hot air flow that did not blow directly on the mouse. As a result, the

temperature of the mouse body, as well as the surrounding environment, was maintained at a more constant value. Another point to note is that in many of the earlier experiments, the mouse body temperature was a few degrees below 37 °C at the time that the MA was injected.

In order to investigate the effect of temperature on signal intensity, several micro tubes filled with various concentrations of the MA in saline, were imaged with the dual modality imaging system while the temperature was changed between 34-43 °C. Even over the large temperature change, the optical signal intensity was nearly constant during the entire experiment. The MR signal intensity also remained almost constant when the temperature dropped from 38 °C to 33.5 °C. However, as soon as the hot air was turned on, the MRI signal intensity dropped significantly. The signal intensity of the microtube with MA concentration of 10 mg/ml, dropped by 38% in the 4 minutes that the hot air was on. Meanwhile, the temperature increased by 9.5 °C from 33.5 °C to 43.0 °C. After hot air was turned off, the signal intensity increased. However, when the temperature decreased to 38 °C, the signal level was lower than the initial signal intensity at the same temperature prior to hot air blow. It appears that the surface coil components, or the microtubes, had not yet cooled down. The MRI signal intensity as a function of temperature variation is plotted in Fig. 6.10.

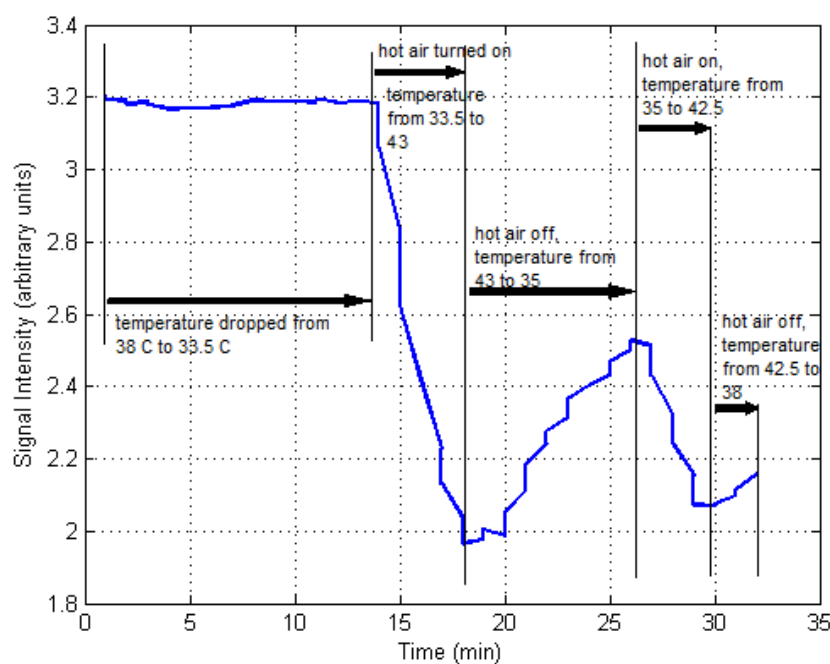


**Fig 6.10.** MRI signal intensity as temperature was varied by means of switching hot air current. The concentration of the MA in the microtube was 10 mg/ml ( $\sim 4.4 \mu\text{mol MA/Kg}$ ).

In addition to the direct effect, temperature might affect intravascular signal intensity in the animal indirectly through vasodilation and vasoconstriction. Vasodilation happens as temperature increases by sending more blood to the heated tissue, and vice versa vasoconstriction occurs as temperature drops. However, the vessel diameter dependence on temperature is not exactly regular.

For example vasodilation might follow vasoconstriction if cold temperature continues to exist through what is called a hunting reaction [7]. It is expected that both MRI and optical signal intensities would increase due to vasodilation. Vasodilation and vasoconstriction of arteries was observed clearly in optical images in correlation with the signal fluctuations. In the veins, it was hard to distinguish vessel size change. This is expected since smooth muscle cells, which cause vasodilation and vasoconstriction, are more prevalent around arteries.

In later experiments, when the hot air flow was kept at a constant level and the temperature was kept reasonably steady, the optical signal fluctuation in the window chamber reduced significantly. Nevertheless, optical signal fluctuations with peak to valley amplitude variation up to 10% of the total signal intensity were still observed. In addition to temperature control, a lower concentration of MA was applied in later experiments. MRI signal fluctuations were still significant in the experiments even when the temperature was kept reasonably constant.

In later experiments, the mouse body temperature was recorded throughout the experiment. The temperature was measured via an optical fiber probe in the mouse rectum. Therefore, the recorded temperature was not precisely the temperature of the window chamber tissue. The temperature recordings are plotted in Appendix 6.A.4. Almost no correlation was observed between the recorded temperature and the MRI signal intensity. This observation is not unexpected. As observed in the phantom, the measured temperature was not well correlated with the signal fluctuation, probably because the temperature in the surface coil and phantom was not exactly the same as the temperature experienced by the coil. In the case of mouse, the measured temperature in the mouse rectum can be significantly different than the temperature of the surface coil and the window chamber.

From the investigation it is concluded that temperature variation can be a cause of signal fluctuation. Temperature rise causes vasodilation that increases both optical and MRI signal. However, blowing hot air on the tissue and the surface coil significantly decreases the MRI signal which can explain the reverse phase of optical and MRI signal intensity observed in earlier experiments. As the intermittent hot air flow was replaced by a continuous flow, vascular size variation reduced as observed in optical images. Since the hot air did not blow directly on the tissue and the surface coil, the signal fluctuations were less and more in phase. However, the MRI signal fluctuations had significantly higher relative amplitude than optical signal fluctuations. The latter observation could not be explained with the given data. If signal fluctuation was caused by MA concentration fluctuation, the MR signal fluctuation would be demagnified due to signal saturation at high concentrations of MA.

### **6.9.3.3: Anesthesia**

Isflurane can cause dose dependent vasodilation [8-10]. Since the level of isoflurane was modified during the experiment to control the respiration rate, it can potentially cause signal variation. Isoflurane variation occurred more abruptly and frequently in the beginning of the

experiment rather than at the later stages. This is in accordance to the observed signal fluctuations, which occurred more frequently in the beginning of the experiment.

#### **6.9.3.4 Respiration Rate and Flow**

In one experiment, we monitored the respiration rate, but no clear correlation was observed between respiration rate and the signal intensity. Blood flow can cause variation in MR signal intensity [11]. However, since the MR and optical signal intensities were mostly correlated, and also that the flow was mostly in plane, blood flow is not considered to be a significant cause of signal variation.

#### **6.9.3.5: T<sub>2</sub> effect**

If the signal intensity fluctuation is caused by MA concentration variations, an anticorrelated signal fluctuation observed in MRI signal relative to optical signal, may be due to the T<sub>2</sub> effect of the MA. An optical signal typically increases monotonically as the concentration of the fluorescent CA increases up to a saturation level. The signal behavior is more complex in MRI where at sufficiently high concentration levels the T<sub>1</sub> shortening effect of the MA will saturate and the T<sub>2</sub> shortening effect can result in a decrease in signal intensity rather than an increase. In the data shown in section 6.7.2 (Experiment 4), it was observed that MR signal intensity reaches its maximum value when the optical signal intensity is at 70% of its peak. Beyond this point, MR signal intensity in V\_ROI follows the optical signal with opposite polarity of signal change. This may indicate that MR signal intensity is reducing as concentration of MA passes a certain limit.

To investigate the T<sub>2</sub> effect on the MRI signal intensity, we sequentially imaged microtubes filled with the dual labeled MA dissolved in phosphate purified saline (PBS) at concentrations of 0.30, 0.18, 0.12, 0.09 and 0.018 mM (corresponding to 25, 15, 10, 7.5 and 1.5 mg/ml) with the dual modality imaging system. To compare these concentrations with the concentrations in the Experiment 4, the highest concentration roughly corresponds to the maximum concentration of the MA in the blood vessels and the lowest concentration roughly corresponds to the situation where the MA is dissolved uniformly in the entire water content of the mouse body. The imaging was carried out with the same optical and MR imaging protocol that was applied in Experiment 4. The highest MRI signal was at the concentration of 0.12 mM. Therefore, at the very high concentration of 0.30 mM, MRI signal intensity is expected to have inverse dependence on MA concentration.

It is expected that if the T<sub>2</sub> effect is the cause of MRI and optical signal phase reversal, the MRI signal intensity fluctuation in T\_ROI, H\_ROI and V\_ROI will be in phase, because most of the signal enhancement in all ROIs is caused by their intravascular content. In section 6.9.2 it was shown that the signal fluctuation in T\_ROI and H\_ROI do not follow V\_ROI exactly, and are in phase with the optical signal fluctuation (see Appendix 6.A.4). Differences between signal fluctuation in vascular and non-vascular ROIs were observed in some other experiments as well. Usually, when the signal fluctuation was in phase in V\_ROI in the optical and MR modalities, it was also in phase in T\_ROI, H\_ROI and V\_ROI in MRI as well. It could be argued that the T<sub>1</sub> effect of MA in smaller vessels saturated at a higher concentration due to water exchange between

the intravascular and extravascular compartments. Also the concentration of the MA in the capillaries might be lower than larger vessels at the initial peak of MA concentration in the larger vessels.

#### **6.9.4: Conclusion**

It is believed that vasodilation and vasoconstriction are the main cause of optical signal fluctuations. Temperature and anesthesia variation can change the vessel size. Vessel size change explains the in-phase optical and MRI signal variation in later experiments. However, by itself, this does not explain the reverse phase between the two imaging modalities in the earlier experiments. Hot air blowing around the tissue and the surface coil, according to the studies done with a phantom, can drop the MR signal significantly. Therefore, in earlier experiments the intense signal fluctuations was probably due to the intermittent hot air flow. The reverse phase of MRI signal could have been caused by the direct effect of hot air on the MRI signal. The signal fluctuations in later experiments were probably due to vasodilation and vasoconstriction that were caused by a combination of physiological effects including temperature and anesthesia level.

$T_2$  effect can also explain certain behavior of the MRI signal. For example, immediately after injection of MA in experiment 4, optical signal intensity increased until minute 7 in Fig. 6.8. During this time, vessel diameter, as observed in optical images, remained the same. Therefore, it is expected that optical signal gain is caused by higher MA concentration in the vasculature. However, MRI signal intensity peaked at minute 4 and decreased afterwards until minute 7. It is expected that at very high dose of MA, the  $T_1$  effect of MA has saturated and the  $T_2$  effect of MA has decreased the signal intensity.

It should be emphasized that the conclusions made in this section for the causes of signal fluctuations are not definitive and require further investigations. It is suggested that in future experiments, in addition to the mouse body temperature, the temperature of the surface coil and window chamber be monitored. Greater care should be taken to maintain all physiological and environmental variables at a constant level, and any inadvertent variation to be precisely monitored.

### **6.10: Estimating Vascular Kinetic Parameters**

#### **6.10.1: Summary**

Estimation of vascular kinetic parameters in our experiments is not accurate due to the signal fluctuations. Signal fluctuations create unrealistic estimations of extravascular concentration variation ( $dC_e/dt$ ), and also intravascular and extravascular concentrations ( $C_i$  and  $C_e$ ). In addition, estimating the vascular content of the tissue, which was part of many kinetic parameter estimation methods described in chapters 4 and 5, will not be accurate due to vasodilation and vasoconstriction. Nevertheless, the methodologies of chapters 4 and 5 were applied to the 8

experiments that were signified in section 6.2 and appendix 6.A.1 to estimate vascular kinetic parameters.

For each experiment, the kinetic parameters are estimated in healthy tissue, tumor center and tumor edge. Tumor edge refers to tumor regions at the margins with dense neovasculature. To estimate the kinetic parameters, four analysis methods are applied to MR images and two analysis methods to the optical images. Therefore, overall 18 analyses are applied to each experiment to estimate the vascular kinetic parameters: six analysis methods applied to three tissue types. The four analysis methods applied to MRI images were reviewed in section 5.9. The two analysis methods applied to optical images were reviewed in section 4.6.4. These methods will be referred to by the order mentioned below:

- 1- MRI approach 1 in section 5.9.
- 2- MRI approach 2 in section 5.9.
- 3- MRI approach 3 in section 5.9.
- 4- MRI approach 4 in section 5.9.
- 5- Wu, et al. approach [10] described in section 4.4.
- 6- Yuan, et al. approach [11] described in section 4.5 and modified in section 4.6.4.

In some cases, it was not possible to apply an analysis method to a tissue type. For example analysis method 5 was sometimes not applicable to tumor regions due to the dense vasculature as discussed in section 4.6.2.

Different analysis methods are capable of measuring different kinetic parameters. The MRI methods all estimate  $K_{trans}$ ,  $k_{ep}$  and  $v_e$ . Analysis method 2 estimates  $v_p$  as well. Whether  $v_p$  is estimated depends on the kinetic equation that the intravascular and extravascular concentrations were fitted to (Eq. 4.3 Or Eq. 5.17). Analysis Method 5 estimates  $k_{ep}$  and vascular permeability. Analysis method 6, can only estimate  $k_{ep}$ . Since  $k_{ep}$  is common among all analysis methods, it is used to compare the results of all the experiments.

For each of the 18 analyses performed on an experiment, several ROIs were selected on vessel, tumor and healthy tissue. The ROIs on vessels are called V\_ROI, the ROIs on tumor, Tu\_ROI and the ROIs on healthy tissue H\_ROI. The term T\_ROI refers both to Tu\_ROI and H\_ROI. The kinetic parameter estimation was applied to every pair of V\_ROI and T\_ROI. Therefore, for each of the 18 performed analyses, several kinetic parameter estimations were done. This allowed testing of the consistency of the results.

The results of the estimations are summarized in Appendix 6.A.5. The mathematical process of estimating kinetic parameters is described in section 6.10.2. The obtained kinetic parameters in different experiments, tissue types, and by different analysis methods, are compared in section 6.10.3.

### 6.10.2: Estimation Process

To estimate the kinetic parameters, first the signal intensity in each ROI was temporally smoothed to remove the high frequency noise. The filtering was done with Matlab locally weighted regression algorithm. The developed GUI analysis program allows for other smoothing and low pass filtering algorithms to be used as well. However, we found that usually by applying the locally weighted regression algorithm the estimated kinetic parameter approaches an asymptotic value at a smaller smoothing range.

The kinetic parameters were obtained by fitting the signal intensities (optical imaging) or concentrations (MRI) to kinetic equations. The fitting algorithm was a linear least square method. Murase, et al illustrated that linear least square method is more accurate than non-linear least square method at low SNR in finding kinetic parameters [12]. In their paper, they fit the kinetic parameters to the integrative form of Eq. 5.17, i.e. to the following equation:

$$v_e C_e(t) = K_{trans} \int_0^t C_i d\tau - k_{ep} \int_0^t C_e d\tau \quad (6.1)$$

A matrix of coefficients was formed by obtaining  $C_e$ ,  $\int C_i d\tau$  and  $\int C_e d\tau$  at each measurement time point. The advantage of using the integrative form is the low pass filtering by integration on the right side of Eq. 6.1. The disadvantage is that the  $C_e$  and  $C_i$  at lower time points affect all equations at higher time points thorough the integrated terms in Eq. 6.1 ( $\int C_i d\tau$  and  $\int C_e d\tau$ ). In effect, concentrations at lower time points are counted more than concentrations at higher time points. In addition, the filtering range of integration is smaller at lower time points due to the smaller span of integration. In other words, the low pass filtering cutoff frequency decreases as time passes. Another problem is that only left side of Eq. 6.1 is effectively low pass filtered. Therefore, in our experiments, we used Eq. 5.17 to form the matrix of coefficients. However, the concentrations were low pass filtered prior to fitting the kinetic parameters. The experiments on our simulation phantoms supported this choice.

The analysis was carried out by the Matlab programs described in section 6.3. The results of all the kinetic parameters estimations were saved in separate files. A separate program read all the result files and obtained the mean, standard deviation, minimum and maximum of the kinetic parameters estimated by each analysis method in each tissue type and experiment.

### 6.10.3: Results

As mentioned in section 6.10.1, all the kinetic parameter estimations are tabulated in appendix 6.A.5. The mean values of  $k_{ep}$  and  $v_e$  for each tissue type are plotted in Fig. 6.11-6.16. Each experiment is indicated by its reference number. In the case of  $k_{ep}$ , the six analysis methods and in the case of  $v_e$ , four analysis methods are plotted next to each other for each experiment in order. The error bars indicate the standard deviation of the estimations among the ROIs that were used for the estimations. The standard deviation is affected by the heterogeneity of the estimated kinetic parameter and the consistency of the analysis methodology within the ROIs considered for the

estimation. According to section 5.5.6, the expected value of  $k_{ep}$  in tumor and healthy tissue are on the order of  $8 \times 10^{-4} \text{ s}^{-1}$  and  $3 \times 10^{-4} \text{ s}^{-1}$  respectively.

As mentioned, the obtained results are not very reliable due to the signal fluctuations; however, initial analysis of the data is done here. The dose of MA injection in experiments 1-4 was 45-52 mg/mouse. The maximum dose was applied in Experiment 4. The dose of MA in experiments 5-6 and 7-8 were 30 and 15 mg/mouse, respectively. Lower dose of MA reduces  $T_2$  effect and avoids complications by the non-linear signal-concentration relation in MRI. However, as mentioned in section 5.7.3, at lower concentration of MA, the contrast created by the extravascular signal in T\_ROI, is small compared to the intravascular signal in the capillaries. The kinetic parameters estimated in the later experiments are less reliable than earlier experiments as indicated by the negative  $v_e$  and  $k_{ep}$  estimates. The most consistent results were obtained in experiment 4 with the highest dose of MA. We believe the reason for better results at higher dose of MA, is the higher value of the extravascular signal. However, definitive conclusions could not be made due to the small number of experiments.

Cancelling the intravascular content of extravascular ROIs in MRI (analysis methods 2 and 4) proved ineffective in healthy tissue in most cases. This is probably due to vessel size change and possibly, water exchange. As a result of water exchange, the MA in capillaries enhances the signal in the extravascular region as well.

Overall, optical methods generated more consistent and physically reasonable results than MRI methods. MRI images had lower signal to noise ratio, spatial resolution and temporal resolution than optical images. In addition, signal fluctuations in most experiments were more significant in MRI than optical imaging. The non-linear signal concentration relation is exasperated by partial volume effect in estimating intravascular concentration. Among optical methods, analysis method 6 was more reliable than analysis method 5 in measuring vascular kinetics in the tumor. It was usually not possible to find isolated vessels in the tumor region. Therefore, method 5, which relies on small distinguishable vessels within tissue with uniform thickness, was not easily applicable to tumor regions.

The results are particularly poor in the tumor regions. The reason is that the tumors had very high vascular content. As a result, the extravascular signal was not easily detectable in tumors. In optical images, higher tumor thickness reduced the image resolution and might have caused saturation of the fluorescent signal due to the tissue absorption of light.

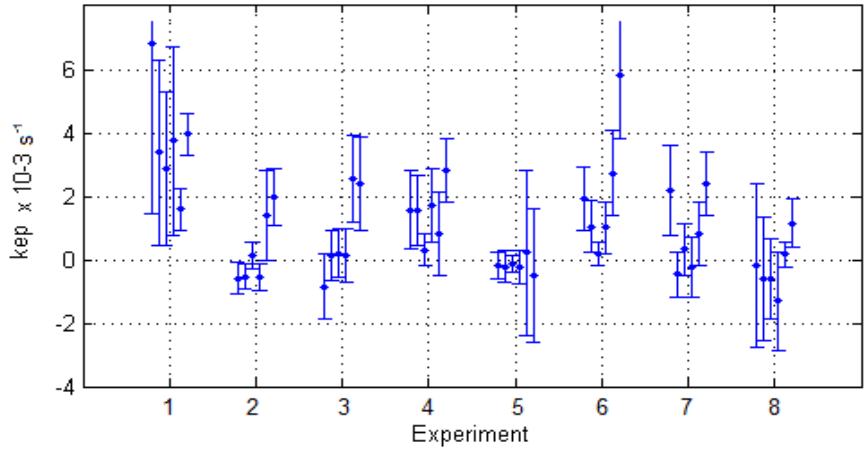


**Fig 6.11.**  $k_{ep}$  in healthy tissue

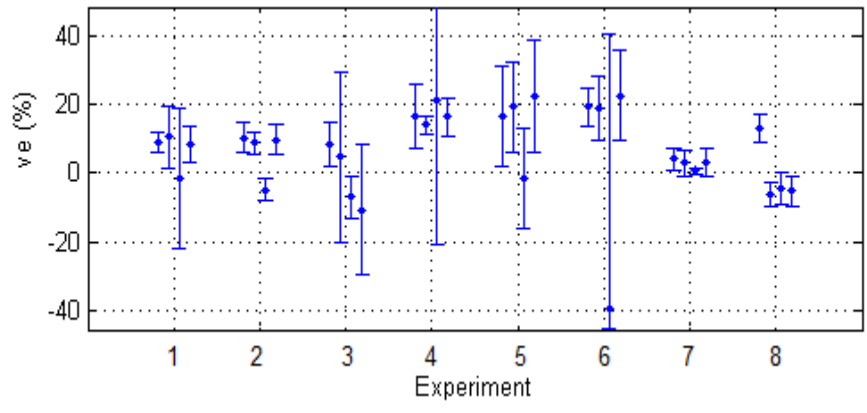


**Fig 6.12.**  $v_e$  in tissue

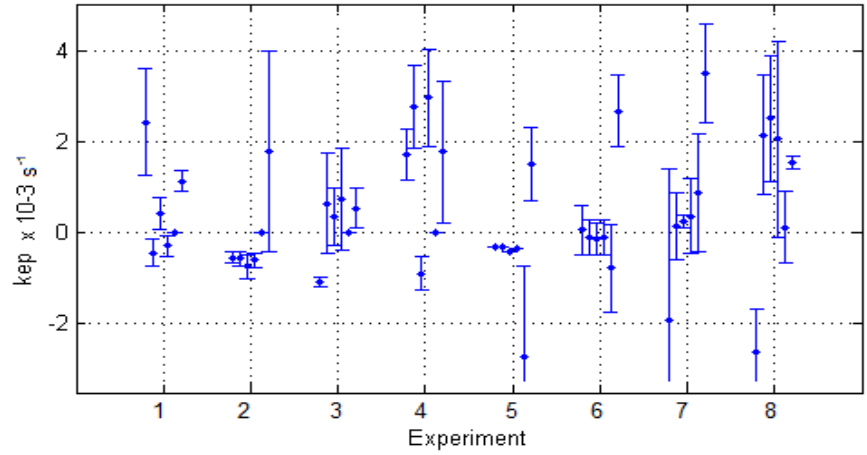


**Fig 6.13.**  $k_{ep}$  in tumor center

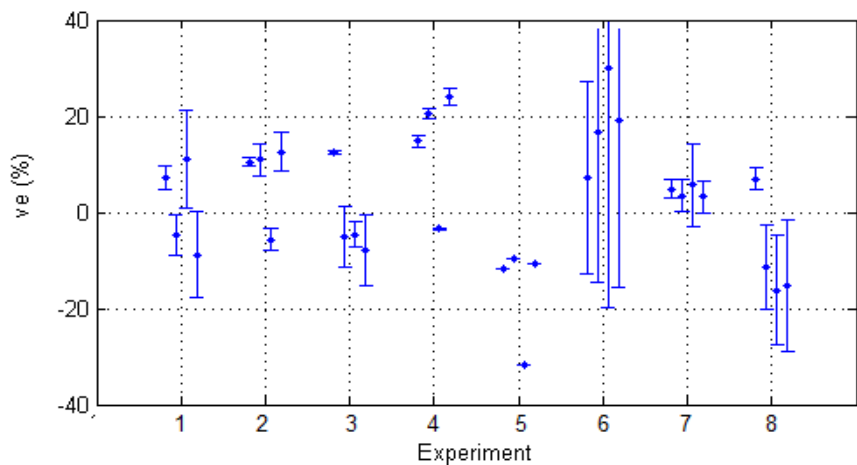


**Fig 6.14.**  $v_e$  in tumor center

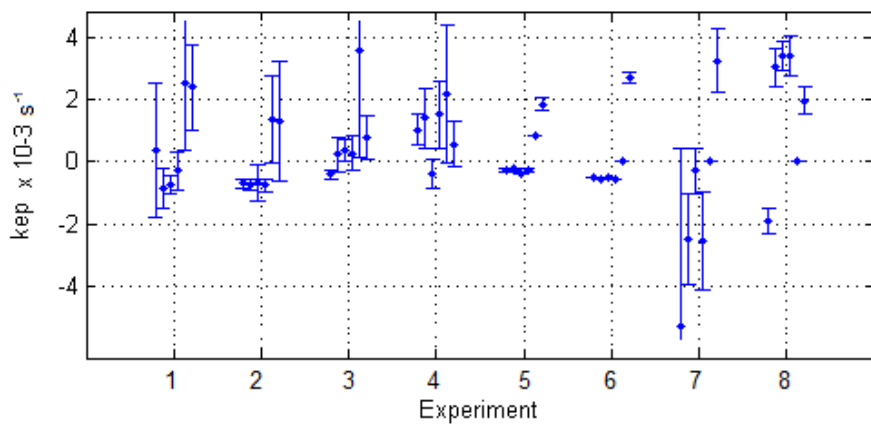


**Fig 6.15.**  $k_{ep}$  in tumor edge

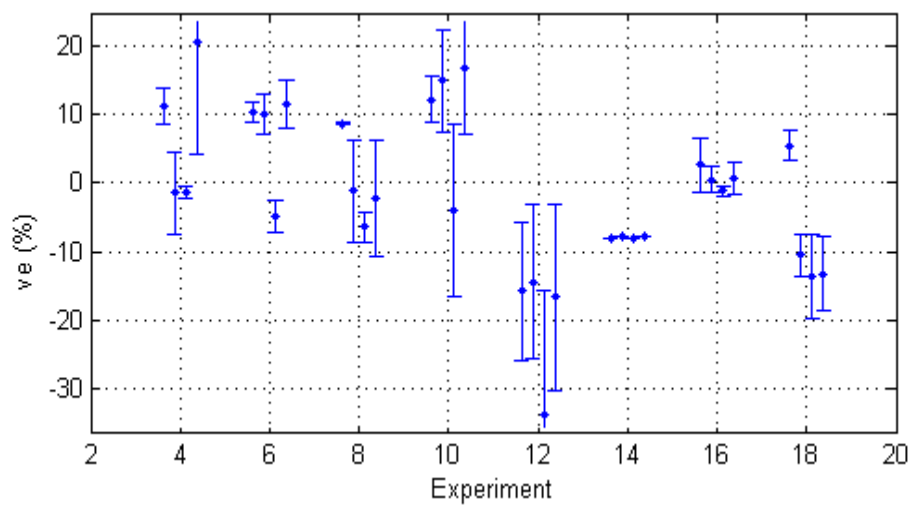


**Fig 6.16.**  $v_e$  in tumor edge

## 6.11: Diffusion Weighted Imaging (DWI)

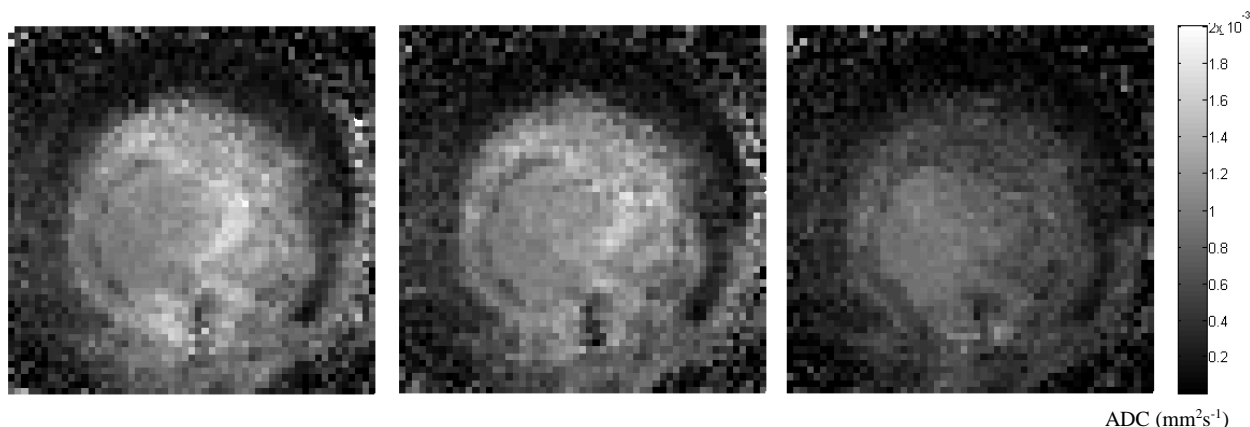
As described in section 5.8, the intravascular and extravascular components of the signal might be separable by diffusion weighted imaging. The theory was described in section 5.8.1. The exact applied sequence was summarized in section 5.8.2 and the applied methodology to separate the intravascular and extravascular signal by DWI was described in section 5.9.3. Here, the theory is tested in an experiment to examine its applicability in future studies. Similar results described in this section, were obtained in two other experiments as well.

In Fig. 6.17 the ADC values estimated by fitting the higher b values ( $b= 200, 400, 800$ ) to the diffusion signal equation, along three perpendicular axes, are shown. The estimated values are expected to correspond to the diffusion of water protons and not perfusion. After removing the slow diffusing component from the DWI signal according to Eq. 5.38, the remaining signal ( $S_v$  in Eq. 5.38) was fitted to the lower b values ( $b=0, 20, 40, 60, 80, 100$ ), along three orthogonal axes. The ADC values in Fig 6.18 are expected to represent only the perfusion of water protons. In larger vessels, the obtained value depends on the direction of the applied gradient due to the directional flow effect as described in section 5.8.1.

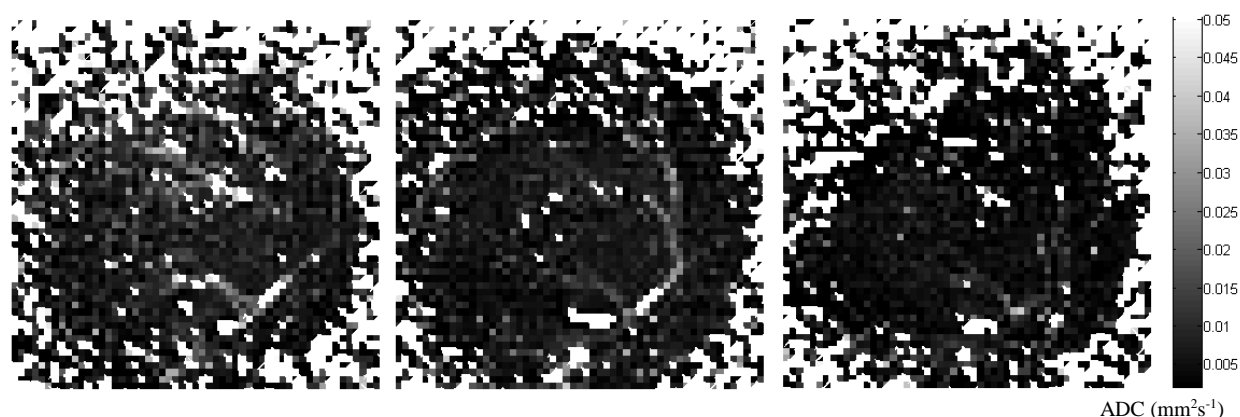
The intravascular signal distribution was obtained by DWI along three orthogonal axes according to the procedure described in section 5.9.3. The obtained results are shown in Fig 6.19. The signal in larger vessels are expected to depend on the direction of diffusion gradient. However, away from large vessels, the obtain vessel signal distribution is expected to be independent of the direction of the applied diffusion gradient.

Fig 6.20 compares the intravascular signal distribution obtained by three methods: 1) by averaging the intravascular signal obtained by DWI along three orthogonal axes 2) by using the signal change in MRI after injection of the MA according to section 5.7.2, and 3) by using the signal change in optics after injection of the MA. The FOV of optical image is smaller than MRI images. The reason is that MRI images have larger FOV than the window chamber and also that skin had covered a small region of the window chamber.

While the intravascular distribution obtained by DWI has some resemblance to the actual intravascular distribution, it is certainly far from accurate. Particularly, the diffusion method is not able to detect the small vessels in the tumor. The reason might be the slow perfusion of the blood in tumor vasculature. As mentioned in section 5.8.1, in order to map the vessels with DWI accurately, more b values are required, particularly at higher range of b values. In addition, the image distortion caused by strong DWI gradients, needs to be compensated.



**Fig. 6.17.** ADC estimates by fitting high  $b$  values to the diffusion signal equation ( $b = 200, 400, 800$ ). The obtained ADC values represent water proton diffusion in the tissue along three orthogonal axes. The gradient in the right image is along the window chamber thickness. (Experiment 8: 0254-R1-3, 7/24/2012). The scale bar unit is  $\text{mm}^2\text{s}^{-1}$ .



**Fig. 6.18.** ADC estimates by fitting low  $b$  values to the diffusion signal equation ( $b = 20, 40, 60, 80, 100$ ). The obtained ADC coefficient represents water proton perfusion in the tissue along three orthogonal axes. The gradient in the right image is along the window chamber thickness. (Experiment 8). The scale bar unit is  $\text{mm}^2\text{s}^{-1}$ .

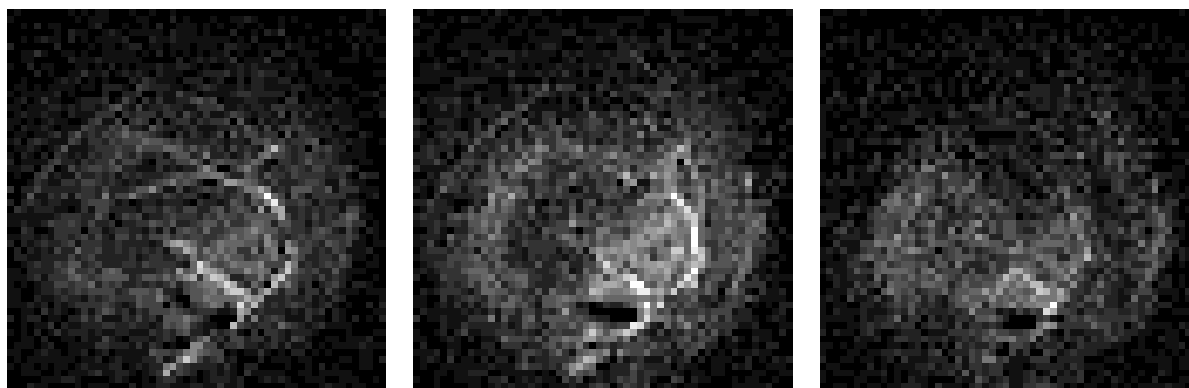


**Fig. 6.19.** Vessel distribution obtained by using the diffusion weighted images with diffusion gradient along three orthogonal axes according to the procedure described in section 5.8.2. (Experiment 8).



**Fig. 6.20.** Vessel distribution obtained by using the diffusion weighted images with diffusion gradient along three orthogonal axes according to the procedure described in section 5.8.2. (Experiment 8).

## CHAPTER 7: FUTURE DIRECTIONS

### 7.1: Overview

In this chapter, suggestions are made for future directions of this research. Future directions are aimed at improving the imaging system, improving the experimental protocols, modifying the MA, and also applying the dual modality imaging system in new studies.

The imaging system could be made more physically stable and resistant to environmental factors such as temperature, humidity and external forces. Suggestions to improve the imaging system are offered in section 7.2.

The main problem in the application of the dual modality imaging system to measure vascular kinetic parameters was signal fluctuation. We believe the signal fluctuation was caused by vessel size changes and hot air blowing on the window chamber. To tackle this problem, data collection should be done with some modifications. This issue is discussed in section 7.3.

Vascular permeability measurement was difficult because of the very low leakage of the MA in the extravascular tissue both in tumor and healthy tissue. To tackle this problem, a smaller MA should be applied. Another problem in measuring vascular permeability with optical imaging, particularly in tumors, was tissue thickness. Suggestions to modify the MA and animal model are offered in section 7.4.

Simultaneous MR and optical imaging facilitates combining the data in one analysis. In section 7.5, suggestions are made to take advantage of this capability for dual modality imaging in measuring vascular permeability and in other applications. The conclusions for future directions of this research are summarized in section 7.6.

### 7.2: Instrumentation

As mentioned in chapter 3, the optical imaging system was made from FullCure720 photopolymer using an Objet 3D printer (Objet Ltd., Object Connex350). The imaging system is subject to hot air, tensile stress, particularly flexural tensile stress, and possibly changing humidity. In many experiments, the bending of the system, caused by stress and heat, shifted the images. The imaging system would be more stable if it was made from a material with higher flexural and tensile modulus, lower water absorption, and lower thermal expansion coefficient. There are materials for the 3D Objet printer, such as FullCure850, that have better stability specifications than FullCure720 [1]. In addition it is possible to machine the device from stiffer non-magnetic material.

A major problem with the dual modality imaging system was hot air blowing on the animal and the MRI surface coil. In later experiments, hot air flow was redirected so that it passed under the mouse and only reached the animal after it had been more uniformly distributed in the MR scanner

bore. We still believe that the hot air was a cause for signal fluctuation and that it would be advantageous to further reduce the hot air flow around the animal. An alternative way to control the temperature is by a hot water flow system that runs under the mouse.

Another issue with the imaging system was illumination uniformity. As mentioned in section 4.6.3, laser light illumination intensity varied  $\pm 15\%$  across window chamber. While the analysis methods that were carried out to measure vascular kinetic parameters were not sensitive to illumination non-uniformity, in other applications illumination uniformity might be important. In addition, as will be discussed in section 7.5.1, comparison of optical and MRI images can become difficult as a result of illumination non-uniformity. The simplest solution to this issue is to increase the NA of the illumination beams or the illumination fiber distance to the window chamber, so that the window chamber resides only at the center of the illumination beam. This allows for a more uniform part of the optical beam to illuminate the window chamber.

The developed optical imaging system is not capable of optical sectioning. Converting the system to a confocal microscope configuration is possible, but difficult and costly [2, 3]. The difficulty rises because the entire system must be made from non-magnetic materials. Another option is to use computational optical sectioning microscopy (COSM) [4, 5]. To do this, first the system must be rigid and stable. Second, the camera must be mounted on a motorized stage. Since the camera resides outside of the MRI scanner, it is not as difficult to implement COSM methodology.

### **7.3: Experimentation**

A major issue with the experiments attempting to measure vascular kinetic parameters was signal fluctuation. As discussed in section 6.9.3, there are several possible causes for signal fluctuation such as temperature and anesthesia level variation. To remove these factors, it is important to maintain animal physiological and environmental conditions as constant as possible during the experiment. It is also important to inject the MA when the animal is in a stable physiological situation; for example, its body temperature is not changing. In many experiments, the MA injection induced a shock in the animal. To minimize this shock, it is advised to lower the dose of the MA and purify the MA as much as possible from residual salt, which is added during the MA labeling process. Suggestions for improved MA preparation are discussed in section 7.4.

While maintaining animals at constant environmental and physiological condition is desired, it is not always possible to do so. Therefore, it is important to record all environmental and physiological variables that are measured throughout the experiment. One issue in studying temperature effects on signal intensity was that the temperature was monitored in the mouse rectum and not at the window chamber. Temperature change at the surface of the body causes vasodilation and vasoconstriction. In addition, temperature change might change the surface coil sensitivity. Therefore, it is important to monitor the temperature at the window chamber as well as inside the animal body.

## 7.4: MA and Animal Preparation

Several experiments failed because the animal died after the injection of the MA or there was too much free Alexa Fluor dye in the injected solution. In many cases, the animal reacted to the injection of the MA by erratic breathing and heart rate variation. It is important that gel filtration of the MA is done precisely. As mentioned in section 2.3, we used prepacked desalting columns for gel filtration. These columns had shorter length than recommended by Life Technologies and in many cases, the boundary between the free dye and labeled protein was not quite clear. We were unsuccessful in our last attempt to label the MA with Alexa Fluor dye for unknown reasons. It is recommended that an experienced synthetic chemist monitors the labeling of the MA and other chemical processes that are carried out.

A major difficulty in measuring vascular permeability of the applied MA was very low leakage of the MA in the tissue. Testing the methodologies of measuring vascular permeability, would be easier if the MA had a higher leakage rate. However, if the MA extracts from the vasculature too fast, it would not be easy to find the intravascular distribution by comparing the signal before and after the injection of the MA. The new MA should have enough suitable binding sites to be labeled effectively with both Alexa Fluor and Gd-DTPA.

Tracking the vessels throughout the experiment, even in the presence of signal fluctuations, might be possible by injecting and monitoring a second MA that stays entirely intravascular throughout the experiment [6]. To do this, the strictly intravascular MA must be labeled with a fluorophore that has different fluorescence emission wavelength than the one used for measuring the vascular kinetic parameters. The illumination system would need to be modified accordingly. The strictly intravascular MA cannot be labeled with MRI CA, since it is not easily possible to separate contrast enhancement from two different MAs in MRI.

As mentioned in section 4.6.3, measuring vascular kinetics in tumors was difficult due to the out of focus light. Both in tumor and in healthy tissue, the optical resolution was limited by the depth of the tissue. If the window chamber limits the thickness of the tissue, as done by Wu, et al. [7], higher resolution optical images could be obtained.

Some tumors have leakier vessels. PC-3 tumors have relatively low permeability to large molecules [8]. By implanting tumors with leakier vessels, it would be easier to measure signal extravasation at least in the tumor.

## 7.4: DCE-MRI

In section 5.7.5, a new methodology was introduced to separate intravascular and extravascular MRI signals. One problem with the application of this method was the high MA injection dose. However, the more important problem in applying this method was signal fluctuation. This method could be tested in the future by injecting a lower dose of MA and avoiding signal fluctuation by better control of the experiment.

DWI was introduced in section 5.8 as a possibility to differentiate intravascular and extravascular MRI signal. While the initial studies were able to separate the intravascular and extravascular signals to some extent, a higher number of diffusion b values can potentially improve the results as described in other studies [9, 10]. In addition, it is necessary to either compensate image distortions caused by strong diffusion gradients or use special DWI sequences that reduce the signal distortions caused by the diffusion gradients [11, 12]. If DWI is successful in separating intravascular and extravascular signal, it could be used to solve the issue of the partial volume effect in DCE-MRI.

## **7.5: Simultaneous Dual Modality Imaging Applications**

### **7.5.1: Measuring Vascular Kinetic Parameters**

MRI and optical imaging can potentially be combined in measuring vascular permeability. In section 4.6.3, it was asserted that measuring  $K_{trans}$  with optical imaging is not readily possible due to the difficulty in measuring capillary to tissue volume ( $V_{cv}/V_T$ ). However, measuring  $V_{cv}/V_T$  might be possible with successful application of DWI in MRI or the methodology of section 5.7.5.

The intravascular signal distribution was found with both modalities as described in sections 4.3 and 5.7.2.2. As mentioned in chapter 5, the obtained intravascular signal distribution with DCE-MRI might not be proportional to intravascular proton density, due to water exchange between microvessels and extravascular tissue. The obtained intravascular distribution by optical imaging could be used to verify the intravascular distribution obtained with MRI. One problem is that in optical imaging, the intravascular signal is proportional to plasma volume whereas in MRI, unless the dose of MA is very low, the intravascular signal is dependent on total blood volume, due to the fast water exchange between plasma and hematocrit. Another issue is that the optical illumination was not strictly uniform. In order to have precise comparison, both imaging modalities must have uniform sensitivity within the window chamber.

It is concluded from the previous discussions that measuring vascular kinetics is more readily possible with lower doses of MA. However, as discovered in section 6.10.3, at lower doses of MA, the extravascular signal is too low and estimating vascular kinetic parameters is usually not accurate. Therefore, the dose of MA should be selected based on vascular permeability to the applied MA.

### **7.5.2: Other Applications**

As mentioned in section 1.2, simultaneous MRI and optical imaging can allow for estimating more physiological parameters in one study. Both MRI and optical imaging have been applied to estimate many physiological parameters of the tumor microenvironment [13, 14]. Therefore, the two modalities could be combined in one study for validation of estimations of a single physiological parameter or to find the interconnection of multiple parameters. Apart from

comparative and complementary studies, simultaneous imaging can reduce the invasiveness of the experimentation by reducing anesthesia time and other therapeutic or surgical interventions.

## **7.6: Conclusions**

Simultaneous MRI and optical imaging allows for less invasive and more accurate study of tumor microenvironment by simultaneous measurement of multiple physiological parameters or more exact estimation of a single physiological parameter. The benefit of simultaneous measurement is more in applications where experimental variability or invasiveness makes sequential measurement problematic. New applications of dual modality imaging system should be verified with experts in the area of cancer biology and physiology.

While many steps were carried out in this research to show that simultaneous MRI and optical imaging is a useful tool in the study of tumor microenvironment, improvements in the animal model, MA preparation, instrumentation, and the experimental protocol, are necessary to conclusively demonstrate the advantage of this novel combination of imaging modalities. Collaboration of specialists in the areas of cancer biology, chemistry, imaging and engineering is necessary in the further steps to bridge application, instrumentation, and experimentation in an efficient way.

## APPENDIX

### Appendix 5.A.1: Exact Solution to the Modified Bloch Equation

The exact solutions to the modified Bloch equations for a nuclear species which is in exchange between two compartments [6] are as follows [7]:

$$1/T_1 = A_1 \pm \{A_1^2 - [(1/\tau_{1A}\tau_{1B}) - (1/\tau_A\tau_B)]\}^{1/2}, \quad (5.A.1)$$

$$1/T_2 = A_2 \pm \frac{1}{\sqrt{2}}\{G + (G^2 + H^2)^{1/2}\}^{1/2}, \quad (5.A.2)$$

$$\omega = [(\omega_A + \omega_B)/2] \pm \frac{1}{\sqrt{2}}[-G + (G^2 + H^2)^{1/2}]^{1/2}, \quad (5.A.3)$$

Where:

$$A_1 \equiv \frac{1}{2}(1/\tau_{1A} + 1/\tau_{1B}),$$

$$A_2 \equiv \frac{1}{2}(1/\tau_{2A} + 1/\tau_{2B}),$$

$$G \equiv \frac{1}{4}(1/\tau_{2A} - 1/\tau_{2B}) + 1/\tau_A\tau_B - \Delta\omega_{AB}^2/4,$$

$$H \equiv \frac{1}{2}(1/\tau_{2A} - 1/\tau_{2B})\Delta\omega_{AB},$$

$$1/\tau_{1A} \equiv 1/T_{1A} + 1/\tau_A,$$

$$1/\tau_{1B} \equiv 1/T_{1B} + 1/\tau_B,$$

$$1/\tau_{2A} \equiv 1/T_{2A} + 1/\tau_A,$$

$$1/\tau_{2B} \equiv 1/T_{2B} + 1/\tau_B,$$

$$1/\tau_{AB} \equiv 1/\tau_A + 1/\tau_B,$$

$$\Delta\omega_{AB} = \omega_A - \omega_B,$$

$\omega_A, \omega_B$ : Resonance frequency of water protons in compartments A and B,

$\tau_A, \tau_B$ : mean resident time of water protons in compartments A and B.

### Appendix 5.A.2: Estimating MA Concentration in the IV and EV Compartments

Assuming the blood volume 7% of mouse weight:

$$V_b \approx 0.07 \times 27 \text{ mg} = 1.9 \text{ ml}$$

Plasma volume is about 60% of blood volume:

$$V_p \approx 0.6 \times 1.9 \text{ ml} = 1.13 \text{ ml}$$

Molar weight of the injected MA when 5, 15, 30 or 45 mg of MA is injected:

$$MA_{MW} = \frac{[5 \ 15 \ 30 \ 45] \times 10^{-3}}{86.2 \times 10^3} = [0.058 \ 0.17 \ 0.35 \ 0.52] \mu\text{mol}$$

Concentration of the MA in the plasma at t=0:

$$C_i(0) = \frac{MA_{MW}}{V_p} = [0.051 \ 0.15 \ 0.31 \ 0.46] \text{ mM.}$$

$$C_v(0) = \frac{C_i}{V_b} = [0.031 \ 0.092 \ 0.18 \ 0.28] \text{ mM.}$$

At t= 30 min

$$C_i(30\text{min}) = C_i(0\text{min})e^{-t/\tau_{cl}} = [0.9 \ 2.8 \ 5.6 \ 9.4]$$

According to Eq. 5.13 at t=30 min:

$$C_e(30\text{min}) = [0.8 \ 2.3 \ 4.7 \ 7.8]$$

$\Delta(T_1^{-1})$  and  $\Delta(T_2^{-1})$  are obtained based on the relaxation rates measured in chapter 2 at different concentrations of MA.

### Appendix 5.A.3: Guided Bi-Exponential Fitting to the T<sub>1</sub> Sequence Signal

In order to avoid unrealistic results, the obtained vessel map in section 5.7.5.2 can potentially be used to guide the double exponential fitting described in section 5.7.5.4. To do this, two regions are selected. These regions will be called ROI1 and ROI2.  $T_{1n}$  is found according to the method described in section 5.7.5.3 in both ROIs. The value of  $T_{1v}$ ,  $\rho_v$  and  $\rho_n$  are then simultaneously found in ROI1 and ROI2, so that the ratio of  $\rho_v$  in the two ROIs, is in accordance with the intravascular signal distribution obtained as described in section 5.7.5.2. Mathematically, the following equations are solved simultaneously by using the T<sub>1</sub> sequence data:

$$S_1 = \rho_{v1} \left(1 - e^{-\frac{TR}{T_{1v}}}\right) + \rho_{n1} \left(1 - e^{-\frac{TR}{T_{1n}}}\right) \quad (5.A.4)$$

$$S_2 = \rho_{v2} \left(1 - e^{-\frac{TR}{T_{1v}}}\right) + \rho_{n2} \left(1 - e^{-\frac{TR}{T_{1n}}}\right) \quad (5.A.5)$$

$$\frac{\rho_{v1}}{\rho_{v2}} = K, \quad (5.A.6)$$

where K is a constant that is obtained from Eq. 5.30.

### Appendix 6.A.1: Experiments

Each experiment is described in 4 rows and 2 columns. In the first column for each experiment qualitative ratings between 0-5 are shown for the entire experiment, the mouse physiological conditions and the implanted tumor, the MR imaging and the optical imaging from up to down, respectively.

In the second column, the first row is the experiment date and name, followed by a short description of the experiment. The following rows describe the mouse physiological condition, the MRI imaging situation and the optical imaging situation respectively.

<b>2.0</b>	<b>2010-08-11 0563-L1 Dead Mouse</b>
2.0	Mouse: Very good tumor and vasculature. However, a little bit skin on the edge of the window chamber.
1.5	MR: data incomplete and very bad contrast.
2.0	Optics: reasonably clear images, however significant image shift made the image out of focus + sequence was very short (113 frames).
<b>4.3</b>	<b>EXP 1: 2010-08-13 0563-R2</b> The two sequences were well correlated. The signal on the vessel oscillated a little bit.
5.0	Mouse: very good tumor and vasculature.
5.0	MR: Good MR data, TR (100,200...) RARE factor = 2 in the dynamic sequence.
3.5	Optics: Signal contrast appeared suddenly after increasing integration time. Excellent resolution. Signal on one vessel saturated at later times. After 3 minutes of the regular dynamic sequence, additional sequential optical images were taken with very good quality.
<b>2.0</b>	<b>2010-08-16 0564-R2-2</b>
3.5	Mouse: small tumor, good vasculature.
1.0	MRI: good quality image, but no contrast agent.
2.0	Optics: Vessels were very unclear. It seems that light is leaking to the system. As time passes, the images get brighter. Contrast is good
<b>2.0</b>	<b>2010-8-23 0564-R1-2</b>
3.0	Mouse: small but clear tumor.
4.5	MRI: Good images, clear contrast on vessels.
2.0	Optics: High quality images, but only 100 frames after injection of the MA.
<b>2.5</b>	<b>2010-10-22 0852-00</b>
2.0	Mouse: Good vessels and clear tumor, but mouse died 1-2 min after injection.
4.0	MRI: Good images but vessels not very clear.
2.5	Optics: 1020 frames but 118 Frames/min, experiment took only 9 minutes. The largest vessel was saturated. In notebook it is mentioned the imaging was done for 34:04 min every 2s, integration time = 378.92ms.
<b>3.7</b>	<b>2010-10-25 0852-R1-1</b>
3.5	Mouse: The tumor is small, the chamber is not very clear in trans-illumination.
5.0	MRI: Very clear image sequence.

3.0	Optics: The integration time was adjusted a few times. The chamber moved downward throughout the experiment. In notebook it is mentioned that the MA leaked out too much. But I did not see it in the recorded images.
<b>2.0</b>	<b>2010-10-27 0852-R1-2</b>
1.5	Mouse: died almost immediately. MA from the previous experiment had remained in the tissue.
3.5	MRI: Vessels were not very clear. It might be the effect of the remaining MA in the tissue from the previous experiment.
3.0	Optics: Camera moved a lot. Some vessels were saturated. Integration time changed once, there was residual MA from the previous experiment.
<b>3.0</b>	<b>2010-12-09 0980-R2, 50mg MA injected</b>
5.0	Mouse: excellent tumor.
4.5	MRI: good images.
1.0	Optics: only 42 images after injection. Signals in vessel were saturated.
<b>4.3</b>	<b>EXP 2: 2010-12-13 0980-00</b> overall it appeared that the signals from the two modalities were out of phase. 45mg MA injected, temperature before injection: 34-35 °C.
4.5	Mouse: Good tumor with necrotic and growing regions, good vasculature,
4.5	MRI: good images.
3.0	Optics: 3:08 min of data was lost (1:04-4:12), integration time changed twice, some signal saturation existed at the beginning of the experiment.
<b>4.5</b>	<b>EXP 3: 2010-12-15 0980-00-2.</b> Signal Oscillations were mostly in phase. Optical signal dropped throughout the experiment, but MRI signal did not. Both MRI and Optical signals oscillated a lot. Oscillations were in phase. Then optical signal dropped significantly, but the MRI signal first stayed constant and after a while dropped gradually. 42 mg MA injected.
4.5	Mouse: Good tumor with necrotic and growing regions, good vasculature.
4.5	MRI: very good images, but a big signal drop around frame 20.
4.5	Optics: very clear images, extra dynamic images were taken for the duration of 4 minutes, after the regular dynamic sequence.
<b>4.8</b>	<b>EXP 4: 2010-12-17 0980-00-3,</b> signal oscillations were, to a good approximation, 180 out of phase. 51mg injected, temperature before injection: 36-36.9 °C.
4.5	Mouse: same mouse as EXP 3, excellent focus.
5.0	MRI: very good images, but a strong dip at frame 16, a lot of oscillation.
5.0	Optics: Very clear images.
<b>3.5</b>	<b>2011-12-15 0554-R1</b> one oscillation that took 30 min. The oscillation was mostly out of phase between the two modalities. Temperature before inject = 35.4°.
4.5	Mouse: huge tumor.
4.5	MRI: good signal, good vessels.
2.5	Optics: Good resolution, integration time changed @ 2365s, 9min:30s lost, starting at 2min:50s after experiment started, focus could have been better.
<b>3.8</b>	<b>EXP 5: 2011-12-19-1 554-00,</b> both Optics and MRI showed clear accumulation of MA in the tumor, temperature before injection =37.2, MA 36.2mg.
4.0	Mouse: Good tumor, OK vasculature, mouse weight = 29g.
5.0+	MRI: Low signal fluctuations, high MA accumulation in the tumor!
3.5	Optics: Acceptable resolution, intensity changed twice (must be fixed), almost no signal fluctuation, frames lost between 2:50 to 12:16 (9:26 lost). Frame rate: 1 every 2 seconds after t=12:16 (3s before t=2:50). Optical integration time was different before t=2:50 and after t=12:16.
<b>3.5</b>	<b>2011-12-19-2 0554-R1-2</b>
2.5	Mouse: Huge tumor, skin covered part of the tissue, mouse died at optical sequence fame 335.
4.0	MRI: Vessel signal raised continuously and had one big oscillation prior to the mouse death. Tumor signal raised clearly. Tissue signal raised gradually.
4.5	Optics: OK resolution. Signal gradually raised in the tumor but remained almost constant in the healthy tissue. Except on tumor, focus was not well.
<b>4.0</b>	<b>EXP 6: 2011-12-21-1 0554-00-2,</b> accumulation of MA in the tumor was small, but visible. Vessel signal had some fluctuations first, but afterwards signal fluctuations gradually decreased. Temperature increased by 0.3° during the experiment. 36.4mg MA injected.

4.5	Mouse: Good size tumor, nice vasculature, skin covered the edges of the window.
4.0	MRI: Vessel signal oscillated; there was clearly visible MA accumulation in the tumor. In healthy tissue, signal remained almost constant up to a point, and then suddenly increased. The reason might be MA migration from tumor tissue.
4.0	Optics: very low resolution. Vessel signal peaked at frame 300 and then dropped gradually afterwards. Extravascular signal was either constant, or decreased. In the center of the tumor, the signal increased with time. Frame rate = 1 per 2 seconds. Optical signal collection started 80 s after MRI.
2.0	<b>2011-12-21-2 0554-R2</b> , Excellent accumulation of MA in the tumor. The signal from the two modalities had reverse phase in the vessels.
2.5	Mouse: large tumor, clear vessels, skin penetrated inside the window chamber.
0.0	MRI: No MR image.
4.0	Optics: very clear images with high resolution, signal curves had humps, tumor signal steadily increased. Tissue signal also increased significantly (possibility because of free dye presence in the injected solution) but much less than tumor. Vessel signal also during the dynamic sequence.
4.2	<b>EXP 7: 2012-07-16 0254-R1</b> , respiration and temp monitored; both were steady. 16mg MA injected
4.0	Mouse: large tumor, clear vessels, skin covered the sides of the window chamber. Mouse weight=24.4g..
5.0	MRI: Very good images along with diffusion weighted Images, TE seq..., vessel signal oscillated, tissue did not.
3.0	Optics: clear images, signal oscillated, tumor and tissue signal increased with oscillations. A few minutes after frame 114 are missing.
2.5	<b>2012-07-18 0254-R1-2</b> , exact same injection as previous experiment
4.0	Mouse: Excellent tumor and vasculature, skin covered the edges, Temp increased from 34.7 to 36.3. Resp dropped from 62 to 27, weight=24.4g, 16mg injected.
4.5	MRI: Very good images along with diffusion weighted Images, only 1 TE, oscillation level low b=10 20 30 40 100 200 400 800.
1.5	Optics: very good snaps and initial collection, but then the image totally saturated.
2.0	<b>2012-07-18-2 0254-R2</b> ,
4.5	Mouse: very good vasculature and tumor, skin covered the edges, Temp increased from 35.6 to 37.7. 16mg injected.
4.5	MRI: Very good images, 8 TEs, oscillation level.
0.5	Optics: No white light image, good initial uptake image but then totally saturated.
3.0	<b>2012-07-24 0254-R2-2</b>
4.0	Mouse: good vasculature and tumor, skin covered the right side, Temp increased from 35.3 to 36.5. Respiration dropped from 45 to 42.
5.0	MRI: Very good images along with diffusion weighted Images in three directions, 8 TEs, oscillation level low b=0 20 40 60 80 100 200 400 800 in three directions.
1.5	Optics: MA leaked out very fast -> free dye
4.0	<b>EXP 8: 2012-07-24 0254-R1-3</b> , 16 mg MA injected.
4.0	Mouse: good vasculature and tumor, skin covered one side of the window chamber. Temperature increased from 32.1 to 32.9 during the dynamic sequence. Respiration dropped from 45 s <sup>-1</sup> to 42 s <sup>-1</sup> .
4.5	MRI: reasonable images along with diffusion weighted Images in three directions, 8 TEs, oscillation level low b=0 20 40 60 80 100 200 400 800 in three directions.
4.0	Optics: Sharp image.
2.5	<b>2012-07-26-2 0254-R2-3</b> , 16 mg MA injected.
4.0	Mouse: No image, but mouse has good tumor. Again skin covered part of the tissue. Temperature increased from 32.1 to 33.9. Respiration dropped from 28-29.
4.5	MRI: reasonable images along with diffusion weighted Images in three directions. Small signal fluctuations. 8 echoes.
2.0	Optics: Clear images first, but very fast leakage (free dye).
2.5	<b>2012-10-26 0371-L1-1</b> Temperature changed from 34.7 to 36.9 and afterwards to 35.8. 10 mg MA injected.
2.0	Mouse: Very Nice Tumor and vasculature. Died after injection. Respiration dropped from 25-33.
4.0	MRI: good images along, diffusion, 8 echoes.
4.0	Optics: low contrast, but very sharp images.

## Appendix 6.A.2: MRI Sequences Details for Each Experiment

For each experiment, the details of the T<sub>1</sub>, dynamic and diffusion sequences, if employed, are summarized below. Format of the descriptions are as follows:

[folder numbers = image number in MRI program] MRI Sequence parameters, Ave = number of averages, Rep = number of repetitions. Img mtx = image matrix size by pixels, FOV = field of view, RARE F=RARE factor, N echoes = number of echoes

FOV and img mtx are by default 2.56 x 2.56 x 0.5 cm and 128 x 128 unless specified otherwise.

### 8/11/2010 - 0563-L1-1

[8 9 10 11 12 13] TE = 10.474, TR = [100 200 800 1000 2000 4000], Ave = [8 8 2 2 1 1]  
[14] TR = 250 ms Rep = 85 Ave = 1

### 8/13/2010 0563-R2-1

[6 7 8 9 10 11 12] TE = 10.474 TR = [100 200 500 800 1000 2000 4000] Ave=[8 8 2 2 1 1]  
[13] TR=100, 1 ave, 80 frames  
[16] TR=250, 2 AVE, 65 Rep, , refocus flip = 158.9, RARE F = 2, 128x128

### 8/16/2010 0564-R2-2

[7 8 9 10 11 12 13] TE = 10.747, TR=[100 200 500 800 1000 2000 4000], flip Ang = 180, MSME, Ave =  
[8 8 4 2 2 1 1], Rep = [1 1 1 1 1 1]  
[14] TE =8.207,TR = 250, Flip Ang = 158.9, RARE Fact = 2, Rep = 65,

### 8/23/2010 0564-R1-2

[7] TE = 9.07, TR=[375 750 1500 3000 6000], flip Ang = 180, Rare Fact=2  
[8] TE =8.207,TR = 250, Flip Ang = 158.9, RARE Fact = 2, Rep = 65,

### 10/22/2010 0852-00, Attn 1, 2= 11.4, 21.4,

[7] TE = 9.07, TR=[375 750 1500 3000 6000], flip Ang = 180, Rare Fact=2  
[8] TE =8.207,TR = 250, Flip Ang = 158.9, RARE Fact = 2, Rep = 65,

### 10/22/2010 0852-R1-1 (3.5)

[6] TE = 9.07, TR=[375 750 1500 3000 6000], flip Ang = 180, Rare Fact=2  
[7] TE =8.207,TR = 250, Flip Ang = 158.9, RARE Fact = 2, Rep = 65,

### 10/25/2010 0852-R1-2 (1.5)

[7] TE = 9.07, TR=[375 750 1500 3000 6000], flip Ang = 180, Rare Fact=2  
[8] TE =8.207,TR = 250, Flip Ang = 158.9, RARE Fact = 2, Rep = 65,

### 12/09/2010 0980-R2 (3.0)

[5] TE = 10.747, TR=[250], Ave = 4, MSME  
[6] TE = 9.07, TR=[375 750 1500 3000 6000], flip Ang = 180, Rare Fact=2  
[7] TE =8.207,TR = 250, Flip Ang = 158.9, RARE Fact = 2, Rep = 65,

### 12/13/2010 0980-00 (4.3)

[6] TE = 9.07, TR=[375 750 1500 3000 6000], flip Ang = 180, Rare Fact=2

[7] TE =8.207,TR = 250, Flip Ang = 158.9, RARE Fact = 2, Rep = 65,

**12/15/2010 0980-00-2 (4.8)**

[19] TE = 10.747, TR = 500, MSME, Ave =4

[20] TE = 9.07, TR=[375 750 1500 3000 6000], flip Ang = 180, Rare Fact=2

[21] TE =8.207,TR = 250, Flip Ang = 158.9, RARE Fact = 2, Rep = 65,

**12/17/2010 0980-00-3 (4.8)**

[19] TE = 10.747, TR = 500, MSME, Nave =4, res = 256x256

[20] TE = 9.07, TR=[375 750 1500 3000 6000], flip Ang = 180, Rare Fact=2

[21] TE =8.207,TR = 250, Flip Ang = 158.9, RARE Fact = 2, Rep = 65,

**12/19/2011 0554-00 (3.8) Attn1, 2= 19.6, 29.6, Reciv gain = 64**

[5] TE = 10.747, TR = 500, Ave = 4

[6-13] TE = 10.747, TR = [31.25 62.5 125 250 500 1000 2000 8000], Rep = [16 8 6 4 2 1 1 1], MSME, img mtx = 128x128, @TR=8000 ADC overflow

[14] TE = 10.747, TR = 400, N Rep =1, Res = 64x64, ADC overflow

[15] TE = 10.747, TR=[250], Repts = 80, N echoes = 8, MSME

**12/21/2011 0554-00-2 (4.0) Attn1, 2= 20.1, 30.1, Reciv gain = 64**

[9-16] TE = 10.747, TR = [31.25 62.5 125 250 500 1000 2000 5000], Rep = [16 8 8 4 2 1 1 1], MSME.

[17] TE = 10.747, TR=[250], Rep = 80, N echoes = 8, MSME

[18] TE = 10.747, TR=[500], Rep = 1, Ave = 4, N echoes = 1, MSME, img mtx = 512x512

[19] TE = 10.747, TR=[250], Rep = 1, Ave = 8, N echoes = 1, MSME, img mtx = 128x128

**5/17/2011 0237-R1 (2.3)**

[12] TE = 9.07, TR=[375 750 1500 3000 6000], flip Ang = 180, Rare Fact=2

[13] TE =8.207,TR = 250, Flip Ang = 158.9, RARE Fact = 2, Rep = 65,

**7/16/2012 0254-R1 (4.2) reciv gain = 101, Attn 1,2 = 20.1, 30.1**

[5-12] TE = 10.747, TR=[31.25 62.5 125 250 500 1000 2000 5000], Rep = [16 8 8 4 2 1 1 1], MSME.

[13] TE =10.747, TR = 250, N Rep = 80, MSME, N Echoes = 8

[14] 256x256, MSME, N Rep = 4, N Echoes = 8

**7/18/2012 0254-R1-2 (2.5) reciv gain = 101, Attn 1,2 = 20.1, 30.1**

[5] TE = 10.747, TR=31.25, Ave = 16, 256x256, MSME.

[6-13] TE = 10.747, TR=[31.25 62.5 125 250 500 1000 2000 5000], Ave = [16 8 8 4 2 1 1 1], MSME.

[14] TE =10.747, TR = 250, Rep = 80, MSME, N Echoes = 8

[15] TE =10.747, TR = 250, Ave = 4, 256x256, MSME,

[16 17] JP sequence

[18] TR = 500, TE = 20, DTI Standard b=[19.7 31.6 43.0 54.2 119.4 225.3 433.6 845.0]

**7/18/2012 0254-R2 (2.0) reciv gain = 101,**

[6-13] TE = 10.747, TR=[31.25 62.5 125 250 500 1000 2000 5000], Ave = [16 8 8 4 2 1 1 1], MSME.

[14] TE =10.747, TR = 250, Rep = 80, MSME, N Echoes = 8

[15] TE =10.747, TR = 250, Ave = 4, MSME,

**7/24/2012 0254-R2-2 (3.0) reciv gain = 101, Attn 1,2 = 20.1, 30.1**

[5-12] TE = 10.747, TR=[31.25 62.5 125 250 500 1000 2000 5000], Ave = [16 8 8 4 2 1 1 1], MSME.

[15] TR = 500, TE = 20, DTI Standard b=[5.6 32.3 55.1 77.2 99.0 120.6 226.8 435.6 848.0 5.6 32.3 55.1 77.2 99.0 120.6 226.8 435.6 848.0 5.6 32.4 55.2 77.3 99.1 120.7 227.0 435.8 848.3]

[14] TE = 10.747, TR = 250, Rep = 80, MSME, N Echoes = 8

[16] TE = 10.747, TR = 500, Ave = 4, MSME,

[17] JP sequence

**7/26/2012 0254-R1-3 (4.0)** reciv gain = 101, Attn 1,2 = 20.1, 30.1

[7-14] TE = 10.747, TR=[31.25 62.5 125 250 500 1000 2000 5000], Ave = [16 16 8 4 2 1 1 1], MSME.

[16] TR = 500, DTI Standard b=[5.6 32.3 55.1 77.2 99.0 120.6 226.8 435.6 849.0 5.6 32.3 55.1 77.2 99.0 120.6 226.8 435.6 848.0 5.6 32.4 55.2 77.3 99.1 120.7 227.0 435.8 848.4]

[15] TE = 10.747, TR = 250, Rep = 80, MSME, N Echoes = 8

### 2/27/2013 Microtube Phantom

[2] TE = 10.747, N TE = 4, TR = 250, Rep = 4, Ave = 1, MSME. Img mtx = 256x256

[3-5] TE = 10.747, N Echoes = 4, TR = [500 1000 2000], Ave = 1, Rep = 1, MSME. Img mtx = 256x256

## Appendix 6.A.3: Estimated T<sub>1</sub> Values (ms)

Mouse	Healthy	Tumor	Vessel	TRs <sup>1</sup>
<b>0563-R2-1</b>	1018	1649	1656	Seq 1
<b>0980-00-1</b>	1825-1938	1754	1447-1689	Seq 2
<b>0980-00-2</b>	1254-1314	1400	1540	Seq 2
<b>0980-00-3</b>	1200	1350	1415	Seq 2
<b>0554-00<sup>2</sup></b>	1750	1900-2050	1500	Seq 3
<b>0554-00-2</b>	1000	1350-1500	1100	Seq 4
<b>0254-R1</b>	1380	1480	1380-1500	Seq 4
<b>0254-R1-3</b>	900-1200	1600-1800	1150	Seq 4

<sup>1</sup>Seq 1: TR = [100 200 500 800 1000 2000 4000]

Seq 2: TR = [375 750 1500 3000 6000]

Seq 3: TR = [31.25 62.5 125 250 500 1000 2000 8000]

Seq 4: TR = [31.25 62.5 125 250 500 1000 2000 5000]

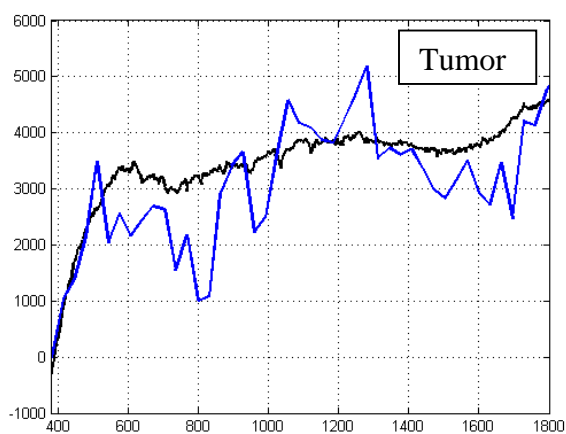
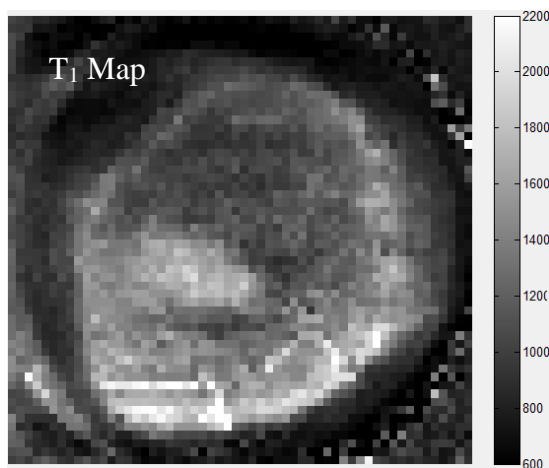
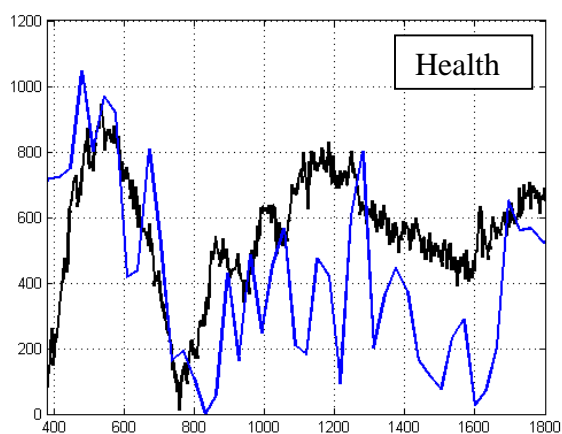
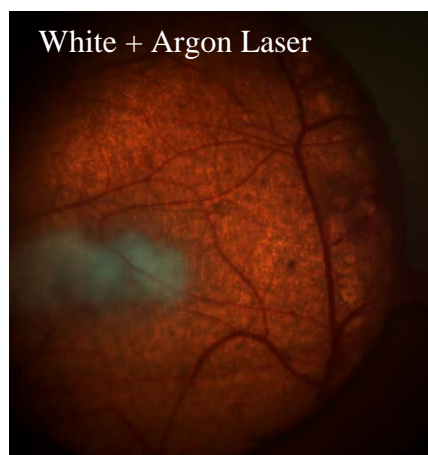
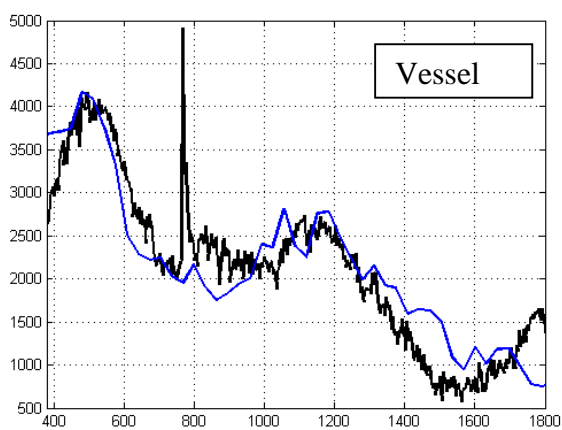
<sup>2</sup>Due to ADC overflow at TR = 8000, the result might be biased.

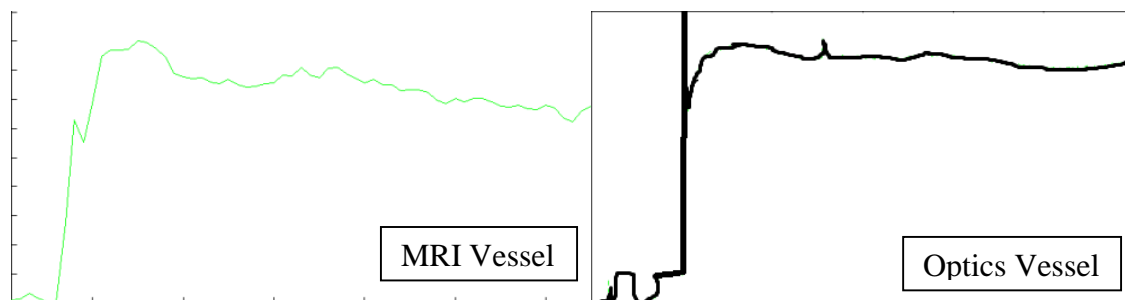
## Appendix 6.A.4: Comparison of MRI and Optical Signal Intensity

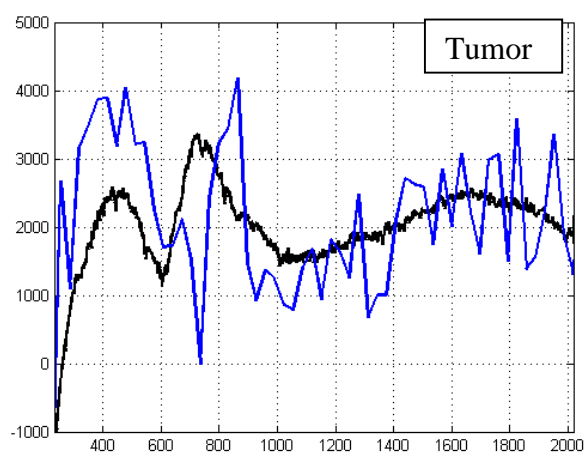
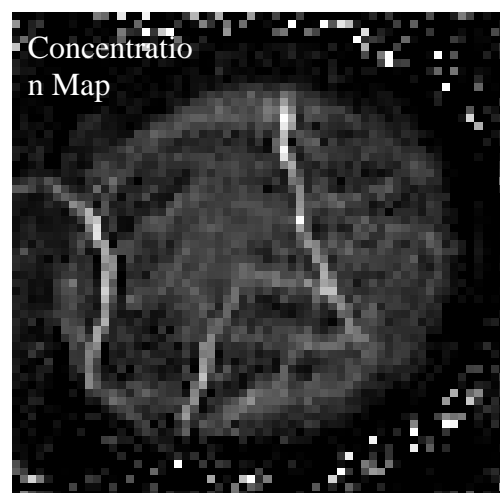
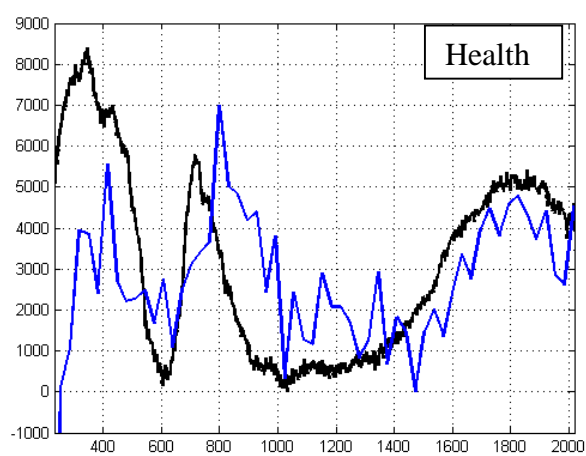
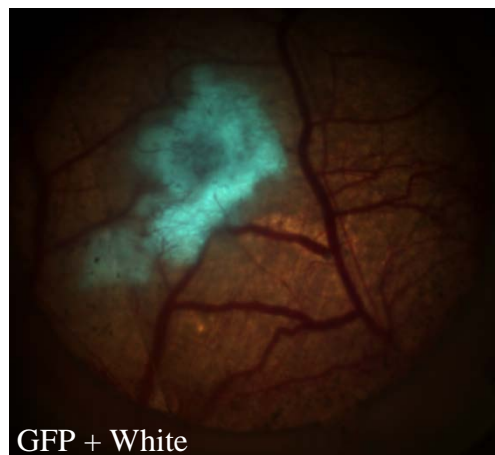
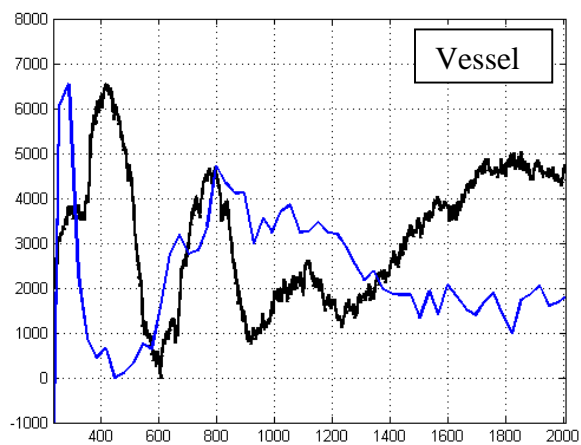
The x-axis in all images is time in seconds. The y-axis is scaled signal intensity. The black and blue curves are optical and MRI signal intensity respectively. Therefore, the signal intensity values do not have any real meaning. The signal intensities in most cases are shown after MA distribution in the vasculature. In some cases, the entire signal intensity curve for one modality is shown separately to show the relative size of signal fluctuations in comparison to total signal intensity. Additional images of the experiments are shown to better illustrate the obtained results.

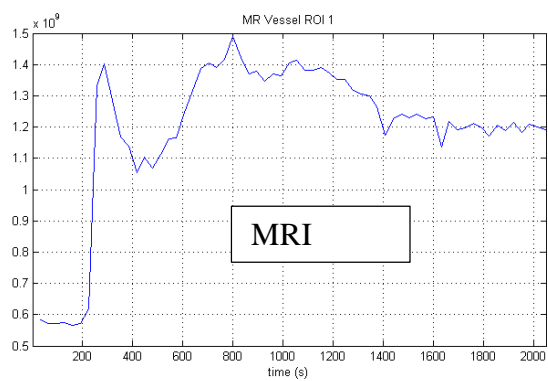
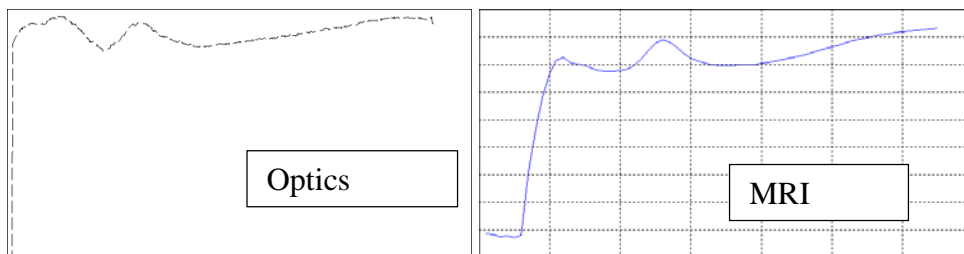
### Experiment 1: 2010-08-13 0563-R2

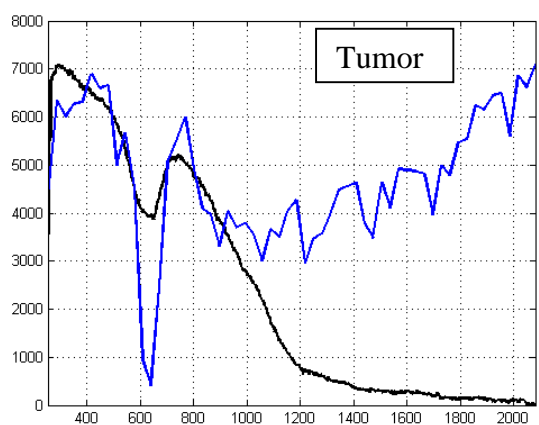
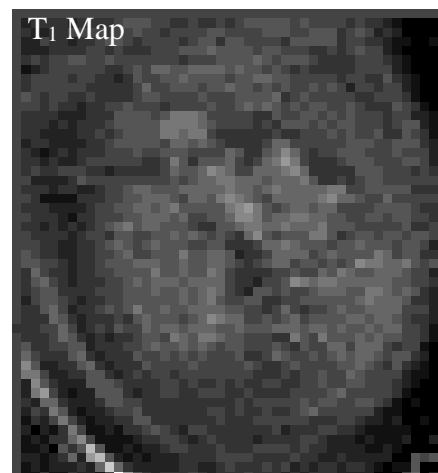
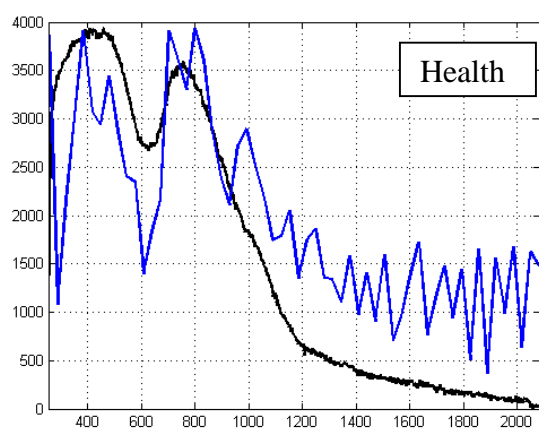
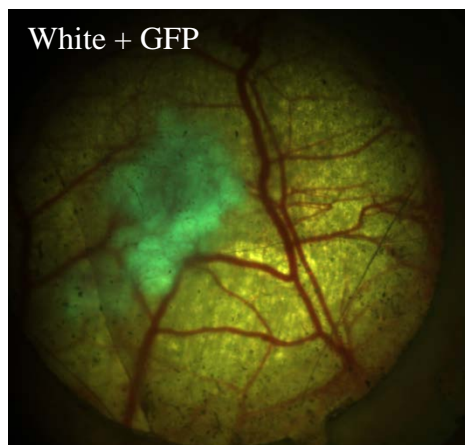
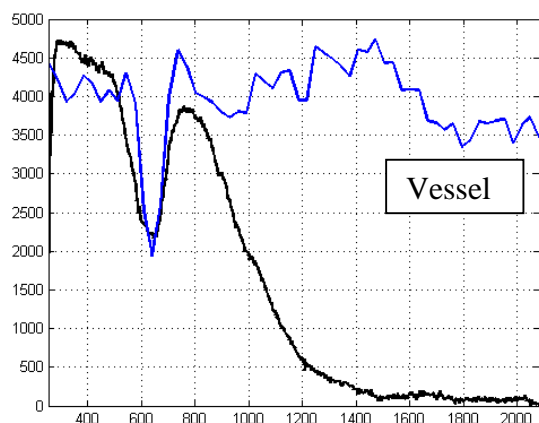
The sudden peak in optics vessel at 800 s only existed in two small regions in the vasculature. In other parts, such a peak in signal intensity did not exist.

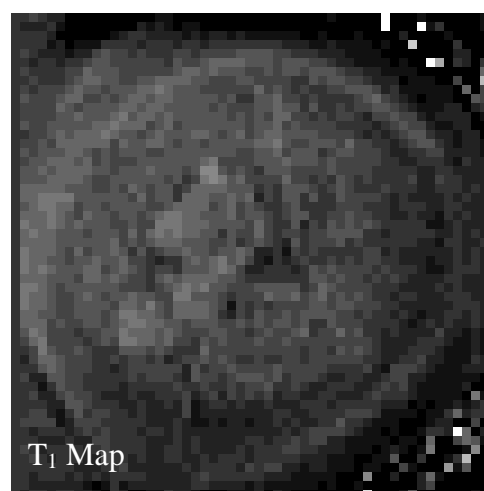
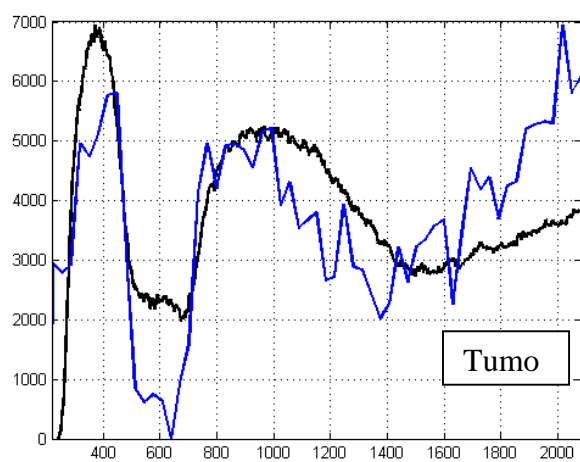
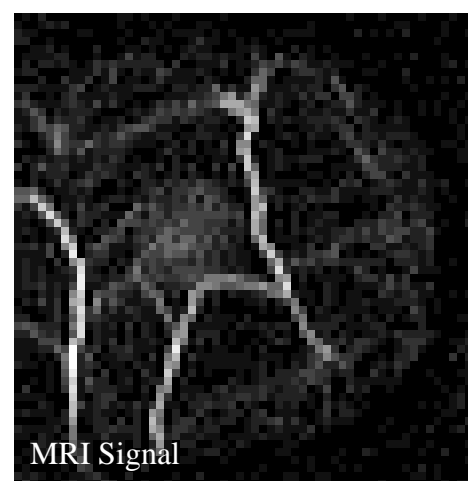
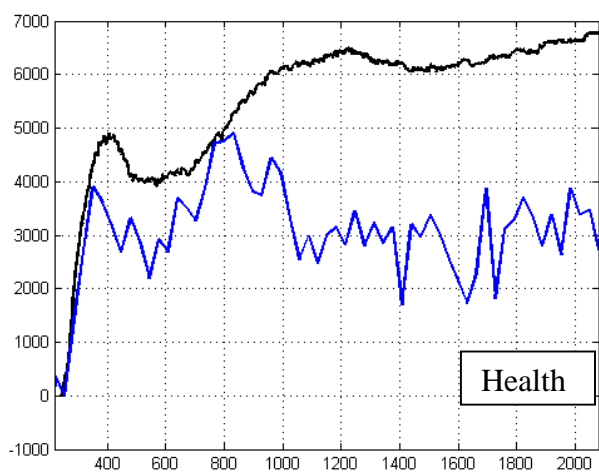
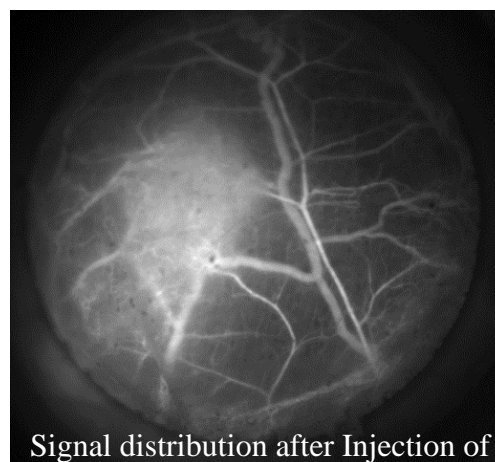
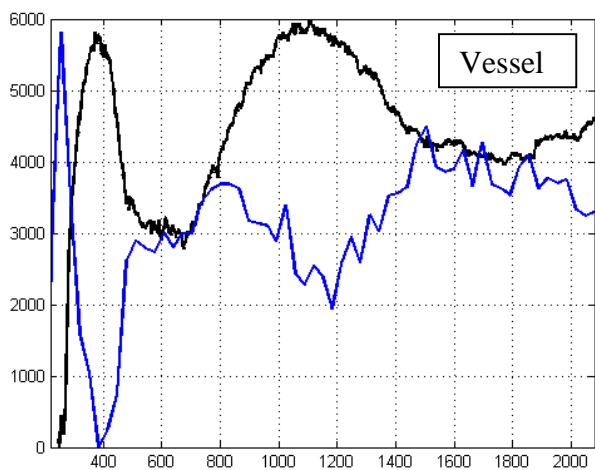




**Experiment 2: 2010-12-13 0980-00-1**

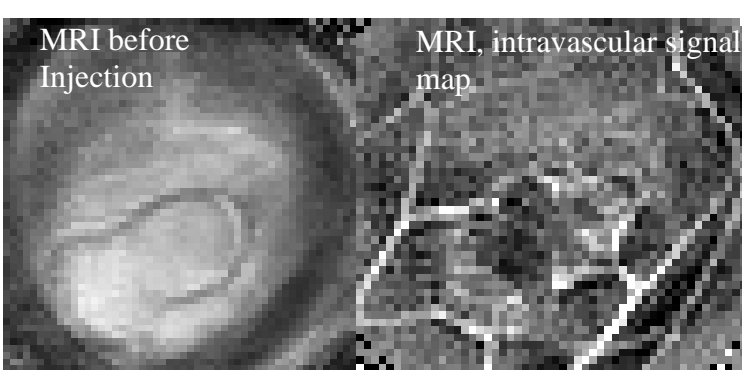
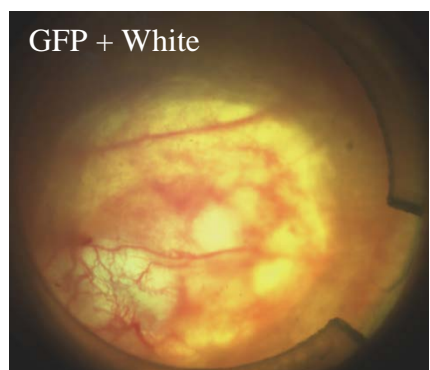
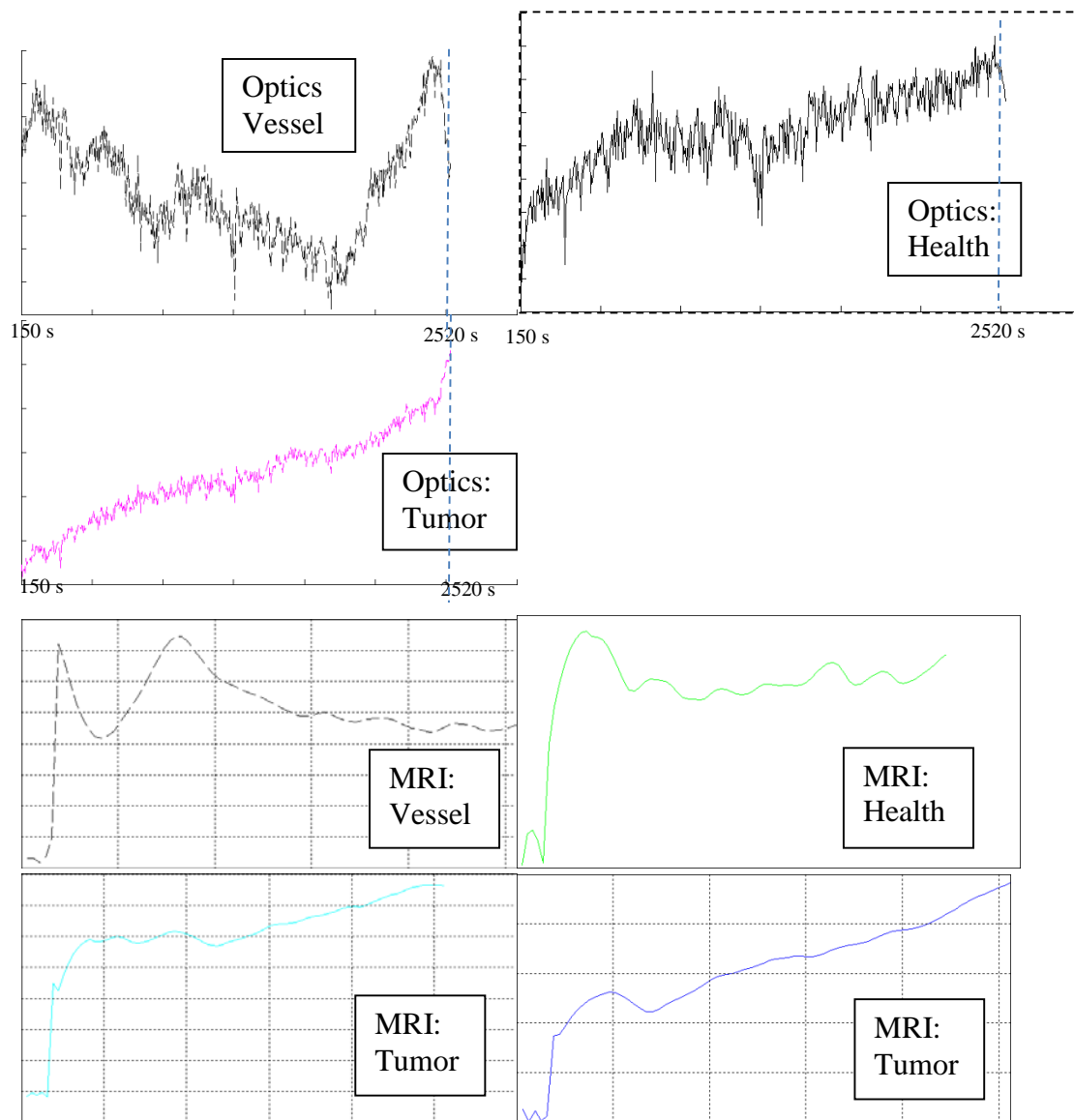


**Experiment 3: 2010-12-15 0980-00-2**

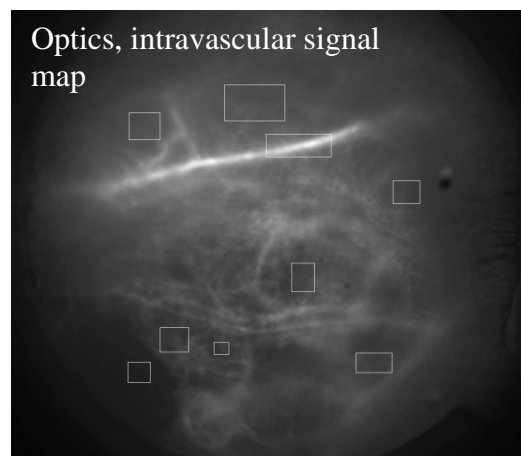
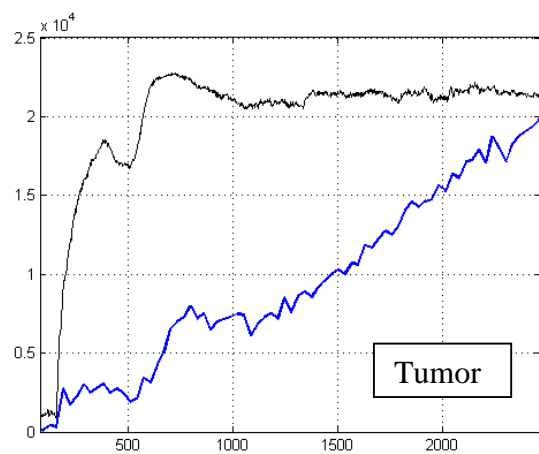
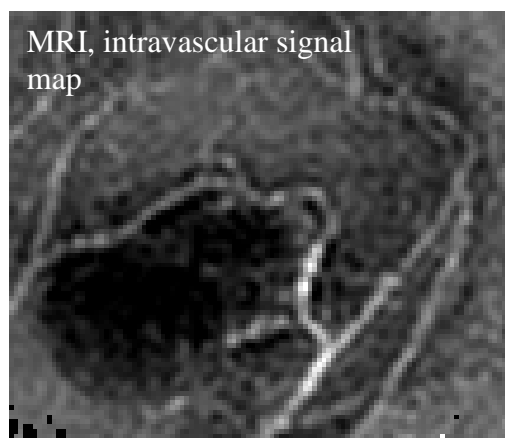
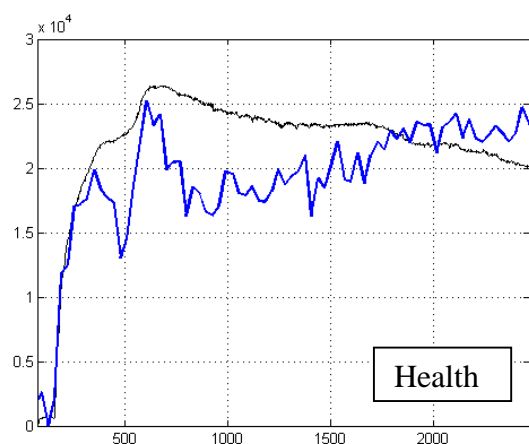
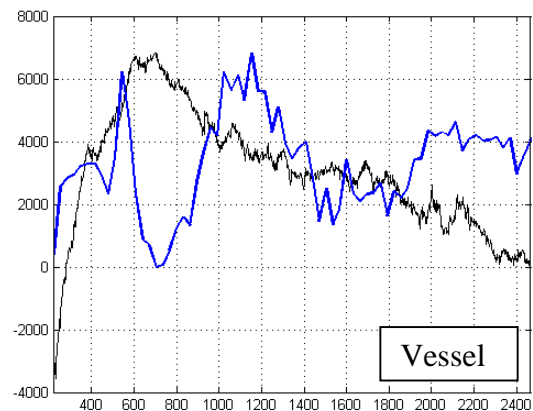
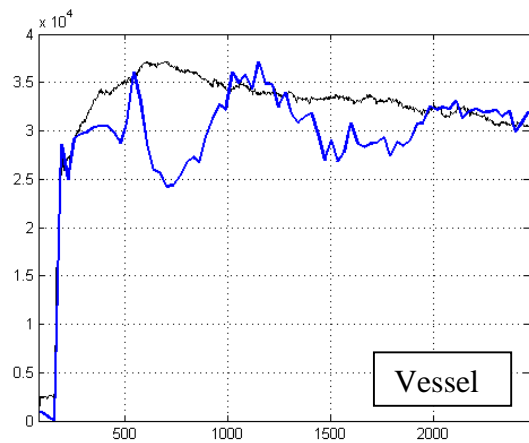
**Experiment 4: 2010-12-17 0980-00-3**

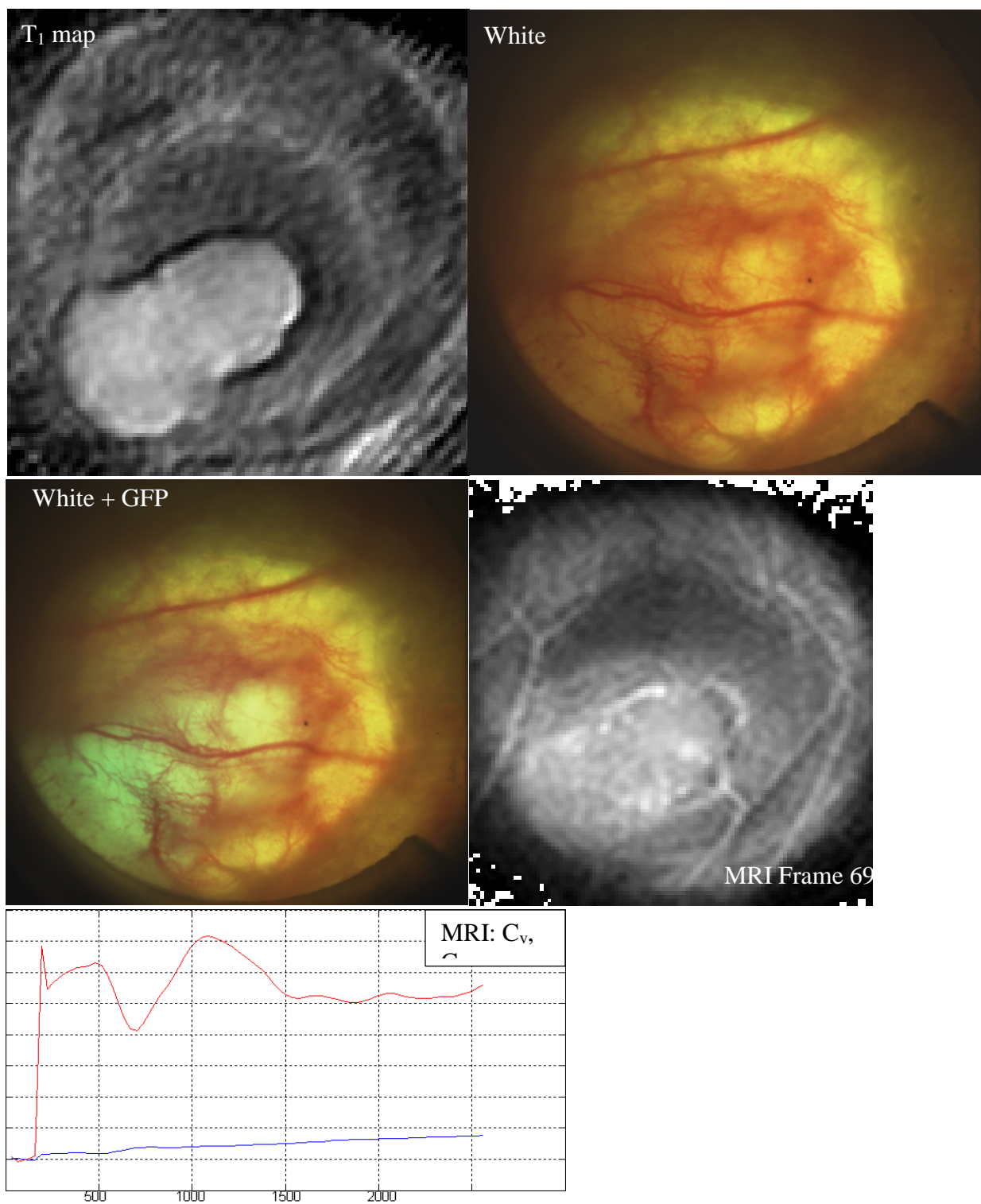
**Experiment 5: 2011-12-19-1 554-00**

Only after frame 300 in optics are shown. Comparison of optical and MR signals are difficult because the optical imaging was stopped for some time.

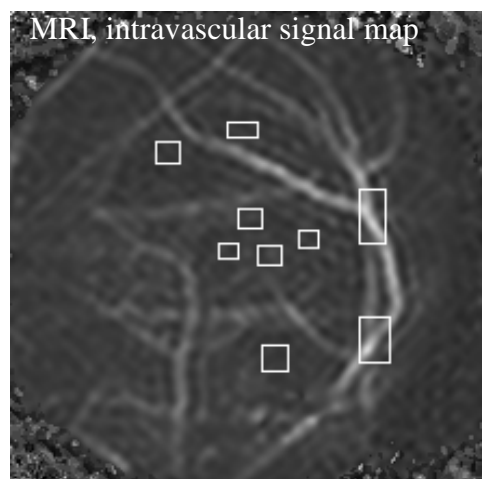
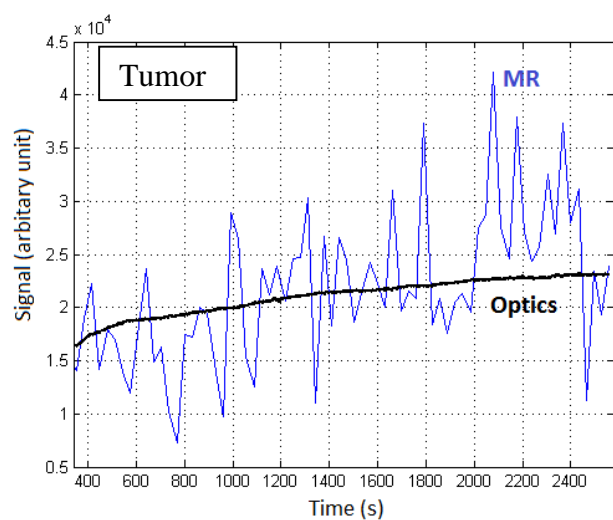
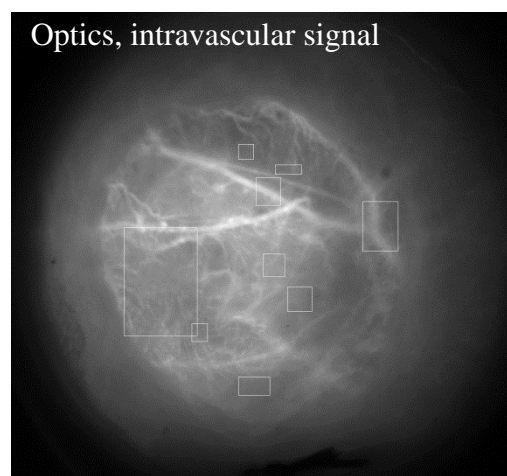
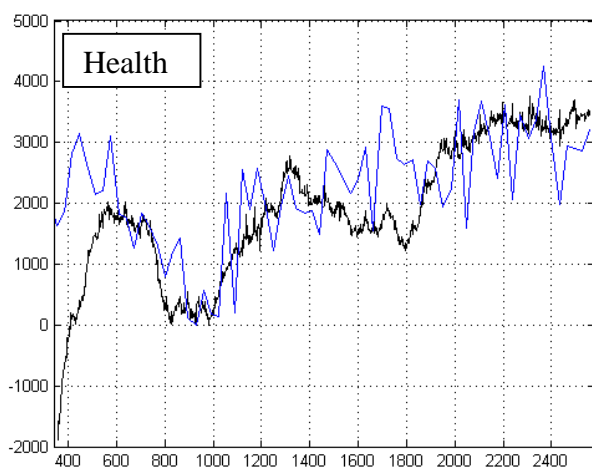
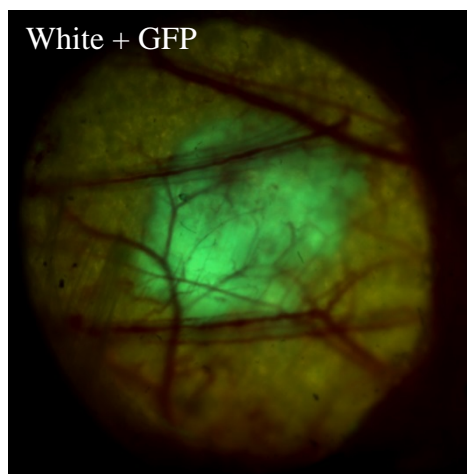
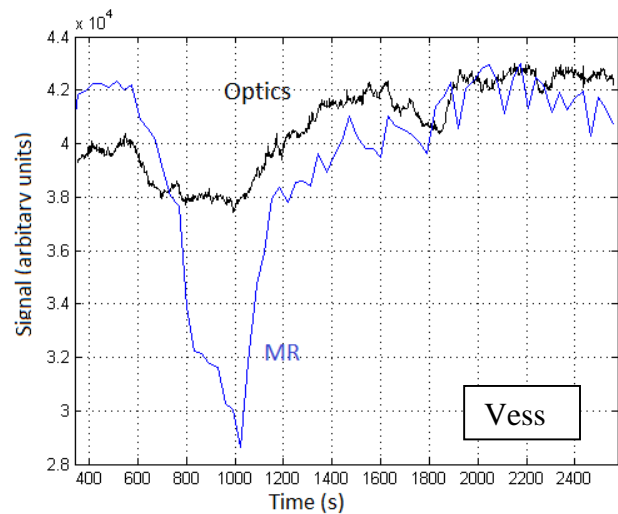


### Experiment 6: 2011-12-21-1 0554-00-2

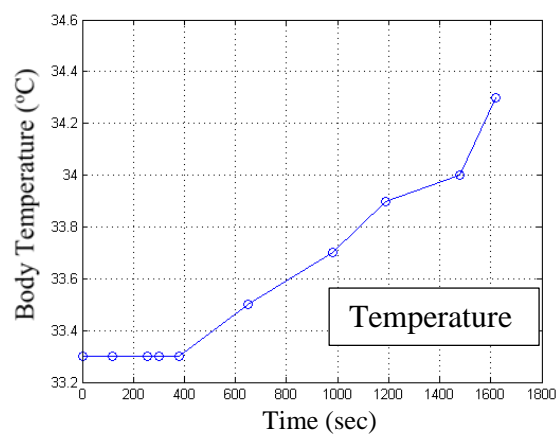
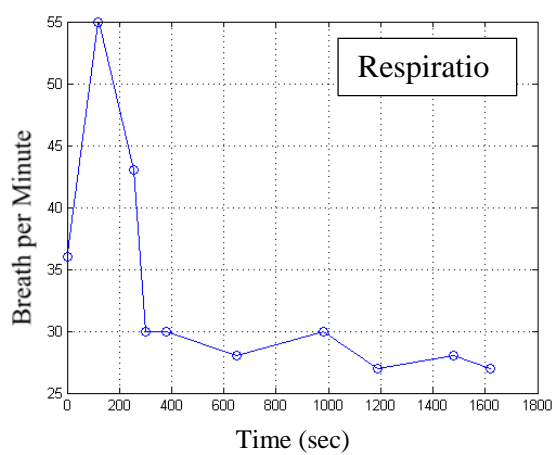
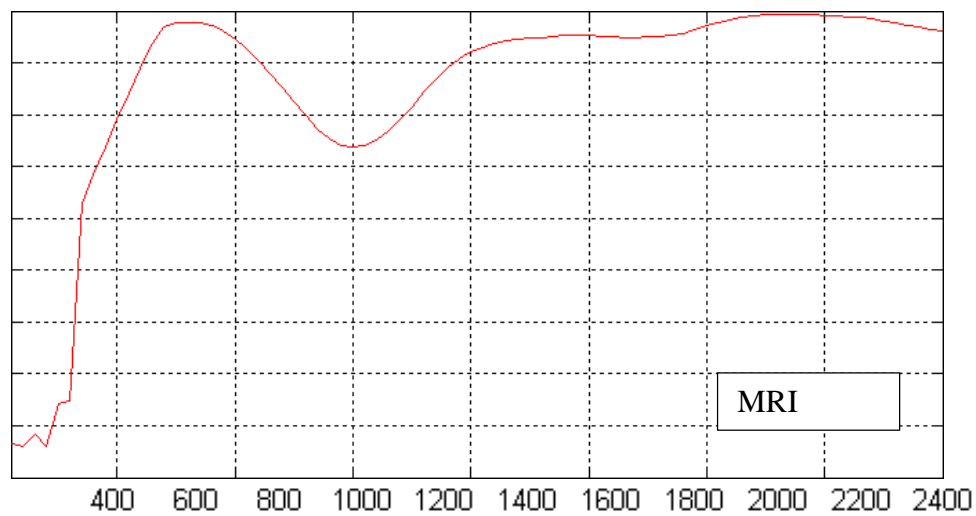




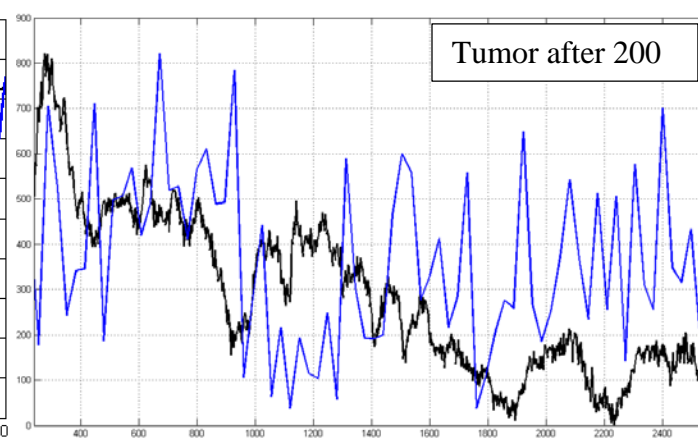
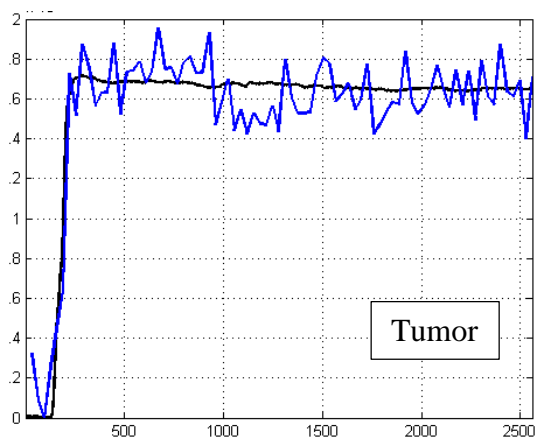
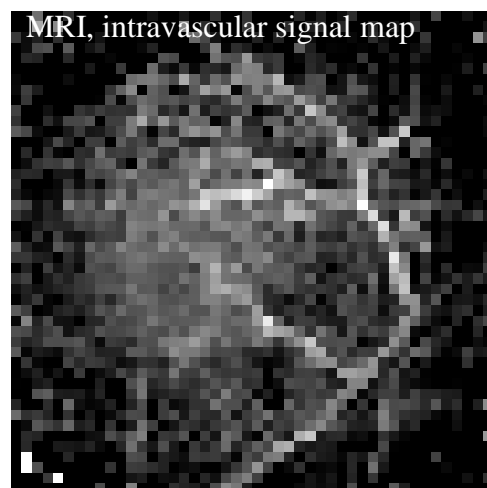
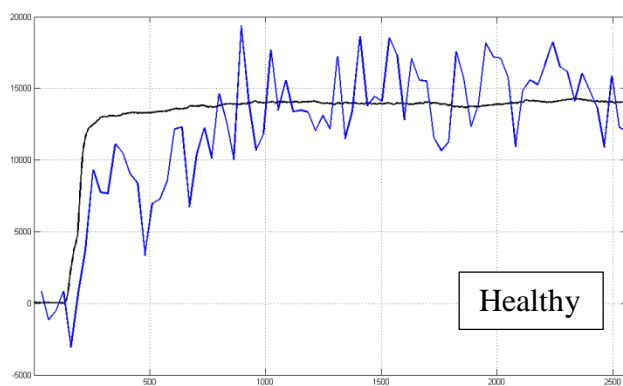
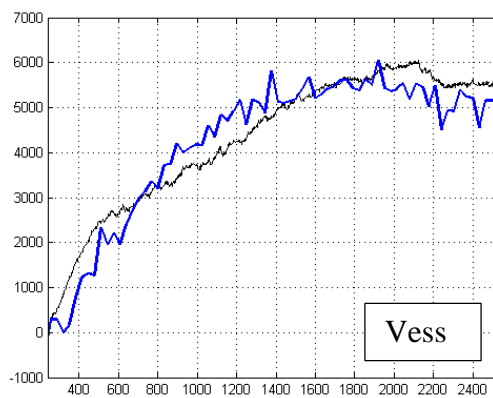
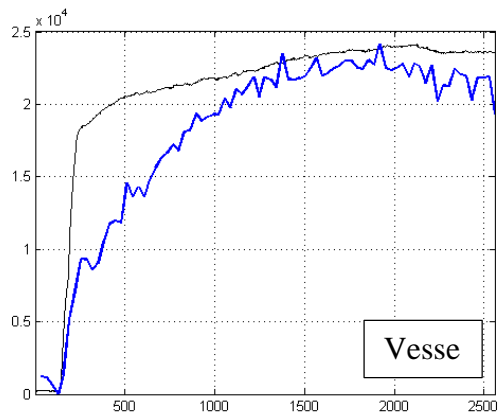
### Experiment 7: 2012-07-16 0254-R1-1



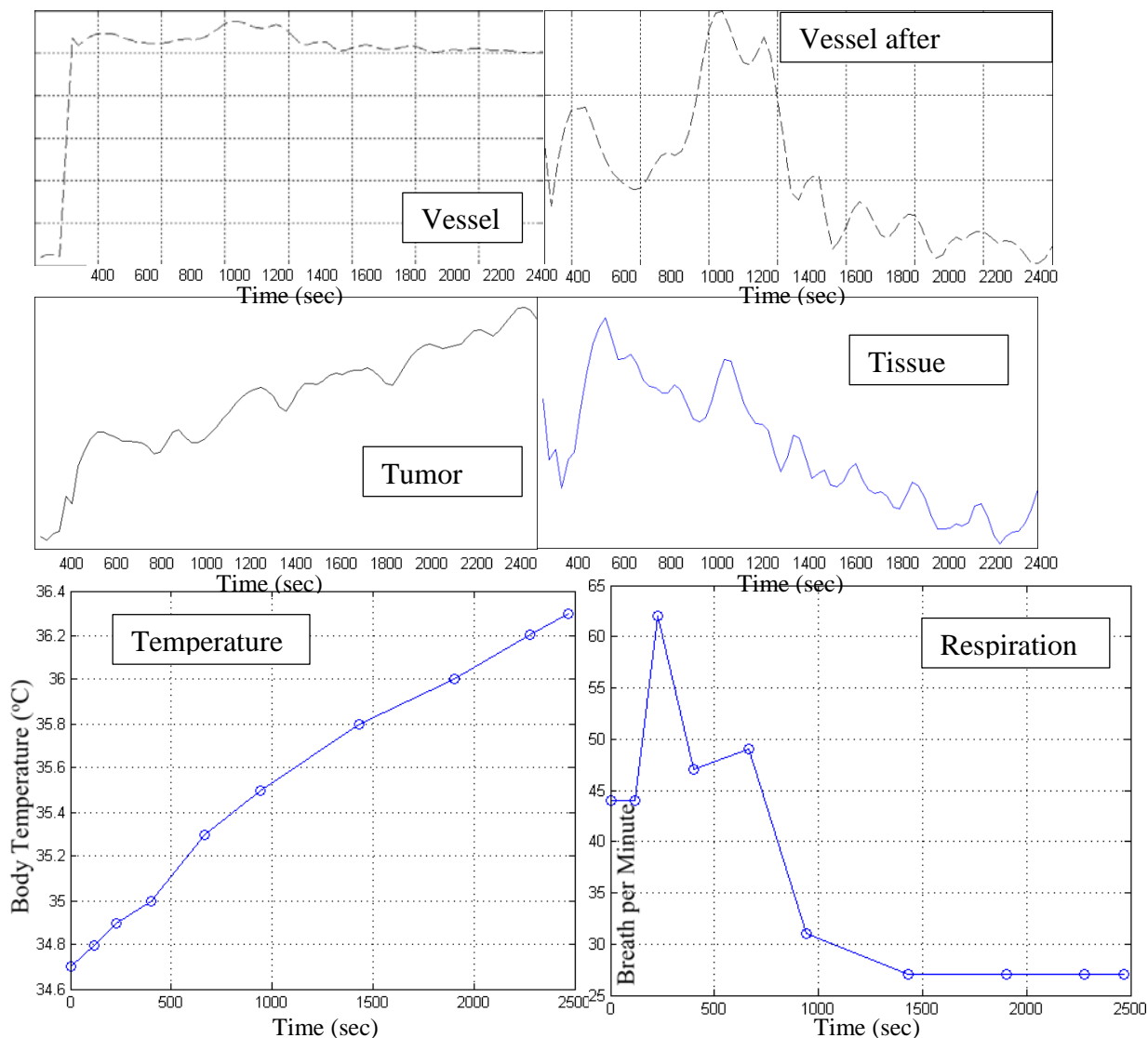
The plotted white squares are the ROIs that were used in the analysis



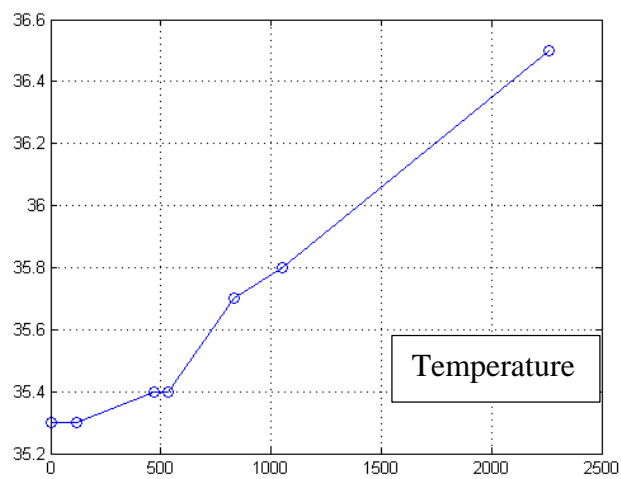
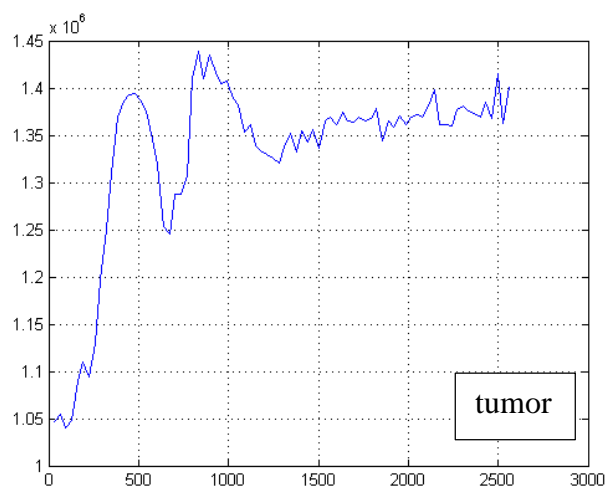
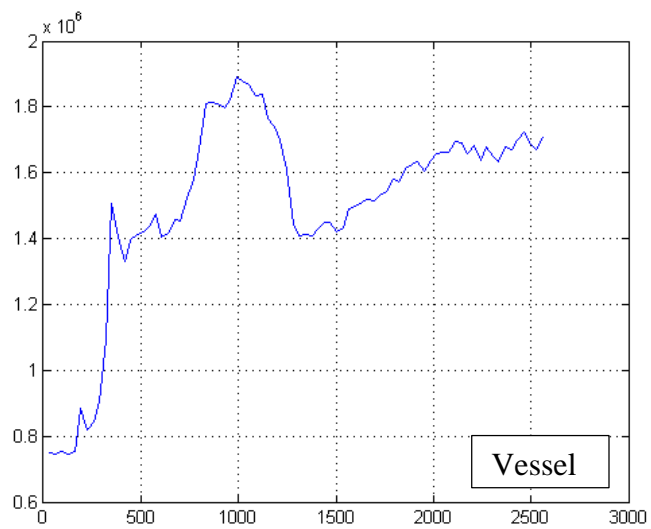
### Experiment 8: 2012-07-24 0254-R1-3



2012-07-18: 0254-R1-2, MRI only



2012-07-24: 0254-R2-2



## Appendix 6.A.5: Kinetic Parameters Estimations

The vascular kinetic parameters of each experiment is estimated in healthy tissue, tumor center and tumor edge. Tumor edge was selected on regions with neovasculature. In each tissue type, the vascular kinetic parameters are estimated via 6 methods: 4 MRI methods and 2 optical methods as described in section 6.10.1. These methods are arranged in the table consecutively for each tissue type of each experiment.

As mentioned in section 6.10.1, several ROIs were used to estimate the kinetic parameters in each tissue type and experiment. The number in the first column of the table indicates the applied analysis method. For each estimated kinetic parameter in every tissue type and experiment, 4 numbers are indicated. The first number is the obtained mean value for that parameter. The second number, which is in parenthesis, is the standard deviation of the estimation. The other two numbers, which are together in one parenthesis bracket, are the minimum and maximum estimation obtained for that parameter.

	$K_{trans}$ or Permeability	$k_{ep}$	$V_e$	$V_p$
<b>1</b>	<b>2010-08-13 0563-R2</b>			
	<b>Healthy Tissue</b>			
1	0.54 (0.39)(0.18,1.2)	6.8 (5.4)(1.3,15)	9 (2.7)(5.8,13)	0 (0)(0,0)
2	0.23 (0.24)(0.028,0.61)	3.4 (2.9)(0.17,7.4)	11 (9.1)(1.7,27)	3 (2.6)(-0.95,5)
3	0.14 (0.097)(0.027,0.24)	2.9 (2.4)(-0.084,6.1)	-1.6 (21)(-43,13)	0 (0)(0,0)
4	0.26 (0.26)(0.042,0.66)	3.7 (3)(0.37,7.6)	8.3 (5.3)(2,17)	-1.5 (1.7)(-3.7,0.57)
5	6.8 (4.8)(2.2,14)	0.77 (0.55)(0.25,1.5)	-	
6	-	3.5 (1.4)(1.2,4.7)	-	
	<b>Tumor Center</b>			
1	0.16 (0.025)(0.14,0.18)	2.4 (1.2)(1.6,3.2)	7.1 (2.4)(5.4,8.8)	0 (0)(0,0)
2	0.015 (0.0057)(0.011,0.019)	-0.47 (0.3)(-0.68,-0.26)	-4.6 (4.2)(-7.6,-1.7)	5.1 (0.63)(4.7,5.6)
3	0.028 (0.0035)(0.026,0.031)	0.41 (0.34)(0.17,0.65)	11 (10)(4,18)	0 (0)(0,0)
4	0.017 (0.0075)(0.012,0.023)	-0.31 (0.23)(-0.47,-0.15)	-8.8 (8.9)(-15,-2.6)	1.1 (0.24)(0.96,1.3)
5	-	-	-	
6	-	0.39 (0)(0.39,0.39)	-	
	<b>Tumor Edge</b>			
1	0.027 (0.23)(-0.35,0.21)	0.36 (2.1)(-3.2,2.2)	11 (2.5)(7.9,15)	0 (0)(0,0)
2	-0.011 (0.033)(-0.059,0.024)	-0.85 (0.64)(-2,-0.19)	-1.4 (6)(-13,4.2)	6.9 (2)(4.6,10)
3	0.0089 (0.0044)(0.0045,0.017)	-0.77 (0.29)(-1.2,-0.45)	-1.3 (0.89)(-3,-0.37)	0 (0)(0,0)
4	0.0033 (0.04)(-0.056,0.044)	-0.29 (0.63)(-1.2,0.19)	21 (16)(3.1,47)	-3.3 (2.7)(-8.3,-0.61)
5	13 (7.7)(4.3,23)	1.4 (0.81)(0.45,2.4)	-	
6	-	1.4 (0)(1.4,1.4)	-	
<b>2</b>	<b>2010-12-13 0980-00</b>			
	<b>Healthy Tissue</b>			
1	-0.075 (0.07)(-0.16,0.0098)	-0.6 (0.5)(-0.99,0.18)	10 (4.4)(5.5,16)	0 (0)(0,0)
2	-0.053 (0.043)(-0.11,0.0097)	-0.55 (0.4)(-0.85,0.18)	8.8 (3.1)(5.5,12)	1.2 (2.6)(-3.2,3.8)
3	-0.0071 (0.017)(-0.036,0.013)	0.13 (0.41)(-0.26,0.77)	-4.8 (3)(-11,-1.9)	0 (0)(0,0)
4	-0.063 (0.056)(-0.13,0.012)	-0.56 (0.43)(-0.9,0.22)	9.7 (4.4)(5.5,16)	-14 (6.8)(-26,-8.4)
5	6.8 (6.2)(1.6,15)	0.77 (0.71)(0.18,1.7)	-	
6	-	1.8 (1.7)(-1.1,3.6)	-	
	<b>Tumor Center</b>			
1	-0.061 (0.018)(-0.079,-0.037)	-0.57 (0.12)(-0.69,-0.4)	10 (0.97)(9.1,11)	0 (0)(0,0)
2	-0.066 (0.029)(-0.11,-0.039)	-0.6 (0.15)(-0.75,-0.39)	11 (3.3)(8.7,16)	-0.49 (3.5)(-5,3.2)

3	0.043 (0.021)(0.023,0.062)	-0.77 (0.26)(-1.1,-0.52)	-5.6 (2.3)(-8.7,-3.1)	0 (0)(0,0)
4	-0.08 (0.035)(-0.13,-0.05)	-0.63 (0.17)(-0.81,-0.41)	13 (4.1)(9.6,18)	-20 (5.3)(-26,-15)
5	-	-	-	
6	-	2.1 (2.7)(0.13,4)	-	
<b>Tumor Edge</b>				
1	-0.072 (0.015)(-0.088,-0.052)	-0.7 (0.16)(-0.82,-0.47)	10 (1.4)(9,12)	0 (0)(0,0)
2	-0.072 (0.028)(-0.11,-0.045)	-0.74 (0.19)(-0.89,-0.45)	9.9 (2.9)(7.4,14)	0.54 (1.8)(-2,2.2)
3	0.029 (0.025)(0.01,0.066)	-0.7 (0.58)(-1.4,-0.19)	-4.9 (2.3)(-8,-2.6)	0 (0)(0,0)
4	-0.086 (0.033)(-0.13,-0.056)	-0.77 (0.21)(-0.95,-0.46)	11 (3.4)(8.6,16)	-17 (4)(-21,-13)
5	7.4 (6.8)(1.7,16)	0.77 (0.71)(0.18,1.7)	-	
6	-	1.5 (1.3)(-0.34,3.3)	-	
<b>3</b>	<b>2010-12-15 0980-00-2</b>			
<b>Healthy Tissue</b>				
1	-0.09 (0.12)(-0.37,0.0036)	-0.85 (1)(-3.3,-0.052)	8.3 (6.6)(-2.2,16)	0 (0)(0,0)
2	-0.035 (0.037)(-0.093,0.0018)	0.15 (0.79)(-1.1,1.7)	4.6 (25)(-15,63)	10 (4.4)(5.1,19)
3	-0.034 (0.038)(-0.097,0.0041)	0.21 (0.78)(-1.2,1.5)	-7.1 (6)(-17,-0.33)	0 (0)(0,0)
4	-0.042 (0.05)(-0.13,0.00055)	0.13 (0.83)(-1,1.7)	-11 (19)(-53,8.6)	-1.3 (2.7)(-5.3,2.4)
5	-5 (7.6)(-16,-0.41)	-0.57 (0.87)(-1.9,-0.046)	-	
6	-	0.86 (1.4)(-0.15,3.5)	-	
<b>Tumor Center</b>				
1	-0.14 (0.014)(-0.16,-0.12)	-1.1 (0.11)(-1.3,-1)	12 (0.28)(12,13)	0 (0)(0,0)
2	-0.084 (0.097)(-0.19,0.0015)	0.63 (1.1)(-0.33,1.8)	-5.2 (6.3)(-11,1)	17 (5.8)(11,22)
3	-0.027 (0.036)(-0.061,0.0056)	0.33 (0.62)(-0.26,0.98)	-4.6 (2.7)(-7.5,-2.1)	0 (0)(0,0)
4	-0.12 (0.14)(-0.26,0.0058)	0.72 (1.1)(-0.25,1.9)	-7.9 (7.4)(-15,-0.72)	3.8 (5)(-1.3,8.2)
5	-	-	-	
6	-	-0.13 (0.48)(-0.48,0.21)	-	
<b>Tumor Edge</b>				
1	-0.034 (0.012)(-0.043,-0.026)	-0.4 (0.14)(-0.5,-0.3)	8.6 (0.13)(8.5,8.7)	0 (0)(0,0)
2	-0.024 (0.024)(-0.041,-0.0075)	0.22 (0.58)(-0.18,0.63)	-1.2 (7.5)(-6.5,4.1)	8.8 (4.7)(5.4,12)
3	-0.028 (0.032)(-0.051,-0.0054)	0.37 (0.37)(0.11,0.63)	-6.4 (2.1)(-8,-4.9)	0 (0)(0,0)
4	-0.029 (0.034)(-0.053,-0.0051)	0.26 (0.56)(-0.14,0.65)	-2.2 (8.4)(-8.2,3.7)	-2.2 (3.4)(-4.6,0.24)
5	7.2 (4.5)(3.6,12)	0.75 (0.47)(0.37,1.3)	-	
6	-	-0.023 (0.7)(-0.53,1.3)	-	
<b>4</b>	<b>2010-12-17 0980-00-3</b>			
<b>Healthy Tissue</b>				
1	0.27 (0.38)(-0.071,1)	1.6 (1.3)(-0.28,3.3)	17 (9.3)(8.9,31)	0 (0)(0,0)
2	0.22 (0.16)(-0.028,0.38)	1.6 (1.1)(-0.19,3.1)	14 (2.8)(12,19)	3.3 (8.1)(-3,15)
3	0.016 (0.024)(-0.015,0.052)	0.31 (0.5)(-0.2,1.1)	22 (42)(1.9,1.1e+02)	0 (0)(0,0)
4	0.27 (0.21)(-0.043,0.57)	1.7 (1.2)(-0.22,3.2)	16 (5.5)(12,26)	-14 (5.7)(-23,-9.8)
5	7.5 (2.7)(5.4,11)	0.86 (0.31)(0.62,1.3)	-	
6	-	2.8 (1)(1.5,4.4)	-	
<b>Tumor Center</b>				
1	0.25 (0.064)(0.2,0.29)	1.7 (0.56)(1.3,2.1)	15 (1.1)(14,16)	0 (0)(0,0)
2	0.57 (0.21)(0.42,0.72)	2.7 (0.92)(2.1,3.4)	21 (0.96)(20,21)	-6.2 (1.8)(-7.4,-4.9)
3	0.031 (0.012)(0.023,0.039)	-0.91 (0.36)(-1.2,-0.66)	-3.5 (0.12)(-3.5,-3.4)	0 (0)(0,0)
4	0.72 (0.31)(0.5,0.94)	3 (1.1)(2.2,3.7)	24 (1.8)(23,25)	-25 (2.7)(-27,-23)
5	-	-	-	
6	-	1.8 (1.6)(0.032,3)	-	
<b>Tumor Edge</b>				
1	0.14 (0.086)(0.031,0.23)	1 (0.52)(0.35,1.6)	12 (3.4)(9,16)	0 (0)(0,0)
2	0.26 (0.25)(0.025,0.55)	1.4 (0.96)(0.32,2.5)	15 (7.5)(7.9,22)	-2.9 (4.4)(-7.7,0.88)
3	0.012 (0.019)(-0.0061,0.038)	-0.37 (0.48)(-1,-0.017)	-4.1 (13)(-20,11)	0 (0)(0,0)
4	0.33 (0.33)(0.026,0.72)	1.5 (1.1)(0.33,2.8)	17 (9.6)(8,26)	-17 (10)(-28,-8.6)
5	18 (11)(4.2,31)	1.9 (1.1)(0.44,3.2)	-	
6	-	0.55 (0.74)(0.074,1.4)	-	
<b>5</b>	<b>2011-12-19-1 554-00</b>			
<b>Healthy Tissue</b>				

1	-0.024 (0.052)(-0.089,0.036)	-0.19 (0.41)(-0.69,0.3)	16 (15)(3.3,37)	0 (0)(0,0)
2	-0.044 (0.089)(-0.16,0.055)	-0.22 (0.49)(-0.81,0.38)	19 (13)(5.7,37)	-3.9 (1.8)(-5.9,-1.6)
3	0.013 (0.017)(-0.0087,0.033)	-0.13 (0.27)(-0.45,0.11)	-1.3 (15)(-14,20)	0 (0)(0,0)
4	-0.056 (0.11)(-0.2,0.062)	-0.23 (0.51)(-0.86,0.39)	-	-19 (5.9)(-25,-12)
5	-	0.15 (0.17)(0.031,0.27)	-	
6	0.066 (0.24)(-0.15,0.52)	-0.5 (2.1)(-3.5,2.6)	0.0075 (0.028)(-0.017,0.06)	
<b>Tumor Center</b>				
1	0.04 (0)(0.04,0.04)	-0.35 (0)(-0.35,-0.35)	-12 (0)(-12,-12)	0 (0)(0,0)
2	0.032 (0)(0.032,0.032)	-0.33 (0)(-0.33,-0.33)	-9.7 (0)(-9.7,-9.7)	-3 (0)(-3,-3)
3	0.15 (0)(0.15,0.15)	-0.46 (0)(-0.46,-0.46)	-32 (0)(-32,-32)	0 (0)(0,0)
4	0.039 (0)(0.039,0.039)	-0.36 (0)(-0.36,-0.36)	-11 (0)(-11,-11)	-28 (0)(-28,-28)
5	1.8 (2.7)(-0.45,4.9)	0.19 (0.29)(-0.046,0.51)	-	
6	-	1.5 (0.81)(0.89,2.7)	-	
<b>Tumor Edge</b>				
1	0.039 (0.019)(0.017,0.052)	-0.27 (0.057)(-0.31,-0.2)	-16 (10)(-26,-6.1)	0 (0)(0,0)
2	0.033 (0.021)(0.0099,0.052)	-0.24 (0.051)(-0.3,-0.2)	-14 (11)(-26,-4.1)	-2.9 (1.7)(-4,-1)
3	0.13 (0.072)(0.047,0.18)	-0.38 (0.036)(-0.42,-0.35)	-34 (18)(-46,-13)	0 (0)(0,0)
4	0.044 (0.031)(0.011,0.072)	-0.27 (0.056)(-0.33,-0.23)	-17 (14)(-31,-4.6)	-28 (13)(-36,-12)
5	-0.44 (0)(-0.44,-0.44)	-0.046 (0)(-0.046,-0.046)	-	
6	-	1.8 (0.2)(1.6,2.1)	-	
<b>6 2011-12-21-1 0554-00-2</b>				
<b>Healthy Tissue</b>				
1	0.33 (0.083)(0.24,0.41)	1.9 (1)(0.98,3)	19 (5.6)(14,25)	0 (0)(0,0)
2	0.14 (0.055)(0.087,0.19)	1 (0.81)(0.29,1.9)	19 (9.6)(10,30)	6.4 (2.4)(4.3,8.9)
3	0.055 (0.0047)(0.052,0.062)	0.17 (0.36)(-0.21,0.54)	-40 (80)(-1.6e+02,13)	0 (0)(0,0)
4	0.15 (0.057)(0.094,0.2)	1 (0.81)(0.25,1.8)	23 (13)(11,38)	-5.6 (0.48)(-6.3,-5.3)
5	82 (0)(82,82)	9.3 (0)(9.3,9.3)	-	
6	-	5.8 (2)(4.1,8)	-	
<b>Tumor Center</b>				
1	0.057 (0.047)(0.023,0.09)	0.041 (0.54)(-0.34,0.42)	7.2 (20)(-6.8,21)	0 (0)(0,0)
2	0.04 (0.025)(0.022,0.057)	-0.13 (0.39)(-0.41,0.15)	17 (31)(-5.4,39)	1.8 (1.2)(0.96,2.6)
3	0.038 (0.023)(0.022,0.054)	-0.17 (0.36)(-0.42,0.083)	30 (50)(-5.2,65)	0 (0)(0,0)
4	0.04 (0.026)(0.022,0.059)	-0.14 (0.39)(-0.41,0.13)	19 (35)(-5.4,44)	-0.32 (0.27)(-0.51,-0.13)
5	4.4 (5)(0.54,10)	0.46 (0.52)(0.056,1)	-	
6	-	2.7 (0.78)(1.8,3.2)	-	
<b>Tumor Edge</b>				
1	0.042 (0)(0.042,0.042)	-0.53 (0)(-0.53,-0.53)	-8 (0)(-8,-8)	0 (0)(0,0)
2	0.043 (0)(0.043,0.043)	-0.55 (0)(-0.55,-0.55)	-7.7 (0)(-7.7,-7.7)	0.63 (0)(0.63,0.63)
3	0.042 (0)(0.042,0.042)	-0.52 (0)(-0.52,-0.52)	-8.1 (0)(-8.1,-8.1)	0 (0)(0,0)
4	0.042 (0)(0.042,0.042)	-0.55 (0)(-0.55,-0.55)	-7.7 (0)(-7.7,-7.7)	0.86 (0)(0.86,0.86)
5	-	-	-	
6	-	2.7 (0.18)(2.6,2.8)	-	
<b>7 2012-07-16 0254-R1</b>				
<b>Healthy Tissue</b>				
1	0.058 (0.039)(0.012,0.12)	2.2 (1.4)(0.11,4.1)	4 (3.3)(1.8,11)	0 (0)(0,0)
2	0.0065 (0.0045)(-0.0017,0.01)	-0.47 (0.7)(-1.3,0.19)	2.8 (4)(-0.81,9.2)	2 (0.72)(1.1,2.7)
3	0.0071 (0.0055)(-4.1e-05,0.015)	0.32 (0.82)(-1.1,1.1)	0.68 (0.9)(-0.71,1.7)	0 (0)(0,0)
4	0.011 (0.0059)(0.0061,0.022)	-0.23 (0.94)(-1.4,0.9)	3 (4)(-0.82,10)	0.29 (1.1)(-1.1,1.5)
5	7.7 (2.2)(6.2,9.3)	0.88 (0.26)(0.7,1.1)	-	
6	-	2.4 (0.98)(1.6,4.3)	-	
<b>Tumor Center</b>				
1	-0.048 (0.13)(-0.19,0.067)	-1.9 (3.3)(-5.6,1)	4.9 (1.9)(3.6,5)	0 (0)(0,0)
2	0.023 (0.029)(-0.0026,0.055)	0.12 (0.75)(-0.58,0.89)	3.4 (3.3)(0.39,6.4)	1.6 (1.4)(0.36,3.1)
3	0.0076 (0.0098)(-0.0013,0.019)	0.23 (0.13)(0.072,0.35)	5.7 (8.6)(-0.43,18)	0 (0)(0,0)
4	0.031 (0.038)(-0.0012,0.07)	0.34 (0.82)(-0.42,1.1)	3.2 (3.3)(0.27,6.1)	-1.6 (1.1)(-2.6,-0.64)
5	6.1 (6.1)(2.3,13)	0.64 (0.64)(0.24,1.4)	-	

6	-	3.5 (1.1)(2.4,5)	-	
	<b>Tumor Edge</b>			
1	-0.31 (0.37)(-0.72,0.0065)	-5.3 (5.7)(-11,-0.32)	2.6 (4.1)(-2,6.3)	0 (0)(0,0)
2	-0.034 (0.058)(-0.095,0.016)	-2.5 (1.5)(-4.1,-1.2)	0.51 (2)(-1.3,2.3)	4.1 (0.45)(3.6,4.7)
3	-0.00046 (0.0066)(-0.0074,0.0056)	-0.3 (0.72)(-1,0.37)	-1.2 (0.75)(-2,-0.46)	0 (0)(0,0)
4	-0.043 (0.067)(-0.11,0.017)	-2.6 (1.6)(-4.2,-1.2)	0.67 (2.2)(-1.4,2.6)	-0.81 (2.4)(-2.9,1.5)
5	-	-	-	
6	-	3.3 (1)(2.3,4.8)	-	
<b>8</b>	<b>2012-07-24 0254-R1-3,</b>			
	<b>Healthy Tissue</b>			
1	0.036 (0.34)(-0.28,0.66)	-0.17 (2.6)(-3.2,4.3)	13 (3.8)(8.9,17)	0 (0)(0,0)
2	-0.016 (0.13)(-0.19,0.093)	-0.6 (1.9)(-2.9,1.8)	-6.1 (3.5)(-11,-2.6)	16 (5.6)(8.8,21)
3	0.0031 (0.049)(-0.076,0.071)	-0.61 (1.3)(-2.3,0.64)	-4.4 (4.5)(-12,-0.1)	0 (0)(0,0)
4	0.052 (0.11)(-0.13,0.2)	-1.3 (1.6)(-2.9,1.1)	-5.2 (4.5)(-12,0.77)	3.9 (2.3)(1.9,7.7)
5	1.6 (0.76)(1.1,2.2)	0.19 (0.086)(0.12,0.25)	-	
6	-	1.2 (0.77)(0.34,2.2)	-	
	<b>Tumor Center</b>			
1	-0.17 (0.041)(-0.21,-0.12)	-2.6 (0.96)(-3.5,-1.5)	7 (2.2)(4.7,9.6)	0 (0)(0,0)
2	-0.33 (0.34)(-0.65,-0.027)	2.1 (1.3)(0.83,3.5)	-11 (8.8)(-19,-3.3)	17 (9.6)(8.8,26)
3	-0.52 (0.51)(-1.1,-0.061)	2.5 (1.4)(1.1,3.9)	-16 (11)(-28,-5.8)	0 (0)(0,0)
4	-0.53 (0.61)(-1.1,-0.0049)	2 (2.2)(0.15,4)	-15 (14)(-28,-2.7)	-0.9 (2.9)(-3.6,2.8)
5	-2.3 (4.6)(-7.6,0.68)	-0.24 (0.48)(-0.79,0.071)	-	
6	-	1.5 (0.15)(1.4,1.6)	-	
	<b>Tumor Edge</b>			
1	-0.11 (0.055)(-0.18,-0.052)	-1.9 (0.41)(-2.3,-1.5)	5.5 (2.3)(3.3,8)	0 (0)(0,0)
2	-0.3 (0.029)(-0.33,-0.27)	3 (0.61)(2.4,3.7)	-10 (3)(-14,-7.5)	15 (4.4)(11,19)
3	-0.45 (0.17)(-0.66,-0.29)	3.4 (0.47)(2.9,3.9)	-14 (6.2)(-21,-7.8)	0 (0)(0,0)
4	-0.42 (0.095)(-0.53,-0.33)	3.4 (0.65)(2.8,4)	-13 (5.3)(-19,-8.4)	-0.46 (1.2)(-2.1,0.62)
5	-	-	-	
6	-	2 (0.44)(1.3,2.5)	-	

## REFERENCES

### Chapter 1

- [1] Del VS, Zannetti A, Iommelli F, Lettieri A, Brunetti A, Salvatore M. Molecular imaging of tumor microenvironment: challenges and perspectives. *Quart J of Nuclear Med and Molecular Imaging*. 2010;54:249-58.
- [2] Pagel MD. The hope and hype of multimodality imaging of contrast agents. *Nanomedicine*. 2011;6:945-48.
- [3] Gaustad JV, Brurberg KG, Simonsen TG, Mollatt CS, Rofstad EK. Tumor Vascularity Assessed By Magnetic Resonance Imaging and Intravital Microscopy Imaging. *Neoplasia*. 2008;10:354-62.
- [4] Cho H, Ackerstaff E, Carlin S, Lupu ME, Wang Y, Rizwan A, O'Donoghue J, Ling CC, Humm JL, Zanzonico PB, Koutcher JA. Noninvasive multimodality imaging of the tumor microenvironment: registered dynamic magnetic resonance imaging and positron emission tomography studies of a preclinical tumor model of tumor hypoxia. *Neoplasia*. 2009;11(3):247-59.
- [5] Pietras P, Östman A. Hallmarks of cancer: Interactions with the tumor stroma. *Experimental Cell Research*. 2010;316(8):1324–31.
- [6] Fukumura D, Jain RK. Tumor Microenvironment Abnormalities: Causes, Consequences, and Strategies to Normalize. *J Cell Biochem*. 2007;101:937–49.
- [7] Bushberg JT, Seibert JA, Leildholdt EM, Boone JM. *The Essential Physics of Medical Imaging*, Second Edition. Lippincott Williams & Wilkins. 2002.
- [8] Torigian DA, Huang SS, Houseni M, Alavi A. Functional Imaging of Cancer with Emphasis on Molecular Techniques. *CA Cancer J Clin*. 2007;57:206-24.
- [9] Parks SK, Chiche J, Pouyssegur J. pH Control Mechanisms of Tumor Survival and Growth. *J Cell Physiol*. 2011;226:299–308.
- [10] West CML, Cooper RA, Loncaster JA, Wilks DP, Bromley M. Tumor Vascularity: A Histological Measure of Angiogenesis and Hypoxia. *Cancer Research*. 2011;61:2907–10.
- [11] Furuya M, Yonemitsu Y, Aoki I. Angiogenesis: Complexity of Tumor Vasculature and Microenvironment. *Current Pharmaceutical Design*. 2009;15:1854-67.
- [12] Nagy JA, Benjamin L, Zeng H, Dvorak AM, Dvorak HF. Vascular permeability, vascular hyperpermeability and angiogenesis. *Angiogenesis*. 2008;11:109–19.
- [13] Vaupel P, Mayer A. Hypoxia in cancer: significance and impact on clinical outcome. *Cancer Metastasis Rev*. 2007;26:225–39.
- [14] Martinez-Outschoorna UE, Pavlidesa S, Howelle A, Pestell RG, Tanowitzf HB, Sotgiaa F, Lisanti MP. Stromal epithelial metabolic coupling in cancer: Integrating autophagy and metabolism in the tumor microenvironment. *The International Journal of Biochemistry & Cell Biology*. 2011;43:1045–51.
- [15] Sarah Jane Lunt, Naz Chaudary, Richard P. Hill. The tumor microenvironment and metastatic disease. *Clin Exp Metastasis*. 2009;26:19–34.
- [16] Fukumura D, Xu L, Chen Y, Gohongi T, Seed B, Jain RK. Hypoxia and acidosis independently up-regulate vascular endothelial growth factor transcription in brain tumors in vivo. *Cancer Res*. 2001;61:6020–24.
- [17] Helmlinger G, Yuan F, Dellian M, Jain RK. Interstitial pH and pO<sub>2</sub> gradients in solid tumors in vivo: High-resolution measurements reveal a lack of correlation. *Nat Med*. 1997;3:177–82.

- [18] Craig S. Levin. Primer on molecular imaging technology. *Eur J Nucl Med Mol Imaging*. 2005;32:S325–45.
- [19] Bushberg JT, Seibert JA, Leildholdt EM, Boone JM. *The Essential Physics of Medical Imaging*, Second Edition. Lippincott Williams & Wilkins, 2002.
- [20] Matsumoto S, Yasui H, Batra S, Kinoshita Y, Bernardo M, Munasinghe JP, Utsumi H, Choudhuria R, Devasahayam N, Subramanian S, Mitchell JB, Krishna MC. Simultaneous imaging of tumor oxygenation and microvascular permeability using Overhauser enhanced MRI. *Proc Natl Acad Sci U S A*. 2009;106(42): 17898–903
- [21] Brahimi-Horn MC, Bellot G, Pouysségur J. Hypoxia and energetic tumour metabolism. *Curr Opin Genet Dev*. 2011;(21):67-72.
- [22] Fukumura D, Xu L, Chen Y, Gohongi T, Seed B, Jain RK. Hypoxia and acidosis independently up-regulate vascular endothelial growth factor transcription in brain tumors in vivo. *Cancer Res*. 2001; 61(16):6020-4.
- [23] Helmlinger G, Yuan F, Dellian M, Jain RK. Interstitial pH and pO<sub>2</sub> gradients in solid tumors in vivo: high-resolution measurements reveal a lack of correlation. *Nat Med*. 1997;3(2):177-82.
- [24] Ponticorvo A, Dunn AK. Simultaneous imaging of oxygen tension and blood flow in animals using a digital micromirror device. *Opt Express*. 2010;18(8):8160-70.
- [25] Matsumoto S, Yasui H, Batra S, Kinoshita Y, Bernardo M, Munasinghe JP, Utsumi H, Choudhuri R, Devasahayam N, Subramanian S, Mitchell JB, Krishna MC. Simultaneous imaging of tumor oxygenation and microvascular permeability using Overhauser enhanced MRI. *Proc Natl Acad Sci USA*. 2009;106(42):17898-903.
- [26] Menke H, Vaupel P. Effect of injectable or inhalational anesthetics and of neuroleptic, neuroleptanalgesic, and sedative agents on tumor blood flow. *Radiation Research*. 1988;114:64-76
- [27] Zaman RT, Rajaram N, Walsh A, Oliver J, Rylander HG, Tunnell JW, Welch AJ, Mahadevan-Jansen A. Variation of fluorescence in tissue with temperature. *Lasers Surg Med*. 2011;43(1):36-42.
- [28] Brurberg KG, Benjaminsen IC, Dorum LM, Rofstad EK. Fluctuations in tumor blood perfusion assessed by dynamic contrast-enhanced MRI. *Magn Reson Med*. 2007;58(3):473-81.
- [29] Brurberg KG, Graff BA, Rofstad EK. Temporal heterogeneity in oxygen tension in human melanoma xenografts. *Br J Cancer* 2003;89(2):350-6.
- [30] Olafsson R, Bauer DR, Montilla LG, Witte RS. Real-time contrast enhanced photoacoustic imaging of cancer in a mouse window chamber. *Optics Express* 2010;18:18625-32.
- [31] Chen L, Gobar LS, Knowles NG, Liu Z, Gmitro AF, Barrett HH. Direct imaging of radionuclide-produced electrons and positrons with an ultra-thin phosphor. *J Nucl Med* 2008;49(7):1141–45.
- [32] Algire GH. An adaptation of the transparent chamber technique to the mouse. *J National Cancer Institute*. 1943;4:1-11.
- [33] Makale M. Intravital imaging and cell invasion. *Methods Enzymol*. 2007;426:375-401.
- [34] Papenfuss HD, Gross JF, Intaglietta M, Treese FA. A transparent access chamber for the rat dorsal skin fold. *Microvasc Res*. 1979;18(3):311-8.
- [35] Objet Ltd., [www.objet.com](http://www.objet.com)
- [36] Koehl GE, Gaumann A, Geissler EK. Intravital microscopy of tumor angiogenesis and regression in the dorsal skin fold chamber: mechanistic insights and preclinical testing of therapeutic strategies. *Clin Exp Metastasis*. 2009;26:329–44.

## Chapter 2

- [1] Bohren CF, Huffmann DR. Absorption and scattering of light by small particles. New York, Wiley –Interscience. 2010 ISBN 3-527-40664-6.
- [2] Taroni P, Pifferi A, Torricelli A, Comelli D, Cubeddu R. In vivo absorption and scattering spectroscopy of biological tissues. *Photochem Photobiol Sci.* 2003;2:124–29.
- [3] Cheong WF, Prahl SA, Welch AJ. A Review of the Optical Properties of Biological Tissues. *IEEE J Quantum Electron.* 1990;26(12):2166-85.
- [4] Panchuk-Voloshina N, Haugland RP, Bishop-Stewart J, Bhalgat MK, Millard PJ, Mao F, Leung WY, Haugland RP. Alexa dyes, a series of new fluorescent dyes that yield exceptionally bright, photostable conjugates. *J Histochem Cytochem.* 1999;47(9):1179-88.
- [5] Life Technologies, Molecular Probes. Amine Reactive Probes. Rev 2. 2013:MAN0001774|MP00143.
- [6] Life Technologies, Molecular Probes. Alexa Fluor Dye Selection Guide. License#B-081152 0609. 2009.
- [7] Sarkar P, Sridharan S, Luchowski R, Desai S, Dworecki B, Nlend M, Gryczynski Z, Gryczynski I. Photophysical properties of a new DyLight 594 dye. *J Photochem Photobiol B.* 2010;98(1):35-9.
- [8] Jennings DL. Dynamic Contrast Enhanced Magnetic Resonance Imaging & Fluorescence Microscopy of Tumor Microvascular Permeability. PhD Dissertation, Dept. of Biomedical Eng., U. of Arizona, 2008.
- [9] Geraldes CF, Laurent S. Classification and basic properties of contrast agents for magnetic resonance imaging. *Contrast Media Mol Imaging.* 2009;4(1):1-23.
- [10] Caravan P, Ellison JJ, McMurry TJ, Lauffer RB. Gadolinium(III) chelates as MRI contrast agents: structure, dynamics, and applications. *Chem Rev* 1999;99: 2293–352.
- [11] Geraldes CF, Laurent S. Classification and basic properties of contrast agents for magnetic resonance imaging *Contrast Media. Mol. Imaging* 2009;4(1):1-23.
- [12] Jackson A, Buckley DL, Parker GJM. Dynamic Contrast-Enhanced Magnetic Resonance Imaging in Oncology. Springer Berlin Heidelberg New York. 2005, Chapter 2. ISBN 3-540-42322-2.
- [13] Pintaske J, Martirosian P, Graf H, Erb G, Lodemann KP, Claussen CD, Schick F. Relaxivity of Gadopentetate Dimeglumine (Magnevist), Gadobutrol (Gadovist), and Gadobenate Dimeglumine (MultiHance) in human blood plasma at 0.2, 1.5, and 3 Tesla. *Invest Radiol.* 2006;41(3):213-21.
- [14] Rohrer M, Bauer H, Mintorovitch J, Requardt M, Weinmann HJ. Comparison of magnetic properties of MRI contrast media solutions at different magnetic field strengths. *Invest Radiol.* 2005;40(11):715-24.
- [15] Kalavagunta C, Metzger GJ. A field comparison of  $r_1$  and  $r_2^*$  relaxivities of Gd-DTPA in aqueous solution and whole blood: 3T versus 7T. *Proc Intl Soc Mag Reson Med.* 2010;18:4990.
- [16] Blockley NP, Jiang L, Gardener AG, Ludman CN, Francis ST, Gowland PA. Field strength dependence of  $R_1$  and  $R_2^*$  relaxivities of human whole blood to ProHance, Vasovist, and deoxyhemoglobin. *Magn Reson Med.* 2008;60(6):1313-20.
- [17] Stanisiz GJ, Henkelman RM. Gd-DTPA relaxivity depends on macromolecular content. *Magn Reson Med.* 2000;44(5):665-7.
- [18] Dafni H, Gilead A, Nevo N, Eilam R, Harmelin A, Neeman M. Modulation of the pharmacokinetics of macromolecular contrast material by avidin chase: MRI, optical, and

- inductively coupled plasma mass spectrometry tracking of triply labeled albumin. *Magn Reson Med.* 2003;50(5):904-14.
- [19] Dreher MR, Liu WG, Michelich CR, Dewhirst MW, Yuan F, Chilkoti A. Tumor vascular permeability, accumulation, and penetration of macromolecular drug carriers. *J Natl Cancer Inst.* 2006;98:335-44.
- [20] Daldrup H, Shames DM, Wendland M, Okuhata Y, Link TM, Rosenau W, Lu Y, Brasch RC. Correlation of dynamic contrast-enhanced magnetic resonance imaging with histologic tumor grade: comparison of macromolecular and small-molecular contrast media. *Pediatr Radiol.* 1998;28(2):67-78.
- [21] Pham CD, Roberts TP, van Bruggen N, Melnyk O, Mann J, Ferrara N, Cohen RL, Brasch RC. Magnetic resonance imaging detects suppression of tumor vascular permeability after administration of antibody to vascular endothelial growth factor. *Cancer Invest.* 1998;16:225-30.
- [22] Vandoorne K, Addadi Y, Neeman M. Visualizing vascular permeability and lymphatic drainage using labeled serum albumin. *Angiogenesis.* 2010;13(2):75-85.
- [23] Su MY, Mühler A, Lao X, Nalcioğlu O. Tumor characterization with dynamic contrast-enhanced MRI using MR contrast agents of various molecular weights. *Magn Reson Med.* 1998;39(2):259-69.
- [24] Boschi F, Marzola P, Sandri M, Nicolato E, Galiè M, Fiorini S, Merigo F, Lorusso V, Chaabane L, Sbarbati A. Tumor microvasculature observed using different contrast agents: a comparison between Gd-DTPA-Albumin and B-22956/1 in an experimental model of mammary carcinoma. *MAGMA.* 2008; 21(3):169-76.
- [25] Kratz F. Albumin as a drug carrier: design of prodrugs, drug conjugates and nanoparticles. *J Control Release.* 2008;132:171-83.
- [26] Schmiedl U, Ogan MD, Moseley ME, Brasch RC. Comparison of the contrast-enhancing properties of albumin-(Gd-DTPA) and Gd-DTPA at 2.0 T: and experimental study in rats. *AJR Am J Roentgenol.* 1986;147(6):1263-70.
- [27] Dafni H, Landsman L, Schechter B, Kohen F, Neeman M. MRI and fluorescence microscopy of the acute vascular response to VEGF165: vasodilation, hyper-permeability and lymphatic uptake, followed by rapid inactivation of the growth factor. *NMR Biomed.* 2002;15(2):120-31.
- [28] Sennino B, Raatschen HJ, Wendland MF, Fu Y, You WK, Shames DM, McDonald DM, Brasch RC. Correlative dynamic contrast MRI and microscopic assessments of tumor vascularity in RIP-Tag2 transgenic mice. *Magn Reson Med.* 2009;62(3):616-25.
- [29] Marzola P, Ramponi S, Nicolato E, Lovati E, Sandri M, Calderan L, Crescimanno C, Merigo F, Sbarbati A, Grotti A, Vultaggio S, Cavagna F, Lorusso V, Osculati F. Effect of tamoxifen in an experimental model of breast tumor studied by dynamic contrast-enhanced magnetic resonance imaging and different contrast agents. *Invest Radiol.* 2005;40(7):421-9.

### Chapter 3

- [1] Gmitro AF, Lin AF, Jennings DL, Gatenby R. Simultaneous Optical and MR Imaging of Window Chambers. *Proc. Intl. Soc. Mag. Reson. Med* 2007;15:132.
- [2] Yuxiang L, Salek MF, Jennings DL, Gmitro AF. An optical imaging system for window chambers in MRI system. *Proceedings of the SPIE.* 2008;6849:684907-684907-5.
- [3] Gmitro AF, Lin Y, Salek MF. A System for Multi-Modality Optical and MR Imaging of Implanted Window Chambers. *Novel Techniques in Microscopy, OSA Technical Digest (CD), Optical Society of America.* 2009;NWD4.

- [4] Salek MF, Pagel MD, Gmitro AF. Simultaneous dual modality optical and MR imaging of mouse dorsal skin-fold window chamber. *Progress in Biomedical Optics and Imaging - Proceedings of SPIE* 2011;7902.
- [5] Doty FD, Entzminger G, Kulkarni J, Pamarthy K, Staab JP. Radio frequency coil technology for small-animal MRI. *NMR Biomed.* 2007 May; 20(3):304-25.
- [6] Zubia J, Arrue J. Plastic optical fibers: an introduction to their technological processes and applications. *Optical Fiber Technology.* 2007; 7:101-140.
- [7] Hayt WH. *Engineering Electromagnetics.* Seventh Edition. New York: McGraw Hill. 2006. ISBN 0-07-310463-9.
- [8] Dobson SJ, Ribeiro JACL. The primary aberration characteristics of thin-lens models of common relay systems. *Meas. Sci. Technol.* 1994; 5:132-36.
- [9] Object Material Datasheets. 2009. Objet Ltd. [www.objet.com](http://www.objet.com).

## Chapter 4

- [1] Dreher MR, Liu WG, Michelich CR, Dewhirst MW, Yuan F, Chilkoti A. Tumor vascular permeability, accumulation, and penetration of macromolecular drug carriers. *J of the Natl Cancer Inst.* 2006;98:335-44.
- [2] Wu NZ, Klitzman B, Rosner G, Needham D, Dewhirst MW. Measurement of material extravasation in microvascular networks using fluorescence video-microscopy. *Microvasc Res.* 1993;46:231-53.
- [3] Yuan F, Leunig M, Berk DA, Jain RK. Microvascular permeability of albumin, vascular surface area, and vascular volume measured in human adenocarcinoma LS174T using dorsal chamber in SCID mice. *Microvasc Res.* 1993;45:269-89.
- [4] Yankeelov TE, Gore JC. *Dynamic Contrast Enhanced Magnetic Resonance Imaging in Oncology: Theory, Data Acquisition, Analysis, and Examples.* *Curr Med Imaging Rev.* 2007;3:91-107.
- [5] Tofts PS, Brix G, Buckley DL, Evelhoch JL, Henderson E, Knopp MV, Larsson HB, Lee TY, Mayr NA, Parker GJ, Port RE, Taylor J, Weisskoff RM. Estimating kinetic parameters from dynamic contrast-enhanced T(1)-weighted MRI of a diffusible tracer: standardized quantities and symbol. *J Magn Reson Imaging.* 1999;10(3):223-32.
- [6] Brooks DJ, Beaney RP, Lammertsma AA, Turton DR, Marshall J, Thomas DG, Jones T. Studies on regional cerebral haematocrit and blood flow in patients with cerebral tumours using positron emission tomography. *Microvasc Res.* 1986;31(3):267-76.
- [7] Krol A, Maresca J, Dewhirst MW, Yuan F. Available volume fraction of macromolecules in the extravascular space of a fibrosarcoma: implications for drug delivery. *Cancer Res.* 1999;59(16):4136-41.
- [8] Feng Y, Jeong EK, Mohs AM, Emerson L, Lu ZR. Characterization of tumor angiogenesis with dynamic contrast-enhanced MRI and biodegradable macromolecular contrast agents in mice. *Magn Reson Med.* 2008;60(6):1347-52.
- [9] Tofts PS, Brix G, Buckley DL, Evelhoch JL, Henderson E, Knopp MV, Larsson HB, Lee TY, Mayr NA, Parker GJ, Port RE, Taylor J, Weisskoff RM. Estimating kinetic parameters from dynamic contrast-enhanced T(1)-weighted MRI of a diffusible tracer: standardized quantities and symbols. *J Magn Reson Imaging.* 1999;10(3):223-32.
- [10] Klitzman B, Duling BR. Microvascular hematocrit and red cell flow in resting and contracting striated muscle. *Am J Physiol.* 1979;237(4):H481-90.

- [11] Brizel DM, Klitzman B, Cook JM, Edwards J, Rosner G, Dewhirst MW. A comparison of tumor and normal tissue microvascular hematocrits and red cell fluxes in a rat window chamber model. *Int J Radiat Oncol Biol Phys*. 1993;25(2):269-76.
- [12] Lorenz C, Benner T, Chen PJ, Lopez CJ, Ay H, Zhu MW, Menezes NM, Aronen H, Karonen J, Liu Y, Nuutinen J, Sorensen AG. Automated perfusion-weighted MRI using localized arterial input functions. *J Magn Reson Imaging*. 2006;24(5):1133-9.
- [13] Parker GJ, Jackson A, Waterton JC, Buckley DL. Automated arterial input function extraction for T1-weighted DCE-MRI. *Proc ISMRM*. Toronto, Canada. 2003;11:1264.
- [14] Jackson A, Buckley DL, Parker GJ. *Dynamic Contrast-Enhanced Magnetic Resonance Imaging in Oncology*. Springer Berlin Heidelberg New York, Chapter 4. 2005;ISBN 978-3-540-26420-0
- [15] Yuan F, Salehi HA, Boucher Y, Vasthare US, Tuma RF, Jain RK. Vascular permeability and microcirculation of gliomas and mammary carcinomas transplanted in rat and mouse cranial windows. *Cancer Res*. 1994;54(17):4564-8.
- [16] Menger MD, Laschke MW, Vollmar B. Viewing the microcirculation through the window: some twenty years experience with the hamster dorsal skinfold chamber. *Eur Surg Res*. 2002;34(1-2):83-91.
- [17] Yuan F, Salehi HA, Boucher Y, Vasthare US, Tuma RF, Jain RK. Vascular permeability and microcirculation of gliomas and mammary carcinomas transplanted in rat and mouse cranial windows. *Cancer Res*. 1994;54(17):4564-8.
- [18] Wu NZ, Klitzman B, Rosner G, Needham D, Dewhirst MW. Measurement of material extravasation in microvascular networks using fluorescence video-microscopy. *Microvasc Res*. 1993;46:231-53.

## Chapter 5

- [1] Yankeelov TE, Gore JC. *Dynamic Contrast Enhanced Magnetic Resonance Imaging in Oncology: Theory, Data Acquisition, Analysis, and Examples*. *Curr Med Imaging Rev*. 2009;3(2):91-107.
- [2] Sourbron S. Technical aspects of MR perfusion. *Eur J Radiol*. 2010;76(3):304-13.
- [3] Østergaard L. Principles of cerebral perfusion imaging by bolus tracking. *J Magn Reson Imaging*. 2005;22(6):710-7.
- [4] Bernstein MA, King KF, Zhou XJ. *Handbook of MRI Pulse Sequences*. 1st ed. Elsevier Inc. ISBN: 978-0-12-092861-3: 2004:587.
- [5] Donahue KM, Weisskoff RM, Burstein D. Water diffusion and exchange as they influence contrast enhancement. *J Magn Reson Imaging*. 1997;7(1):102-10.
- [6] McConnell HM. Reaction rates by nuclear magnetic resonance. *J Chem Phys*. 1958;28:430-1.
- [7] Leigh JS. Relaxation times in systems with chemical exchange: Some exact solutions. *J Magn Reson*. 1971;4:308-11.
- [8] McLaughlin AC, Leigh JS. Relaxation times in systems with chemical exchange. *J Magn Reson* 1973; 9:296-304.
- [9] Hazlewood C, Chang D, Nichols B, Woessner D. Nuclear magnetic resonance transverse relaxation times of water protons in skeletal muscle. *Biophys J*. 1974;14:583-606.
- [10] Buckley DL, Kershaw LE, Stanisz GJ. Cellular-interstitial water exchange and its effect on the determination of contrast agent concentration in vivo: dynamic contrast-enhanced MRI of human internal obturator muscle. *Magn Reson Med*. 2008;60(5):1011-9.

- [11] Blockley NP, Jiang L, Gardener AG, Ludman CN, Francis ST, Gowland PA. Field strength dependence of R1 and R2\* relaxivities of human whole blood to ProHance, Vasovist, and deoxyhemoglobin. *Magn Reson Med.* 2008;60(6):1313-20.
- [12] Blockley NP, Jiang L, Gardener AG, Ludman CN, Francis ST, Gowland PA. Field strength dependence of R1 and R2\* relaxivities of human whole blood to ProHance, Vasovist, and deoxyhemoglobin. *Magn Reson Med.* 2008;60(6):1313-20.
- [13] Landis CS, Li X, Telang FW, Molina PE, Palyka I, Vetek G, Springer CS Jr. Equilibrium transcytolemmal water-exchange kinetics in skeletal muscle in vivo. *Magn Reson Med.* 1999;42(3):467-78.
- [14] Landis CS, Li X, Telang FW, Coderre JA, Micca PL, Rooney WD, Latour LL, Véték G, Pályka I, Springer CS Jr. Determination of the MRI contrast agent concentration time course in vivo following bolus injection: effect of equilibrium transcytolemmal water exchange. *Magn Reson Med.* 2000 Oct;44(4):563-74.
- [15] Stanisz GJ, Henkelman RM. Gd-DTPA relaxivity depends on macromolecular content. *Magn Reson Med.* 2000;44(5):665-7.
- [16] Sluiter W, Oomens LW, Brand A, Van Furth R. Determination of blood volume in the mouse with 51chromium-labelled erythrocytes. *J Immunol Methods.* 1984;73(1):221-5.
- [17] Brenstein SE. *Biology of the Laboratory Mouse.* McGraw-Hill NY. 1966;337.
- [18] Klitzman B, Duling BR. Microvascular hematocrit and red cell flow in resting and contracting striated muscle. *Am J Physiol.* 1979;237(4):H481-90.
- [19] Yuan F, Salehi HA, Boucher Y, Vasthare US, Tuma RF, Jain RK. Vascular permeability and microcirculation of gliomas and mammary carcinomas transplanted in rat and mouse cranial windows. *Cancer Res.* 1994;54(17):4564-8.
- [20] Yuan F, Dellian M, Fukumura D, Leunig M, Berk DA, Torchilin VP, Jain RK. Vascular permeability in a human tumor xenograft: molecular size dependence and cutoff size. *Cancer Res.* 1995;55(17):3752-6.
- [21] Yuan F, Leunig M, Berk DA, Jain RK. Microvascular permeability of albumin, vascular surface area, and vascular volume measured in human adenocarcinoma LS174T using dorsal chamber in SCID mice. *Microvasc Res.* 1993;45:269-89.
- [22] Wu NZ, Klitzman B, Rosner G, Needham D, Dewhirst MW. Measurement of material extravasation in microvascular networks using fluorescence video-microscopy. *Microvasc Res.* 1993;46:231-53.
- [23] Feng Y, Jeong EK, Mohs AM, Emerson L, Lu ZR. Characterization of tumor angiogenesis with dynamic contrast-enhanced MRI and biodegradable macromolecular contrast agents in mice. *Magn Reson Med.* 2008;60(6):1347-52.
- [24] Boschi F, Marzola P, Sandri M, Nicolato E, Galiè M, Fiorini S, Merigo F, Lorusso V, Chaabane L, Sbarbati A. Tumor microvasculature observed using different contrast agents: a comparison between Gd-DTPA-Albumin and B-22956/1 in an experimental model of mammary carcinoma. *MAGMA.* 2008; 21(3):169-76.
- [25] Feng Y, Jeong EK, Mohs AM, Emerson L, Lu ZR. Characterization of tumor angiogenesis with dynamic contrast-enhanced MRI and biodegradable macromolecular contrast agents in mice. *Magn Reson Med.* 2008;60(6):1347-52.
- [26] Shames DM, Kuwatsuru R, Vexler V, Mühler A, Brasch RC. Measurement of capillary permeability to macromolecules by dynamic magnetic resonance imaging: a quantitative noninvasive technique. *Magn Reson Med.* 1993;29(5):616-22.

- [27] Daldrup H, Shames DM, Wendland M, Okuhata Y, Link TM, Rosenau W, Lu Y, Brasch RC. Correlation of dynamic contrast-enhanced magnetic resonance imaging with histologic tumor grade: comparison of macromolecular and small-molecular contrast media. *Pediatr Radiol*. 1998;28(2):67-78.
- [28] Su MY, Najafi AA, Nalcioglu O. Regional comparison of tumor vascularity and permeability parameters measured by albumin-Gd-DTPA and Gd-DTPA. *Magn Reson Med*. 1995;34(3):402-11.
- [29] Cyran CC, Fu Y, Raatschen HJ, Rogut V, Chaopathomkul B, Shames DM, Wendland MF, Yeh BM, Brasch RC. New macromolecular polymeric MRI contrast agents for application in the differentiation of cancer from benign soft tissues. *J Magn Reson Imaging*. 2008;27(3):581-9.
- [30] Brasch R, Turetschek K. MRI characterization of tumors and grading angiogenesis using macromolecular contrast media: status report. *Eur J Radiol*. 2000;34(3):148-55.
- [31] Li KL, Wilmes LJ, Henry RG, Pallavicini MG, Park JW, Hu-Lowe DD, McShane TM, Shalinsky DR, Fu YJ, Brasch RC, Hylton NM. Heterogeneity in the angiogenic response of a BT474 human breast cancer to a novel vascular endothelial growth factor-receptor tyrosine kinase inhibitor: assessment by voxel analysis of dynamic contrast-enhanced MRI. *J Magn Reson Imaging*. 2005;22(4):511-9.
- [32] Ostrowitzki S, Fick J, Roberts TP, Wendland MF, Aldape KD, Mann JS, Israel MA, Brasch RC. Comparison of gadopentetate dimeglumine and albumin-(Gd-DTPA)<sub>30</sub> for microvessel characterization in an intracranial glioma model. *J Magn Reson Imaging*. 1998;8(4):799-806.
- [33] Wu X, Feng Y, Jeong EK, Emerson L, Lu ZR. Tumor characterization with dynamic contrast enhanced magnetic resonance imaging and biodegradable macromolecular contrast agents in mice. *Pharm Res*. 2009;26(9):2202-8.
- [34] Gossmann A, Okuhata Y, Shames DM, Helbich TH, Roberts TP, Wendland MF, Huber S, Brasch RC. Prostate cancer tumor grade differentiation with dynamic contrast-enhanced MR imaging in the rat: comparison of macromolecular and small-molecular contrast media--preliminary experience. *Radiology*. 1999;213(1):265-72.
- [35] Krol A, Maresca J, Dewhirst MW, Yuan F. Available volume fraction of macromolecules in the extravascular space of a fibrosarcoma: implications for drug delivery. *Cancer Res*. 1999;59(16):4136-41.
- [36] Roberts TP. Physiologic measurements by contrast-enhanced MR imaging: expectations and limitations. *J Magn Reson Imaging*. 1997;7(1):82-90.
- [37] Schabel MC, Parker DL. Uncertainty and bias in contrast concentration measurements using spoiled gradient echo pulse sequences. *Phys Med Biol*. 2008;53(9):2345-73.
- [38] De Naeyer D, Debergh I, De Deene Y, Ceelen WP, Segers P, Verdonck P. First order correction for T<sub>2</sub>\*-relaxation in determining contrast agent concentration from spoiled gradient echo pulse sequence signal intensity. *J Magn Reson Imaging*. 2011;34(3):710-5.
- [39] Kiselev VG. Transverse relaxation effect of MRI contrast agents: a crucial issue for quantitative measurements of cerebral perfusion. *J Magn Reson Imaging*. 2005;22(6):693-6.
- [40] Fritz-Hansen T, Rostrup E, Larsson HBW, Sondergaard L, Ring P, Henrikson O. Measurement of the arterial concentration of Gd-DTPA using MRI: a step toward quantitative perfusion imaging. *Magn Reson Med* 1996;36:225-31.
- [41] McIntyre DJO, Ludwig C, Pasan A, Griffiths JR. A method for interleaved acquisition of a vascular input function for dynamic contrast-enhanced MRI in experimental rat tumours. *NMR Biomed* 2004;17:132-43.

- [42] Yankeelov TE, Luci JJ, Lepage M, Li R, Debusk L, Lin PC, Price RR, Gore JC. Quantitative pharmacokinetic analysis of DCE-MRI data without an arterial input function: a reference region model. *Magn Reson Imaging*. 2005;23(4):519-29.
- [43] Bammer R. Basic principles of diffusion-weighted imaging. *Eur J Radiol*. 2003;45(3):169-84.
- [44] Le Bihan D, Breton E, Lallemand D, Aubin ML, Vignaud J, Laval-Jeantet M. Separation of diffusion and perfusion in intravoxel incoherent motion MR imaging. *Radiology*. 1988;168(2):497-505.
- [45] Koh DM, Collins DJ. Diffusion-weighted MRI in the body: applications and challenges in oncology. *AJR Am J Roentgenol*. 2007;188(6):1622-35.
- [46] Le Bihan D. Intravoxel incoherent motion perfusion MR imaging: a wake-up call. *Radiology*. 2008; 249(3):748-52.
- [47] Koh DM, Collins DJ, Orton MR. Intravoxel incoherent motion in body diffusion-weighted MRI: reality and challenges. *AJR Am J Roentgenol*. 2011;196(6):1351-61.
- [48] Koc Z, Erbay G, Ulasan S, Seydaoglu G, Aka-Bolat F. Optimization of b value in diffusion-weighted MRI for characterization of benign and malignant gynecological lesions. *J Magn Reson Imaging*. 2012; 35(3):650-9.
- [49] Wirestam R, Borg M, Brockstedt S, Lindgren A, Holtås S, Ståhlberg F. Perfusion-related parameters in intravoxel incoherent motion MR imaging compared with CBV and CBF measured by dynamic susceptibility-contrast MR technique. *Acta Radiol*. 2001;42(2):123-8
- [50] Suzuki K, Igarashi H, Watanabe M, Nakamura Y, Nakada T. Separation of perfusion signals from diffusion-weighted image series enabled by independent component analysis. *J Neuroimaging*. 2011; 21(4):384-94.
- [51] Haselgrove JC, Moore JR. Correction for distortion of echo-planar images used to calculate the apparent diffusion coefficient. *Magn Reson Med*. 1996;36(6):960-4.
- [52] Reese TG, Heid O, Weisskoff RM, Wedeen VJ. Reduction of eddy-current-induced distortion in diffusion MRI using a twice-refocused spin echo. *Magn Reson Med*. 2003;49(1):177-82.

## Chapter 6

- [1] Yankeelov TE, Gore JC. Dynamic Contrast Enhanced Magnetic Resonance Imaging in Oncology: Theory, Data Acquisition, Analysis, and Examples. *Curr Med Imaging Rev*. 2009;3(2):91-107.
- [2] Sourbron S. Technical aspects of MR perfusion. *Eur J Radiol*. 2010;76(3):304-13.
- [3] Østergaard L. Principles of cerebral perfusion imaging by bolus tracking. *J Magn Reson Imaging*. 2005;22(6):710-7.
- [4] Bernstein MA, King KF, Zhou XJ. Handbook of MRI Pulse Sequences. 1st ed. Elsevier Inc. ISBN: 978-0-12-092861-3: 2004:587.
- [5] Donahue KM, Weisskoff RM, Burstein D. Water diffusion and exchange as they influence contrast enhancement. *J Magn Reson Imaging*. 1997;7(1):102-10.
- [6] McConnell HM. Reaction rates by nuclear magnetic resonance. *J Chem Phys*. 1958;28:430-1.
- [7] Leigh JS. Relaxation times in systems with chemical exchange: Some exact solutions. *J Magn Reson*. 1971;4:308-11.
- [8] McLaughlin AC, Leigh JS. Relaxation times in systems with chemical exchange. *J Magn Reson* 1973; 9:296-304.

- [9] Hazlewood C, Chang D, Nichols B, Woessner D. Nuclear magnetic resonance transverse relaxation times of water protons in skeletal muscle. *Biophys J*. 1974;14:583-606.
- [10] Buckley DL, Kershaw LE, Stanisz GJ. Cellular-interstitial water exchange and its effect on the determination of contrast agent concentration in vivo: dynamic contrast-enhanced MRI of human internal obturator muscle. *Magn Reson Med*. 2008;60(5):1011-9.
- [11] Blockley NP, Jiang L, Gardener AG, Ludman CN, Francis ST, Gowland PA. Field strength dependence of R1 and R2\* relaxivities of human whole blood to ProHance, Vasovist, and deoxyhemoglobin. *Magn Reson Med*. 2008;60(6):1313-20.
- [12] Blockley NP, Jiang L, Gardener AG, Ludman CN, Francis ST, Gowland PA. Field strength dependence of R1 and R2\* relaxivities of human whole blood to ProHance, Vasovist, and deoxyhemoglobin. *Magn Reson Med*. 2008;60(6):1313-20.
- [13] Landis CS, Li X, Telang FW, Molina PE, Palyka I, Vetek G, Springer CS Jr. Equilibrium transcytolemmal water-exchange kinetics in skeletal muscle in vivo. *Magn Reson Med*. 1999;42(3):467-78.
- [14] Landis CS, Li X, Telang FW, Coderre JA, Micca PL, Rooney WD, Latour LL, Véték G, Pályka I, Springer CS Jr. Determination of the MRI contrast agent concentration time course in vivo following bolus injection: effect of equilibrium transcytolemmal water exchange. *Magn Reson Med*. 2000 Oct;44(4):563-74.
- [15] Stanisz GJ, Henkelman RM. Gd-DTPA relaxivity depends on macromolecular content. *Magn Reson Med*. 2000;44(5):665-7.
- [16] Sluiter W, Oomens LW, Brand A, Van Furth R. Determination of blood volume in the mouse with 51chromium-labelled erythrocytes. *J Immunol Methods*. 1984;73(1):221-5.
- [17] Brenstein SE. *Biology of the Laboratory Mouse*. McGraw-Hill NY. 1966;337.
- [18] Klitzman B, Duling BR. Microvascular hematocrit and red cell flow in resting and contracting striated muscle. *Am J Physiol*. 1979;237(4):H481-90.
- [19] Yuan F, Salehi HA, Boucher Y, Vasthare US, Tuma RF, Jain RK. Vascular permeability and microcirculation of gliomas and mammary carcinomas transplanted in rat and mouse cranial windows. *Cancer Res*. 1994;54(17):4564-8.
- [20] Yuan F, Dellian M, Fukumura D, Leunig M, Berk DA, Torchilin VP, Jain RK. Vascular permeability in a human tumor xenograft: molecular size dependence and cutoff size. *Cancer Res*. 1995;55(17):3752-6.
- [21] Yuan F, Leunig M, Berk DA, Jain RK. Microvascular permeability of albumin, vascular surface area, and vascular volume measured in human adenocarcinoma LS174T using dorsal chamber in SCID mice. *Microvasc Res*. 1993;45:269-89.
- [22] Wu NZ, Klitzman B, Rosner G, Needham D, Dewhirst MW. Measurement of material extravasation in microvascular networks using fluorescence video-microscopy. *Microvasc Res*. 1993;46:231-53.
- [23] Feng Y, Jeong EK, Mohs AM, Emerson L, Lu ZR. Characterization of tumor angiogenesis with dynamic contrast-enhanced MRI and biodegradable macromolecular contrast agents in mice. *Magn Reson Med*. 2008 Dec;60(6):1347-52.
- [24] Boschi F, Marzola P, Sandri M, Nicolato E, Galiè M, Fiorini S, Merigo F, Lorusso V, Chaabane L, Sbarbati A. Tumor microvasculature observed using different contrast agents: a comparison between Gd-DTPA-Albumin and B-22956/1 in an experimental model of mammary carcinoma. *MAGMA*. 2008; 21(3):169-76.

- [25] Feng Y, Jeong EK, Mohs AM, Emerson L, Lu ZR. Characterization of tumor angiogenesis with dynamic contrast-enhanced MRI and biodegradable macromolecular contrast agents in mice. *Magn Reson Med*. 2008;60(6):1347-52.
- [26] Shames DM, Kuwatsuru R, Vexler V, Mühler A, Brasch RC. Measurement of capillary permeability to macromolecules by dynamic magnetic resonance imaging: a quantitative noninvasive technique. *Magn Reson Med*. 1993;29(5):616-22.
- [27] Daldrup H, Shames DM, Wendland M, Okuhata Y, Link TM, Rosenau W, Lu Y, Brasch RC. Correlation of dynamic contrast-enhanced magnetic resonance imaging with histologic tumor grade: comparison of macromolecular and small-molecular contrast media. *Pediatr Radiol*. 1998;28(2):67-78.
- [28] Su MY, Najafi AA, Nalcioglu O. Regional comparison of tumor vascularity and permeability parameters measured by albumin-Gd-DTPA and Gd-DTPA. *Magn Reson Med*. 1995;34(3):402-11.
- [29] Cyran CC, Fu Y, Raatschen HJ, Rogut V, Chaopathomkul B, Shames DM, Wendland MF, Yeh BM, Brasch RC. New macromolecular polymeric MRI contrast agents for application in the differentiation of cancer from benign soft tissues. *J Magn Reson Imaging*. 2008;27(3):581-9.
- [30] Brasch R, Turetschek K. MRI characterization of tumors and grading angiogenesis using macromolecular contrast media: status report. *Eur J Radiol*. 2000;34(3):148-55.
- [31] Li KL, Wilmes LJ, Henry RG, Pallavicini MG, Park JW, Hu-Lowe DD, McShane TM, Shalinsky DR, Fu YJ, Brasch RC, Hylton NM. Heterogeneity in the angiogenic response of a BT474 human breast cancer to a novel vascular endothelial growth factor-receptor tyrosine kinase inhibitor: assessment by voxel analysis of dynamic contrast-enhanced MRI. *J Magn Reson Imaging*. 2005;22(4):511-9.
- [32] Ostrowitzki S, Fick J, Roberts TP, Wendland MF, Aldape KD, Mann JS, Israel MA, Brasch RC. Comparison of gadopentetate dimeglumine and albumin-(Gd-DTPA)<sub>30</sub> for microvessel characterization in an intracranial glioma model. *J Magn Reson Imaging*. 1998;8(4):799-806.
- [33] Wu X, Feng Y, Jeong EK, Emerson L, Lu ZR. Tumor characterization with dynamic contrast enhanced magnetic resonance imaging and biodegradable macromolecular contrast agents in mice. *Pharm Res*. 2009;26(9):2202-8.
- [34] Gossmann A, Okuhata Y, Shames DM, Helbich TH, Roberts TP, Wendland MF, Huber S, Brasch RC. Prostate cancer tumor grade differentiation with dynamic contrast-enhanced MR imaging in the rat: comparison of macromolecular and small-molecular contrast media--preliminary experience. *Radiology*. 1999;213(1):265-72.
- [35] Krol A, Maresca J, Dewhirst MW, Yuan F. Available volume fraction of macromolecules in the extravascular space of a fibrosarcoma: implications for drug delivery. *Cancer Res*. 1999;59(16):4136-41.
- [36] Roberts TP. Physiologic measurements by contrast-enhanced MR imaging: expectations and limitations. *J Magn Reson Imaging*. 1997;7(1):82-90.
- [37] Schabel MC, Parker DL. Uncertainty and bias in contrast concentration measurements using spoiled gradient echo pulse sequences. *Phys Med Biol*. 2008;53(9):2345-73.
- [38] De Naeyer D, Debergh I, De Deene Y, Ceelen WP, Segers P, Verdonck P. First order correction for T2\*-relaxation in determining contrast agent concentration from spoiled gradient echo pulse sequence signal intensity. *J Magn Reson Imaging*. 2011;34(3):710-5.
- [39] Kiselev VG. Transverse relaxation effect of MRI contrast agents: a crucial issue for quantitative measurements of cerebral perfusion. *J Magn Reson Imaging*. 2005;22(6):693-6.

- [40] Fritz-Hansen T, Rostrup E, Larsson HBW, Sondergaard L, Ring P, Henrikson O. Measurement of the arterial concentration of Gd-DTPA using MRI: a step toward quantitative perfusion imaging. *Magn Reson. Med* 1996;36:225–31.
- [41] McIntyre DJO, Ludwig C, Pasan A, Griffiths JR. A method for interleaved acquisition of a vascular input function for dynamic contrast-enhanced MRI in experimental rat tumours. *NMR Biomed* 2004;17:132-43.
- [42] Yankeelov TE, Luci JJ, Lepage M, Li R, Debusk L, Lin PC, Price RR, Gore JC. Quantitative pharmacokinetic analysis of DCE-MRI data without an arterial input function: a reference region model. *Magn Reson Imaging*. 2005;23(4):519-29.
- [43] Bammer R. Basic principles of diffusion-weighted imaging. *Eur J Radiol*. 2003;45(3):169-84.
- [44] Le Bihan D, Breton E, Lallemand D, Aubin ML, Vignaud J, Laval-Jeantet M. Separation of diffusion and perfusion in intravoxel incoherent motion MR imaging. *Radiology*. 1988;168(2):497-505.
- [45] Koh DM, Collins DJ. Diffusion-weighted MRI in the body: applications and challenges in oncology. *AJR Am J Roentgenol*. 2007;188(6):1622-35.
- [46] Le Bihan D. Intravoxel incoherent motion perfusion MR imaging: a wake-up call. *Radiology*. 2008; 249(3):748-52.
- [47] Koh DM, Collins DJ, Orton MR. Intravoxel incoherent motion in body diffusion-weighted MRI: reality and challenges. *AJR Am J Roentgenol*. 2011;196(6):1351-61.
- [48] Koc Z, Erbay G, Ulasan S, Seydaoglu G, Aka-Bolat F. Optimization of b value in diffusion-weighted MRI for characterization of benign and malignant gynecological lesions. *J Magn Reson Imaging*. 2012; 35(3):650-9.
- [49] Wirestam R, Borg M, Brockstedt S, Lindgren A, Holtås S, Ståhlberg F. Perfusion-related parameters in intravoxel incoherent motion MR imaging compared with CBV and CBF measured by dynamic susceptibility-contrast MR technique. *Acta Radiol*. 2001;42(2):123-8
- [50] Suzuki K, Igarashi H, Watanabe M, Nakamura Y, Nakada T. Separation of perfusion signals from diffusion-weighted image series enabled by independent component analysis. *J Neuroimaging*. 2011; 21(4):384-94.
- [51] Haselgrove JC, Moore JR. Correction for distortion of echo-planar images used to calculate the apparent diffusion coefficient. *Magn Reson Med*. 1996;36(6):960-4.
- [52] Reese TG, Heid O, Weisskoff RM, Wedeen VJ. Reduction of eddy-current-induced distortion in diffusion MRI using a twice-refocused spin echo. *Magn Reson Med*. 2003;49(1):177-82.

## Chapter 7

- [1] Object Material Datasheets. 2009. Objet Ltd. [www.objet.com](http://www.objet.com).
- [2] Wind RA, Minard KR, Holtom GR, Majors PD, Ackerman EJ, Colson SD, Cory DG, Daly DS, Ellis PD, Metting NF, Parkinson CI, Price JM, Tang XW. An integrated confocal and magnetic resonance microscope for cellular research. *J Magn Reson*. 2000;147(2):371-7.
- [3] Majors PD, Minard KR, Ackerman EJ, Holtom GR, Hopkins DF, Parkinson CL, Weber TJ, Wind RA. A combined confocal and magnetic resonance microscope for biological studies. *Rev Sci Instrum*. 2002;73:4329-38.
- [4] Conchello JA, Lichtman JW. Optical sectioning microscopy. *Nat Methods*. 2005;2(12):920-31.
- [5] Sibarita JB. Deconvolution microscopy. *Adv Biochem Eng Biotechnol*. 2005;95:201-43.

- [6] Dreher MR, Liu WG, Michelich CR, Dewhirst MW, Yuan F, Chilkoti A. Tumor vascular permeability, accumulation, and penetration of macromolecular drug carriers. *J of the Natl Cancer Inst.* 2006;98:335-44.
- [7] Wu NZ, Klitzman B, Rosner G, Needham D, Dewhirst MW. Measurement of material extravasation in microvascular networks using fluorescence video-microscopy. *Microvasc Res.* 1993;46:231-53.
- [8] Wu X, Feng Y, Jeong EK, Emerson L, Lu ZR. Tumor characterization with dynamic contrast enhanced magnetic resonance imaging and biodegradable macromolecular contrast agents in mice. *Pharm Res.* 2009;26(9):2202-8.
- [9] Wirestam R, Borg M, Brockstedt S, Lindgren A, Holtås S, Ståhlberg F. Perfusion-related parameters in intravoxel incoherent motion MR imaging compared with CBV and CBF measured by dynamic susceptibility-contrast MR technique. *Acta Radiol.* 2001;42(2):123-8
- [10] Suzuki K, Igarashi H, Watanabe M, Nakamura Y, Nakada T. Separation of perfusion signals from diffusion-weighted image series enabled by independent component analysis. *J Neuroimaging.* 2011; 21(4):384-94.
- [11] Haselgrove JC, Moore JR. Correction for distortion of echo-planar images used to calculate the apparent diffusion coefficient. *Magn Reson Med.* 1996;36(6):960-4.
- [12] Reese TG, Heid O, Weisskoff RM, Wedeen VJ. Reduction of eddy-current-induced distortion in diffusion MRI using a twice-refocused spin echo. *Magn Reson Med.* 2003;49(1):177-82.
- [13] Yihan Wu, Wenjie Zhang, Jinbo Li, Yan Zhang. Optical imaging of tumor microenvironment. *Am J Nucl Med Mol Imaging.* 2013;3(1):1-15.
- [14] Gillies RJ, Raghunand N, Karczmar GS, Bhujwala ZM. MRI of the tumor microenvironment. *J Magn Reson Imaging.* 2002;16(4):430-50.